Title

X-Ray Computed Tomography of Microstructure Evolution during Polymer Impregnation and Pyrolysis Processing of Ceramic Matrix Composites

Author

Larson, Natalie Marie

Publication Date

2018

University of California
Santa Barbara

X-Ray Computed Tomography of Microstructure Evolution during Polymer Impregnation and Pyrolysis Processing of Ceramic Matrix Composites

A dissertation submitted in partial satisfaction
of the requirements for the degree

Doctor of Philosophy
in
Materials

by

Natalie Marie Larson

Committee in charge:

Professor Frank W. Zok, Chair
Professor Matthew R. Begley
Professor Carlos G. Levi
Professor Frederic Gibou

December 2018

The dissertation of Natalie Marie Larson is approved.

Professor Matthew R. Begley

Professor Carlos G. Levi

Professor Frederic Gibou

Professor Frank W. Zok, Committee Chair

December 2018

X-Ray Computed Tomography of Microstructure Evolution during Polymer Impregnation and Pyrolysis Processing of Ceramic Matrix Composites

by

Natalie Marie Larson

For John Williams and Nadia, Craig, & Garrett Larson

Acknowledgments

I would like to express my sincere gratitude to my advisor Frank Zok for granting me freedom to approach challenges in my own way. His continuing guidance and support have been of great value to my professional growth and have afforded me unique opportunities to explore my interests.

I would also like to express my appreciation to my mentors Dula Parkinson and Alastair MacDowell at the Advanced Light Source (ALS) at Lawrence Berkeley National Laboratory (LBNL). I have been very privileged to perform a large part of my graduate research in residence at the ALS, and my professional development has benefited tremendously from the mentoring and support I received there.

I would also like to thank my remarkable colleagues at UCSB and LBNL for their help, suggestions, feedback and support. In particular, I would like to thank my committee, Matthew Begley, Carlos Levi, and Frederic Gibou, for their continued guidance on my research. I would also like to thank Tresa Pollock for her continued support, in particular regarding my activities aimed at advancing diversity, equity and inclusion in STEM. I also express my gratitude to Harold Barnard, Jonathan Ajo-Franklin, John Shaw, Ben Callaway, Mike MacNeil, James Davies, Ilir Beta, Pete Maxwell, Deryck Stave and Richard Bock for assistance with experiments and data analysis. I also thank Jana Staudt, Charlene Cuellar, and Richard Sim for their contributions to this work during their internships. I would also like to acknowledge Wennie Wang and Rebecca Reitz for their support both professionally and personally.

Finally, I thank my partner John Williams, my brother Garrett Larson, and my parents Nadia and Craig Larson for their enduring love, support and encouragement, and for always believing in me.

* * *

I gratefully acknowledge the Office of Naval Research (grant N00014-13-1-0860, monitored by Dr. David A. Shifler) for funding this work. I am also very grateful for the following fellowship support: a Holbrook Foundation Graduate Fellowship through the UCSB IEE; a UCSB Chancellor's Graduate Fellowship; a Doctoral Fellowship from the Advanced Light Source (ALS), a Division of Lawrence Berkeley National Laboratory (LBNL), with funding provided by the U.S. Department of Energy (DOE); and a National Science Foundation (NSF) Graduate Research Fellowship under Grant No. 1144085. I also gratefully acknowledge support from Beamline 8.3.2 at the ALS, a Division of LBNL, and the Molecular Foundry at LBNL. The ALS and the Molecular Foundry are supported by the Director, Office of Science, Office of Basic Energy Sciences, of the U.S. DOE under Contract No. DE-AC02-05CH11231. The SiC fibers used in this study were kindly provided by Pratt and Whitney. Finally, I acknowledge the MRL Shared Experimental Facilities at UCSB which are supported by the MRSEC Program of the NSF under Award No. DMR 1121053, a member of the NSF-funded Materials Research Facilities Network.

Curriculum Vitæ

Natalie Marie Larson

Education

2018 Ph.D. in Materials, University of California, Santa Barbara.

2013 B.S. in Materials Science & Engineering, University of Washington, Seattle, WA.

Publications

8. **Natalie M. Larson**, Frank W. Zok. "*In-situ* 3D visualization of crack formation during polymer-to-ceramic conversion in microtube geometries". *In Preparation*
7. **Natalie M. Larson**, Charlene Cuellar, Frank W. Zok. "X-ray computed tomography of microstructure evolution during matrix impregnation and curing in unidirectional fiber beds". *Composites Part A* (available online Nov. 2018). **[doi]**
6. **Natalie M. Larson**, Frank W. Zok. "Insights from in-situ x-ray computed tomography during axial impregnation of unidirectional fiber beds". *Composites Part A* **107**, 124-134 (2018). **[doi]**
5. **Natalie M. Larson**, Frank W. Zok. "In-situ 3D visualization of composite microstructure during polymer-to-ceramic conversion". *Acta Materialia* **144**, 579-589 (2018). **[doi]**
4. Harold S. Barnard, Alastair A. MacDowell, Dilworth Y. Parkinson, **Natalie M. Larson**, Josh C. Peterson, Francesco Panerai, Nagi N. Mansour, Yan Gao. "Synchrotron X-ray Micro Tomography at the Advanced Light Source: In-Situ Sample Environments for Advanced Aerospace Materials". *Microscopy and Microanalysis* **24** (S2), 444-445 (2018). **[doi]**
3. Talita Perciano, Daniela Ushizima, Harinarayan Krishnan, Dilworth Parkinson, **Natalie M. Larson**, Daniël M. Pelt, Wes Bethel, Frank Zok and James Sethian, "Insight into 3D micro-CT data: exploring segmentation algorithms through performance metrics". *Journal of Synchrotron Radiation* **24**, 1065 – 1077 (2017). **[doi]**
2. Harold S. Barnard, Alastair A. MacDowell, Dilworth Y. Parkinson, Pratiti Mandal, Michael Czabaj, Yan Gao, Emmanuel Maillet, B. Blank, **Natalie M. Larson**, Robert O. Ritchie, Bernd Gludovatz, Claire Acevedo, Dong Liu. "Synchrotron X-ray micro-tomography at the Advanced Light Source: Developments in high temperature in-situ mechanical testing". *Journal of Physics: Conf. Series* **849** 012043 (2017). **[doi]**
1. Alastair A. MacDowell, Harold Barnard, Dilworth Y. Parkinson, Abdel Haboub, **Natalie M. Larson**, Frank Zok, Francesco Parerai, Nagi N. Mansour, Hrishikesh Bale, Bernd Gludovatz, Claire Acevedo, Dong Liu, Robert O. Ritchie. "High Temperature X-Ray Micro-Tomography". *AIP Conference Proceedings* **1741**, 050005 (2016). **[doi]**

Abstract

X-Ray Computed Tomography of Microstructure Evolution during Polymer Impregnation and Pyrolysis Processing of Ceramic Matrix Composites

by

Natalie Marie Larson

SiC_f/SiC ceramic matrix composites (CMCs) have the potential to enable significant increases in thermal efficiency of aerospace engines. However, fabrication of dense CMCs that can operate for extended periods at targeted use temperatures (1500°C) remains an outstanding challenge. In this dissertation, fundamental studies on one promising fabrication approach – polymer impregnation and pyrolysis (PIP) – provide new insights on microstructure evolution during matrix processsing. X-ray computed tomography (XCT) is used to elucidate the key underlying phenomena, including fluid flow, fiber movement, bubble formation, and pyrolysis crack formation, during the first PIP cycle in unidirectional fiber beds. New analysis techniques are developed to enable qualitative observations and quantitative metrics of microstructure evolution. The results are used to elucidate coupled effects of capillary number, fiber movement and preferred flow channeling on axial permeability of fiber beds. Additionally, relationships between processing conditions, local fiber bed porosity, fiber movement, and void locations and sizes after both impregnation and curing are identified. Finally, a unified taxonomy of pyrolysis crack geometries and crack structures is developed, and the temporal sequence of their formation is revealed. Effects of local microstructural dimensions on crack spacing, initiation temperature and final hierarchical order are also quantified. Techniques employed in this work as well as the resulting insights on microstructure evolution could be used in development and validation of physics-based models for advancement of PIP processing.

Contents

List of Figures

Chapter 1

Introduction

1.1 Ceramic Matrix Composites for More Efficient Engines

SiC_f/SiC ceramic-matrix composites (CMCs) are of significant technological interest for development of more powerful and more efficient aerospace engines [1–5]. Increasing engine efficiency demands materials that can operate in more hostile conditions with higher temperatures and higher stresses [1–5]. While development of thermal barrier coatings (TBCs) has enabled significant increases in operating temperatures over the last several decades, the temperature capability of the primary structural materials, Ni-based superalloys, has shown relatively smaller gains (Fig. 1.1(A)). Due to the widening gap in temperature capability between TBCs and superalloys, additional cooling is required and inefficiency losses are greater (Fig. 1.1(B)). To combat this issue, primary structural materials with higher temperature capability are required. Relative to Ni-based superalloys currently used in engines, SiC_f/SiC CMCs offer about triple the specific strength and can survive sustained loading up to temperatures that are 100-200°C higher (Fig. 1.2) [1, 3, 4].

CMCs of prime interest comprise continuous SiC fibers with thin BN coatings surrounded by a matrix of SiC. The coatings promote crack deflection and frictional pullout, imparting high toughness to the CMC [1, 3, 5]. The SiC matrix protects the fibers and distributes load [3, 6, 7]. Despite their promise, fabrication of fully-dense, compositionally-pure SiC matrices that can withstand the targeted upper-use temperatures (1500°C) remains an outstanding challenge [1, 3]. One promising fabrication approach, polymer impregnation and pyrolysis (PIP), is explored in this dissertation. This Chapter provides an overview of four potential matrix processing methods (including PIP) and potential hybrid approaches (Section 1.2) as well as an outline of the remainder of the dissertation (Section 1.3).

1.2 Matrix Processing Methods

SiC matrices in SiC_f/SiC CMCs may be processed via several routes. In all cases, fibers are first coated with a thin layer of BN followed by a thin protective layer of SiC or Si_3N_4 by chemical vapor infiltration (CVI) [2, 3, 8]. Next, the matrix phase is introduced via one or more processes: (1) CVI, (2) slurry infiltration, (3) (reactive) melt infiltration ((R)MI), and (4) polymer impregnation and pyrolysis (PIP) [2–4, 6, 8]. An overview of these and hybrid approaches follows.

1.2.1 Chemical Vapor Infiltration

In the CVI route, SiC is deposited within the preform from gaseous precursors. The process is carried out at relatively low temperatures (900-1100°C) with minimal risk of fiber degradation [2, 8]. Furthermore, CVI is amenable to fabrication of CMCs with large and complex shapes, yielding near-net-shape parts [2, 8]. The resulting layers of deposited SiC are pure, crystalline, and fully dense, with high local hermeticity and high thermal conductivity and creep resistance [2, 3, 8].

The key challenge with CVI is to maintain open porosity through the end of densification [2, 3, 8]. As the layers of SiC build within the fiber tows and on the tow surfaces, small channels within the preform close off, trapping large, sharp and irregularly shaped voids in the matrix [2, 3, 8]. Strategies for delaying void entrapment include the use of low deposition rates, engineered pressure and temperature gradients (e.g., low temperatures at void entrances), and periodic surface machining to re-open sealed void entrances [2, 3, 8]. Because of the low deposition rates required to minimize pore entrapment, the CVI process is relatively slow and costly [2, 8]. Furthermore, even under the best circumstances, significant residual porosity (typically 10-15%) remains, yielding composites with compromised thermal conductivity, low matrix cracking strength, and low interlaminar strength [2, 3, 8].

1.2.2 Slurry Infiltration

In the slurry infiltration route, the matrix precursor consists of a suspension of SiC powder in a liquid typically containing sintering aids and a fugitive binder [2, 3]. After the fiber preform is impregnated with the slurry, the matrix is sintered at high temperature under pressure [2]. However, even with sintering aids, sintering of SiC particles is extremely slow at temperatures below which SiC fibers begin to degrade [2]. Additionally, due to physical constraints imposed by the fibers, full densification of the matrix cannot be achieved by sintering alone.

Despite challenges with sintering, the use of SiC powders in SiC matrix processing is highly advantageous because slurry impregnation can be used to fill interstices between fibers and tows with pure, dense, crystalline SiC at high particle packing densities. The remaining challenge is to bind the particles together via subsequent processing routes such as PIP or (R)MI [2, 3, 8–11]. In the case of PIP processing, SiC particles may also be introduced to the preceramic polymer prior to impregnation, eliminating the need for a separate slurry impregnation and drying stage [2–4, 12–15].

1.2.3 (Reactive) Melt Infiltration

Matrix processing via (reactive) melt infiltration ((R)MI) involves two steps. In the first, the fiber preform is filled with (passive) SiC or (active) C fillers via slurry infiltration, tape-casting with a polymer-based binder, or impregnation and pyrolysis of a liquid SiC or C precursor [2, 3, 8]. In the second step, residual open pores are impregnated with liquid Si or Si-based alloy [2, 3, 8]. In the case where C fillers are used, Si reacts with C to form SiC [2, 3, 8]. Relative to the other SiC matrix processing techniques, (R)MI offers a short processing time and yields composites with minimal porosity and thus excellent hermeticity, high thermal conductivity, high interlaminar strength, and high in-plane matrix cracking stress [2, 3].

The most successful RMI SiC_f/SiC thus far was developed by General Electric, leading to the first large-scale use of SiC_f/SiC CMCs in commercial gas turbine engines in 2016 [1, 3, 8]. Here coated tows are pre-pregged into unidirectional tapes with a polymer binder containing SiC and C particles [3, 8]. The prepreg tapes are then cut, oriented, laid up, and consolidated at high temperature [3, 8]. In the final step, the preform is impregnated with molten Si which reacts with the C particles to form SiC [3, 8]. Although ideally the molten Si would be fully consumed by reaction with C in the formation of SiC, in practice some amount of free Si always remains [3].

There are several drawbacks to the (R)MI process. First, impregnation temperatures for liquid Si and Si alloys are relatively high (1,400-1,600°C), thus requiring use of fibers with high thermal stability [2, 3]. Additionally, in the case of reactive melt infiltration, reaction products may block the channels for Si infiltration via a phenomenon known as reaction choking [2, 16]. Thus, special care must be taken in optimizing the preform microstructure and the impregnation process to ensure that flow channels for liquid Si remain open long enough for complete impregnation [2, 16]. Finally, since (R)MI yields some free Si, the upper use temperature of the composite is limited by the (relatively low) melting point of Si (1,400°C) [2, 3, 8, 16]. At temperatures approaching 1,400°C, free Si can attack the BN coatings and SiC fibers, and beneficial residual stresses resulting from RMI processing tend to disappear [2, 8]. Even below the Si melting point, the low creep resistance of Si leads to undesirable matrix creep starting at about 1,100°C and becoming excessive above 1,300°C, thus limiting the CMC use temperature to ≈1250°C [8].

Efforts to eliminate free Si from RMI products primarily involve utilizing Si alloys that display (i) low eutectic points (<1,400°C, to enable low-temperature impregnation) and (ii) residual silicides with high melting points (to enable higher CMC use temperatures) [3, 16].

1.2.4 Polymer Impregnation and Pyrolysis

The PIP process involves impregnation of a preceramic polymer into a fiber preform, followed by curing and pyrolysis to produce a polymer-derived ceramic (PDC) matrix [2, 3, 6, 8, 11, 13, 14, 17]. A variety of SiC precursors may be employed, such as polycarbosilanes or polyvinylsilanes, which are converted to amorphous SiC after pyrolysis to ≈800-1,000°C and may be subsequently crystallized at 1,000-1,600°C [2, 3, 6, 17–21]. Due to shrinkage of the preceramic polymer during polymer-to-ceramic conversion (≈20-30% volumetric yield), the resulting matrix is heavily micro-cracked with high residual porosity [2, 3, 8, 21, 22]. In order to further densify the matrix, the PIP process is repeated several times (typically 6-14 times), progressively filling voids and shrinkage cracks remaining from previous processing cycles [2, 3, 6, 8, 11, 13, 14, 17]. Even after several repeated PIP cycles, the resulting matrix is typically micro-cracked and somewhat friable, with relatively low matrix cracking strength and thermal conductivity [2, 3, 8, 11, 13, 14]. Furthermore, the resulting microstructures are often heterogeneous in nature, with pores and cracks in the matrix ranging in size from nanometers to hundreds of micrometers [3, 6, 7, 23]. These heterogeneities can, in turn, lead to spatial inhomogeneities in the degree of protection that the matrix can provide to the fibers and hence compromise long-term composite durability [3, 6, 7]. Additional drawbacks of the PIP process include the time-consuming (and often costly) nature of repeated impregnation and pyrolysis, the high temperatures required (typically 1,400-1,600°C) to crystallize the matrix on a reasonable time scale, and the potential for oxygen and free carbon impurities that reduce composite durability [2, 3, 6, 8, 17].

Despite these shortcomings, the PIP process offers a highly flexible route for producing CMCs without free Si, with opportunities for process developments that could produce denser, stronger and more thermally conductive matrices [2, 4, 8, 10, 12–14, 17, 24]. One of the advantages of the PIP process is that it can make use of well-established methods of fabrication of polymer matrix composites (PMCs) [2, 8, 13, 24]. These methods have demonstrated (1) ease of large-scale processing with complex part geometry, (2) low cost, and (3) potential for high impregnation efficiency [13, 14, 24]. Processing with preceramic polymers also offers control over ceramic yield, chemical composition, microstructure, and nanostructure through careful design of polymer type and molecular structure and through tailoring of the temperature, pressure and gaseous environment during curing, pyrolysis and crystallization [12, 13, 17, 22, 24, 25].

1.2.5 Hybrid approaches

None of the aforementioned processes in isolation have proven effective in producing SiC matrices that can operate under sustained loading at target use temperatures of 1,500°C. It is widely recognized that innovative approaches involving hybrids of these processes need to be developed to reach performance goals. Already, CVI is the method of choice for the first stage of processing: deposition of a thin coating of the interphase (BN) followed by a thin protective coating of SiC or Si_3N_4 [2, 3, 8]. Remaining matrix densification may be performed with various combinations of CVI, slurry infiltration, (R)MI, and PIP [2–4, 8]. One proposed combination involves first performing CVI or several rounds of PIP to maximize the fraction of pure SiC in the matrix, followed by (R)MI to fill the residual pores inherent to both techniques and thus increase hermeticity and thermal conductivity [2, 3]. Another approach involves partial densification with CVI followed by PIP (additional details below) [8]. Alternatively, several rounds of PIP (and subsequent crystallization) might be followed by (R)MI or CVI to fill remaining pores [2, 3]. In another approach, infiltration of a SiC powder slurry is performed first to rapidly fill a significant amount of the preform with pure, crystalline SiC [2]. Slurry infiltration may be followed by repeated PIP and (possibly) a final round of CVI, or by MI [2, 8–11]. Alternatively, the first PIP cycle (in any of the aforementioned processes starting with PIP) may be performed with a preceramic polymer loaded with an inactive filler, typically fine SiC particles, to increase the effective volumetric yield [2–4, 12–15]. Later PIP cycles require preceramic polymers alone as particles tend to clog narrow channels in the remaining pore network and thus prevent full impregnation [11]. In all cases, these multi-step processes require that a contiguous network of ingress pathways is present after intermediate PIP or CVI stages to attain nearly-full densification in subsequent processing steps.

Potential benefits of a hybrid route for fabricating CMCs without free Si have been demonstrated [8]. The route utilizes CVI for partial filling of the preform followed by PIP to fill the remaining pores (process designated CVI-PIP). This method was designed to exploit the advantages of full CVI and full PIP while avoiding some of their drawbacks (Fig. 1.3). For example, utilizing only partial CVI allows for shorter deposition times and reduced closed-void entrapment, while retaining some of the high strength, creep resistance and thermal conductivity of CVI SiC. Meanwhile, utilizing PIP for the final densification stages allows for more rapid processing of SiC with fewer cycles and thus fewer opportunities for oxygen contamination than the PIP approach alone. Although this approach does not achieve full densification, the resulting composites appear to show the best high-temperature stress rupture behavior relative to those made by other routes (Fig. 1.4).

1.3 Dissertation Outline

The PIP process is of great interest because it can be used to fabricate SiC_f/SiC CMCs without free Si and because of its processing flexibility and potential to be further developed for use in independent or hybrid approaches. The goal of the research presented in this dissertation is to enable advancement of the PIP process through development of a stronger fundamental understanding of microstructure evolution during each stage of PIP. The research approach involves direct observation of microstructure in 3D using X-ray computed tomography (XCT), paired with complementary studies on preceramic polymer pyrolysis. Novel experimental methods and analysis techniques are developed to enable detailed qualitative observations and quantitative metrics of microstructure evolution. Insights gained from this work provide a foundation for development of a physics-based modeling framework for advancement of the PIP process.

The dissertation is organized in the following way. Chapter 2 presents background on the use of the PIP process in engineering practice and on the materials and fundamental processes involved in PIP. Chapter 2 concludes with a discussion on preliminary studies that demonstrate the critical importance of the first PIP cycle in repeated PIP processing. The preliminary studies set the foundation for work presented in the remaining Chapters. Chapters 3-5 present original research on microstructural evolution during the first impregnation, curing, and pyrolysis cycle in unidirectional fiber beds. The focus of the work is on unidirectional minicomposites in order to obviate the complexities associated with multidirectional laminates or weaves, and thus enable fundamental studies on the key underlying phenomena associated with microstructure evolution during PIP. Chapter 3 presents a study in which XCT imaging is performed *in-situ* during impregnation, enabling observation of fiber movement, preferred flow channeling, and void formation over a range of capillary numbers. Quantification of the effects of fiber movement and preferred flow channeling on permeability are used to rationalize the increase in measured permeability with capillary number. Chapter 4 presents methods and analysis techniques to reveal correlations between void sizes, void locations, and local fiber packing over the course of impregnation and curing. Notably, the results reveal the combined effects of capillary number and pressure removal on void formation during impregnation. In Chapter 5, experimental results revealing the three-dimensional nature and evolution of CMC microstructure during pyrolysis to 1,200°C are presented. In this study, a unified taxonomy of crack structures is developed, and the temporal hierarchy of their formation is identified. Additionally, the effects of local microstructural dimensions on the conditions required to form various crack types are quantified. Finally, conclusions and recommendations for future research are discussed in Chapter 6.

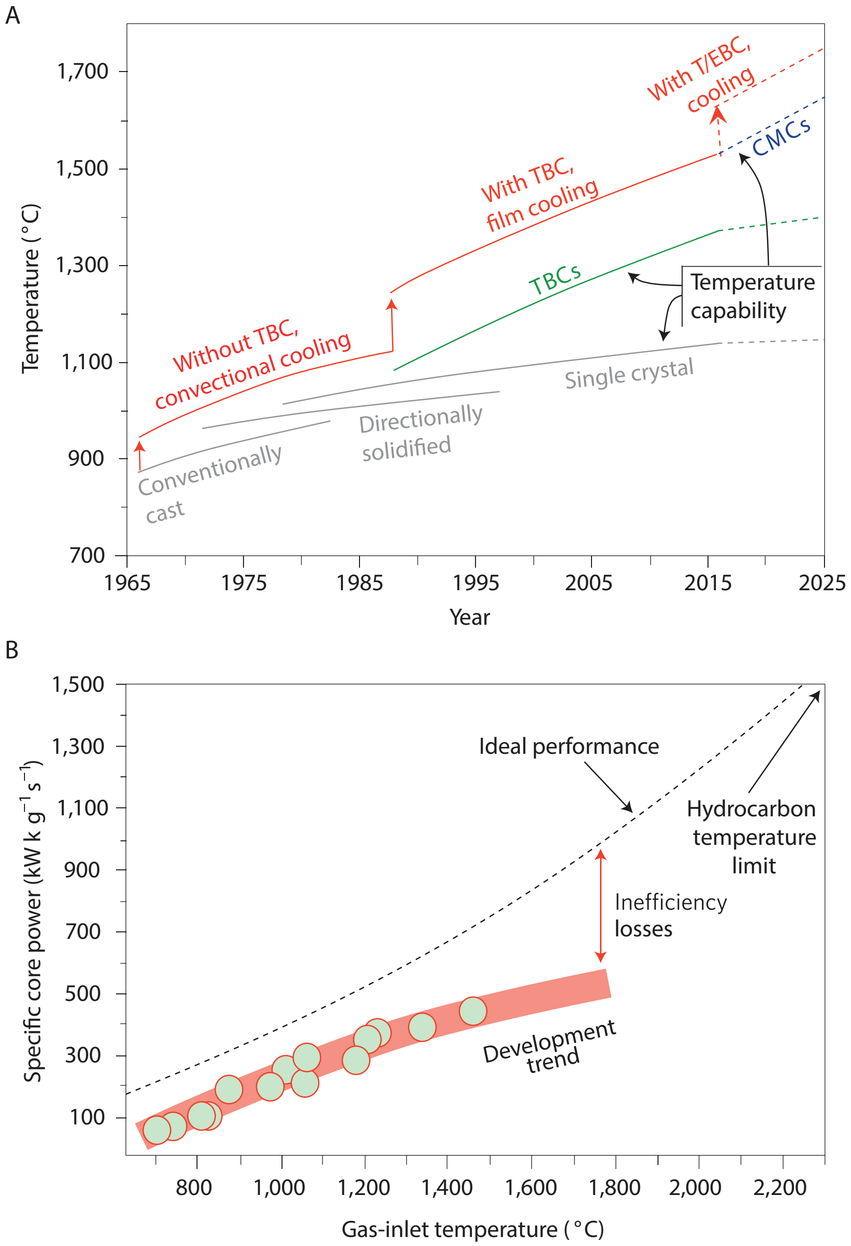

Figure 1.1: (A) Evolution and projection of temperature capabilities of TBCs (green), CMCs (blue), and Ni-based superalloys (grey), and highest allowable gas temperatures with cooling (red). Projected use of CMCs is expected to enable significant increases in gas temperature. (B) Specific core power of gas-turbine engines increases with gas-inlet temperature. Increasing inefficiency losses with temperature, caused in part by increases in cooling air, preclude realization of ideal engine performance with current material systems. Figure reprinted from Padture [1] with permission from Springer Nature.

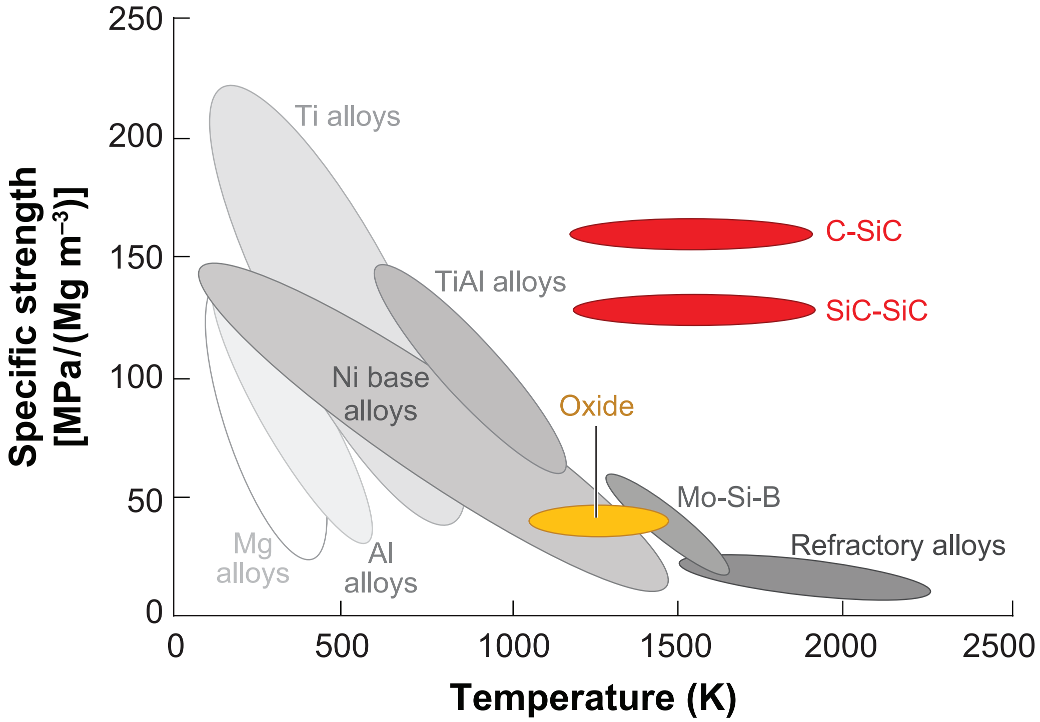

Figure 1.2: SiC$_f$/SiC CMCs offer significant increases in specific strength and temperature capability over Ni-based superalloys. Figure reprinted from Marshall & Cox [4] with permission from Annual Reviews.

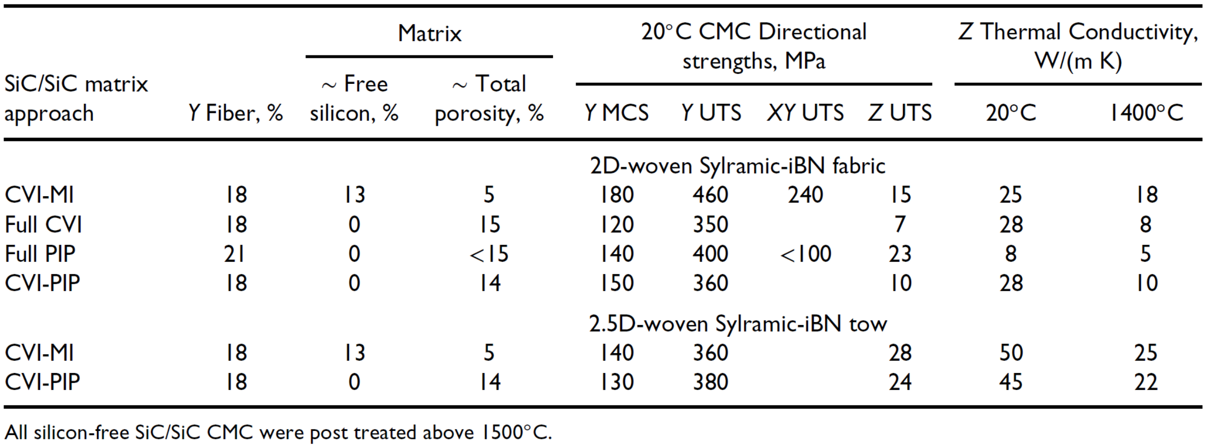

SiC/SiC matrix approach	Y Fiber, %	Matrix ~ Free silicon, %	Matrix ~ Total porosity, %	20°C CMC Directional strengths, MPa Y MCS	Y UTS	XY UTS	Z UTS	Z Thermal Conductivity, W/(m K) 20°C	1400°C
				2D-woven Sylramic-iBN fabric					
CVI-MI	18	13	5	180	460	240	15	25	18
Full CVI	18	0	15	120	350		7	28	8
Full PIP	21	0	<15	140	400	<100	23	8	5
CVI-PIP	18	0	14	150	360		10	28	10
				2.5D-woven Sylramic-iBN tow					
CVI-MI	18	13	5	140	360		28	50	25
CVI-PIP	18	0	14	130	380		24	45	22

All silicon-free SiC/SiC CMC were post treated above 1500°C.

Figure 1.3: Typical effect of matrix processing methods on properties of SiC/SiC panels. (MCS = matrix cracking strength, UTS = ultimate tensile strength). Figure reprinted from DiCarlo [8] with permission from John Wiley and Sons.

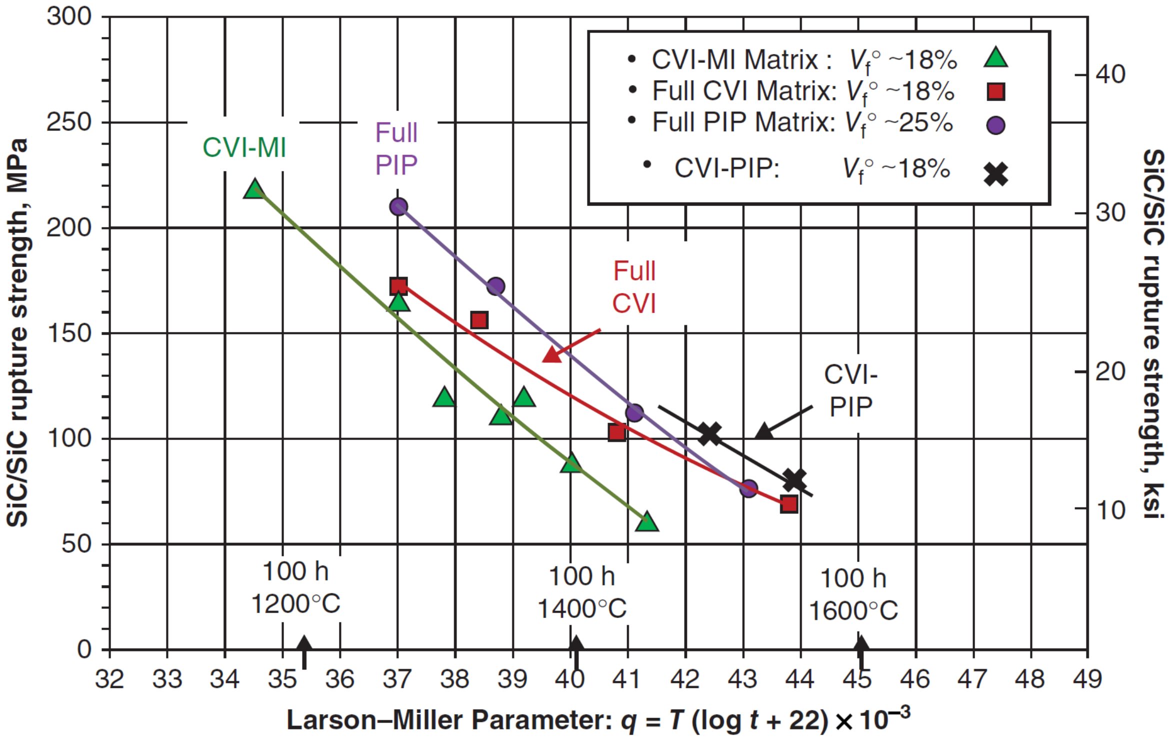

Figure 1.4: On-axis rupture strength in air for SiC/SiC CMCs fabricated with different matrix processing methods. Fiber reinforcement consists of 2D-woven 0°/90°-balanced Sylramic-iBN fabric. The Larson-Miller parameter, q, depends on absolute temperature, T, and rupture time, t. Figure reprinted from DiCarlo [8] with permission from John Wiley and Sons.

Chapter 2

Polymer Impregnation and Pyrolysis: Engineering Practice and Fundamentals

This Chapter begins with a review of studies on PIP processing in engineering practice (Section 2.1). The next three Sections provide context for the fundamental studies presented in Chapters 3-5 of this dissertation. First, Section 2.2 presents background on preceramic polymers, methods used to characterize polymer-to-ceramic conversion, and previous studies on allylhydridopolycarbosilane (AHPCS, *trade name* SMP-10): the state-of-the-art SiC precursor used in this work. Next, Section 2.3 presents background on impregnation and curing in fiber preforms, with focuses on impregnation kinetics, permeability, and void formation mechanisms. Finally, Section 2.4 provides background on the mechanics of shrinkage cracking in thin films and adhesive joints. The Chapter closes with a presentation of preliminary processing studies performed in the present work that highlight compounding effects of heterogeneous microstructure evolution and demonstrate the critical importance of the first PIP cycle (Section 2.5).

2.1 PIP Processing in Engineering Practice

Research on the PIP process has explored the effects of preceramic polymer composition, temperature and pressure profiles, use of particle fillers, and use of novel preprocessing routes and composite geometries [4, 9–15, 22, 25–27]. This section provides a review of the findings of those studies and provides motivation for the research presented in this dissertation.

To provide a broad picture, the review includes studies on a variety of PIP derived CMCs, including oxide CMCs, CMCs with carbon fibers, CMCs with SiCN matrices, and the SiC_f/SiC CMC systems of present interest. Despite differences in composition, CMCs fabricated with preceramic polymers exhibit similar microstructural defects and thus provide meaningful insights and background pertinent to PIP-derived SiC_f/SiC CMCs.

A predominant modification to the PIP process is the use of inert particulate fillers, incorporated either independently via slurry infiltration (prior to PIP) or loaded into the preceramic polymer itself [4, 9–15]. In one study, Kotani, et al. [13] investigated the effects of particle filler content in preceramic polymers in the first round of PIP. SiC_f/SiC CMCs were processed via seven repeated PIP cycles using varying filler contents in the first PIP cycle (the 2nd-7th PIP cycles did not employ particle fillers). Particle loading of 57% was identified as being optimal from the perspective of reducing matrix porosity (Fig. 2.1(A)) and maximizing ultimate flexural strength and work-of-fracture (Fig. 2.1(B)). This optimum provides an appropriate balance between fiber volume fraction and inter-fiber porosity (Fig. 2.1(B)). For lower particle loadings, mechanical properties are compromised by poor inter-fiber densification, even though the fiber volume fraction is at its highest. For higher particle loadings, the lower fiber volume fraction leads to reduced mechanical properties.

The use of particle fillers of varying sizes (coarse and fine) introduced via slurry infiltration prior to PIP processing was studied by Nannetti, et al. [11]. Here, SiC_f/SiC CMCs were processed by first depositing thin layers (0.2μm) of pyrolytic carbon and then SiC by CVI, followed (in some cases) by infiltration of an aqueous SiC slurry, and then 7-14 PIP cycles with allylhydridopolycarbosilane. In the specimens infiltrated with particle slurries (both coarse and fine), the particles effectively filled the macro- and meso-porosity between the fiber tows, leading to the attainment of lower composite porosity with a reduced number of PIP cycles (Fig. 2.2). Furthermore, CMCs processed with the slurry infiltration step showed higher thermal diffusivity than those processed by PIP alone.

Another approach, investigated by Yin, et al. [10], involves the use of particle fillers introduced via electrophoretic deposition (EPD) prior to PIP processing. Here, SiC_f/SiC CMCs were fabricated by first immersing a pyro-carbon coated 2D SiC woven cloth into a suspension of nano-SiC powder. Direct-current EPD was used to direct SiC particles onto the SiC fabric. After EPD, the plies were stacked into a laminate and subjected to seven PIP cycles using allylhydridopolycarbosilane (SMP-10). The EPD pre-treatment followed by PIP yielded a CMC with 7% higher relative density than a CMC processed by PIP cycling alone.

Slurry impregnation (prior to PIP) utilizing monomodal and bimodal particle size distributions was investigated by Yang, et al. in the fabrication of oxide composites [9]. In the baseline method, a monomodal slurry of fine ($\leq 1\mu$m) mullite and alumina particles is introduced into a 3D oxide fiber preform via vacuum-assisted infiltration. Following drying, two rounds of PIP using an alumina precursor solution were employed. The matrices invariably contain ”mud cracks” that result from shrinkage of the particle networks during drying (Fig. 2.3(A)). A mitigation strategy using a bimodal slurry containing both fine ($\leq 1\mu$m) mullite and alumina particles and coarse (23μm) SiC particles was developed. The coarse particles fill large inter-tow spaces and show less shrinkage during drying, while the fine particles fill spaces within tows and between coarse particles. The most effective strategy for introducing both particle types into the preform appears to be vacuum- and vibration- assisted infiltration of a bimodal slurry. This method effectively mitigates the formation of mud cracks in matrix-rich regions in both 3D (Fig. 2.3(B)) and 2D composites.

An innovative modification on the use of particle fillers involves the use of chopped fiber or whisker fillers to reinforce large matrix pockets, referred to as *microcomposite matrices* [4]. Microcomposite matrices are of particular interest in 3D textile preforms which tend to have large gaps between fiber tows (Fig. 2.4(A)(inset)) and require a tough matrix that can withstand in-service thermal cycling. One successful implementation of microcomposite matrices is illustrated in Fig. 2.4. Here, a carbon fiber preform was coated and infiltrated with chopped SiC fibers and then coated with thin layers of pyrolytic carbon and SiC using CVI. PIP processing with a SiC-particle loaded SiC preceramic polymer was used for further densification. This method produces matrices that can be machined and polished to a smooth finish.

Another common approach to modifying CMC microstructures involves tailoring temperature and pressure profiles during PIP processing [12, 14, 15, 26, 27]. In one study, by Kotani, et al. [14], effects of curing temperature during green body processing and pressure and heating rate during consolidation were explored systematically for PIP processing of a SiC_f/SiC CMC. The CMCs were processed by first dipping the fiber preform into polyvinylsilane containing 25wt.% particle fillers and then curing the sheets at varying temperatures. Next, the consolidated body was formed by stacking the cured sheets and heating to 1200°C at varying heating rates under varying pressures. Finally, six additional rounds of PIP with polyvinylsilane (without fillers) were performed to further densify the composite. The study demonstrated that the composite density tends to increase as the heating rate decreases due to increased PDC volumetric yield and reduced gas evolution (Fig. 2.5(A)). Furthermore, composites with good consolidation (high density, minimal cracks and pores) and the maximal flexural strength were obtained by curing at low temperatures and consolidating under intermediate applied pressures (Fig. 2.5(B)). At low curing temperatures, the matrix was plastically formable, allowing increased consolidation under pressure and ultimately a higher fiber volume fraction (Fig. 2.5(C)). By consolidating at intermediate pressures, issues associated with low pressure (e.g., formation of voids and cracks due to insufficient compression) and high pressure (e.g., pushing too much matrix out of the fiber bed) are avoided.

In another study, by King, et al. [12], a vacuum heat treatment process was developed to volatilize low molecular weight oligomers in allylhydridopolycarbosilane (SMP-10) prior to curing. As illustrated in Fig. 2.6, this heat treatment improves the mass yield of SMP-10 (from a room-temperature liquid state) by ≈6-9%, with the variability being attributed to differences in molecular weight distributions between SMP-10 lots provided by the manufacturer. Vacuum heat treatment of SMP-10 prior to PIP processing thus enables higher ceramic yield within the fiber preform. Building on their understanding of the low-temperature behavior of SMP-10, King, et al. developed a B-staging process in which heat treated SMP-10 is impregnated into a fiber preform and semicured to produce solid but flexible prepreg plies that can be subsequently layed-up, ply-by-ply, and autoclave cured. This process enables ply-by-ply control of matrix compositions with PMC-like prepreg layup, and results in less waste than conventional wet layup fabrication methods. The study demonstrated that B-staging does not adversely affect densification during subsequent PIP processing (Fig. 2.7).

One drawback of the PIP process is the lengthy pyrolysis cycles (ranging from several hours to days) [10, 12–15, 17, 22, 25, 26]. In an effort to make the PIP process more time-efficient, Dong, et al. investigated the use of high frequency microwave radiation to pyrolyze CMC matrices in under 5 minutes [15]. An even faster pyrolysis approach, referred to as *flash pyrolysis*, was developed by Zoli, et al. [26] and Azarnoush, et al. [27]. The method was successfully implemented for processing minicomposites composed of SiCN matrices within tows of uncoated carbon fibers [26] and tows of uncoated SiC fibers [27]. Minicomposites were fabricated by depositing a dilute (0.01 wt.% to 1 wt.%) solution of polysilazane precursor dissolved in tetrahydrofuran (THF) on a fiber tow, drying at 300-350°C to evaporate the solvent and crosslink the precursor, flash pyrolyzing the composite under an infrared radiation furnace for about one second, and finally cooling with a heat sink [26, 27]. The entire process was performed manually and took about 1-3 minutes (for one cycle) [26]. This process produced a uniform and crack-free nanometer-scale SiCN coating on the fibers [26, 27]. The process was repeated up to 80 times to deposit SiCN layer-by-layer, resulting in relatively dense, crack-free SiCN matrices with porosity as low as 6% [26, 27].

Preceramic polymer chemistry also influences the microstructure and properties of PIP-derived CMCs. Important considerations in choosing a precursor include mass yield, volumetric yield, viscosity at relevant processing temperatures, and wetting properties [9, 10, 12, 13, 17, 22, 25]. Several studies have compared the use of various precursors in CMC processing.

In one such study, the densification efficiency of polyvinylsilane (PVS) was compared with that of polycarbosilane (PCS) [13]. SiC_f/SiC CMCs were fabricated by performing the first PIP cycle with particle-loaded PVS, followed by six PIP cycles with PVS or PCS (without particle fillers). The primary differences between PVS and PCS as matrix precursors were their yields and their states at room temperature. The mass yield of PCS (68%) is much greater than that of PVS (32%). However, at room temperature PVS is a liquid while PCS is a solid. Thus, the PCS needed to be diluted with a solvent for the impregnation process, which reduced its effective ceramic yield. During densification, the PVS-derived CMC formed closed porosity while the PCS-derived CMC did not. This behavior was attributed to poor wetting of the PCS solution and reduced impregnation into small pores, resulting in a final composite with about 1% higher porosity than the composite processed with PVS (Fig. 2.1(A,B)). The PVS-derived composite also showed superior mechanical properties (Fig. 2.1(B)).

In another study, the densification efficiency and mechanical properties of C_f/SiC CMCs produced with two different polycarbosilane precursors were compared [25]. The primary focus of the study was a novel high yield (83 wt%) commercial liquid polycarbosilane (LPCS), which is similar to AHPCS but contains vinyl groups instead of allyl groups. For comparison, composites fabricated using solid-state polycarbosilane (PCS) diluted with a solvent were also studied. The LPCS shows superior densification behavior compared to PCS, reaching a higher final density after 9 PIP cycles (2.13 g/cm^3) than the PCS-derived composites after 13 cycles (1.87 g/cm^3) (Fig. 2.8(A)). The superior performance of LPCS is attributed to its higher ceramic yield, lower viscosity, and solvent-free composition. The LPCS-derived CMCs also show superior mechanical properties, with significantly higher bending strength and flexural modulus than the PCS-derived CMC (Fig. 2.8(B)).

Three types of polycarbosilane precursors were investigated by Yin, et al. for processing of SiC_f/SiC CMCs [22]. The precursors – SMP-10, SMP-730, and NaBond – have mass yields of about 82%, 62-67%, and 55-64% (variations account for crosslinked and non-crosslinked polymers) and densities of 2.43, 2.22, and 2.21 g/cm^3, respectively, after pyrolysis at 1400°C. Both SMP-730 and NaBond are solid at room temperature, while SMP-10 is a liquid. SiC_f/SiC CMCs were fabricated using seven PIP cycles in which pyrolysis was conducted under a constant pressure of 75kPa up to a maximum temperature of 1400°C. For the PCS precursors (solid at room temperature), impregnation was conducted above the polymer softening temperature, enabling efficient filling of the preform. The densification behaviors of the three precursors are shown in Fig. 2.9. Despite having a lower ceramic yield than SMP-10, SMP-730 produced CMCs with a higher relative density over the course of the entire PIP sequence. This disparity may be due to differences in impregnation efficiency or accessibility of void space after each PIP cycle.

2.2 Polymer-Derived Ceramics

Polymer-derived ceramics (PDCs) have gained substantial interest because of their unique properties and processing flexibility [17, 28]. Preceramic polymers can be formed into fibers, thin layers, composites and bulk parts by methods such as fiber drawing, extrusion, injection molding and resin transfer molding – approaches not available through traditional ceramic processing techniques [17, 28]. Following proper thermal treatment, preceramic polymers yield ceramics of well-defined composition and microstructure [17, 28]. Applications of PDCs include thermal protection systems, biomedical components, micro- and nano- electromechanical systems, electronic device packaging, propulsion components, porous burners, and *in-situ* crack repair in space shuttle heat shields [17, 29]. In addition to their myriad of diverse applications, PDCs have a wide variety of molecular design and processing parameters which significantly influence the final ceramic component [17, 28]. This section provides a brief overview on organosilicon polymer molecular structures, polymer-to-ceramic conversion, and PDC characterization methods. Additional background on allylhydridopolycarbosilane (AHPCS, *trade name* SMP-10) – the preceramic polymer used in this work – is also provided.

The molecular structure of a preceramic polymer influences its processability, including rheology and ceramic yield, and properties of the final ceramic, including composition, number of phases, and microstructure [17, 28]. A general simplified molecular structure for an organosilicon preceramic polymer (for production of Si-based ceramics) is shown below [17].

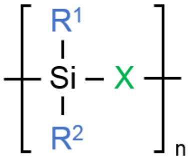

$$\left[-\begin{array}{c} R^1 \\ | \\ \mathrm{Si} \\ | \\ R^2 \end{array} - X - \right]_n$$

The X group in the polymer backbone determines the class of the Si-based polymer [17]. For example, if X=CH_2, the polymer is a polycarbosilane and produces a SiC-based ceramic. Alternatively, if X=NH, the polymer is a polysilazane and produces a SiCN-based ceramic [17, 28]. Molecular structures for each of the main organosilicon classes are shown in Fig. 2.10 [17]. The R groups in the polymer backbone influence chemical and thermal stability, solubility and rheological properties [17, 28]. Typically the R groups comprise hydrogen, aliphatic groups or aromatic groups [17]. The R groups may therefore be used to tailor the amount of excess carbon in the ceramic which in turn influences thermal stability of metastable amorphous phases and crystallization behavior (grain size, degree of crystallinity, grain boundary composition) [17].

The yield of a preceramic polymer is influenced by the degree to which it can be cross-linked, the use of initiators (to promote cross-linking), and its molecular weight and degree of branching [17, 28]. If a preceramic polymer is not cross-linked before mineralization and ceramization, depolymerization and volatilization of low-molecular weight polymers and oligomers will occur upon heating, significantly reducing the ceramic yield [17, 28]. By incorporating crosslinking groups of latent reactivity into the molecular structure, the polymer may be cross-linked during or after shaping via thermal curing or photo curing (among other methods), allowing more of the mass to be retained and thus increasing ceramic yield [17, 28]. Furthermore, initiators may be used to increase the degree of cross-linking and/or initiate thermal cross-linking at lower temperatures, further reducing evaporation of low molecular weight polymers and oligomers and thus further increasing the ceramic yield [17]. In addition, the preceramic polymer must be of sufficiently high molecular weight to avoid volatilization and depolymerization [17, 28].

Polymer-to-ceramic conversion is accompanied by significant chemical, volumetric, and microstructural changes [17, 19–21, 28] The process involves crosslinking (100-650°C), ceramization (800-1100°C), and, optionally, crystallization and grain growth (1000-2000°C) [17, 20, 21]. Ceramization refers to conversion of the polymer into an amorphous ceramic, and thus requires complete decomposition or elimination of organic moieties [17]. Crystallization of the resulting PDC is desired in some applications while others demand that the metastable amorphous state be retained [17]. For example, the remarkable properties of amorphous SiBCN ceramics (e.g., high temperature stability, oxidation resistance, and creep resistance) are due to the B and C atoms that kinetically stabilize the amorphous state and the absence of grain boundaries that could otherwise control creep properties [17]. In the case of PIP-derived SiC matrices for CMC applications, low thermal conductivity, poor mechanical properties and poor oxidation resistance have been associated with the amorphous state and with excess carbon [6, 30]. In these cases, stoichiometric crystalline SiC is desired [6, 30]. In general, crystallization involves a phase separation process in which free carbon is segregated into nanosized turbostratic or graphitic sheets while crystalline SiC domains nucleate and grow [17].

Various processing parameters influence the characteristics of the final ceramic product [17, 28]:

- The heating profile affects the ceramic yield, composition and microstructure [17]. During crosslinking, the heating rate and hold temperatures affect both the extent of crosslinking and the reactivity of the crosslinked polymer [17]. If the heating rate is too high, there will be insufficient time for crosslinking [17]. Subsequent depolymerization and volatilization alter the final ceramic composition and reduce the ceramic yield [17]. The heating profile also affects the extent of crystallization, carbothermal reduction reactions, and reactions with active fillers [17].

- The gaseous environment influences the composition and yield of the PDC [17]. For example, AHPCS readily absorbs and reacts with oxygen and environmental moisture, invariably leading to oxygen impurities in the (ideally pure) SiC PDC if the polymer is not handled in an oxygen-free environment [18]. Additionally, oxygen contamination in the inert gas during pyrolysis can lead to unwanted removal of carbon-containing moieties [17].
- Pressure application, either mechanical or gaseous, during pyrolysis has been shown to affect the composition, density, and crystallization of the PDC [17]. Pressure application has been used to suppress bubble formation during curing and to consolidate the material during curing and pyrolysis. Furthermore, at high gas pressures (up to 200 atm) it is possible for gas molecules to become incorporated into the final ceramic, allowing tailoring of the composition [17]. Pressure has also been shown to affect crystallization. For example, vacuum favors carbothermal reduction reactions and can thus promote crystallization [17]. Conversely, high gaseous or mechanical pressure can hinder crystallization [17].

Various techniques have been implemented to monitor polymer-to-ceramic conversion in-situ and to characterize the final and intermediate stages of the PDC. These techniques include X-ray diffractometry (XRD) [6, 17, 20–22], selected area electron diffraction (SAED) [6], fourier transform infrared spectroscopy (FTIR) [17, 19–21], energy dispersive x-ray spectroscopy (EDS) [6], electron energy-loss spectroscopy (EELS) [6], elemental analysis [20], magic-angle spinning nuclear magnetic resonance (MAS-NMR) [17, 19], mass spectrometry (MS) [17, 20, 22], gel permeation chromatography (GPC) [12], rheometry [10, 12, 17], thermogravimetric analysis (TGA) [12, 17, 20–22], differential thermal analysis (DTA) [17, 21], thermomechanical analysis (TMA) [17], pycnometry [21, 22], scanning electron microscopy (SEM) [6, 17, 20], transmission electron microscopy (TEM) [6, 17, 19, 21], and nanoindentation [21]. These techniques have been used to monitor curing, ceramization and crystallization kinetics, microstructure evolution, and chemical transformations. In the next section, the use of several of these techniques will be illustrated for the characterization of allylhydridopolycarbosilane.

2.2.1 Allylhydridopolycarbosilane (AHPCS)

Allylhydridopolycarbosilane (AHPCS) is a commercially-available state-of-the-art SiC preceramic polymer manufactured by Starfire Systems, Inc. under trade name SMP-10. A simplified depiction of the molecular structure of AHPCS is shown in Fig. 2.11. AHPCS consists of a hyperbranched carbosilane oligomer backbone with allyl side groups to facilitate subsequent crosslinking [18]. Because the addition of allyl groups introduces excess carbon into the otherwise Si:C stoichiometric balance of the polymer, the molecular design has been optimized to ensure that allyl groups are incorporated uniformly on the outer fringes of the polymer clusters, to maximize crosslinkability while avoiding excessive allylation [18]. The resulting SMP-10 has an allyl content of about 10-15% [18, 20, 21]. One study found that the peak linear differential molar mass[1] of as-received SMP-10 is at a molar mass of 290g/mol (Fig. 2.12) [12]. It can be increased to a molar mass of 380g/mol via a heat treatment at 86°C for 15h which volatilizes low molecular weight oligomers (Fig. 2.12) [12].

The benefit of AHPCS for PIP processing is its engineered balance between rheological properties, ceramic yield, and Si:C stoichiometry. At room temperature (25°C) AHPCS is a liquid with viscosity ranging from 40×10^{-3} to 100×10^{-3} Pa s, allowing it to be readily impregnated into a fiber preform without the use of solvents or

---

[1] The cumulative mass distribution as a function of molar mass (measured with gel permeation chromatography) is differentiated to give the linear differential molar mass as a function of molar mass.

higher temperatures (viscosity values from StarPCS™ SMP-10 Technical Data Sheet). Additionally, AHPCS can form near-stoichiometric SiC in the final pyrolyzed product [18, 20, 21]. Although the resulting ceramics invariably contain oxygen impurities and excess carbon, treatments at elevated temperatures (≈ 1500-1700°C) can significantly reduce oxygen and excess carbon contents (Figs. 2.13 and 2.14) [6, 20]. Finally, the ceramic yield of AHPCS pyrolyzed to ≥900°C is typically in the range of 68-81wt% [12, 20–22]. Reported variability in ceramic yield may arise from batch variability, as well as variations in heating rate and maximum temperature employed in these studies. As discussed in Section 2.1, the ceramic yield of AHPCS may be increased via a vacuum heat treatment that volatilizes low molecular weight oligomers prior to shaping, curing, and pyrolysis (Fig. 2.6) [12].

Polymer-to-ceramic conversion of AHPCS includes three crosslinking steps between 120-650°C, complete ceramization by ≈1150°C, and crystallization between 1150-1650°C [6, 18, 20, 21]. The first crosslinking step, free radical crosslinking, consumes allyl groups and may be initiated by a butyl or cumyl peroxide at temperatures of ≈100°C [18, 31]. The second crosslinking step, hydrosilylation, is completed by 250°C and also consumes allyl groups [20]. The hydrosilylation reaction and accompanying FTIR spectra illustrating the complete consumption of allyl groups are shown in Fig. 2.15 [20]. The third crosslinking step, dehydrocoupling, occurs between 300-650°C and corresponds to a large mass loss due to evolution of hydrogen [20]. The dehydrocoupling reaction and accompanying thermogravimetry and mass spectrometry (TGMS) results are shown in Fig. 2.16 [20]. Completion of the ceramization process by 1150°C is illustrated in the FTIR spectra in Fig. 2.17, in which the C-H and Si-H peaks have disappeared and an Si-C peak remains at 1150°C [21]. The crystallization behavior of AHPCS has been characterized via XRD, DTA and TEM, among other methods [6, 20, 21]. The onset of β-SiC crystallization occurs at about 1100°C, as illustrated by a distinct peak in DTA measurements (Fig. 2.18) and by the appearance of distinct β-SiC peaks in XRD patterns (Fig. 2.19) [6, 21]. With increasing temperature (at constant dwell time) and increasing dwell time (at constant temperature), the fraction of crystalline β-SiC and the crystallite size tend to increase (Figs. 2.19 and 2.20) [6, 21]. Crystallization is rather sluggish at 1300°C, with only slight increases in the fraction of crystalline β-SiC and the crystallite size with increasing dwell time [6]. After 100h at 1300°C, the fraction of crystalline β-SiC is only 68wt% and the crystallite size only 6nm [6]. In contrast, crystallization is more rapid at 1400°C and 1500°C, with a 100h treatment at 1500°C yielding 80wt% crystalline β-SiC and $\approx$120nm crystallite size [6].

2.3 Impregnation and Curing in Fiber Preforms

One of the advantages of CMC matrix processing with preceramic polymers is that it can build upon the large science-base and advanced fabrication infrastructure in the polymer matrix composite (PMC) community [2, 8, 13, 24]. Impregnation and curing of a preceramic polymer in the first PIP cycle is analagous to impregnation and curing of a thermosetting polymer in PMC fabrication. Thus, in this section, background on microstructure evolution during impregnation and curing is provided largely by studies from the PMC community.

The processing technique of interest in this work involves pressure-assisted impregnation of a liquid precursor into a dry fiber preform, a process referred to as liquid composite molding (LCM). It is well understood that void content is correlated with the capillary number, $Ca = \mu v / \gamma$, during impregnation, where v is the tracer velocity, μ is the liquid viscosity, and γ is the liquid surface tension [32–34]. Thus, controlling impregnation kinetics is crucial for minimizing void content in the composite. In this section, background is provided on both impregnation kinetics (Section 2.3.1) and void formation mechanisms (Section 2.3.2).

2.3.1 Impregnation Kinetics

Saturated fluid flow through fibrous preforms is typically modeled by Darcy's Law [32–40]. The Darcy velocity is given by

$$\vec{q} = -\frac{\tilde{\kappa}_s}{\mu}\nabla P \tag{2.1}$$

where $\tilde{\kappa}_s$ is the saturated permeability tensor of the fibrous preform and ∇P is the pressure gradient [32–40]. The tracer velocity, $\vec{v}$ is related to the Darcy velocity by $\vec{v} = \vec{q}/\varepsilon$, where ε is the porosity of the fiber bed [32].

As fluid displaces air within the preform, the saturation, S, typically rises from zero at the flow front to a steady-state value at some distance behind the flow front [32]. A modified version of Darcy's law that accounts for incomplete saturation is given by

$$\vec{q} = -\frac{\tilde{\kappa}_u}{\mu}\nabla P = -\frac{k_r(S)\tilde{\kappa}_s}{\mu}\nabla P \tag{2.2}$$

where $\tilde{\kappa}_u = k_r(S)\tilde{\kappa}_s$ is the unsaturated permeability and k_r is a non-dimensional relative permeability, ranging from 0 to 1 as S varies from 0 to 1 [32, 41]. In this case, the tracer velocity is related to the Darcy velocity by $\vec{v} = \vec{q}/(\varepsilon S)$ [32].

Controlling the Darcy velocity (and thus the capillary number during impregnation) thus requires an accurate estimate of saturation and both saturated permeability and relative permeability (in order to estimate unsaturated permeability). The remainder of this section provides an overview of (1) analytical models for saturated permeability, (2) studies on effects of fiber packing on permeability, and (3) experimental findings on the effects of Ca on permeability.

Notable analytical models of longitudinal saturated permeability were developed by Gebart (known as the Kozeny-Carman (KC) equation) [42] and Shou, et al. [37]. The KC equation was derived on the basis of a static, idealized, ordered fiber array and provides a simple, general expression for saturated permeability in terms of properties of the fibrous medium:

$$\kappa_s^{(KC)} = \frac{1}{4\kappa_0}\frac{\varepsilon^3}{(1-\varepsilon)^2}\bar{r}_f^2 \tag{2.3}$$

where $\bar{r}_f$ is the average fiber radius and κ_0 is the Kozeny constant [35, 37, 42]. Gebart derived values of the Kozeny constant for longitudinal flow in square ($\kappa_0 = 1.78$) and hexagonal ($\kappa_0 = 1.66$) fiber arrangements. However, these Kozeny "constants" show a dependence on fiber bed porosity [37, 42]. Furthermore, the Kozeny "constant" has been found to vary by over an order of magnitude ($\approx 0.3 - 3$), requiring experimental measurement for real fiber preforms [35–37, 40]. In an effort to develop a more accurate analytical model for longitudinal permeablity, Shou, et al. used a scaling analysis to determine a scaling relationship between κ_s, ε, and $\bar{r}_f$ and then calibrated the model with primarily numerical results for permeability of both square and hexagonally packed fiber beds [37]. As illustrated in Fig. 2.21, the model developed by Shou, et al. (labeled Present Model in Fig. 2.21) shows an excellent fit with numerical permeability results over the entire range of fiber volume fraction for both square and hexagonal arrays (fiber volume fraction is equal to $1 - \varepsilon$) [37]. Meanwhile, the KC equation (labeled Gebart in Fig. 2.21) shows significant deviations, especially at low values of fiber volume fraction [37].

The analytical models presented above were developed on the basis of unit cell geometries that tile to create uniform fiber arrays [35, 37, 42]. Several studies have shown that the longitudinal saturated permeability of fiber beds increases with non-uniformity in fiber packing due to the presence of both wide and narrow channels within the medium [36–39]. The wider channels accommodate a higher fluid flux per unit area because the fluid speed increases proportionally with the gap area, allowing for increased overall fluid flux in non-uniform fiber beds [38, 39]. In the study by Shou, et al., effects of non-uniformity on permeability were explored by computing the permeability of an assemblage of unit cells with a distribution of cell areas [37].

The study demonstrated that a random distribution of fibers has a higher permeability than an ordered fiber bed at the same fiber volume fraction, and that the permeabilities of random fiber arrangements more closely align with experimentally measured permeabilities (Fig. 2.22) [37]. Shou, et al. also explored effects of the degree of non-uniformity by varying parameters of the distribution of cell areas [37]. A parameter to describe the degree of non-uniformity was defined: $\alpha = \langle A^2 \rangle / \langle A \rangle^2$, which is the ratio of the average cell area squared to the square of the average area of the cells [37]. Fig. 2.23 shows how permeability increases with increasing non-uniformity [37]. Effects of non-uniformity on longitudinal permeability were also studied by Chen, et al. [39]. Longitudinal permeabilities of non-uniformly packed fiber beds were estimated using computational fluid dynamics [39]. In this study, the mean minimum inter-fiber distance (MIFD) was used to describe the degree of non-uniformity in fiber packing (MIFD decreases with increasing non-uniformity) [39]. The results of this study also quantitatively illustrate that permeability increases with increasing non-uniformity (Fig. 2.24) [39]. The aforementioned studies assume saturated flow through a static fiber bed. During impregnation, fibers may rearrange as a result of fluid-fiber interactions. Several studies have suggested that increases in permeability with capillary number may be due in part to cooperative fiber rearrangement that increases the degree of non-uniformity and hence permeability [43–45]. The first direct evidence of this phenomenon is given in Chapter 3.

Increases in permeability with capillary number have been observed experimentally in several studies [43, 46–49]. In addition to potential effects of fiber rearrangement (as previously mentioned), two other potential origins of this trend have been proposed. The first involves preferential flow channeling, wherein fluid preferentially travels in either the smaller or the larger channels in the preform. Several studies on unsaturated flow in woven fabrics have suggested that the increase in permeability with Ca is due to preferential flow channeling through larger channels (typically intra-tow channels in a weave) as the flow rate increases [43, 44, 46, 47]. The second involves the degree of saturation behind the flow front during impregnation, as unsaturated permeability increases with S. At sufficiently high capillary numbers, bubbles can be mobilized and swept away by subsequent fluid flow [32, 33]. In fiber beds with a monomodal fiber packing distribution, infiltration at higher Ca correlates with a higher final degree of saturation due to increased bubble mobilization [33]. The effects of both preferred flow channeling and saturation on permeability are explored in Chapter 3.

2.3.2 Void Formation

The evolution of voids during liquid composite molding and subsequent curing occurs via several mechanisms [32–34, 50–55]. During impregnation, voids may be entrapped in the composite or they may be mobilized and swept out of the composite, both mechanisms depending strongly on capillary number [32–34, 50–52]. Pressure changes during impregnation can lead to void compression, dissolution and/or exsolution [32]. Finally, during curing, gas evolution and exsolution from the matrix precursor can lead to additional void formation [53–55]. In this section, each of these mechanisms and their implications for composites processing are reviewed.

Void entrapment occurs during impregnation when the flow front advances non-uniformly, pinching off bubbles in regions where impregnation is lagging [32, 34, 50–52, 56]. Non-uniformity in fluid flow can occur when the fiber preform itself is non-uniformly arranged and thus the relative effects of capillary forces and viscous forces vary depending on the local spacing between the fibers [32, 34, 50–52, 56]. Fiber preforms consisting of tows of fibers exhibit a dual-scale structure with micron-scale spaces between fibers within tows –where capillary forces dominate– and comparatively larger-scale (hundreds of microns) channels between tows – where viscous forces are more important [32, 34, 51, 52, 56]. If liquid flows faster in the large channels between tows, needle-like or cylindrical voids will be entrapped within tows (referred to as tow voids) as illustrated in Fig. 2.25(A,C) [32, 34, 51, 52]. On the other hand, if liquid flow is faster inside the tows, voids will form in the large channels (referred to as channel voids) as illustrated in Fig. 2.25(B,D) [32, 34, 51, 52]. It is then unsurprising that numerous studies have shown that both the void type (tow vs. channel) and void content have been correlated with the capillary number [32, 34, 51, 52]. Experimental results for different liquids fall on a master curve relating the void content to the capillary number for a given fiber preform (Fig. 2.26) [32, 34, 51, 52]. When the capillary number is low, the leading flow front occurs in the small channels within tows, leading to the formation of channel voids [32, 34, 51, 52]. Tow voids form when the capillary number is high [32, 34, 51, 52]. Correspondingly, there is an optimal capillary number at which the flow speeds within the tows and the channels are matched to the greatest degree possible and hence the void content is minimized [32, 34, 51, 52]. For bidirectional woven fabrics, the void content does not drop to zero at the optimal capillary number because it is not possible to match flow speeds for channels and tows in different orientations [32]. However, several studies with random mats and unidirectional fabrics have demonstrated removal of virtually all voids at the optimal capillary number [32].

In an effort to better understand the physical mechanisms of fluid flow and void formation, various models have been developed to predict void content in simplified systems [32, 50, 51, 56]. One of the simplest systems yielding insights into the fundamentals of bubble entrapment is that of the pore doublet model (PDM) [50, 56]. A PDM developed by Wielhorski, et al. is shown schematically in Fig. 2.27 [50]. The PDM consists of two circular capillaries of different radii: a *microchannel* with radius R_m, and a *macrochannel* with radius $R_M > R_m$. In one section, the capillaries are continuously interconnected over a length, l. In the other section, the capillaries are connected only at nodes on both ends, separated by a distance L. Bubbles entrapped within the second section are referred to as microbubbles (in the microchannel) and macrobubbles (in the macrochannel). Per the assumptions and definition of the model, fluid flow is driven by capillary forces (the fluid is assumed to be wetting) and may be assisted by an injection pressure, P_i. Another key assumption of the model is that the macrochannel supplies mass to the microchannel in the first section. This hypothesis is referred to as the ”supplying principle” and, depending on P_i, either the macrochannel flow front or the microchannel flow front may reach the first node faster. When the capillaries are not connected (as in the second section of the PDM), the flow front inside the large channel will always move faster than that in the small channel. In real fiber preforms, channels are often interconnected and allow mass transfer. The PDM illustrates the effects of interconnectivity between dual-scale flow channels.

In the PDM defined by Wielhorski, et al., the formation of either macrobubbles or microbubbles is possible [50]. First, an injection pressure, P^*, is defined for which the menisci in the macrochannel and microchannel arrive at the first node at the same time. Below this pressure, the meniscus in the microchannel reaches the first node first. If the meniscus in the microchannel has a sufficiently large lead, it can reach the second node first, leaving a macrobubble in the macrochannel. However, if the flow front in the macrochannel catches up and overtakes that in the microchannel, a microvoid will form in the microchannel. In the case that the injection pressure is larger than P^*, the meniscus in the macrochannel will reach both the first and second nodes first, leaving a microvoid in the microchannel. One set of results for this model is shown in Fig. 2.28 [50]. This plot shows minimal bubble content at $P_i = P^*$, increasing macrobubble content as P_i decreases below P^* and increasing microbubble content as P_i increases above P^*. For $P_i < P^*$, the microbubble content is negligible compared to the macrobubble content. This behavior is analagous to that in Fig. 2.26 where the content of channel and tow voids is plotted against capillary number.

The capillary number also affects the mobility of bubbles with continued fluid flow

[32, 33, 51]. Bubble mobility also depends on both bubble size and constriction size [32, 33, 51]. When the viscous drag force due to the pressure gradient across the bubble is larger than the capillary force resisting bubble movement in the capillary constriction, the bubble is mobilized [32, 33, 51]. Thus, there exists a critical capillary number for the onset of void mobilization [32, 33].

This mechanism of void transport offers a route to eliminate residual voids even if formation of voids at the flow front cannot be avoided [32, 51]. In a process called ″bleeding″, the injection pressure is increased and kept high for a period of time after the mold filling process is complete [32, 51]. With the increase in pressure, the fluid velocity increases and existing bubbles may be compressed (thus reducing the bubble radius) or dissolved, facilitating void migration and elimination [32].

Another approach for eliminating bubbles is to apply vacuum on the outlet during impregnation and bleeding [32]. This ensures that the initial air pressure within voids is low and reduces the amount of dissolved gas that may be exsolved during pressure removal or heating [32]. The combined effects of pressure changes and capillary number on microstructure evolution during impregnation are explored further in Chapter 4.

Voids may also form during curing by exsolution of dissolved gases or of gases formed through the curing reaction [53, 54, 57–61]. In practice, temperature and pressure profiles are carefully engineered, accounting for evolving rheological properties of the polymer [53, 57–59]. In some cases, the bleeding process is performed at higher temperatures, while the polymer has a low viscosity (i.e., before gelling), to drive out voids and excess resin [57, 58]. In many cases, composites are cured under autoclave pressure in order to maximally evacuate, dissolve, and compress voids [53, 57–59, 61]. To enable on-line control and optimization of complex curing processes, many models have been developed to predict profiles of polymer pressure, polymer flow velocity, void mobilization and void compression/dissolution as a function of temperature, applied pressure, polymer properties, and fiber bed geometry [57–59]. The effects of curing on microstructure evolution in unidirectional minicomposites are explored in Chapter 4.

2.4 Mechanics of Shrinkage Cracking

Pyrolysis of AHPCS gives a ceramic yield of roughly 20-30 vol% [21, 22]. When this shrinkage is constrained, stresses that build up in the PDC are relieved in part by cracking. The constraints imposed by continuous fibers are complex and can change over the course of pyrolysis if the fibers rearrange to accommodate matrix shrinkage. Prior to the present work, geometries and evolution patterns of shrinkage cracks within PDCs confined by a fiber preform were largely unknown. The work presented in Chapter 5 uses XCT to observe shrinkage crack formation *in-situ* during pyrolysis. The study reveals that primary cracks – the first cracks to form in a particular local matrix region – nucleate almost exclusively from fiber-matrix interfaces. If the putative cracks kink into the matrix, they may stop upon reaching other fibers surrounding the local matrix region or they may evolve into alternating or wavy geometries. As pyrolysis continues, additional cracks may form in regions containing primary cracks. The crack geometries and evolution patterns described in Chapter 5 show parallels to those observed in thin films and adhesive joints [62–68]. Thus, in this section, a brief background on pertinent topics within fracture mechanics of layered bimaterial systems is provided.

The Dundurs' parameters, α_D and β_D, are used to characterize the elastic mismatch in bimaterial systems [62, 65, 66, 68]. These parameters, defined below for plane strain conditions, are greater than zero for a compliant film or adhesive (material #2) on or between a stiffer substrate (material #1):

$$\alpha_D = \frac{\mu_1(1-\nu_2) - \mu_2(1-\nu_1)}{\mu_1(1-\nu_2) + \mu_2(1-\nu_1)} \tag{2.4}$$

$$\beta_D = \frac{1}{2} * \frac{\mu_1(1-2\nu_2) - \mu_2(1-2\nu_1)}{\mu_1(1-\nu_2) + \mu_2(1-\nu_1)} \tag{2.5}$$

where μ_i and ν_i are shear modulus and Poisson's ratio of material i [62, 65, 66, 68].

Energy release rates, G, for cracks in thin films and adhesive layers follow the scaling

$$G = Z\frac{\sigma^2 h}{\bar{E}_2} \tag{2.6}$$

where h is the film/adhesive thickness, σ is the stress in the film/adhesive, $\bar{E}_2 = E_2/(1-\nu_2)^2$ is the plane strain film/adhesive modulus, E_2 is the elastic modulus of the film/adhesive, and Z is a dimensionless driving force that depends on crack geometry and elastic mismatch [62–64]. The energy release rate increases with film/adhesive thickness and stress [62–64]. Driving forces for additional cracks between existing cracks exhibit similar trends [62].

In adhesive layers, cracks in both wavy (Fig. 2.29(A)) and alternating (Fig. 2.29(B-C)) geometries have been observed [62, 65, 68]. The alternating geometry has been studied in depth by Akisanya and Fleck [65, 68]. In the alternating mode, cracks alternate between the two interfaces at regular intervals [62, 65, 68]. They form by periodic kinking of interfacial cracks into the adhesive, followed by growth across the adhesive layer and formation of new interfacial cracks at the other interface [62, 65, 68]. Kinking occurs when the phase angle of a kink-like flaw at the tip of the interfacial crack reaches a critical value [65–68]. The interfacial crack length at which kinking occurs is a function of adhesive layer thickness, elastic mismatch, remote stress intensity factor, residual stress, interfacial toughness, adhesive layer toughness, angle and length of putative flaws, and Young's moduli of the two materials[65, 68]. These studies on alternating cracks in adhesive layers provide a foundation for interpreting alternating cracks observed in minicomposites (Chapter 5).

2.5 Preliminary Processing Studies on Repeated PIP

Preliminary processing studies on repeated PIP were performed using model systems consisting of unidirectional fiber beds. The composite specimens were fabricated by first inserting nine to ten tows ($\approx 4500 - 5000$ fibers) of BN-coated Hi-Nicalon™ Type-S SiC fibers into quartz or borosilicate tubes with $1.5mm$ inner diameter (VitroTubes™), and then heat-shrinking the tubes onto the fibers under vacuum. Next, the fiber bed was impregnated with AHPCS via pressure-assisted impregnation. Prior to impregnation, the AHPCS was mixed with 0.2 wt% dicumyl peroxide (DP) initiator to promote subsequent curing. A standard cure cycle was performed at 120°C for two hours. A standard pyrolysis was performed under flowing argon with a temperature profile recommended by Starfire® Systems: 25°C to 250°C at 2°C/min, 250°C to 650°C at 1°C/min, 650°C to 850°C at 3°C/min, 850°C hold 1hr, and cool to room temperature at -5°C/min [31]. Specimens were further densified via repeated PIP cycles with AHPCS + 0.2 wt% DP precursor using the same curing and pyrolysis cycles.

Minicomposites were imaged with XCT[2] after various stages of processing: (A) after first impregnation and cure, (B) after one PIP cycle, (C) after one PIP cycle and the second impregnation and cure, (D) after two PIP cycles and the third impregnation and cure, (E) after three PIP cycles and the fourth impregnation and cure, and (F) after four PIP cycles and the fifth impregnation and cure. Transverse sections from each of these specimens are presented in Fig. 2.30. The microstructures are highly heterogeneous. First, the fiber packing is non-uniform: fibers tend to appear in rel-

---

[2] XCT was performed at Beamline 8.3.2 at the Advanced Light Source at Lawrence Berkeley National Laboratory. Tomographic slices were reconstructed using a commercial reconstruction algorithm (Octopus v8; IIC UGent, Zwijnaarde).

atively closely packed clusters separated by large channels that are several fiber diameters wide and up to hundreds of fiber diameters long. Second, matrix material is found preferentially in smaller channels between the fibers, with large voids typically present in larger channels. Third, continued densification is observed in smaller channels with continued PIP processing, while large empty channels remain mostly vacant. Due to the cyclic compounding nature of the repeated PIP process, microstructural heterogeneities introduced in early stages of the process are expected to set the stage for continued heterogeneous processes in later stages. The following pathway for microstructure evolution is proposed:

1. During impregnation and curing in the first cycle, non-uniformity in fiber packing causes non-uniformity in fluid flow and bubble formation, leading to void formation primarily in the largest channels (due to the lower capillary pressure) and possibly further increasing non-uniformity in fiber packing.

2. During the first pyrolysis, non-uniform distribution of the precursor creates non-uniform forces on the fibers as the precursor shrinks. Shrinkage within the smaller channels may bring closely-packed fibers closer together and cause expansion of large empty neighboring channels. Furthermore, shrinkage cracks of various geometries may form heterogeneously with a dependence on channel size and local fiber configuration.

3. Non-uniformity in void microstructure after the first PIP cycle further exacerbates non-uniformity in fluid flow and bubble formation during impregnation and curing in the second cycle. During pyrolysis, shrinkage and cracking again occur heterogeneously. Continued PIP processing is expected to follow this pattern.

4. In addition, with continued PIP cycling, access to large voids may be closed off due to densification of smaller connected channels.

This preliminary study demonstrates the compounding effects of a PIP process that fails to fill the largest channels between the fibers. It also highlights the importance of understanding the fundamentals of microstructure evolution during PIP processing. In particular, it illustrates the critical importance of the first PIP cycle and its impact on microstructures during subsequent PIP cycles. Several critical open questions about the first PIP cycle motivate the work of this dissertation:

1. How do fiber movement and preferred flow channeling influence precursor impregnation?
2. How do fibers rearrange during impregnation and curing?
3. What factors influence formation, location, and size of bubbles that form during impregnation and curing?
4. What types of cracks form during pyrolysis and how does the local geometry influence their formation?

The remainder of the dissertation aims to provide insights that address these questions through direct observation of microstructures in unidirectional minicomposites paired with complementary studies on preceramic polymer pyrolysis.

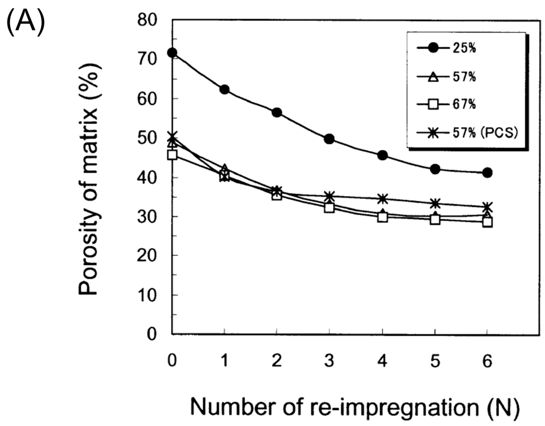

(B)

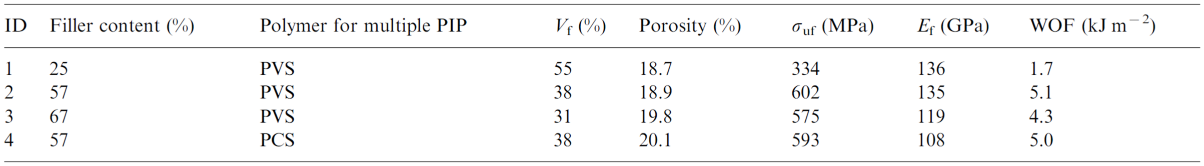

ID	Filler content (%)	Polymer for multiple PIP	V_f (%)	Porosity (%)	σ_{uf} (MPa)	E_f (GPa)	WOF (kJ m^{-2})
1	25	PVS	55	18.7	334	136	1.7
2	57	PVS	38	18.9	602	135	5.1
3	67	PVS	31	19.8	575	119	4.3
4	57	PCS	38	20.1	593	108	5.0

Figure 2.1: Effects of particle loading on composite properties [13]. (A) Matrix porosity decreases with repeated re-impregnations of the preceramic polymer. In the key, percentages indicate SiC particle content in the preceramic polymer during the 0th re-impregnation. (Subsequent PIP cycles did not use particle fillers.) The first three specimens (filled circle, empty triangle, empty square) were densified with a polyvinylsilane (PVS) precursor, while the fourth specimen (star symbol) was densified with a polycarbosilane (PCS) precursor. (B) Microstructural and mechanical properties of the composites. Figures reprinted from Kotani [13] with permission from Elsevier.

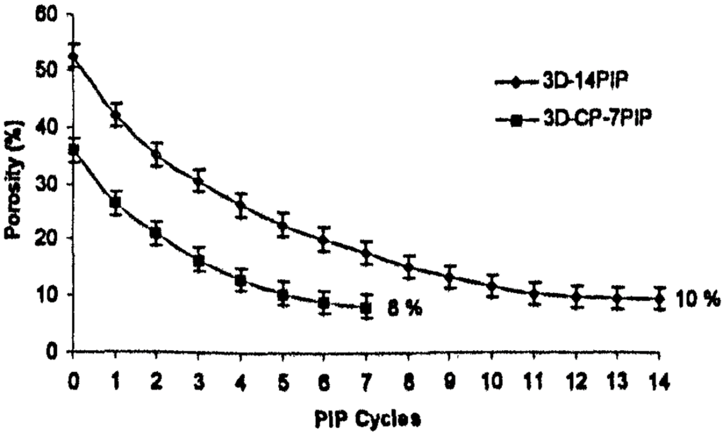

Figure 2.2: Porosity reduction during repeated PIP cycles for 3D composites processed with and without slurry infiltration. Figure reprinted from Nannetti [11] with permission from John Wiley and Sons.

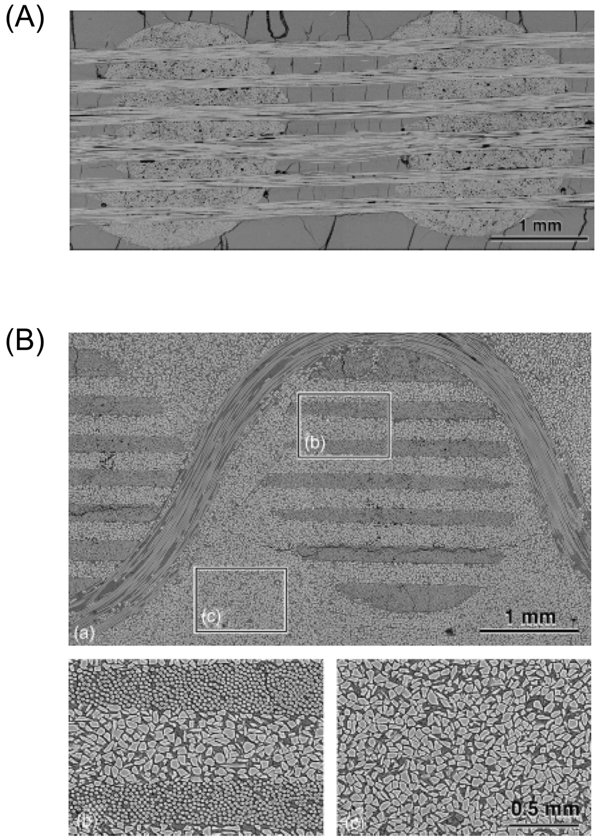

Figure 2.3: Representative microstrutures of composites with 3D fiber architectures fabricated with vibration- and vacuum- assisted slurry infiltration [9]. (A) Composite fabricated with a monomodal slurry of fine ($\leq 1\mu$m) mullite and alumina particles [9]. (B) Composite fabricated via coinfiltration of a bimodal slurry containing coarse (23μm) SiC particles and fine ($\leq 1\mu$m) mullite/alumina particles [9]. Figures reprinted from Yang [9] with permission from John Wiley and Sons.

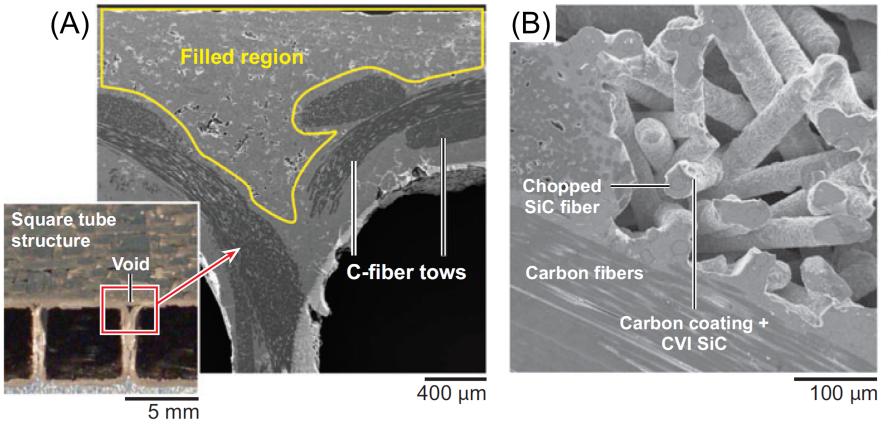

Figure 2.4: Robust microcomposite matrix in a C_f/SiC CMC. (A) (inset) Heat exchanger reinforcement contains tricorn-shaped voids at the intersection of a wall and the outer surface. (A) Tricorn-shaped voids are effectively filled with a robust microcomposite matrix consisting of chopped SiC fibers and a PIP-derived SiC matrix. (B) Tricorn-shaped region filled with chopped SiC fibers coated with CVI pyrolytic carbon and SiC. Figure reprinted from Marshall and Cox [4] with permission from Annual Reviews.

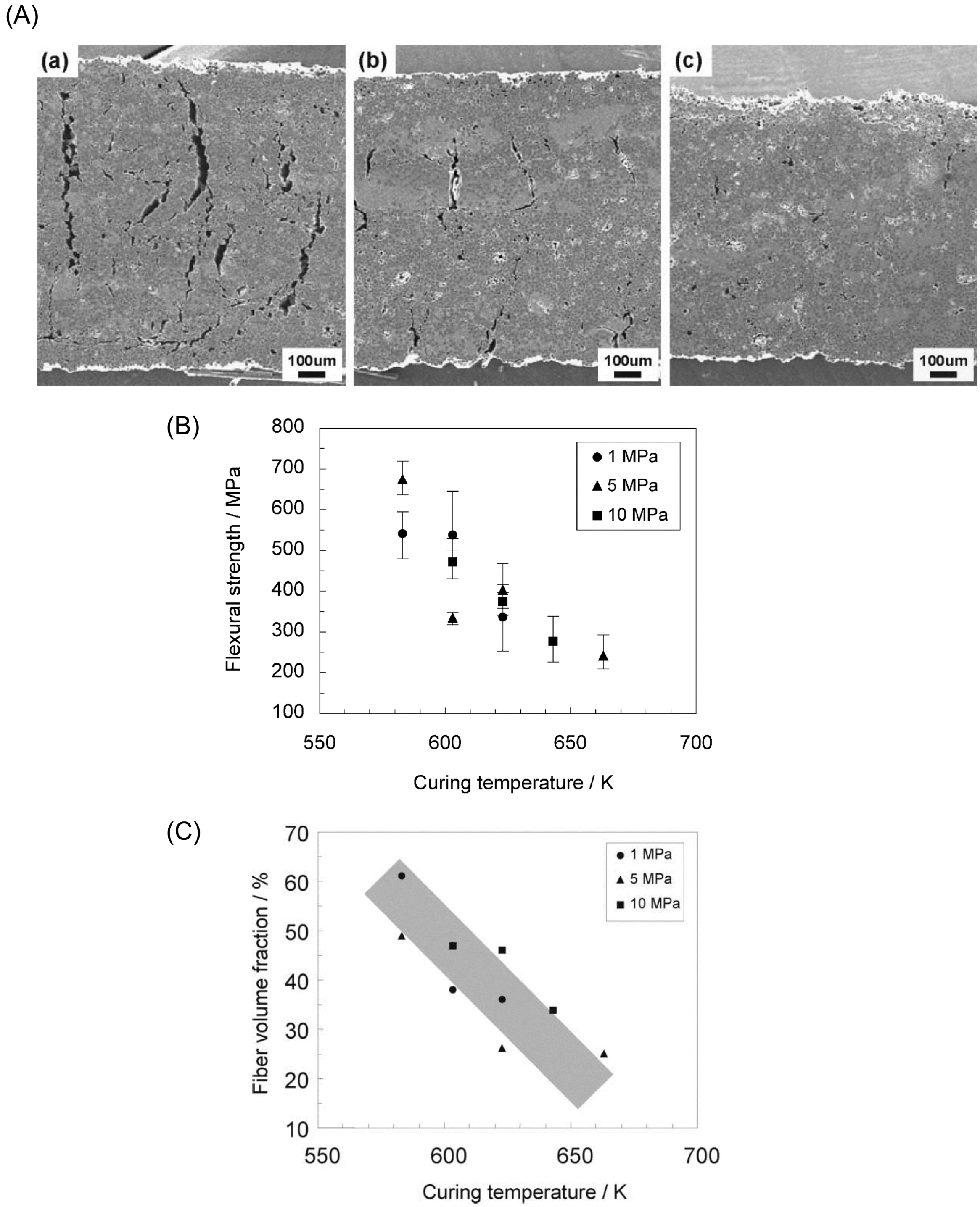

Figure 2.5: Effects of curing temperature, consolidation pressure and heating rate on composite microstructure and mechanical properties. (A) SEM images of CMCs consolidated at (a) 600 K/h, (b) 300 K/h, and (c) 10 K/h. (B) Flexural strength and (C) fiber volume fraction increase as curing temperature decreases. Figures reprinted from Kotani [14] with permission from Elsevier.

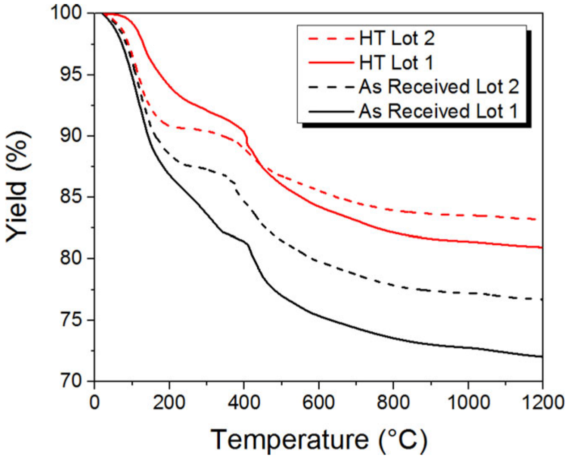

Figure 2.6: Mass yield of two lots (solid and dashed lines) of SMP-10 with (red lines) and without (black lines) vacuum heat treatment (HT) at 90°C for 10 h [12]. In both lots, vacuum heat treatment increases the mass yield of the PDC [12]. Figure reprinted from King [12] with permission from John Wiley and Sons.

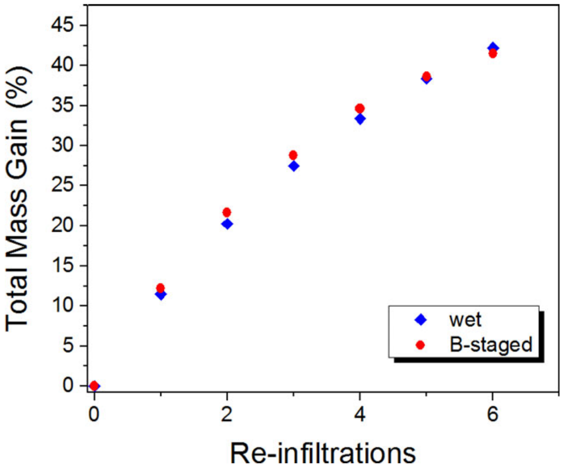

Figure 2.7: Mass gain of wet and B-staged CMC laminates after each re-infiltration [12]. B-staging shows no adverse effects on the rate of densification in subsequent PIP cycles [12]. Figure reprinted from King [12] with permission from John Wiley and Sons.

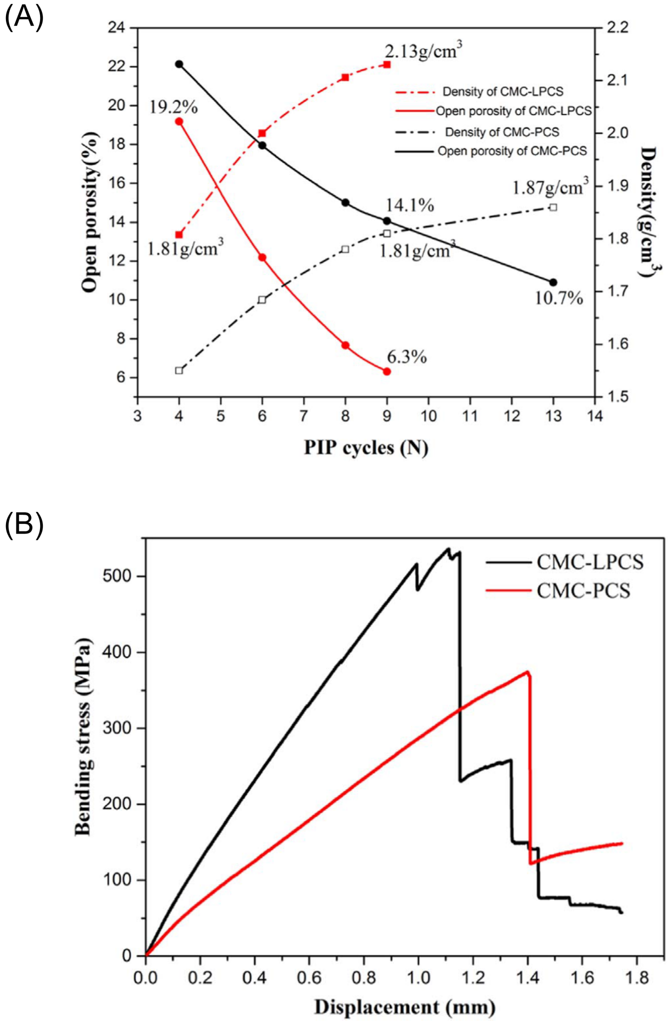

Figure 2.8: Densification efficiency and mechanical properties of LPCS- and PCS-derived CMCs. (A) LPCS shows superior densification behavior compared to PCS over several PIP cycles. (B) Flexural testing reveals superior mechanical properties of LPCS-derived CMCs. Figures reprinted from Zhong [25] with permission from Elsevier.

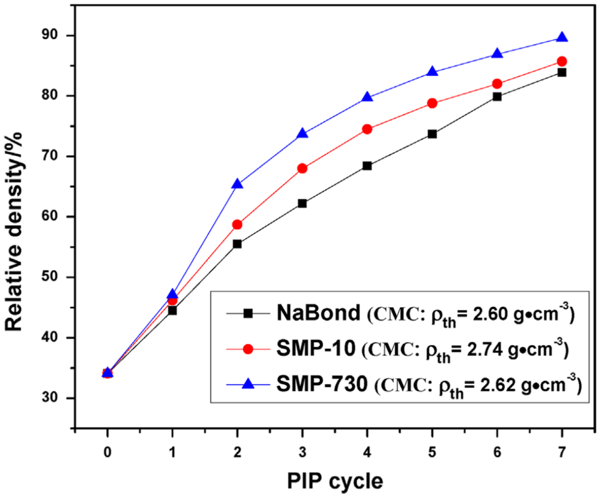

Figure 2.9: Densification of SiC_f/SiC CMCs fabricated with three different polycarbosilane precursors [22]. Figure reprinted from Yin [22] with permission from Elsevier.

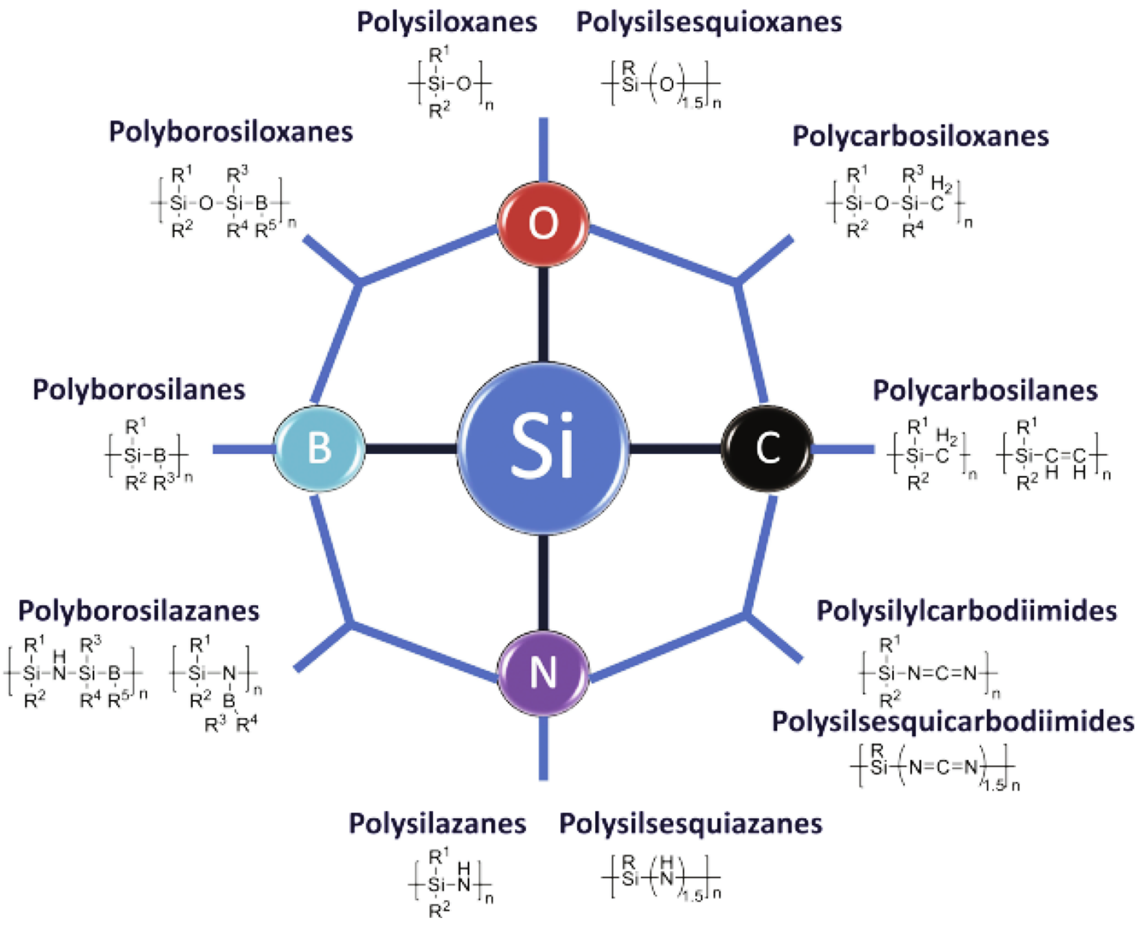

Figure 2.10: Classes of organosilicon preceramic polymers. Figure reprinted from Colombo [17] with permission from John Wiley and Sons.

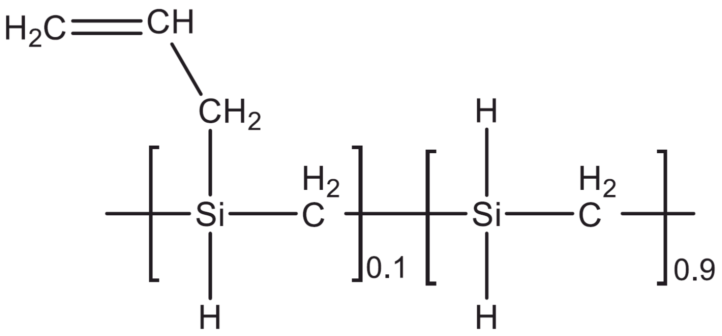

Figure 2.11: Schematic depiction of AHPCS molecular structure. Figure reprinted from Kaur [20] with permission from Elsevier.

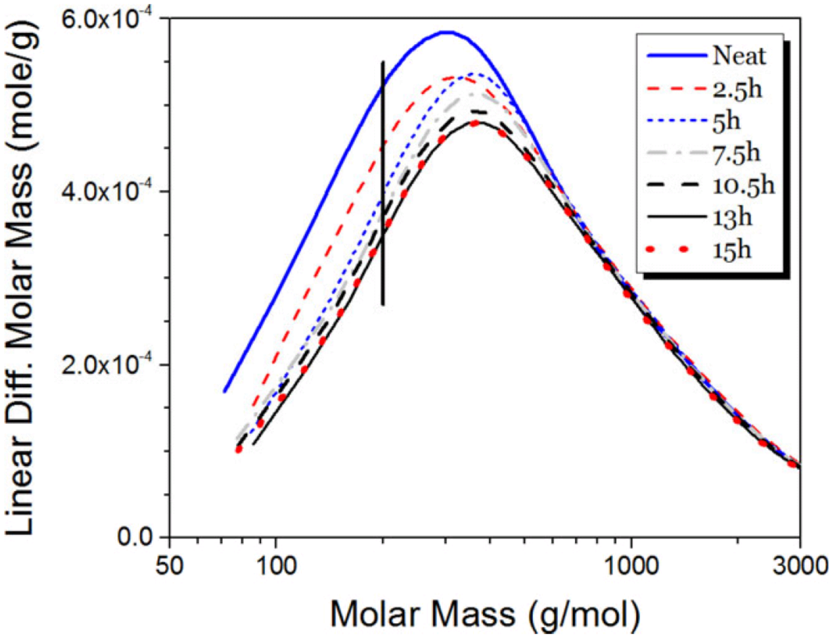

Figure 2.12: The molecular weight distribution of SMP-10 shifts to higher molecular weights with increasing time duration of thermal treatment at 86°C in vacuum [12]. This is due to the volatilization of low molecular weight oligomers from the SMP-10. Molecular weight measurements were performed using gel permeation chromatography. Figure reprinted from King [12] with permission from John Wiley and Sons.

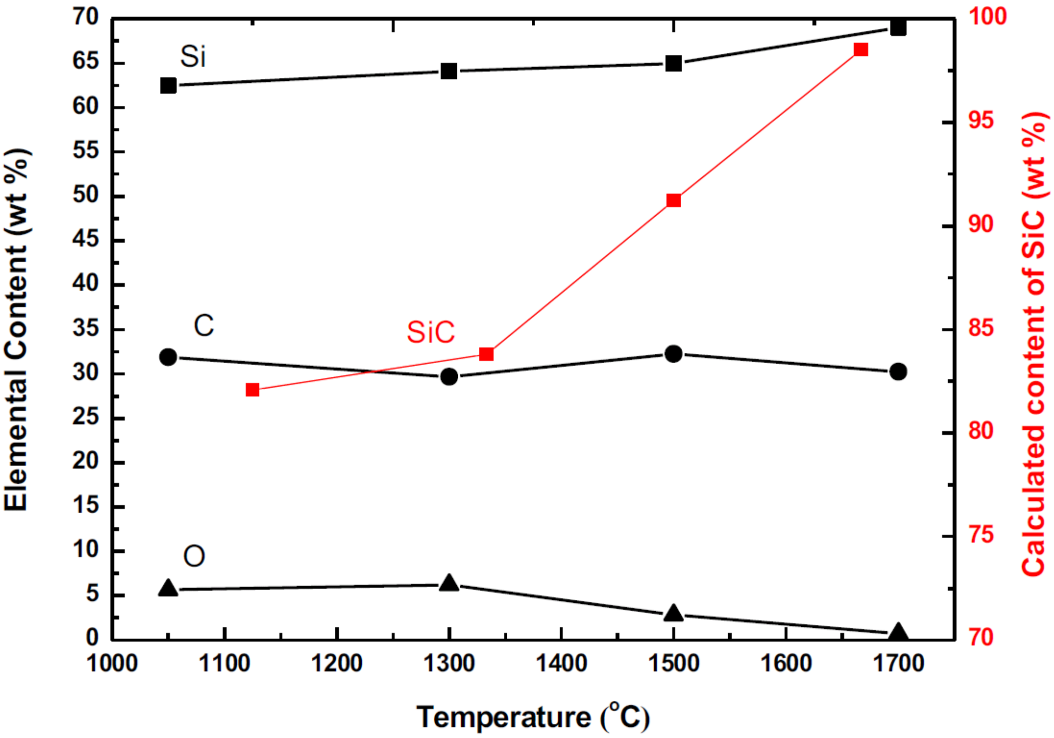

Figure 2.13: Elemental content of AHPCS-derived ceramic after annealing at various temperatures for 3h in argon [20]. With increasing annealing temperature, the fraction of oxygen and excess carbon decrease while the fraction of stoichiometric SiC increases. Figure reprinted from Kaur [20] with permission from Elsevier.

(a) Amorphous Si-O-C (As Pyrolyzed)

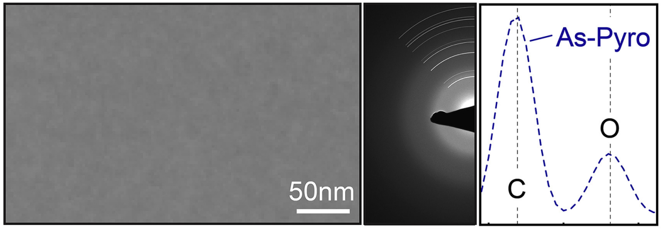

(b) Nanoscale β-SiC Crystallites Nucleate (1400ºC, 0h)

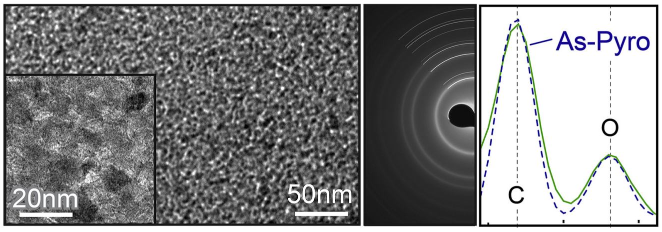

(c) Continued Coarsening with Loss of C, O (1500ºC, 1h)

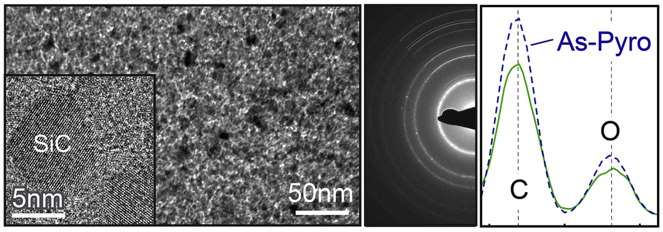

(d) Interphase Limits Coarsening (1500ºC, 24h, Interior)

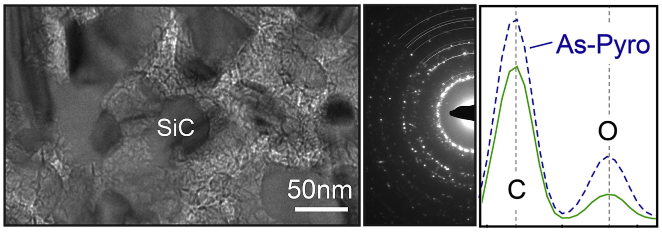

(e) Intergranular Phase Removed (1500ºC, 24h, Exterior)

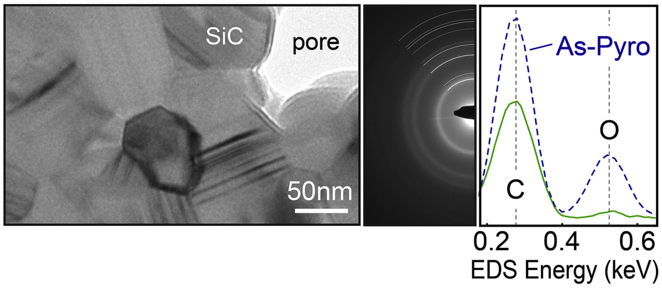

Figure 2.14: Progression of crystallization and elimination of oxygen and excess carbon with thermal treatment of AHPCS-derived ceramic in gettered argon [6]. Brightfield-TEM micrographs, SAED patterns, and TEM-EDS spectra are illustrated for each thermal treatment. EDS spectra are normalized to the Si peak intensity (not shown). The results show reductions in C and O content with increasing temperature and time. The results also show that both crystallization and C and O reduction occur more readily along particle surfaces (exterior) than particle interiors, suggesting that egress of gaseous decomposition products limit crystallization. Figure reprinted from Poerschke [6] with permission from Elsevier.

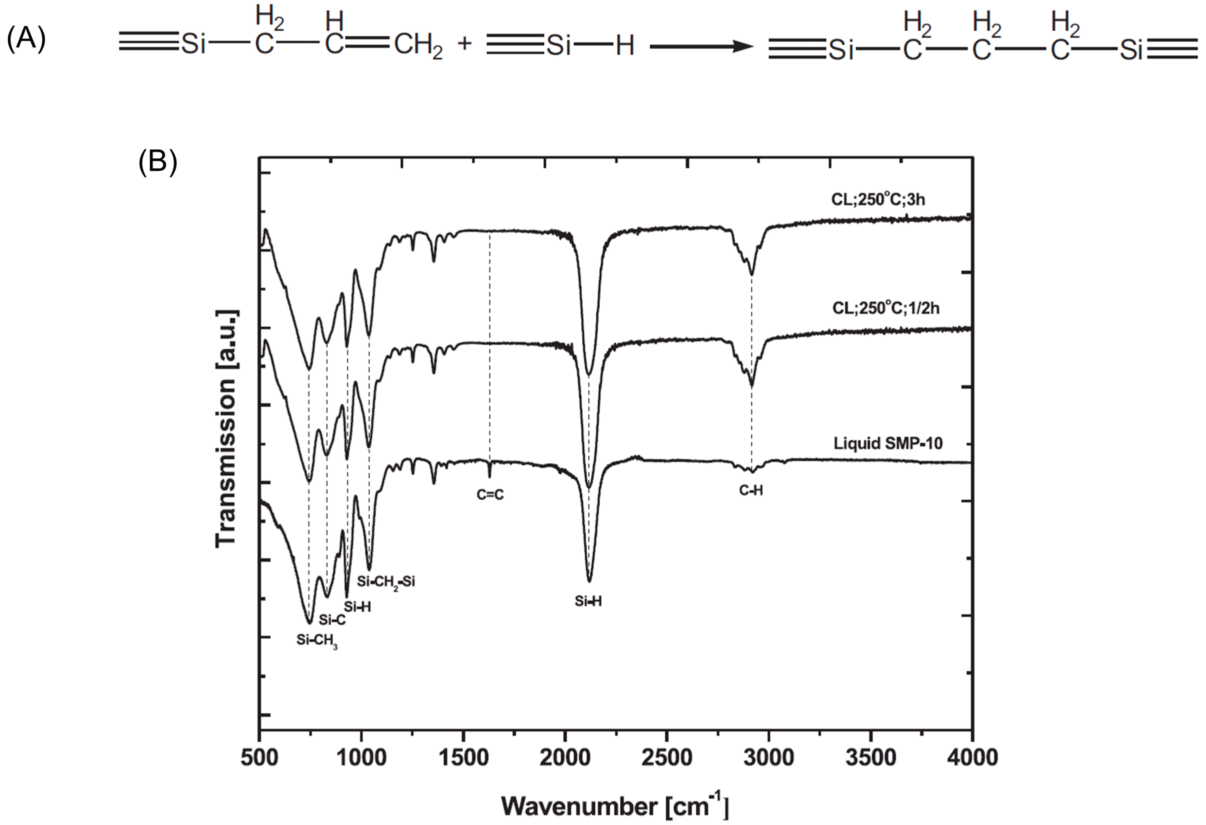

Figure 2.15: (A) Simplified schematic of the hydrosilylation crosslinking mechanism and (B) accompanying FTIR spectra showing the corresponding consumption of allyl groups [20]. The band at 1631cm^{-1} represents the C=C bond in the allyl group. This band completely disappears after treatment at 250°C, suggesting that hydrosilylation has ooccured. Figure reprinted from Kaur [20] with permission from Elsevier.

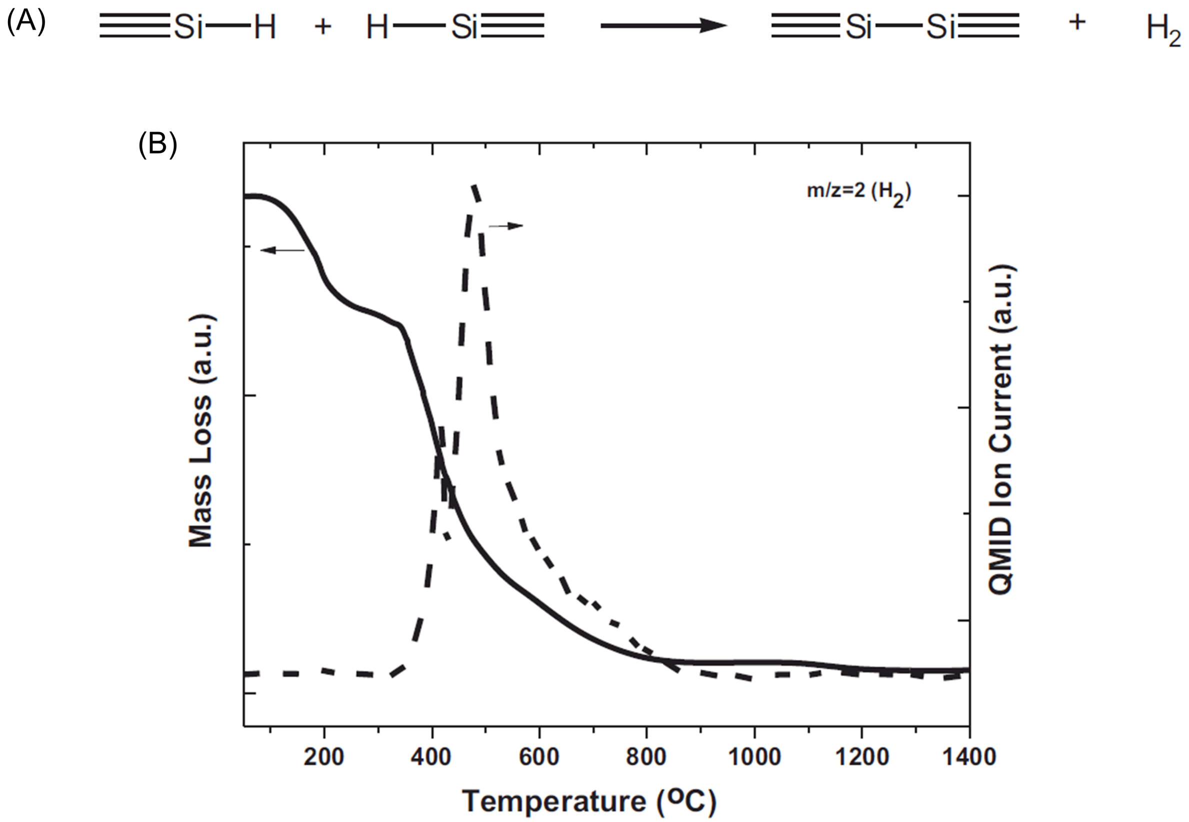

Figure 2.16: (A) Simplified schematic of the dehydrocoupling crosslinking mechanism and (B) accompanying TGMS results showing hydrogen evolution (dashed line) and mass loss (solid line) [20]. Figure reprinted from Kaur [20] with permission from Elsevier.

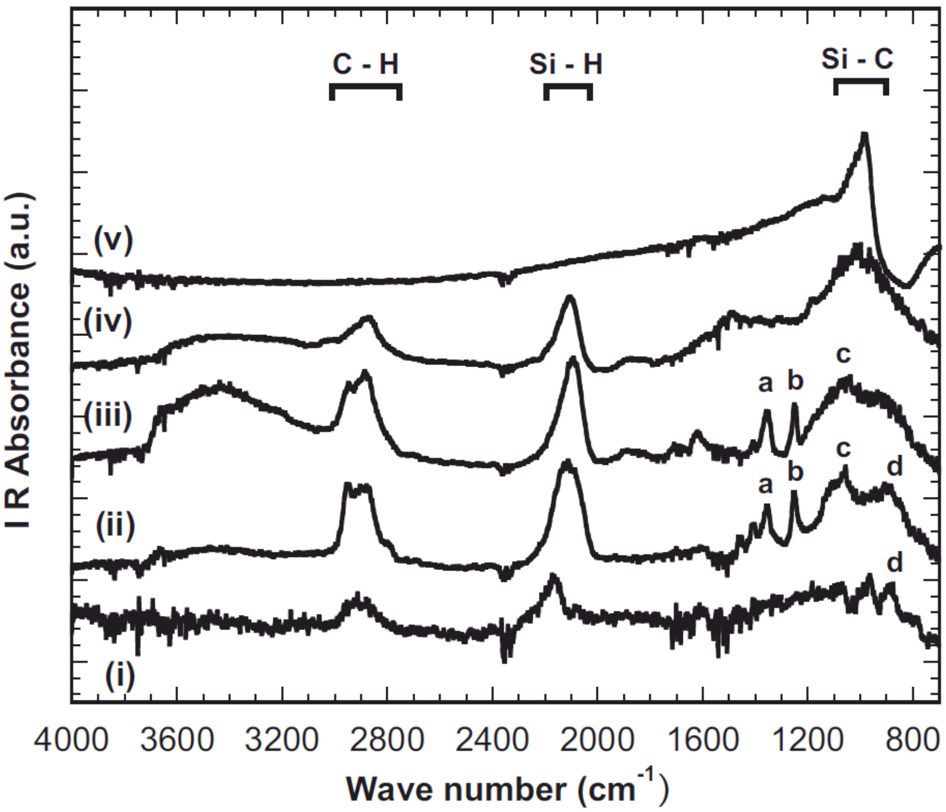

Figure 2.17: FTIR spectra showing the disappearance of C-H and Si-H peaks and appearance of a Si-C peak during the ceramization process [21]. Figure reprinted from Zunjarrao [21] with permission from John Wiley and Sons.

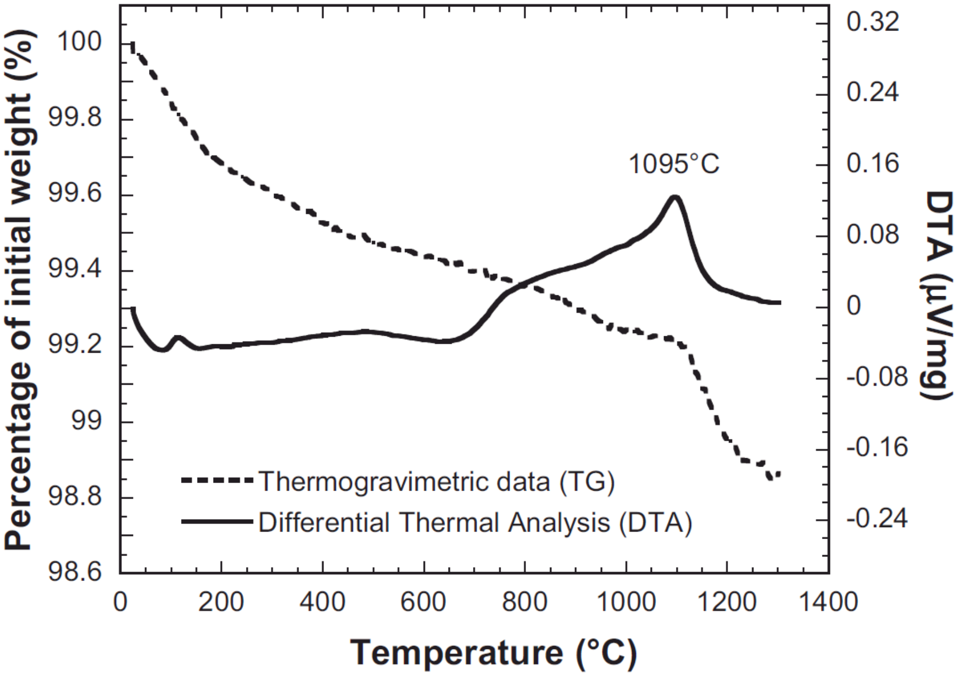

Figure 2.18: DTA and TG curves for AHPCS during thermal treatment to 1300°C at a heating rate of 5°C/min [21]. The peak in the DTA curve at about 1100°C is attributed to the onset of crystallization. Figure reprinted from Zunjarrao [21] with permission from John Wiley and Sons.

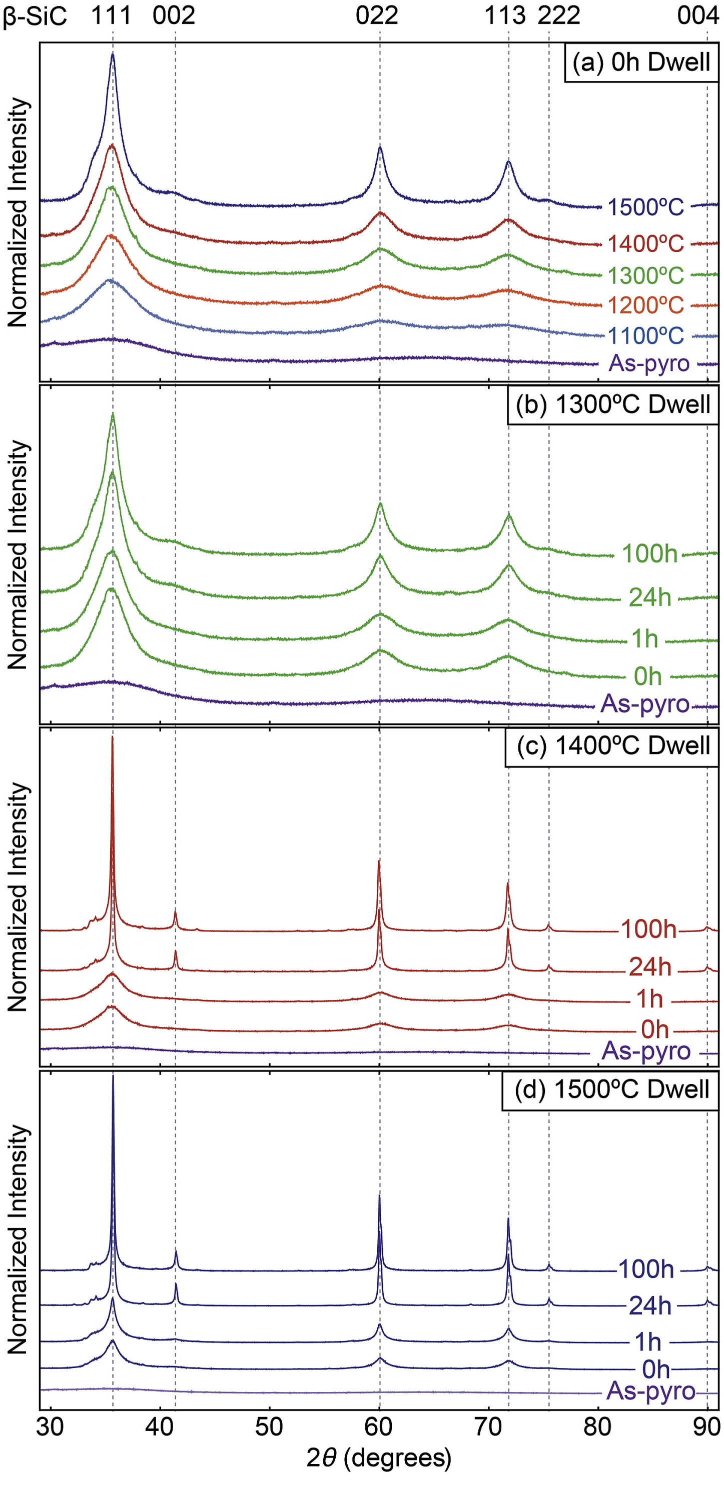

Figure 2.19: XRD patterns illustrate crystallization progress with increasing temperature and increasing dwell time [6]. The as-pyrolyzed (as-pyro) pattern indicates an amorphous microstructure and is for specimens pyrolyzed to a maximum temperature of 800°C. Figure reprinted from Poerschke [6] with permission from Elsevier.

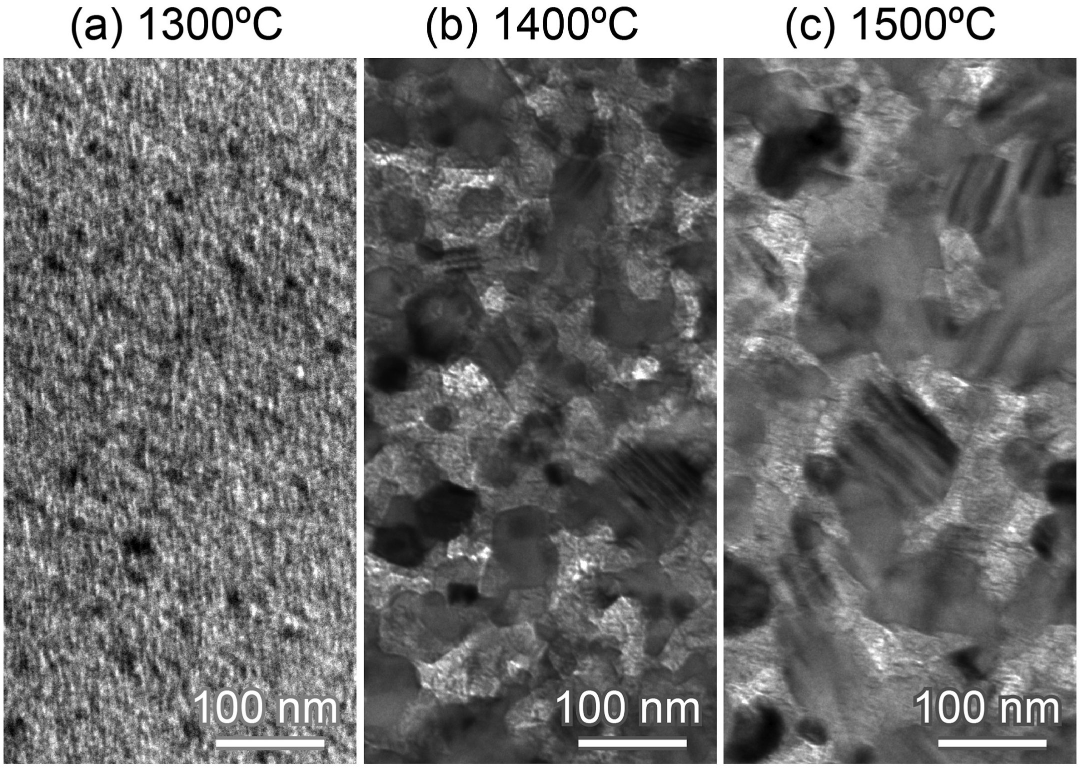

Figure 2.20: Brightfield-TEM images of specimens annealed for 100h at (a) 1300°C, (b) 1400°C, and (c) 1500°C [6]. The specimen treated at 1500°C shows the highest fraction of crystalline β-SiC and the largest crystallite size. Figure reprinted from Poerschke [6] with permission from Elsevier.

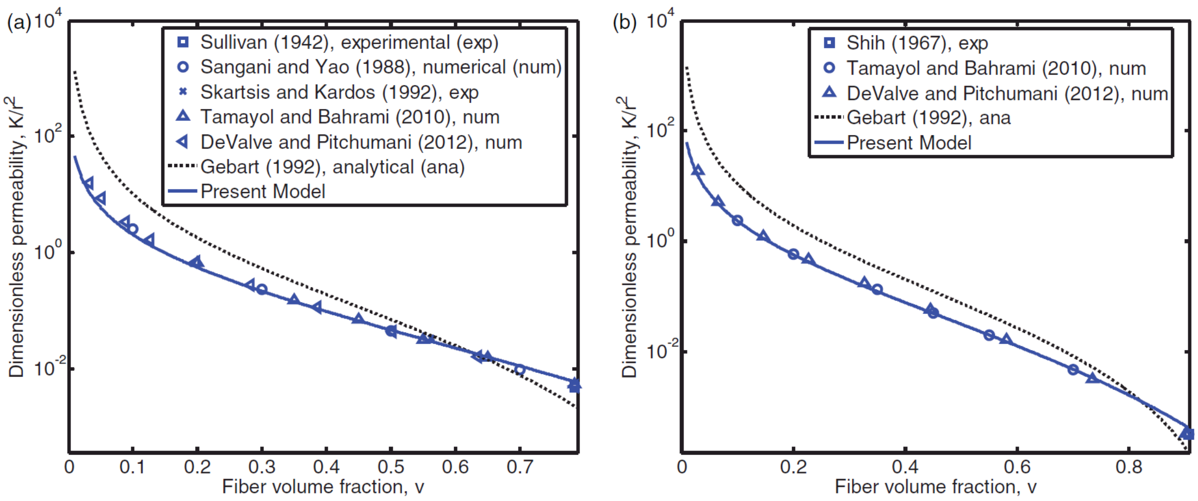

Figure 2.21: Comparison of models for longitudinal permeability with experimental and numerical results for (a) square and (b) hexagonal fiber arrangements [37]. The KC model (labeled Gebart) is shown with a dashed black line and the model developed by Shou, et al. is shown with a solid blue line. Dimensionless permeability is defined as the permeability divided by the fiber radius, r, squared. Figure reprinted from Shou [37] with permission from SAGE Publications.

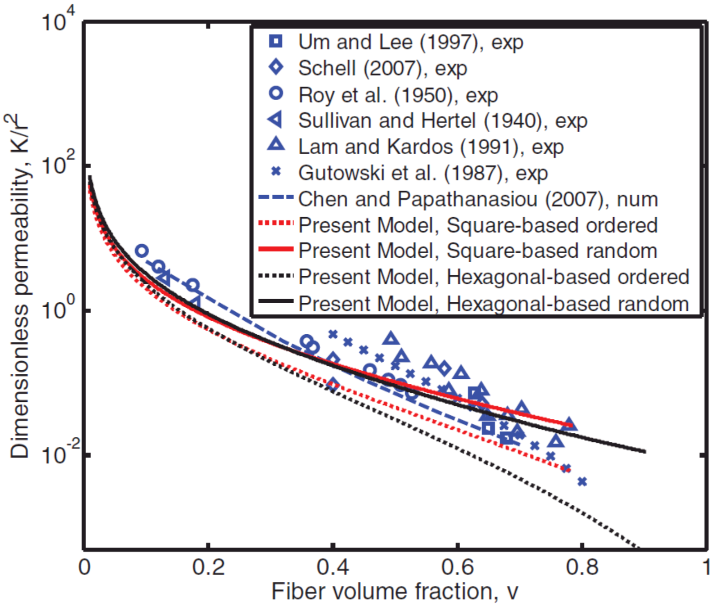

Figure 2.22: Comparison of models for longitudinal permeability of random fiber arrays with experimentally measured permeabilities [37]. Models for uniform (ordered) fiber arrays are also plotted for comparison. Figure reprinted from Shou [37] with permission from SAGE Publications.

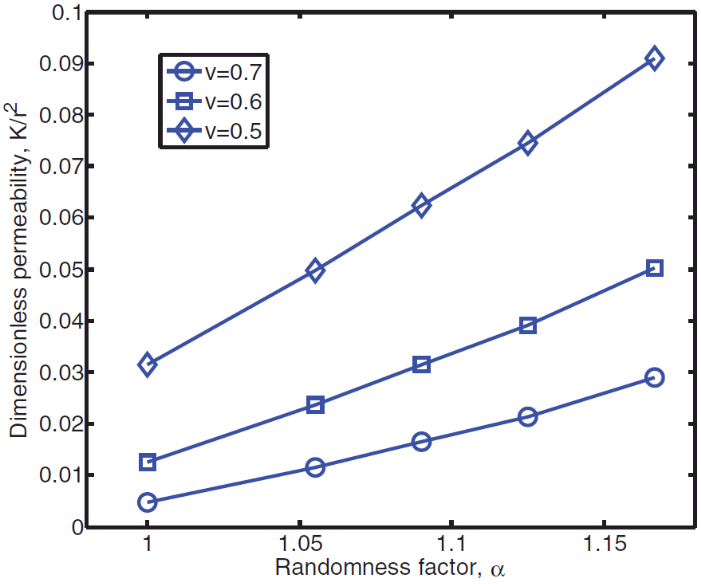

Figure 2.23: Longitudinal permeability increases with increasing degree of non-uniformity as defined by a randomness factor α [37]. Results are shown for three different fiber volume fractions, v. Figure reprinted from Shou [37] with permission from SAGE Publications.

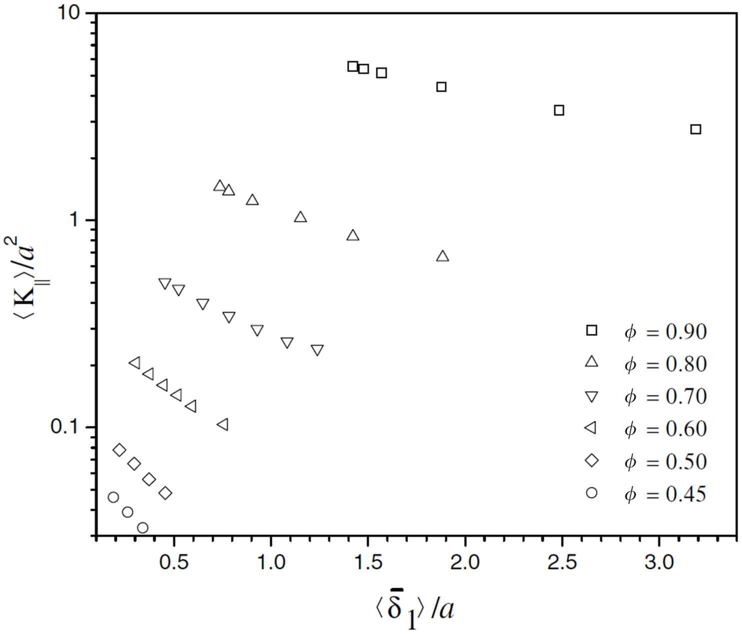

Figure 2.24: Longitudinal permeability increases as mean minimum inter-fiber distance decreases [39]. Results are shown for several fiber bed porosities, ϕ [39]. The permeability, $\langle K_{||} \rangle$ is normalized by the fiber radius, a, squared. The mean minimum inter-fiber distance, $\langle \bar{\delta}_1 \rangle$ is normalized by the fiber radius. Figure reprinted from Chen [39] with permission from Elsevier.

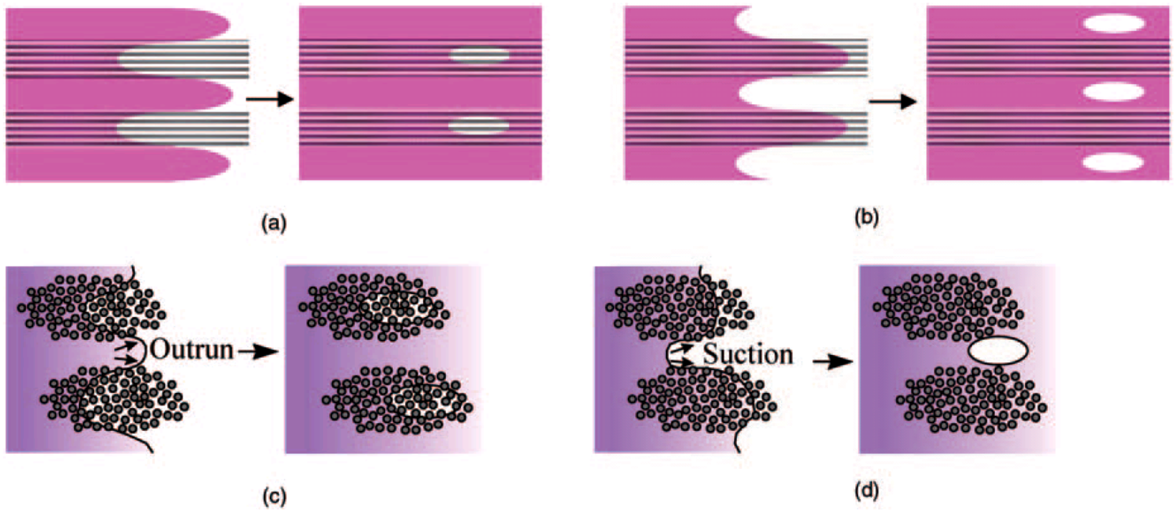

Figure 2.25: Entrapment of voids due to non-uniform fluid flow in (a-b) the longitudinal direction and (c-d) the transverse direction [32]. In (a) and (c), the leading flow front occurs in the large channels between tows, leading to entrapment of tow voids. In (b) and (d), the leading flow front occurs within the tows, leading to entrapment of channel voids. Figure reprinted from Park [32] with permission from SAGE Publications.

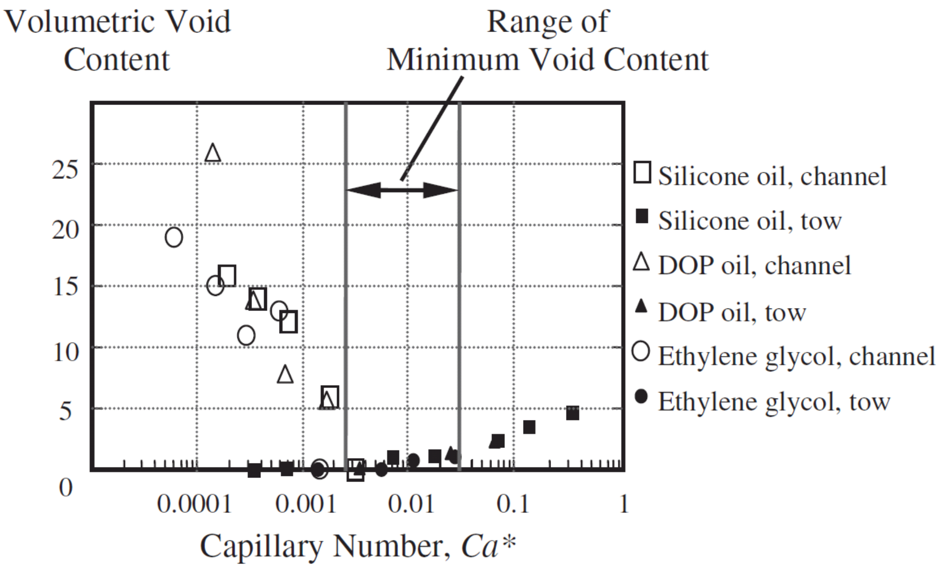

Figure 2.26: Void type and void content correlate with capillary number for various liquids within the same type of fiber bed [32]. Channel voids are plotted with open symbols and tow voids are plotted with filled symbols. Figure reprinted from Park [32] with permission from SAGE Publications.

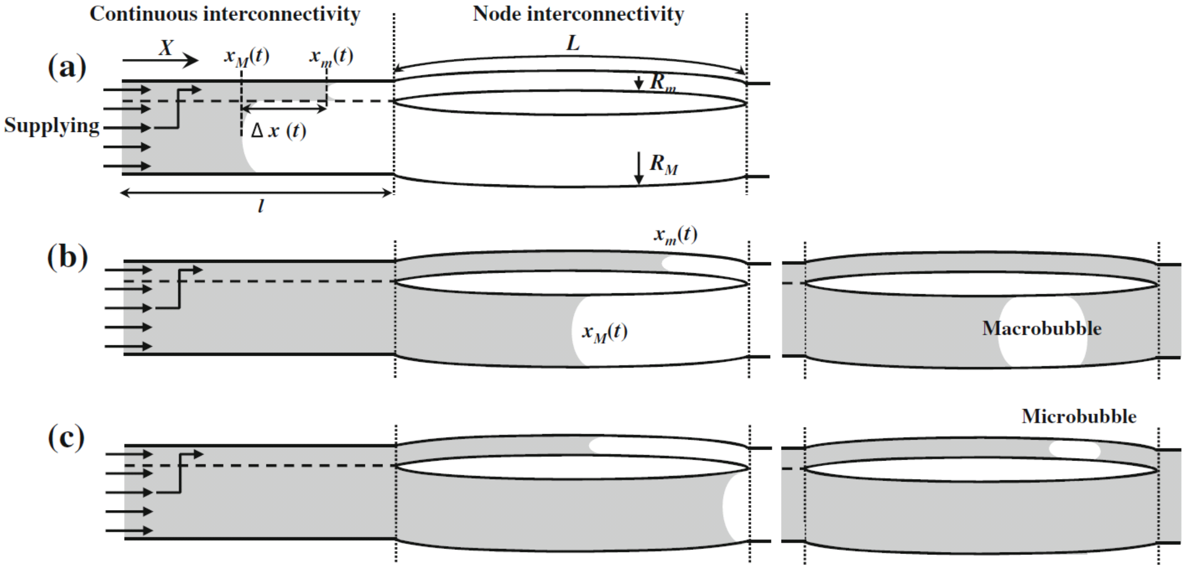

Figure 2.27: Schematic of the pore doublet model (PDM) developed by Wielhorski, et al., illustrating (a) the supplying principle, (b) formation of a macrobubble, and (c) formation of a microbubble [50]. Figure reprinted from Wielhorski [50] with permission from Springer.

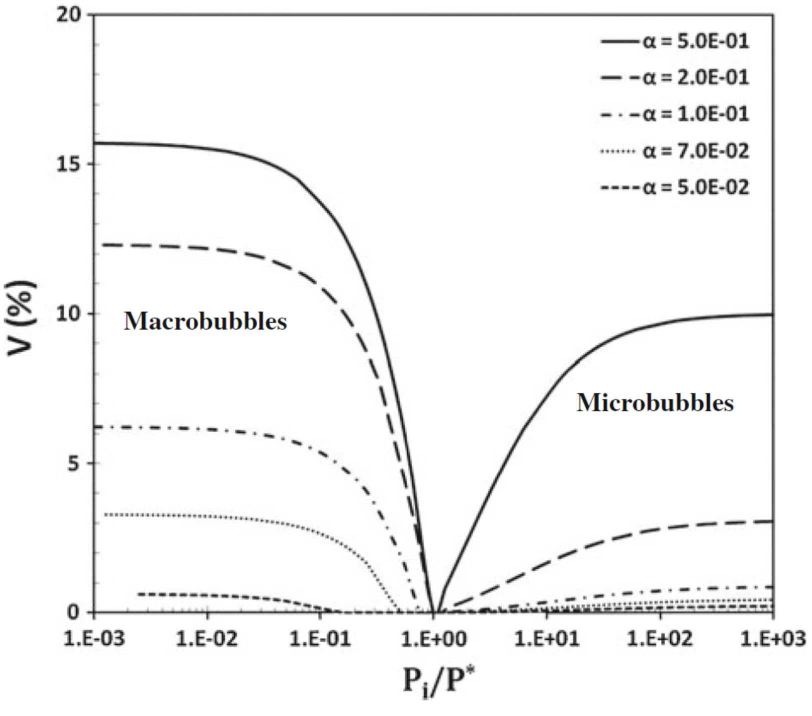

Figure 2.28: Content of macrobubbles and microbubbles as a function of dimensionless injection pressure (P_i/P^*) in pore doublet model [50]. Results are shown for different values of $\alpha = R_m/R_M$ with $\beta = L/l = 0.002$, $l = 500$mm and $R_m = 10\mu$m. Figure reprinted from Wielhorski [50] with permission from Springer.

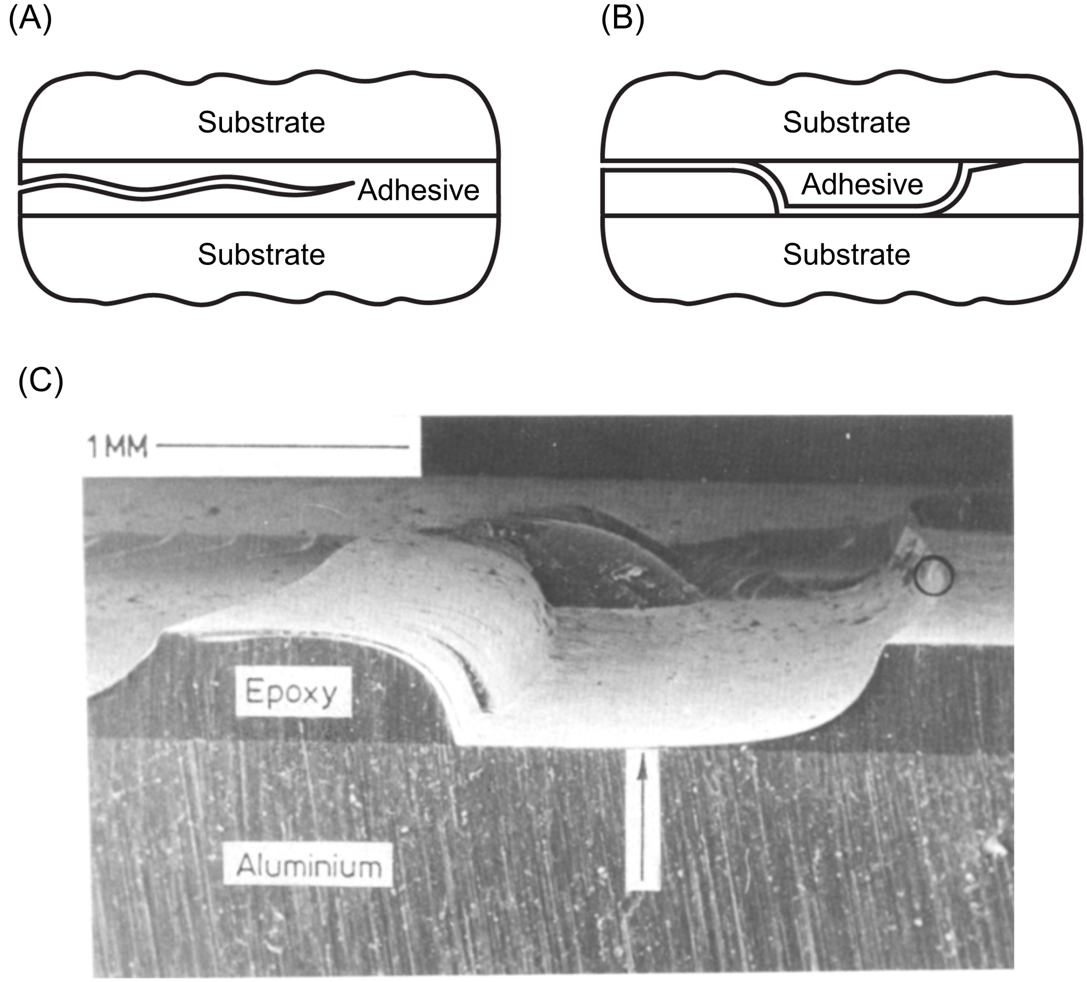

Figure 2.29: Schematics of (A) wavy and (B) alternating crack geometries. (C) Fracture surface of an alternating crack in an epoxy/aluminum double cantilever beam specimen [68]. Figure (C) reproduced from Akisanya [68] with permission from Springer Nature.

(A) 1st I&C (B) 1st PIP

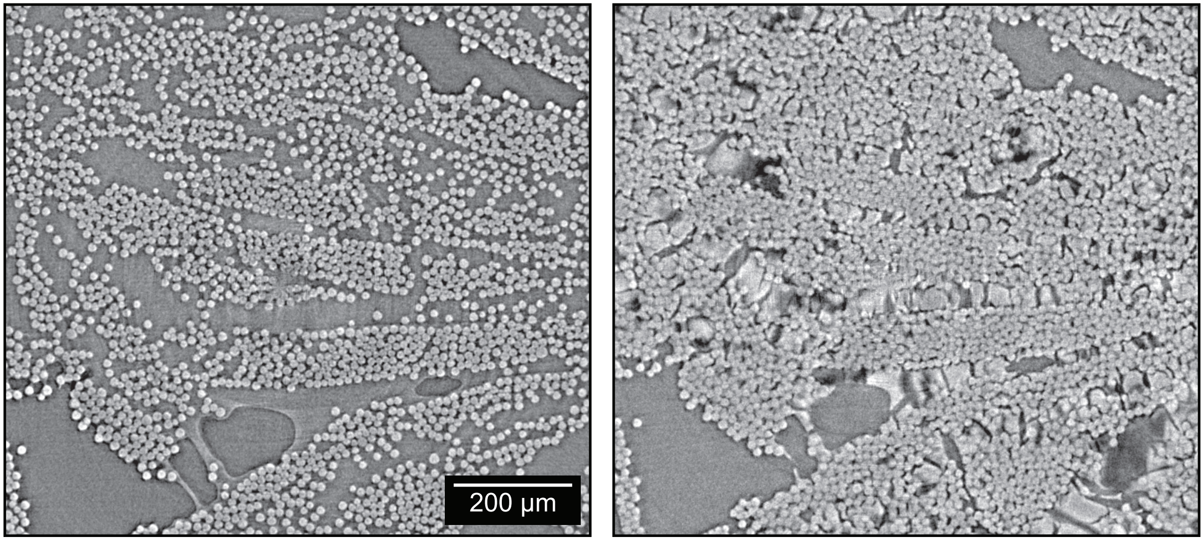

(C) 1st PIP + 2nd I&C (D) 2nd PIP + 3rd I&C

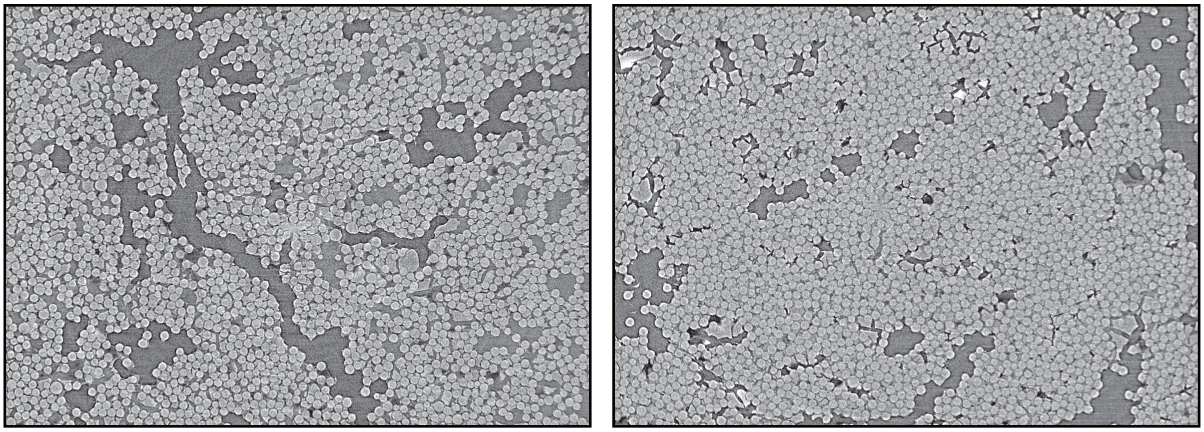

(E) 3rd PIP + 4th I&C (F) 4th PIP + 5th I&C

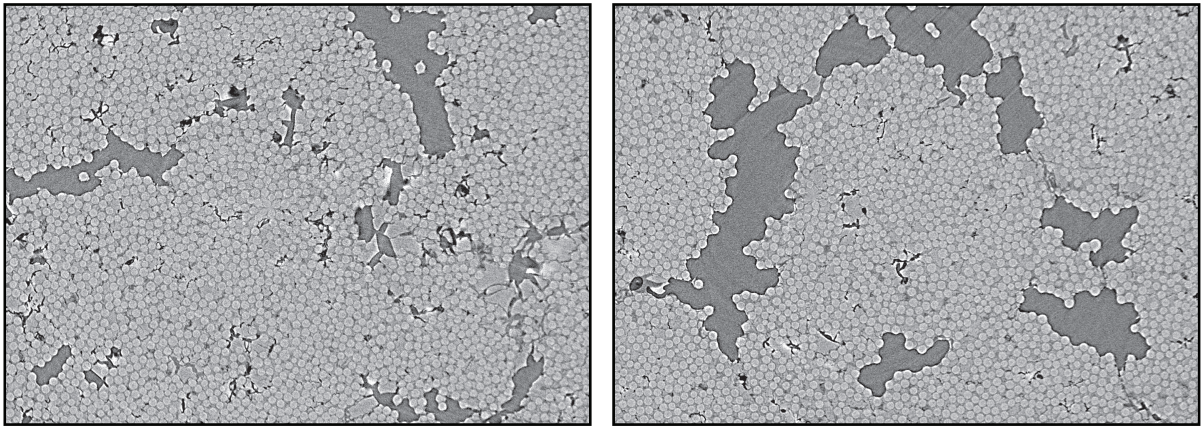

Figure 2.30: Transverse sections from XCT of unidirectional fiber beds after various stages of repeated PIP. Processing stages shown are (A) after 1st impregnation and cure (I& C), (B) after 1st PIP*, (C) after 1st PIP + 2nd impregnation and cure, (D) after 2nd PIP + 3rd impregnation and cure, (E) after 3rd PIP + 4th impregnation and cure, and (F) after 4th PIP + 5th impregnation and cure. Transverse sections in (A) and

(B) are from the same location within the same specimen before and after pyrolysis. Transverse sections in (C)-(F) are all from different specimens. Scale bar applies to all images.

*The pyrolysis temperature profile used for this specimen is different from that of the standard pyrolysis. The primary difference is the maximum pyrolysis temperature, which was 1200°C instead of 850°C. The thermal profile used for this specimen was: 25°C to 250°C at 2°C/min, 250°C to 700°C at 1°C/min, 700°C to 930°C at 3°C/min, 930°C hold 70min, 930°C to 1090°C at 3°C/min, 1090°C hold 70min, 1090°C to 1200°C at 2°C/min, 1200°C hold 70min, cool at -5°C/min. This profile is similar to that recommended by Starfire® Systems [31]; slight differences are due to limitations in calibration precision and temperature control for the heating system used in this experiment.

Chapter 3

Axial Permeability of Unidirectional Fiber Beds

Abstract

In-situ X-ray computed tomography during axial impregnation of unidirectional fiber beds is used to study coupled effects of fluid velocity, fiber movement and preferred flow channeling on permeability. In order to interpret the experimental measurements, a new computational tool for predicting axial permeability of very large 2D arrays of non-uniformly packed fibers is developed. The results show that, when the impregnation velocity is high, full saturation is attained behind the flow front and the fibers rearrange into a less uniform configuration with higher permeability. In contrast, when the velocity is low, fluid flows preferentially in the narrowest channels between fibers, yielding unsaturated permeabilities that are lower than those in the saturated state. These insights combined with a new computational tool will enable improved prediction of permeability, ultimately for use in optimization of composite

manufacturing via liquid impregnation[1].

3.1 Introduction

In manufacturing of fiber-reinforced composites, the matrix phase is commonly introduced by pressure-assisted impregnation of a fluid into a dry fiber preform, a process referred to as liquid composite molding (LCM) [32]. One of the challenges with this process involves formation and entrapment of voids and hence incomplete saturation of the fiber preform [32–34, 50]. Experimental studies have demonstrated that void content is correlated with the capillary number, $Ca = \mu v/\gamma$, where v is the tracer fluid velocity, μ is the fluid viscosity, and γ is the fluid surface tension [32–34]. In preforms of woven tows of fibers, void content attains a minimum at an optimal capillary number [32]. Below the optimum, fluid flows faster in the small channels *within* tows, due to capillary wicking, leading to remnant voids *between* tows [32]. In contrast, at high capillary numbers, preferred flow within the large channels *between* tows leads to voids *within* tows [32]. In unidirectional fiber beds subject to transverse flow, void content decreases with increasing Ca [33]. This effect has been attributed to increased mobilization of voids at higher Ca [33].

Controlling the impregnation velocity (and thus the capillary number) during liquid composite molding is crucial for minimizing void content in the final composite product. Impregnation kinetics through fiber beds are typically modeled by Darcy's Law. The Darcy velocity (or Darcy flux) during *saturated* fluid flow is given by

$$\vec{q} = -\frac{\tilde{\kappa}_s}{\mu}\nabla P \tag{3.1}$$

---

[1] The content of this chapter has previously appeared in Composites Part A: Applied Science and Manufacturing (**Natalie M. Larson**, Frank W. Zok. "Insights from in-situ x-ray computed tomography during axial impregnation of unidirectional fiber beds". *Composites Part A* **107**, 124-134 (2018)) [69]. It is reproduced here with the permission of Elsevier.

where $\tilde{\kappa}_s$ is the saturated permeability tensor and ∇P is the pressure gradient [32–40]. The corresponding tracer velocity is:

$$\vec{v} = \frac{\vec{q}}{\varepsilon} \tag{3.2}$$

where ε is the porosity of the fiber bed [32]. Fundamental models for saturated permeability of fiber beds have been developed on the basis of analyses of unit cells representing static, uniformly-packed fibers and idealizations of flow fields in the intervening channels [35–37, 42, 47]. The longest-standing model for the permeability of a unidirectional fiber bed is attributed to Kozeny and Carman and is based on an analysis of a collection of uniform aligned tubes [33, 35–37, 40, 42, 70].

In composite processing, impregnation involves displacement of air by fluid within the fiber preform and thus the *unsaturated* permeability is also relevant [32, 41, 43]. In this process, there generally exists a partially-saturated zone in which the saturation S increases from zero at the flow front to a steady-state value at some distance behind the flow front [32]. Preferred flow channeling may occur in either small or large channels within the preform *at* the flow front [32]. Furthermore, the steady-state saturation may be less than unity due to bubble entrapment, which may also result in continued preferred flow channeling well *behind* the flow front and partially-saturated zone. To account for incomplete saturation, Darcy's law (eq. 3.1) and the tracer velocity (eq. 3.2) are modified as follows [32]:

$$\vec{q} = -\frac{k_r(S)\tilde{\kappa}_s}{\mu}\nabla P \tag{3.3}$$

$$\vec{v} = \frac{\vec{q}}{\varepsilon S} \tag{3.4}$$

where k_r is a non-dimensional relative permeability, ranging from 0 to 1 as S varies from 0 to 1 [32, 41]. The unsaturated permeability, $\tilde{\kappa}_u$, is defined as $\tilde{\kappa}_u = k_r(S)\tilde{\kappa}_s$ [32, 41].

Estimating unsaturated permeability requires knowledge of S, $k_r(S)$, and $\tilde{\kappa}_s$. These parameters have been shown to depend on uniformity of fiber packing and capillary number as follows [41, 43, 44, 46, 47, 71]. First, the axial *saturated* permeability increases with the degree of non-uniformity in fiber packing [36–39]. It has been further suggested that cooperative fiber movement may lead to an increase in the degree of non-uniformity and hence permeability [43–45]. However, direct evidence of such movement and its effect on permeability are lacking. Second, the unsaturated permeability of fiber preforms increases with Ca [43, 46–49]. In woven fabrics, this behavior has been attributed to preferred flow channeling *at* the flow front within the large inter-tow channels at high Ca [43, 46, 47]. As noted earlier, unsaturated fluid flow can occur preferentially in either the smallest or the largest channels *at* or well *behind* the flow front and partially-saturated zone, depending on the impregnation velocity and the fiber bed geometry. Direct microstructural evidence of preferred flow channeling and its effects on permeability are also lacking.

The present study aims to address these deficiencies through direct observations of fiber movement and preferred flow channeling via *in-situ* X-ray computed tomography (XCT) during impregnation over a wide range of velocities. An improved understanding of such effects should lead to improved permeability models which, in turn, could be used to enhance process control in liquid composite molding.

Mechanisms of fluid flow and void transport within fiber tows were previously studied by Vilà et al. [72] using XCT. In that study, fluid was impregnated into the tow incrementally (not continuously) using a syringe [72]. Since the acquisition time for each XCT scan in that study was long (about 2 h), the fluid front could only be imaged under static conditions [72]. (Otherwise, significant blurring would have occurred.) The experiments in the present study differ from those of Vilà et al. [72] in two important respects. First, imaging was performed *in-situ during* impregnation. Second, the XCT scan times were much shorter (1.5 min). As a result, the present experiments enable observation of fiber movement and preferred flow channeling over a range of impregnation velocities. One drawback of the short scan time and potential movement of the phases during impregnation is reduced image quality. Consequently, a significant amount of manual intervention is required to properly segment the various phases during image processing.

In order to interpret the observations of fiber movement and preferred flow channeling as well as their effects on permeability, we also present and employ a new computational tool for estimating permeability of very large arrays of non-uniformly-packed fibers. Here 2D segmented XCT images of fibers, voids and fluid are used as inputs into the computations; preferred flow channeling and changes in fiber position before and during impregnation are therefore explicitly addressed. The results are calibrated and assessed through comparisons with results from computational fluid dynamics (CFD) simulations of flow in uniform and non-uniform fiber beds. Comparisons of predicted permeabilities with those obtained using computational schemes based on unit-cell analyses of non-uniform fiber beds demonstrate the superiority of the current approach.

3.2 Materials and methods

3.2.1 Test specimens

The material system selected for the study is based on a commercial SiC fiber and a SiC preceramic polymer that, together, have been the focus of attention in the ceramic matrix composites community in recent years [1, 5, 73]. Unidirectional fiber beds were made by filling 10 cm long thin-walled borosilicate glass tubes (1.5 mm ID, 1.8 mm OD, VitroCom, Mountain Lakes, NJ) with 10-12 tows of Hi-Nicalon$^{\text{TM}}$ Type S

SiC fibers (500 fibers/tow), and then heat-shrinking the tubes onto the fibers under vacuum. During heat shrinking, the tubes conform to the profile of the outermost fibers. The terminal inner diameter of the tubes was about 1.4 mm. The resulting fiber bed porosity within the tubes was $0.32 - 0.38$. Based on analysis of ≈3,800 fibers over a length of 1.4 mm in a representative specimen, fiber misalignment relative to the tube axis was determined to be $1.4 \pm 0.8°$. The polyvinyl alcohol sizing that had been present on the fibers at the outset was removed with a 1h thermal treatment at 600°C.

A commercial SiC pre-ceramic polymer — allylhydridopolycarbosilane (SMP-10, Starfire Systems, Inc., Glenville, NY) — was used as the impregnating fluid (surface tension, $\gamma = 30 \times 10^{-3}$ J/m^2, provided by manufacturer). SMP-10 is a transparent amber fluid at room temperature. It is converted to SiC by pyrolysis at temperatures above 850°C. The fluid was stored under Ar in a freezer to inhibit cross-linking and liberation of hydrogen. Notwithstanding, some changes occur over periods of several months. Their effects manifest in a gradual increase in viscosity. All experiments were conducted with the same batch of SMP-10. Its viscosity was measured periodically over the course of the study; it ranged from 68×10^{-3} Pa s at the outset to 82×10^{-3} Pa s at the end. Viscosity values pertinent to the subsequent analysis were obtained by interpolating the measurements to the time of each experiment. Immediately before using the precursor, 0.2 wt% dicumyl peroxide was added to it, to promote subsequent curing at 120°C.

3.2.2 Impregnation experiments

Two types of impregnation experiments were conducted. The first was designed to measure unsaturated axial permeability from impregnation rates under constant pressure (Fig. 3.1(A)). Impregnation was performed with the tubes oriented horizontally. Pressure was applied in one of two ways. For high pressures (> 100 kPa), compressed air at constant pressure P_m was applied to the fluid reservoir while the outlet was left open to atmospheric pressure. Pressures up to 607 kPa were used. For low pressures (< 100 kPa), the reservoir was left open to atmospheric pressure and vacuum was drawn at the tube outlet. In other cases, neither compressed air nor vacuum were applied ($P_m = 0$); here capillary pressure alone drives imbibition. The distance, x_{ff}, from the tube inlet to the flow front was monitored over time (Fig. 3.1(B,C)) with a Dino-Lite AD7013MZT optical microscope with resolution of 1280×960 pixels and a field of view of 2.8 mm×2.1 mm. The specimen was manually translated beneath the microscope lens in order to keep the flow front within the field of view. Uniformly-spaced fiducial marks on the tube surface were used for distance measurements. Following impregnation, specimens were cured at 120°C in air for 2 h and imaged *ex-situ* with XCT.

In a complementary set of experiments, impregnations into six comparable fiber beds were performed while continuous *in-situ* XCT imaging was performed at one location within the tube. These experiments were performed with the tubes oriented vertically: the fluid reservoir and inlet being at the top of the specimen and the outlet at the bottom. Pressures up to 552 kPa were employed. To minimize specimen vibration during rotation, the compressed air line was sent through a slip ring that rotates with the specimen. The pressure due to gravity was calculated to be ≈ 1.5 kPa: more than an order of magnitude less than the average capillary pressure, $\bar{P}_c = 16 \pm 1$ kPa (discussed in section 3.2.5). XCT images were taken before, during and after impregnation as well as after pressure removal. By definition, data taken at time $t = 0$ are from images taken prior to impregnation. Because the location of the flow front could not be monitored in these experiments, capillary numbers were estimated from the results of the first set of experiments at the corresponding pressures.

3.2.3 X-ray computed tomography (XCT)

XCT was performed at Beamline 8.3.2 at the Advanced Light Source at Lawrence Berkeley National Laboratory. *Ex-situ* imaging was performed in multilayer mode using 17 keV light (20-30% transmission) with a PCO edge camera and 10x optique lens. For each scan, a total of 1,025 radiographs each with 500-800 ms exposure time were collected over the course of about 14-22 minutes. The field of view was about $1.6\times1.6\times1.4$ mm^3 and the voxel edge length was 0.65 μm. *In-situ* imaging was performed in white light mode with a dimax camera and 10x lens. The field of view was about $2.0\times2.0\times2.0$ mm^3 and the voxel edge length was 1 μm. A full dataset, consisting of 1,025 radiographs each with 40 ms exposure time, was collected over the course of about 1.5 minutes; an additional 3.5 min was required to export the data from the camera between scans. The images were reconstructed using filtered back-projection methods.

3.2.4 Image segmentation

XCT images of the composites were segmented using the MATLAB image processing toolbox in the following way. First, fibers were identified using the Circle Hough Transform. Improperly identified pixels were corrected with filters based on connected region size and pixel value, and by using a slice-by-slice comparison of the identified fibers in the 10 slices above and below the slice of interest. Next, regions outside of the composite were identified using a grayscale threshold, 2D order-statistic filtering with a 5 by 5 pixel domain, and a flood-fill operation. The segmentation was improved by filtering out incorrectly identified pixels based on connected region size and by using a slice-by-slice comparison of the identified non-composite regions in the 17 slices above and below the slice of interest.

For one slice of each *in-situ* scan, fluid and void regions were segmented by manually tracing and labeling the various regions. (Segmentation based on grayscale thresholds alone is not effective.) Regions with and without fluid were identified on the basis of several image characteristics and their variation with time and location. First, surfaces of bare fibers (adjacent to voids) typically produce boundaries that are slightly darker than those at the fiber-fluid interfaces. Second, fluid regions appear slightly lighter than voids. Third, fluid-void interfaces show a relatively abrupt change in grayscale values (Fig. 3.2(A)(ii)). In addition to using these characteristics to identify the pertinent boundaries from individual transverse cross-sections, *changes* in these characteristics from one transverse section to the next or from one scan to the next were used for verification. For example, scrolling through a series of transverse sections from one scan reveals changes in grayscale when passing from void to fluid. Analogous changes are obtained by comparing scans taken at different times during impregnation. A representative raw image and corresponding segmented image are shown in Fig. 3.2.

Segmented images from *in-situ* experiments were used to compute the areas of fluid, fibers and voids, denoted A_l, A_f and A_v, respectively, as well as porosity and degree of saturation in accordance with $\varepsilon = (A_l + A_v)/(A_l + A_v + A_f)$ and $S = A_l/(A_l + A_v)$. For the *ex-situ* images, fluid and void regions were not segmented and only ε was computed; the area $A_l + A_v$ was obtained from the difference between the total composite area and the fiber area.

3.2.5 Measurement of permeability from impregnation rates

Impregnation rates were analyzed using Darcy's law for one-dimensional flow: $q = -[k_r(S)\kappa_s/\mu][dP/dx]$ where $\nu = q/\varepsilon S$, κ_s is the axial saturated permeability, $\kappa_u = k_r(S)\kappa_s$ is the axial unsaturated permeability, q is the Darcy velocity in the flow direction, and ν is the corresponding tracer velocity. Here we assume a sharp flow front dividing the dry regions and the impregnated regions at a steady-state saturation.

(That is, the partially saturated zone at the flow front and time dependence of saturation at the flow front are neglected.) In this case, mass conservation requires that $dq/dx = 0$, yielding $dP/dx = -P_m/x_{ff}$. Accounting for capillary pressure, P_c, the results can be re-expressed as [32–40]:

$$\frac{x_{ff}^2}{t} = \frac{2k_r(S)\kappa_s(P_m + P_c)}{\mu\varepsilon S}. \tag{3.5}$$

The capillary pressure is given by:

$$P_c = \frac{F\gamma cos(\theta)(1-\varepsilon)}{2\varepsilon\bar{r}_f} \tag{3.6}$$

where θ is the contact angle between the fluid and the fibers, $\bar{r}_f$ is the average fiber radius ($\bar{r}_f = 6.3 \pm 0.9\mu$m, as measured from XCT images), and F is a form factor that depends on flow direction and fiber bed geometry [40, 74]; for axial flow in unidirectional fiber beds, $F = 4$ [40, 72, 74]. The contact angle was measured from voids identified in *in-situ* XCT images taken after pressure removal (Fig. 3.1(D)). Fifty such measurements were made, yielding $\theta = 26.3 \pm 8.2°$.

Linear regression analyses of impregnation rate data, presented as x_{ff}^2 vs. t, yield the Darcy slopes, D (Fig. 3.1(B)). In turn, the instantaneous capillary number Ca_{ff} at the flow front is:

$$Ca_{ff} = \frac{\mu v_{ff}}{\gamma} = \frac{\mu}{\gamma}\frac{D}{2x_{ff}}. \tag{3.7}$$

and the permeability in the form of κ_u/S is:

$$\frac{\kappa_u}{S} = \frac{\mu\varepsilon D}{2(P_m + P_c)} \tag{3.8}$$

The results are ultimately cast in terms of a non-dimensional permeability, $\hat{\kappa}_u/S = \kappa_u/S\bar{r}_f^2$.

3.2.6 Geometric Permeability Estimator (GPE)

In order to interpret the experimental measurements, we developed a new computational tool for estimating saturated and unsaturated permeability of very large arrays of non-uniformly packed fibers conducting flow with full or incomplete steady-state saturation. The development is motivated by deficiencies in previous computational methods based on a combination of analytical results of permeabilities of unit cells and distributions in local porosities (detailed in Section 3.2.7). It also recognizes that computational fluid dynamics (CFD) simulations of the entire array (comprising about 5000-6000 fibers) would be intractable and that identification of a representative subset of the entire fiber array would not be feasible because of the non-uniformity in fiber movement. Being based solely on the geometry of a 2D fiber array and spatial distributions of fluid and voids from segmented images, the tool is referred to as the Geometric Permeability Estimator (GPE).

The GPE calculates relative axial fluid velocities, hereafter referred to as pseudo-velocities, at each pixel location at which fluid flow is allowed. Pseudo-velocities are calculated on the basis of the Hagen-Poiseuille model for steady-state laminar flow of an incompressible fluid through a cylindrical tube. Here the velocity in the direction of the tube axis at each point scales as $v \propto R^2 - r^2$, where R is the cylinder radius and r is the distance between the point of interest and the tube center. The algorithm follows.

1. The Euclidean distance transform of regions available for fluid flow is computed. In turn, the Euclidean distance d between each pixel and the nearest boundary (either fiber, glass tube or void) is determined.

2. Local maxima of d from the first step are identified. Each maximum represents the radius R of the largest cylindrical tube that would fit within that region. At these pixel locations, $r = 0$ and thus the pseudo-velocity, v_i, is assigned a value

of R^2.

3. For every other pixel, the nearest local maximum is identified and the distance r between the two is computed. These pixels are assigned a pseudo-velocity $v_i = R^2 - r^2$. Examples of pseudo-velocity contour maps for saturated flow from the GPE are shown in Fig. 3.3(D).
4. The corresponding non-dimensional pseudo-permeability, $\hat{\Psi}$, is then calculated as: $\hat{\Psi} = \sum_i v_i / A_{cp}\bar{r}_{fp}^2$, where $\bar{r}_{fp}$ is the average fiber radius (in pixels) and A_{cp} is the total cross-sectional area of the composite (in pixels).

The GPE results were calibrated using CFD simulations of Stokes flow in the axial direction through unidirectional hexagonally-packed fiber beds with porosities in the range 0.2-0.7 [39]. The hexagonally-packed beds analyzed with the GPE technique contained 518 full fibers and 70 partial fibers (along image edges), each with a radius of about 10 pixels (Fig. 3.3(A)). We find that the saturated pseudo-permeability is approximately proportional to the CFD permeability results [39] over the entire porosity range. To relate the two, we use a calibration factor, c, defined by $\hat{\Psi}_s = c\hat{\kappa}_s^{(CFD)}$, where $\hat{\Psi}_s$ is the saturated pseudo-permeability. The calibration curve, shown in Fig. 3.3(B), falls in the (relatively narrow) range of 1.8–3.1 over the entire range of porosities[2]. Additionally, c varies monotonically with ε in a nearly linear fashion, thereby enabling use of simple interpolation functions to obtain real permeabilities from pseudo-permeabilities for other porosity values via: $\hat{\kappa}^{(GPE)} = \hat{\Psi}/c(\varepsilon)$.

An assessment of the calibrated GPE technique was made by comparisons with CFD results for two non-uniformly packed 2D fiber arrays with porosity $\varepsilon = 0.7$ [39]. The permeability results are shown in Figs. 3.3(A-B); the fiber beds and the velocity

---

[2] The GPE results depend on image resolution. As a result, the images were re-sized to obtain a common resolution, characterized by a mean fiber radius of $\bar{r}_{fp} \approx 10$ pixels. Our studies showed that c decreases as r_{fp} increases, converging to a constant value (for a given porosity) at r_{fp} of several hundred pixels. Furthermore, as r_{fp} increases, the dependence of c on porosity weakens, indicating that the accuracy of the GPE technique improves with increasing image resolution.

maps from both CFD and GPE are shown in Figs. 3.3(C-D). Upon applying a calibration factor of $c = 1.82$ (the value inferred from the hexagonally-packed fiber bed for $\varepsilon = 0.7$), the estimated permeabilities of the two non-uniformly packed beds fall within about 6% of the values obtained by CFD. This correlation indicates that the GPE technique, calibrated accordingly, can indeed provide useful quantitative predictions of changes in permeability associated with non-uniform fiber packing.

In applying the GPE technique to the fiber beds obtained from *in-situ* XCT, the formula $\hat{\kappa}^{(GPE)} = \hat{\Psi}/c(\varepsilon)$ was used with the pertinent calibration factors obtained from a linear regression fit of the results for hexagonal fiber arrays (Fig. 3.3(B)) over the porosity range $\varepsilon = 0.3 - 0.4$. This fit yields $c(\varepsilon) = 3.98 - 3.09\varepsilon$.

3.2.7 Alternative numerical techniques for estimating permeability

Various other schemes for estimating permeability of non-uniformly packed fiber arrays have been explored previously [36, 37, 72]. Broadly, these schemes combine analytical results for permeabilities of unit cells with distributions in local porosities of fiber arrays of interest.

Notable analytical models of permeability are those of Gebart (known as the Kozeny-Carman (KC) equation) [42] and of Shou [37]. In these models, permeabilities are expressed in terms of unit cell porosity and a shape factor dependent on cell geometry (typically square or hexagonal). For uniformly packed hexagonal fiber arrays, the permeabilities predicted by KC and Shou are given by [37, 42]:

$$\hat{\kappa}_s^{(KC)} = \frac{8}{53}\frac{\varepsilon^3}{(1-\varepsilon)^2} \tag{3.9}$$

$$\hat{\kappa}_s^{(Shou)} = 0.9\frac{(1-0.9(1-\varepsilon)^{0.5})^4}{1-\varepsilon} \tag{3.10}$$

In applying these results to non-uniformly packed fiber arrays, area-weighted local porosity distributions are first calculated using one of three methods.

1. A Voronoi tessellation, with each cell containing one fiber, is constructed and the cell porosities are computed. [37].
2. A Delaunay triangulation, with fiber centers used as vertices, is constructed and the cell porosities are computed [36].
3. A pixel-by-pixel sliding cell technique is used, whereby the average porosity within a prescribed radial distance from each pixel of interest is computed [72].

The local permeability for each cell (for the Voronoi and Delaunay methods) or each pixel (for the sliding cell method) is computed using the local porosity and either the KC or the Shou models for square or hexagonal packing. The permeability of the entire fiber bed is then taken as the area-weighted average of local permeabilities [36, 37]. One drawback of these computational schemes is that they tacitly assume that fiber arrangements are locally either square or hexagonal.

To assess these approaches, permeabilities of the fiber beds in Fig. 3.3(C-D) and of a hexagonally-packed fiber bed with $\varepsilon = 0.7$ (518 full fibers and 70 partial fibers) were computed using every combination of local porosity measurement (Voronoi tessellation, Delaunay triangulation, sliding cell) and permeability model for hexagonal packing (KC: eq. 3.9 and Shou: eq. 3.10). These six computational schemes for permeability estimation, referred to collectively as *unit-cell models*, are denoted Voronoi KC, Voronoi Shou, Delaunay KC, Delaunay Shou, sliding cell KC, and sliding cell Shou. To facilitate valid comparisons with the GPE results, the fiber radius was taken to be 10 pixels. For the Voronoi cell calculations, cell areas were adjusted to account for cell-boundary pixels; the saturated permeability was computed from an area-weighted average of the cell permeabilities. An analogous averaging procedure for overlapping cell-boundary pixels was followed for the Delaunay triangulation. For the pixel-by-pixel sliding cell technique, a circular cell was used. The cell size was selected to be large enough so that every cell contained at least one fiber pixel (*ie*. each cell must have porosity < 1 and hence finite permeability). For the current analysis, the cell radius was selected to be 41 pixels. The saturated permeability was computed as the average of the permeabilities calculated for each pixel. The resulting computed permeabilities along with those from CFD [39] and from the GPE are shown in Fig. 3.4(A). Among the computational methods considered here, the GPE yields results that most closely match those from CFD for all three fiber beds (maximum 6% error).

Also shown in Fig. 3.4(A) are the analytical solutions for the hexagonal KC and Shou expressions for a unit cell porosity of 0.7. If the unit-cell models properly capture the fiber bed geometry, their results should match very closely with the analytical solution for the hexagonal fiber bed (small differences are expected due to the finite resolution of the images used, with fiber radius = 10 pixels, and pixel-scale estimation of the local porosities and permeabilities). For both the Voronoi and sliding cell techniques, the estimated permeabilities differ by $< 2\%$ from the analytical solutions. However, for the Delaunay techniques, the estimated permeabilities differ by about 20%, suggesting that this technique does not adequately capture the local geometries and porosities within the fiber bed at the pertinent image resolution.

In Fig. 3.4(B) the results are re-expressed in terms of ratios of permeabilities of non-uniformly and hexagonally packed fiber beds for each computational technique (the goal being to assess the sensitivities of the techniques to non-uniformity, independent of the absolute values of permeability). Again, the GPE technique yields the closest match to the CFD results. Three of the unit-cell models (Voronoi KC, Voronoi Shou, and sliding cell Shou) significantly underestimate the effects of increasing non-uniformity on permeability, while the Delaunay KC technique significantly overestimates it. In light of these results, the GPE technique was chosen for analysis of the XCT images.

3.3 Results and discussion

3.3.1 Unsaturated permeability measurements

The *measured unsaturated* permeabilities, in the form of $\hat{\kappa}_u^{(m)}/S$, of specimens imaged *ex-situ* with XCT were computed from the measured impregnation rates as described in section 3.2.5. Representative results for impregnation kinetics, presented as x_{ff}^2 vs. t, are plotted in Fig. 3.1(B,C). Linearity of the data in this form affirms that impregnation follows Darcy's law and that the permeability is constant over the length of the infiltrated region. The instantaneous capillary number at the flow front, $Ca_{ff} = \mu v_{ff}/\gamma$ (v_{ff} being velocity of the flow front), decreases as the flow front advances; its variation over the duration of an individual experiment typically falls in the (relatively narrow) range of about 2 - 4. By comparison, variations in Ca_{ff} among various tubes (because of pressure differences) span a range of almost a factor of 100, from about 10^{-5} to 10^{-3}. The latter effects are the ones of interest in subsequent analyses.

The measured unsaturated permeabilities (in the form of $\hat{\kappa}_u^{(m)}/S$) were calculated for 31 locations across 22 specimens. The results are plotted against Ca_{ff} (taken at the XCT imaging location) in Fig. 3.5. The measured permeabilities increase by nearly an order of magnitude over the tested range of Ca_{ff}. Elucidating the origins of this trend represents the principal goal of the remainder of the study.[3]

---

[3] To assess the effects of slight variations in porosity between specimens (ranging from 0.32-0.38), we performed a multivariable linear fit of the form: $Log_{10}(\hat{\kappa}_u^{(m)}/S) = BLog_{10}(Ca_{ff}) + C\varepsilon + D$. The fit yields: $B = 0.37 \pm 0.04$ ($p = 1.4 \times 10^{-9}$), $C = 2.4 \pm 1.9$ ($p = 0.20$) and $D = -1.3 \pm 0.7$ ($p = 0.09$) (values following ± signs are standard errors). The results indicate that the variation in *measured unsaturated* permeability with capillary number is statistically significant (as manifest in the low p-value for B) whereas the variation with porosity is not (high p-value for C). The latter is attributable to the narrow range of porosities probed by these experiments coupled with the scatter in the measurements.

3.3.2 In-situ observations of fluid flow and fiber movement

Capillary imbibition

Two specimens that were infiltrated without applied pressure were imaged *in-situ* at the same location, 1.5 cm from the top of the tube ($Ca_{ff} \approx 4 \times 10^{-5}$). Fluid flow is driven by capillary forces alone; for these two specimens, the capillary pressure falls between $15 - 16$ kPa. The first sign of fluid appears within the narrowest channels between fibers where the local capillary pressure is highest, illustrating preferred flow channeling at the flow front (Fig. 3.6(A)(i)). As impregnation proceeds, other (slightly larger) channels are filled (*e.g.*, Fig. 3.6(B,C)). The degree of saturation increased from about 0.02 to 0.81 during a transient period of about 5 min (corresponding to passage of the partially saturated zone). One of the specimens was given additional time for the flow front to move well past the imaging location; it exhibited only minimal increase in saturation, to a steady-state value of about 0.83, about 5 min later. Many of the largest channels contain trapped voids even after long times (Fig. 3.6(C)). In some cases, such as the middle-top region of Fig. 3.6B(i) and C(i), channels that were once filled contain voids. We surmise that this is due to trapped voids migrating longitudinally or transversely within the fiber beds as flow proceeds.

The images also reveal fiber movement during capillary imbibition. For example, Fig. 3.7(A) shows that, by $t = t^*$ (the time of the first scan after the flow front had passed the imaging location), some fibers within the filled channels had moved closer to one another. In turn, channels in adjacent unfilled regions became somewhat larger. This fiber rearrangement is attributed to elastocapillary effects [75–79], wherein fibers in closely-packed regions, which are imbibed first, are pulled together by capillary forces.

Distributions of local porosity and their differences before and after impregnation are given in Fig. 3.8(A). Local porosity at each pixel was calculated over a 17 μm

radius circle centered at the pixel of interest. (This was the smallest radius for which every cell contained at least one fiber pixel and at least one fluid or void pixel, yielding $0 < \varepsilon < 1$). Typically, the most significant changes occur in regions where the local porosity is initially higher than average. Either the large channels open wider or the fibers rearrange to form other large channels nearby. Cooperative fiber movement of this kind leads to a greater density of both small and large channels and fewer intermediate-sized channels. This is illustrated quantitatively in Fig. 3.9(A-B). The figure shows the differences in the porosity probability density, $\Delta PD(t) = PD(t) - PD(0)$, in the dry and the impregnated states. At $t = t$*, both specimens exhibit positive values of ΔPD at low and high porosity levels and negative values of ΔPD at intermediate porosities. The physical interpretation is that the fiber bed becomes less uniformly packed, with more small and large channels and fewer intermediate-sized channels as a result of impregnation.

Pressure-driven impregnation

A different sequence of events was obtained at high impregnation pressures ($P_m > 276$ kPa $>> P_c$, $Ca_{ff} \approx 7 \times 10^{-4} - 2 \times 10^{-3}$). The first XCT image obtained after the fluid front had passed the imaging location showed essentially full saturation ($S > 0.99$). Evidently saturation occurs over a time scale shorter than that needed for imaging (1.5 min). Thus, manifestations of preferred flow channeling *at* the flow front, if present, were not observed. However, the fluid is expected to first find the paths of least resistance within the larger channels because $P_m/P_c >> 1$ and thus capillary imbibition is slow compared to pressure-driven flow.

XCT again reveals fiber movement during impregnation (Figs. 3.7(B), 3.8(B), and 3.9(D-F)), often leading to expansion or rearrangement of regions with high local porosity to form larger channels locally. Similarly to the specimens infiltrated by capillary pressure alone, Figs. 3.9(E-F) show greater densities of small and large channels and fewer intermediate-sized channels at $t = t^*$. However, at higher pressures, the changes in porosity probability density are significantly larger, suggesting that the applied pressure plays a significant role in fiber movement.

Over the range of local porosities present in the fiber bed, the capillary pressure ranges between $6 - 40$kPa. Meanwhile, the applied pressure drops from P_m at the fiber bed entrance to zero at the flow front. Fiber movement may occur ahead of, at, or behind the flow front in response to these forces. If the fluid does indeed first find the path of least resistance within relatively large channels, two potential mechanisms of fiber movement may be operative. Among the narrower of the relatively large channels, capillary forces are more likely to dominate, causing relatively closely-packed fibers to be pulled closer together – in some cases potentially increasing local non-uniformity and in other cases decreasing it. Among the widest channels, it is possible for the applied pressure to dominate fluid flow and fiber movement, causing wide channels to expand. Furthermore, even under saturated flow conditions, fibers may move because of pressure variations resulting from slightly misaligned fibers and corresponding changes in channel width (convergent or divergent) along the flow direction. In practice, fiber movement is likely a combination of drifting and bending. After pressure removal (at $t = 15.6$ min in Fig. 3.9(E) and at $t = 15.2$min in Fig. 3.9(F)), the distributions of ΔPD are similar to those at $t = t^*$, suggesting that most of the fiber movement is due to drift; stress relaxation of bent fibers produces a small effect over the time period of these experiments (specimens were imaged within five minutes after pressure removal).

Fig. 3.8(B) shows the spatial distributions of local porosity and porosity change at the highest impregnation pressure (552 kPa); changes in porosity distributions are plotted in Fig. 3.9(F). As we show in section 3.3.3, the changes in the porosity distributions lead to an increase in saturated permeability. The results in Fig. 3.9(D), for an intermediate pressure, show slightly different behavior at $t = t^*$: a slight increase in the density of very small and very large channels and, as shown in section 3.3.3, a slight increase in saturated permeability.

3.3.3 Effects of fiber movement

To examine effects of fiber movement on permeability, the GPE was used, first, to estimate the *saturated* permeability, $\hat{\kappa}_s^{(GPE)}$, from 2D segmented XCT images of the six specimens imaged *in-situ*. Fig. 3.10 shows the variation in $\hat{\kappa}_s^{(GPE)}$ with time t. In all cases, $\hat{\kappa}_s^{(GPE)}$ is initially greater than that of a uniform, hexagonally-packed fiber bed with the same porosity level, consistent with previously-reported results for non-uniform fiber beds [36–39]. Once impregnation begins, the accompanying fiber movement leads to an increase in $\hat{\kappa}_s^{(GPE)}$. This is followed in some cases by a slight reduction in computed permeability as the pressure is released, presumably due to internal relaxation of stress.

The values of $\hat{\kappa}_s^{(GPE)}$ for these six specimens at both $t = 0$ and $t = t^*$ are also plotted in Fig. 3.5. Although these permeabilities invariably increase during infiltration, the effects are most pronounced at high values of Ca_{ff}, consistent with the finding that the degree of fiber movement is greatest in this domain. Changes in geometry and in the fluid pseudo-velocity field for the specimen infiltrated at the highest pressure ($P_m = 552$ kPa, $Ca_{ff} \approx 0.002$) are illustrated in Fig. 3.11(A,B). The images show both expansion of initially larger-than-average channels during impregnation and corresponding elevations in computed fluid pseudo-velocity.

3.3.4 Effects of preferred flow channeling

To assess effects of preferred flow channeling *behind* the flow front, the GPE was employed to compute the *unsaturated* permeability, in the form of $\hat{\kappa}_u^{(GPE)}/S$, of the fiber beds from XCT images taken *in-situ* at time $t = t^*$. Segmented images of fibers and voids were used as inputs[4]. In these calculations, fluid flow was allowed only in regions where fluid was evident in the XCT images. If fluid flow were random (not preferred in either small or large channels), $\hat{\kappa}_u^{(GPE)}/S$ would be identical to $\hat{\kappa}_s^{(GPE)}$ (i.e. $k_r = S$). Meanwhile, preferred flow in the small channels would yield $\hat{\kappa}_u^{(GPE)}/S < \hat{\kappa}_s^{(GPE)}$ while preferred flow in large channels would yield $\hat{\kappa}_u^{(GPE)}/S > \hat{\kappa}_s^{(GPE)}$.

At the highest impregnation pressures ($P_m > 276$ kPa, $Ca_{ff} \geq 7 \times 10^{-4}$), saturation is essentially complete at $t = t^*$ and thus the values of $\hat{\kappa}_u^{(GPE)}/S$ and $\hat{\kappa}_s^{(GPE)}$ are nearly identical to one another (Fig. 3.5). Moreover, the values at $t = t^*$ are broadly consistent with (though slightly lower than) the measured permeabilities. The slight underestimate may be associated with preferred flow channeling in the largest channels *at the flow front*, a phenomenon not captured in the present work.

In contrast, without applied pressure ($Ca_{ff} \approx 4 \times 10^{-5}$), saturation is incomplete well behind the flow front, with steady-state saturation $S \approx 0.81$ at $t = t^*$. In these cases, the computed unsaturated permeabilities ($\hat{\kappa}_u^{(GPE)}/S$) are lower than the corresponding saturated values at $t = t^*$ by about 30% (on average) and fall broadly in line with measured permeabilities ($\hat{\kappa}_u^{(m)}/S$) (Fig. 3.5). The differences are a direct result of incomplete saturation behind the flow front in which flow is preferred in the narrowest channels, wherein the fluid flux is lower than average.

In the intermediate pressure domain ($P_m =$138 kPa, $Ca_{ff} \approx 3 \times 10^{-4}$) a saturation of $S \approx 0.93$ was achieved as the flow front passed ($t = t^* = 11.5$ min). The degree of saturation remained essentially the same after longer time periods ($t = 21.7$ min). The results show only a very slight reduction in GPE-computed permeability, from $\hat{\kappa}_s^{(GPE)} = 0.0214$ to $\hat{\kappa}_u^{(GPE)}/S = 0.0196$ at $t = t^*$.

---

[4] As discussed in section 3.2.4, fluid and void regions were segmented manually. To quantify error made by manual segmentation, an image taken at t^* for one of the specimens impregnated without applied pressure was manually re-segmented months after the original segmentation was performed. The percent variance in fluid area between the two segmented images was 0.6%. The percent variance in the unsaturated permeability, $\hat{\kappa}_u^{(GPE)}/S$, computed for the two segmented images was 2.7% – a small error relative to the effects of preferred flow channeling at low Ca (*i.e.*, $Ca_{ff} \approx 4 \times 10^{-5}$).

3.4 Conclusions and outlook

Through this study we have elucidated the coupled effects of fiber movement, preferred flow channeling and impregnation velocity on axial permeability of aligned fiber beds. For beds with porosity of about 1/3, the measured unsaturated permeability (in the form of $\hat{\kappa}_u^{(m)}/S$) increases by about an order of magnitude as the capillary number increases from 10^{-5} to 10^{-3}. The effects are attributed in part to increased fiber movement at high Ca and corresponding elevations in non-uniformity and thus permeability. At low Ca, wherein flow is dominated by capillarity, preferred flow channeling in the smallest channels causes contraction of those imbibed regions and a corresponding increase in the size of the largest (often unfilled) channels. The combination of incomplete saturation and preferred flow channeling in the narrowest channels well behind the flow front leads to reduced unsaturated permeability (in the form of $\hat{\kappa}_u^{(GPE)}/S$) at low Ca. These insights could be used to improve existing permeability models, ultimately for use in optimizing liquid composite molding. Moreover, they could be used to rationalize microstructural changes caused by impregnation.

We have also developed a new computational tool (GPE) for estimating the axial permeability of large, non-uniform, 2D fiber beds. We have found that the GPE method, when calibrated, yields useful quantitative predictions of permeability in non-uniform fiber beds and is superior to alternative computational methods that employ results from unit cell analyses. In fact, many of the techniques based on unit cell analyses significantly over or underpredict the effects of non-uniformity on permeability. With the development of the GPE, we present an alternative technique that enables exploration of effects of fiber packing and preferred flow channeling on axial permeability.

In summary, we have demonstrated that *in-situ* XCT can be used to study dynamic processes during fiber bed impregnation over a wide range of velocities, and that the

GPE can be used to quickly compute the axial permeability of non-uniform unidirectional fiber beds. An extension of this study would involve exploring the effects of varying fiber volume fraction on permeability in the contexts of both preferred flow channeling and fiber movement. We expect that the effect of fiber movement on permeability would be greater at lower fiber volume fractions, because of the larger amount of space available for fiber movement. The experimental methods presented here could also be adapted to study impregnation into preforms with more complex architecture, *e.g.*, woven cloth. Such studies would allow the coupled effects of flow parallel and perpendicular to the fibers as well as through large inter-tow channels to be probed and their effects on permeability and remnant porosity to be uncovered.

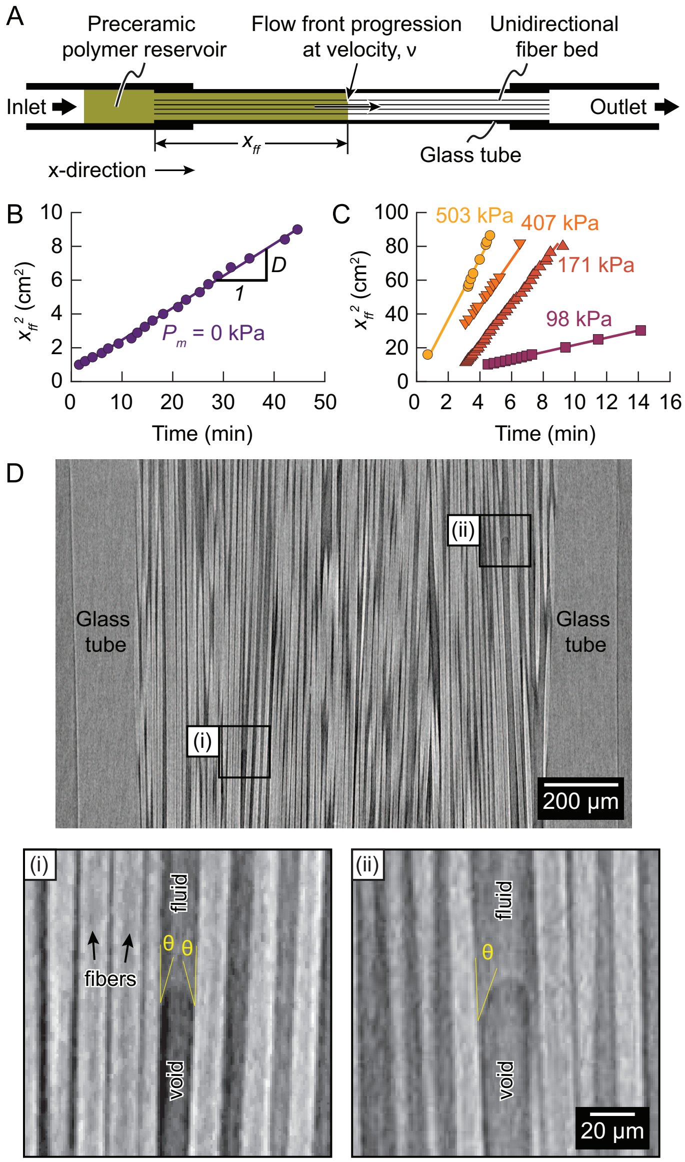

Figure 3.1: (A) Test geometry used in impregnation experiments. (B-C) Impregnation kinetics from several representative specimens, (B) without and (C) with applied pressure. (D) Representative longitudinal raw XCT image illustrating contact angle (θ) measurements at void/fluid interfaces.

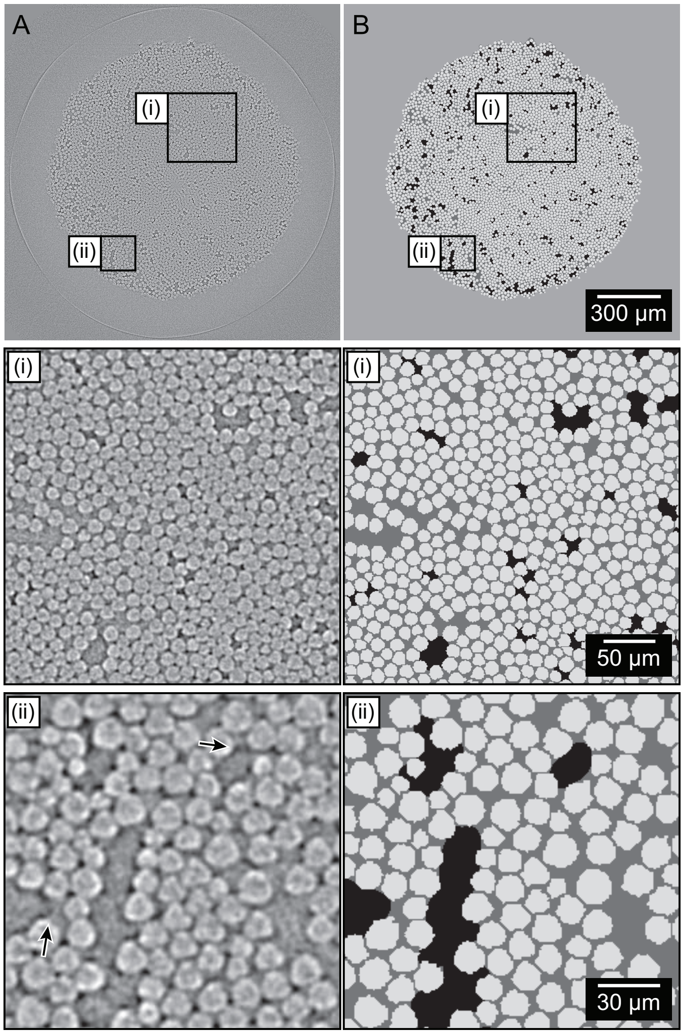

Figure 3.2: (A) Representative transverse raw XCT image of infiltrated fiber bed and (B) corresponding segmented image. In the latter, fibers are light gray, fluid is medium gray, voids are black, and regions outside the specimen are light gray. In (A)(ii), arrows point to locations where void/fluid interfaces are evident.

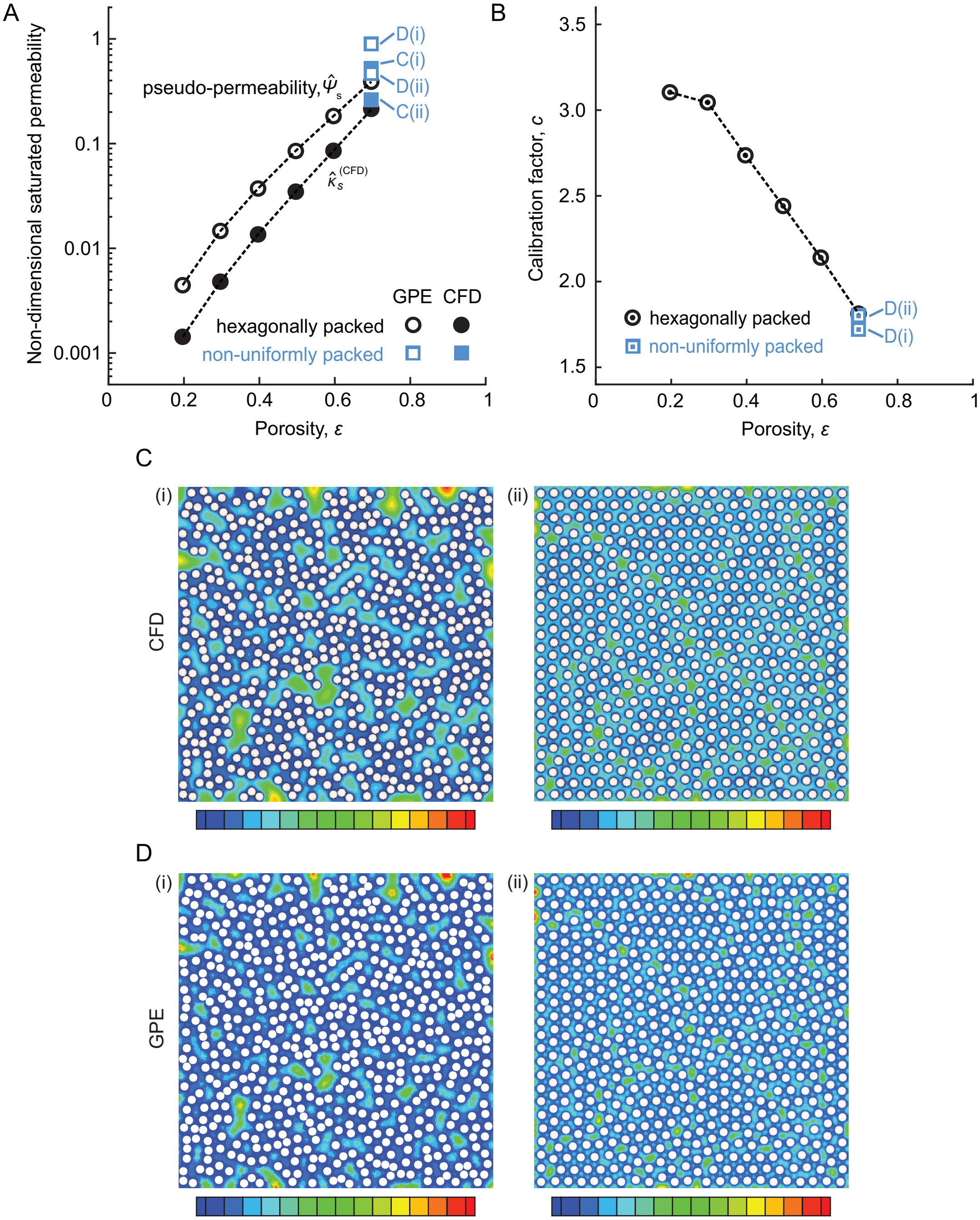

Figure 3.3: GPE and CFD results. (A) Non-dimensional saturated permeability of hexagonally-packed fiber beds with porosities from 0.2-0.7 and two non-uniformly packed fiber beds with porosity of 0.7, obtained from CFD simulations [39]. Also shown are the corresponding pseudo-permeabilities from the GPE technique. (B) Variation in the calibration factor, *c*, with porosity for both hexagonally-packed and non-uniformly-packed fiber beds. (C-D) Maps of relative axial fluid velocity (*i.e.*, into the page) in non-uniformly packed fiber beds from CFD [39] and from the GPE. Scales

selected to depict only relative values of velocity: blue being low and red being high. All four scales represent different ranges of relative velocity. (C) Reprinted from Composites Science and Technology, 67, X. Chen and T. D. Papathanasiou, Microscale modeling of axial flow through unidirectional disordered fiber arrays, 1286-1293, Copyright 2006, with permission from Elsevier.

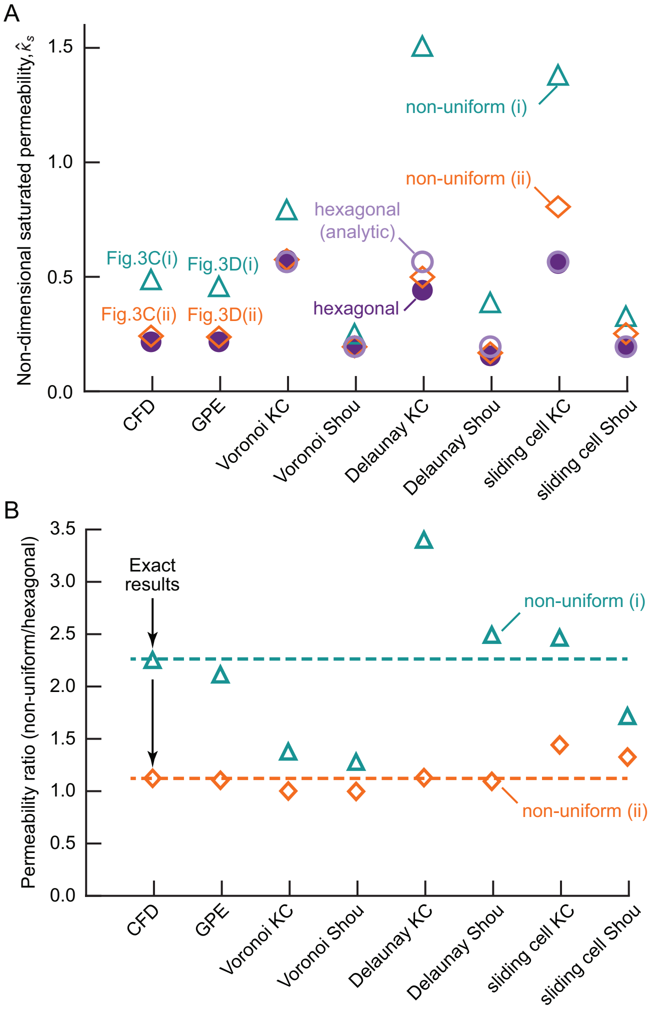

Figure 3.4: Comparisons of permeability estimates from CFD, GPE, and unit-cell models. (A) Non-dimensional saturated permeability of a hexagonally-packed fiber bed and the two non-uniformly packed fiber beds from Fig. 3.2, all with porosity of 0.7. (B) Ratio of permeabilities for non-uniformly and hexagonally-packed fiber beds for the cases considered in (A).

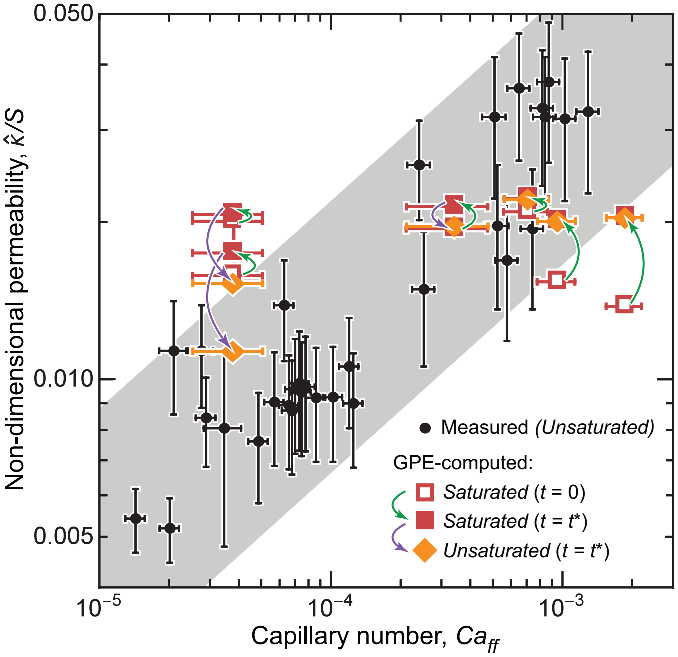

Figure 3.5: Variations in measured and GPE-computed permeabilities with capillary number. The range of measured permeabilities is indicated by the shaded band. For the GPE-computed permeabilities, green arrows indicate elevations due to fiber movement; purple arrows show subsequent reductions, to the unsaturated permeabilities, for low values of Ca_{ff}.

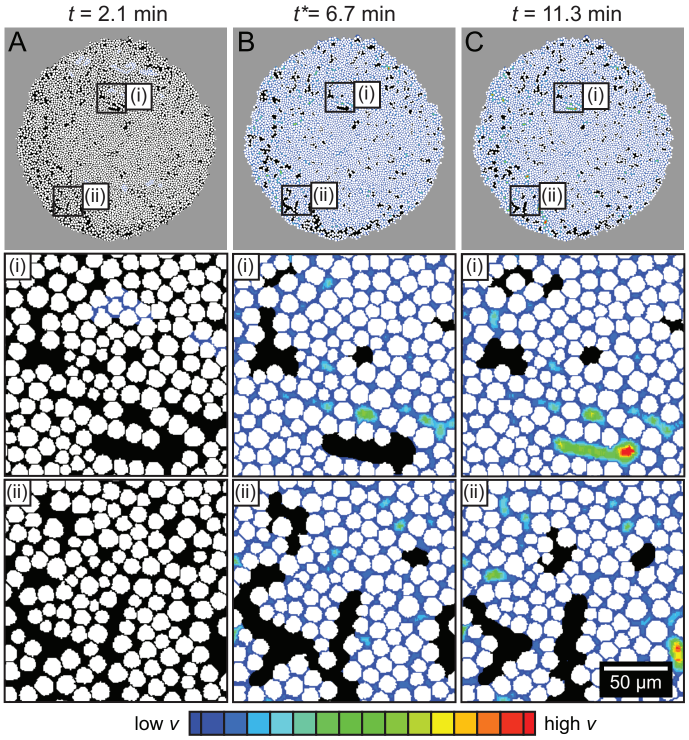

Figure 3.6: Segmented XCT images and superimposed pseudo-velocity maps for unsaturated flow in a specimen infiltrated by capillary pressure alone ($P_m = 0$, $Ca_{ff} \approx 4 \times 10^{-5}$). Non-infiltrated regions shown in black.

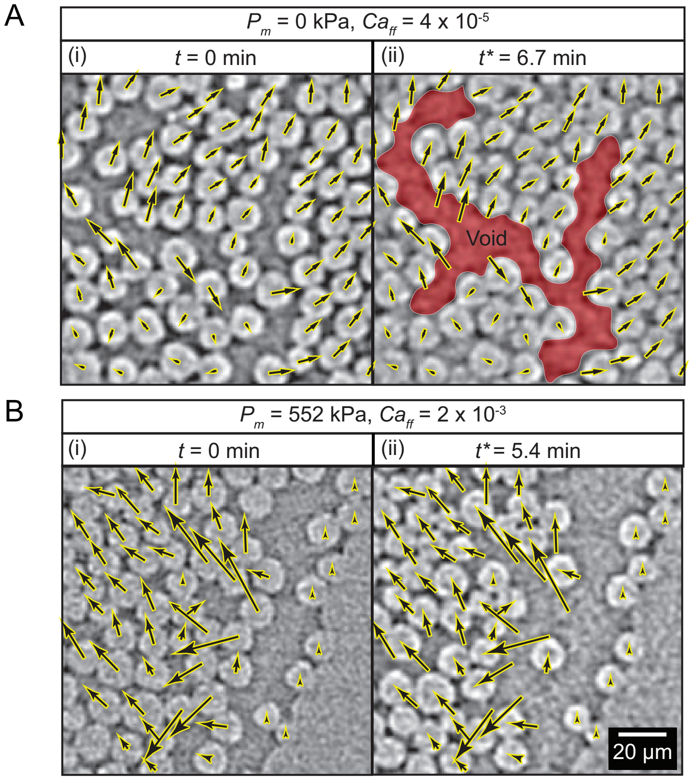

Figure 3.7: XCT images taken prior to impregnation (A(i) and B(i)) and at time t^* (A(ii) and B(ii)). (A) $P_m = 0$, $Ca_{ff} = 4 \times 10^{-5}$, (B) $P_m = 552$ kPa, $Ca_{ff} = 2 \times 10^{-3}$. Arrows indicate movement of fiber centroids from their positions in the dry (unimpregnated) state ($t = 0$) to their positions at t^*. Fiber locations at $t = 0$ and $t = t^*$ were correlated with a combination of manual and algorithmic techniques. In A(ii), a void is highlighted in red. All other channels in the region shown are impregnated. In B(ii), the fiber bed is fully impregnated.

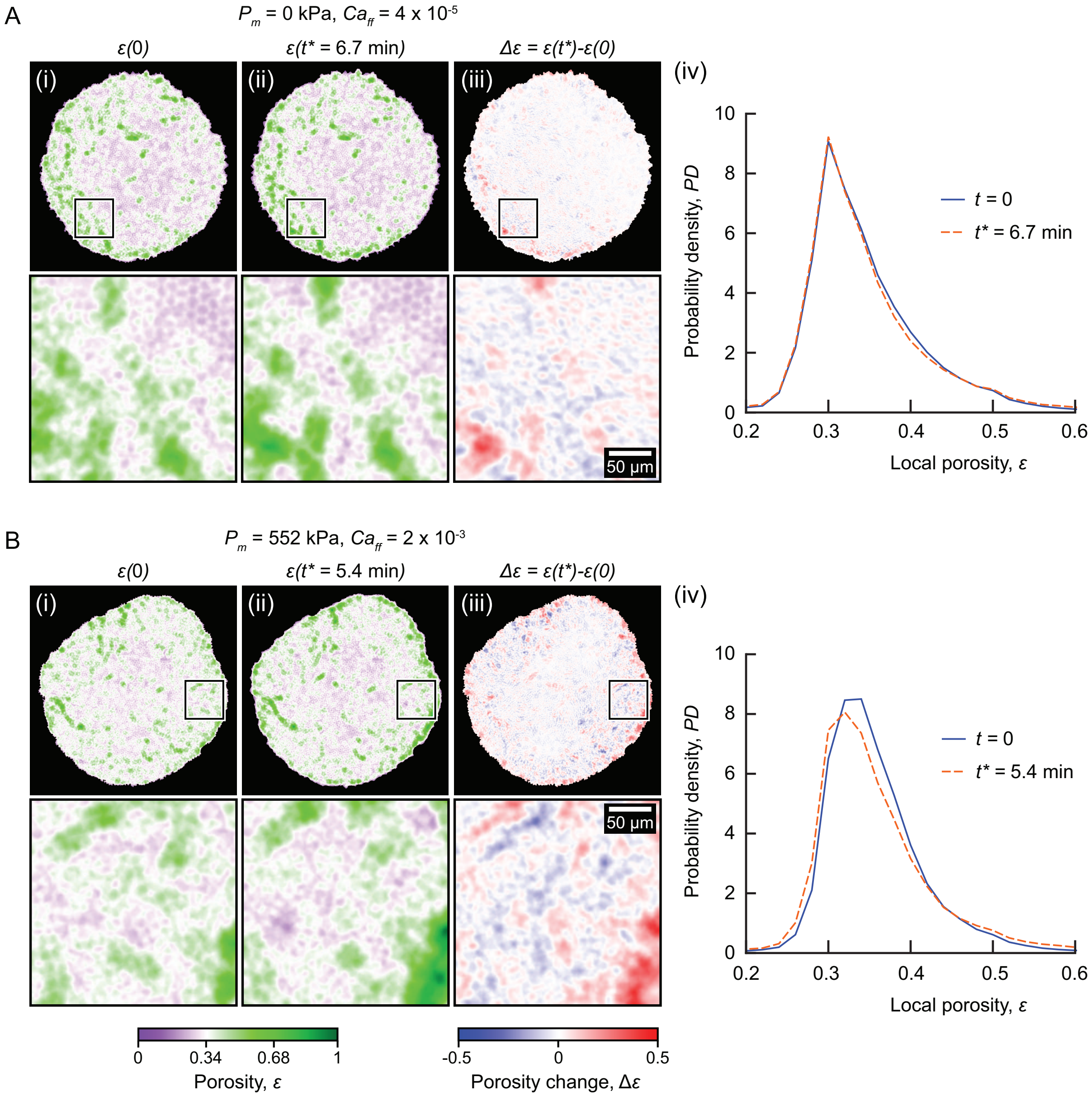

Figure 3.8: Distribution of local porosity at (i) $t = 0$ and (ii) t^* and (iii) change in local porosity at time t^* following infiltration: $\Delta\varepsilon(t^*) = \varepsilon(t^*) - \varepsilon(0)$. Local porosities are calculated over 17 μm radius circles centered at pixels of interest. Local porosity probability densities (PD) are plotted in (iv). (A) $P_m = 0$, $Ca_{ff} = 4 \times 10^{-5}$, (B) $P_m =$ 552 kPa, $Ca_{ff} = 2 \times 10^{-3}$.

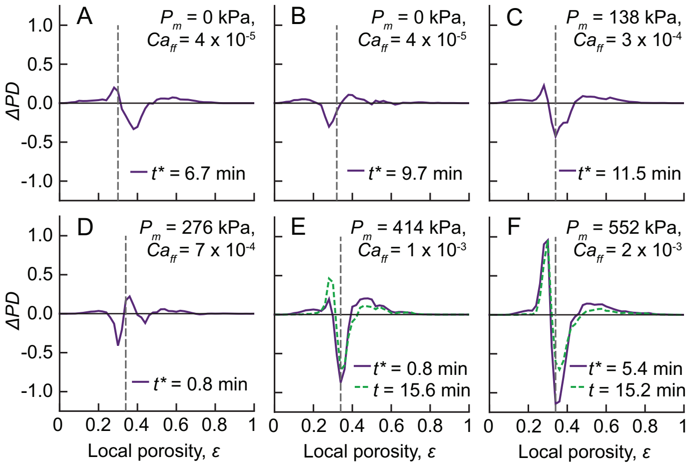

Figure 3.9: Changes in porosity probability density during impregnation for six specimens imaged *in-situ* with XCT. Vertical dashed lines indicate the mode porosity in the initial (dry) state.

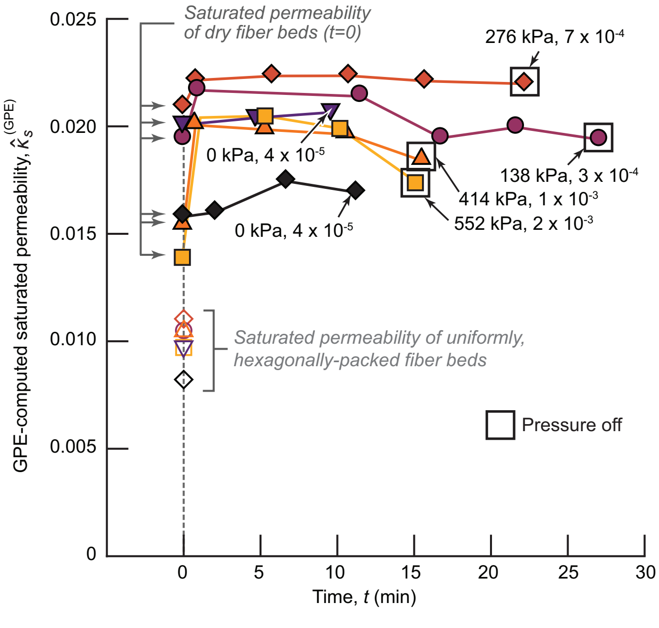

Figure 3.10: Variation in computed saturated permeability with time for six specimens imaged *in-situ* with XCT during impregnation. Each data point represents a separate XCT scan and is plotted at the time midway through the 1.5 minute scan. Data sets are labeled with impregnation pressure and estimated capillary number. Saturated permeabilities for hexagonally-packed fiber beds (open symbols) were obtained from a quadratic fit to the CFD results [39] over the porosity range $\varepsilon = 0.2 - 0.5$.

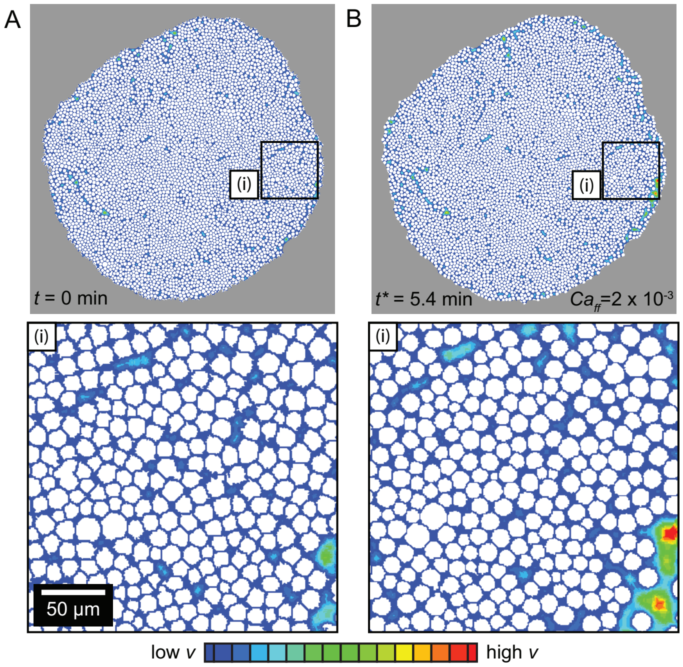

Figure 3.11: Pseudo-velocity maps for saturated flow at high pressure (P_m = 552 kPa, $Ca_{ff} \approx 2 \times 10^{-3}$), for (A) dry fiber bed and (B) infiltrated fiber bed (at $t = t^* = 5.4$ min).

Chapter 4

Microstructure Evolution During Matrix Impregnation and Curing in Unidirectional Fiber Beds

Abstract

Microstructural evolution during axial impregnation and subsequent curing of a preceramic polymer in unidirectional ceramic fiber beds is studied using x-ray computed tomography. The principal goal is to identify connections between void locations, void sizes, local fiber bed porosity, fiber movement, and impregnation conditions. The degree of saturation after impregnation is found to increase with instantaneous capillary number. But, because of the need to create pathways for gas escape during curing, fiber beds with high saturation after impregnation show the largest reductions in saturation during curing. Notwithstanding, saturation after curing increases with instantaneous capillary number. Voids tend to form in the largest channels between fibers, where the local fiber bed porosity is high, during both impregnation and curing. Void formation is typically accompanied by fiber movement that

increases both the local fiber bed porosity near voids and the overall non-uniformity in the fiber bed, as measured by local porosity entropy[1].

4.1 Introduction

Fiber-reinforced ceramic-matrix composites (CMCs) promise to enable higher temperatures and increased efficiency for hot section components in aerospace gas turbine engines, hypersonic jet engines, nuclear reactors, and space vehicles [1–3, 5]. Composites currently of most interest consist of SiC matrices and BN-coated SiC fibers. The coatings promote crack deflection and frictional pullout, imparting high toughness to the CMC [1, 3, 5]. The SiC matrix protects the fibers and distributes load [3, 6, 7]. Despite their promise, fabrication of fully-dense, compositionally-pure SiC matrices that can withstand the targeted upper use temperatures (1500°C) remains an outstanding challenge [3]. One processing method that might achieve this goal involves impregnation of preceramic polymers into fiber preforms, followed by curing and pyrolysis (to temperatures of $\sim$ 1000 to 1600°C) [2, 3, 6, 11, 13, 14, 17, 23, 24]. The process of polymer impregnation and pyrolysis (PIP) is repeated several times in order to further densify the matrix, progressively filling voids and shrinkage cracks remaining from previous processing cycles [2, 3, 6, 11, 13, 14, 17, 24]. Although the process is straightforward in principle, the resulting microstructures are often heterogeneous in nature, with pores and cracks in the matrix ranging in size from nanometers to hundreds of micrometers [3, 6, 7, 23]. These heterogeneities can, in turn, lead to spatial inhomogeneities in the degree of protection that the matrix can provide to the fibers and hence compromise long-term composite durability [3, 6, 7]. The present study investigates changes in matrix microstructure during the first impregnation and curing cycle of a SiC prece-

---

[1] The content of this chapter has previously appeared in Composites Part A: Applied Science and Manufacturing (**Natalie M. Larson**, Charlene Cuellar, Frank W. Zok. "X-ray computed tomography of microstructure evolution during matrix impregnation and curing in unidirectional fiber beds". *Composites Part A* (available online Nov. 2018)) [80]. It is reproduced here with the permission of Elsevier.

ramic polymer in a SiC fiber bed. The work is motivated in part by the expectation that, due to the cyclic compounding nature of the PIP process, microstructural heterogeneities introduced in early stages of the process will set the stage for continued heterogeneous processes in later stages [23].

Previous studies have shown that voids can form during impregnation of polymer resins into fiber beds by two sets of mechanisms: those dependent primarily on capillary number (void entrapment, mobilization), and those dependent on changes in pressure within the impregnating fluid (void compression, dissolution, exsolution) [32, 81, 82]. Numerous experimental studies have shown that void content is correlated with the capillary number, $Ca = \mu v / \gamma$, where v is tracer fluid velocity, μ is fluid viscosity, and γ is fluid surface tension [32–34, 81]. (Ca represents the relative effects of viscous drag and capillary forces.) Because both viscous drag and capillary forces depend on channel size, non-uniformities in fiber packing can cause the flow front to advance in a non-uniform fashion, potentially leading to void entrapment within regions in which the flow front impregnates most slowly [32]. Voids entrapped in this manner can be, under some circumstances, effectively transported away by subsequent fluid flow. Void mobilization and hence the propensity for void removal increases with capillary number [32, 33]. In many manufacturing processes, the injection pressure (and thus capillary number) is increased for a period of time after initial impregnation is complete to facilitate further void mobilization and removal [32]. Entrapped voids may also be dissolved or compressed as the pressure within the impregnating fluid increases over time [32]. If the applied pressure is subsequently removed, dissolved gas may be exsolved, leading to the formation of new bubbles. These effects can be mitigated by drawing vacuum at the outlet [32].

Thermal curing of allylhydridopolycarbosilane (AHPCS) – the preceramic polymer used in this study – involves crosslinking and decompostion, accompanied by evolution of low molecular weight gases [18, 20]. Thermogravimetric mass spectrometry (TGMS) of this polymer during the ramp-up to the curing temperature (120°C in this work) shows evolution of hydrogen, methane, and silanes (TGMS results presented in Fig. 4.1). When this evolution occurs within the confines of a fiber tow, gas bubbles form within the (still-fluid) polymer, displacing the surrounding fluid and, possibly, neighboring fibers. Similarly, in polymer matrix composite (PMC) processing, voids may form during curing due to evolution of gases dissolved in the polymer or formed as curing reaction products [53, 54, 57–61]. For high performance PMCs, the curing process typically consists of carefully-engineered temperature and pressure profiles designed to evacuate, dissolve, and compress voids to achieve minimal matrix porosity [53, 57–59].

Over the course of impregnation and curing, interactions between fibers and matrix precursor can lead to fiber rearrangement and void formation. Effects of processing conditions and initial fiber arrangement on fiber movement and void location and size have yet to be fully elucidated. The present study aims to provide direct observations and quantitative measurements of microstructural evolution via X-ray computed tomography (XCT) of unidirectional fiber beds over the course of processing. To this end, we develop metrics to characterize fiber arrays, including the local porosity entropy and spatial distribution of local fiber bed porosity, and correlate them with the locations and sizes of voids within the matrix.

Some aspects of impregnation and curing have previously been studied using XCT [53, 69, 72, 83]. In one study, by Hernández et al. [53], laminates consisting of ten plies of commercial carbon/epoxy prepreg sheets were subjected to various thermal curing cycles. The shapes and spatial distributions of the resulting voids were characterized by XCT (image resolution 0.6-1.8 pixels across a fiber diameter). The study found that most of the voids were the result of air entrapment and wrinkles produced during the layup process. In a more recent study, by Vilà et al. [72], a single vacuum-bagged tow of glass fibers was impregnated axially with a water/syrup mixture that demonstrated non-wetting behavior at the flow front. The tow was imaged at high resolution (about ten pixels across a fiber diameter) at three points in time: (1) prior to impregnation, (2) when the flow front had reached the imaging location in the middle of the tow, and (3) when the flow front had reached the end of the tow. Due to the long XCT acquisition time (about 2 h), impregnation was paused periodically, allowing imaging under static conditions [72]. The study revealed that the flow front was non-uniform, with flow occurring preferentially in regions of low fiber volume fraction, and that the resulting voids were elongated in the longitudinal direction. In an even more recent study, by Hemmer et al. [83], a vacuum-bagged stack of plies of a quasi-unidirectional non-crimp glass fabric with dual-scale porosity was impregnated with glycerol. The specimen was imaged in the dry state and the saturated state (*in-situ* during continuous axial fluid flow). Because of the focus on mesoscale phenomena – notably changes in stack thickness, tow swelling, and tow displacement during saturated fluid flow – imaging was performed at relatively low resolution (0.7-1.6 pixels across a fiber diameter). Patterns in mesoscopic reorganization of the preform were identified and their effects on in-plane permeability were explored.

The experiments in the present study (and our previous study [69]) differ from the aforementioned studies in two important respects. First, some specimens were imaged *in-situ* during continuous impregnation over a wide range of capillary numbers, starting from the dry state and up until after pressure removal. XCT scan times for these experiments were relatively short (1.5 min). Second, other specimens were imaged dry, after impregnation and pressure removal, and after curing. Imaging was performed at high resolution (13-20 pixels across a fiber diameter). In combination, the two sets of experiments provide information on fiber rearrangement and void formation through critical stages of the process cycle. With the goal of developing fundamental insights into the processes affecting microstructural heterogeneity, the present study focuses on model systems consisting of unidirectional fiber beds.

4.2 Materials and methods

4.2.1 Test specimens

The test specimens used here are essentially the same as those used in our previous work [69]. Each consists of 10-12 tows of Hi-Nicalon$^{\text{TM}}$ Type S SiC fibers (500 fibers/tow) shrink-wrapped within thin-walled borosilicate glass capillary tubes (1.5 mm ID, 1.8 mm OD, VitroCom, Mountain Lakes, NJ) with terminal inner diameter of about 1.4 mm. The resulting global fiber bed porosity within the tubes was $0.32 - 0.39$ and the average fiber radius was 6.4 $\pm$0.9 μm (standard deviation), as measured from XCT images. The polyvinyl alcohol sizing that had been present on the fibers at the outset was removed with a 1h treatment at 600°C.

The fiber beds were impregnated with allylhydridopolycarbosilane (SMP-10, Starfire Systems, Inc., Glenville, NY), a commercial SiC pre-ceramic polymer with surface tension $\gamma = 30 \times 10^{-3}$ J/m^2 and fluid density $\rho = 0.998$ g/cm^3 at room temperature (values provided by manufacturer). All experiments were conducted with the same batch of SMP-10. The polymer viscosity, measured periodically at room temperature over the course of the several-month study, ranged from 68×10^{-3} Pa s at the outset to 82×10^{-3} Pa s at the end. Viscosity values pertinent to the subsequent analysis were obtained by interpolating the measurements to the time of each experiment. Immediately before impregnation, 0.2 wt% dicumyl peroxide (DP) was added to the polymer, to promote subsequent curing[2]. Our previous study on this system demonstrates that the polymer (including DP) wets the fibers (with contact angle of 26±8°) and that impregnation occurs spontaneously with no applied pressure [69]. Curing was performed in air at 120°C for 2 h, after which the polymer density was 1.009 ± 0.003 g/cm^3 [23].

---

[2] Effects of the addition of 0.2 wt% DP on polymer surface tension were not considered in this study.

4.2.2 Impregnation and curing

Fiber beds were impregnated axially either by capillary imbibition alone or via application of pressure on the fluid reservoir, using one of two test configurations. In the first, specimens were oriented horizontally and situated beneath an optical microscope. The distance, x_{ff}, from the glass tube inlet to the flow front was monitored continuously during impregnation until the flow front reached the end of the tube (Fig. 4.2). Our previous work showed that impregnation rates, presented as x_{ff}^2 vs. t, follow a linear relationship, *i.e.* they adhere to Darcy's Law combined with mass conservation for one-dimensional flow under constant impregnation pressure [69]. Linear regression of the data was used to determine the Darcy slope, D, and, in turn, the instantaneous capillary number Ca_{ff} at the flow front via:

$$Ca_{ff} = \frac{\mu v_{ff}}{\gamma} = \frac{\mu}{\gamma}\frac{D}{2x_{ff}}. \tag{4.1}$$

Following impregnation and after pressure removal, specimens were imaged in the wet state *ex-situ* with XCT. Reported values of Ca_{ff} for each specimen are taken at the XCT imaging location, x_I (i.e., at $x_{ff} = x_I$ in Eq. 4.1). In these experiments, reported values of Ca_{ff} fell in the range of 3×10^{-5} to 1×10^{-2}. A subset of the specimens were then cured in a horizontal orientation at 120°C in air for 2 h and re-imaged at the same location. A subset of specimens had also been imaged in the dry state (prior to impregnation).

In the second test configuration, impregnations were performed while continuous *in-situ* XCT imaging was performed at one location within the tube. (These experiments are also reported in our previous work [69]). The tubes were oriented vertically: the fluid reservoir and inlet being at the top of the specimen and the outlet at the bottom. Pressures, P_m, ranging from 138 to 552 kPa were applied to the fluid reservoir with compressed air. The pressure due to gravity was calculated to be ≈ 1.5 kPa:

more than an order of magnitude less than the average capillary pressure, $\bar{P}_c = 16 \pm 1$ kPa, and almost two orders of magnitude less than the minimum pressure applied [69]. XCT images were taken before and during impregnation as well as immediately before and immediately after pressure removal. The time interval between the start of the latter scans was about 5-7 min. Because the location of the flow front could not be monitored in these experiments, Darcy slopes and thus values of Ca_{ff} at the imaging location were estimated from the results of a previously reported set of experiments at the corresponding pressures [69]. The fluid pressure, P_I, at the imaging location at a given time was estimated assuming a linear pressure drop (expected based on Darcy's Law and mass conservation) between the tube inlet (at $P = P_m$) and the flow front (at $P = 0$):

$$P_I(t) = P_m \frac{x_{ff}(t) - x_I}{x_{ff}(t)} \tag{4.2}$$

The flow front position was estimated by $x_{ff}(t) = \sqrt{Dt}$. In cases where the flow front had reached the end of the specimen, the flow front position was set equal to the specimen length. In the remainder of this work, reported values of P_I are taken at the average time of the XCT scan performed immediately before pressure removal.

4.2.3 X-ray computed tomography (XCT)

XCT was performed at Beamline 8.3.2 at the Advanced Light Source (ALS) at Lawrence Berkeley National Laboratory. *Ex-situ* imaging was performed in multilayer mode using 17 keV light (20-30% transmission) with a PCO edge camera and 10x optique lens. The field of view was about $1.7 \times 1.7 \times 1.4$ mm^3 and the voxel edge length was 0.65 μm. In one set of scans (performed while the ALS was in normal multibunch mode), a total of 1025 radiographs each with 500 ms exposure time were collected over the course of about 13-15 min. In another (performed while the ALS was operating in a low flux, two-bunch mode), a total of 4097 radiographs each with 1500 ms exposure time were collected over the course of about 3 hours.

In-situ imaging was performed in white light mode with a dimax camera and 10x lens while the ALS was in normal multibunch mode. The field of view was about $2.0\times2.0\times2.0$ mm^3 and the voxel edge length was 1 μm. A full dataset, consisting of 1025 radiographs each with 40 ms exposure time, was collected over the course of about 1.5 minutes; an additional 3.5 min was required to export the data from the camera between scans.

4.2.4 Image segmentation

Tomographic slices were reconstructed using TomoPy [84]. Ring removal parameters were optimized to minimize imaging artifacts. All datasets were reconstructed without phase retrieval. For the *ex-situ* scans of wet and cured specimens, additional reconstructions were performed with phase retrieval for automated segmentation of voids and matrix as described below. The reconstructed 3D data from dry and cured specimens were registered with the corresponding wet scans, to facilitate point-to-point comparisons of microstructures. Registration was performed by selecting eight well-defined stationary points in the corresponding volumes (*e.g.* at bubbles or fibers in the tube wall) and then solving for the rotations and the translations needed to bring the sets of points into coincidence using Horn's quaternion-based method[3]. These rotations and translations were then applied to the reconstructed images of the dry and cured specimens using bilinear interpolation.

Segmentation was performed using the MATLAB Image Processing Toolbox™[4] and ImageJ[5]. For reference, representative raw *ex-situ* XCT images and corresponding segmented images are shown in Fig. 4.3. Fiber segmentation was performed slice-

---

[3] Matt J (2015). Absolute Orientation - Horn's method, MATLAB Central File Exchange. Retrieved March 22, 2018.

[4] R2017b, The MathWorks, Inc., Natick, Massachusetts, United States

[5] Rasband, W.S., ImageJ, U. S. National Institutes of Health, Bethesda, Maryland, USA, http://imagej.nih.gov/ij/, 1997-2016

by-slice using the transverse XCT images reconstructed without phase retrieval (Fig. 4.3(A)). Fibers were initially detected using the Circle Hough Transform. Improperly identified pixels were corrected with filters based on connected region size and pixel value and through comparisons with the 10 slices above and below the slice of interest. Finally, fibers were separated using the watershed algorithm. Fiber segmentation was evaluated and optimized via visual inspection of fiber outlines overlaid on corresponding XCT images; the final segmentations showed excellent agreement with visual identifications.

Next, regions outside of the composite were identified slice-by-slice using transverse images reconstructed without phase retrieval. Regions outside of the composite were identified using one of two algorithms. In cases in which the glass tube contained bubbles (as in Fig. 4.3), regions outside of the composite were identified by dilating the fiber segmentation mask, filling in holes in the dilated mask, and then eroding and inverting the mask. In cases in which the glass tube did not contain bubbles, regions outside of the composite were identified using a gray-scale threshold followed by 2D order-statistic filtering. In both cases, segmentation was improved by filtering out incorrectly identified pixels based on connected region size and by using a slice-by-slice comparison of non-composite regions in the 17 slices above and below the slice of interest. Finally, remaining unidentified regions outside of the composite were identified as those that were not filled during a hole-filling operation. Segmentation was evaluated via visual inspection of the composite boundary overlaid on corresponding XCT images; the final segmentations showed excellent agreement with visual identifications.

Next, void and matrix regions were segmented as follows. For 1000 slices of each *ex-situ* scan (totaling $2560 \times 2560 \times 1000$ voxels), void and matrix regions were segmented slice-by-slice using the transverse images reconstructed with phase retrieval (Fig. 4.3(B)). For scans performed under low-flux conditions, a background subtraction operation was performed on the images prior to segmentation to remove ring artifacts that had not been removed during reconstruction. In the first step of segmentation (for both normal and low-flux scans), void area was identified using a gray-scale threshold. Additional void area was identified by thresholding the results of the Sobel operator on the images. Candidate void regions in the latter results were filtered based on maximum pixel intensity and then dilated. Next, the candidate void regions from both thresholds were combined and a sequence of operations (dilation, erosion, hole-filling) and filters on connected void regions (based on maximum intensity, mean intensity, and eccentricity) were used to further refine the segmentation. Finally, the segmentation was refined via slice-by-slice comparisons of the voids identified in the 4 slices above and below the slice of interest. All remaining unlabeled regions were identified as matrix.

The fidelity of algorithmic segmentation of voids was evaluated by comparing the degree of saturation, S, within eight randomly-selected slices obtained from algorithmic void segmentation and from manual void segmentation (the latter being more reliable but time-prohibitive for segmentation of entire data sets). The mean of the absolute values of the percent error between the values of S for the eight algorithmically and manually segmented images was 0.95% This value is used subsequently as an estimate of uncertainty on S for specimens imaged *ex-situ*.

For *in-situ* scans, detection of void and matrix regions was hindered by reduced image quality resulting from the short scan times and potential movement of the phases. Thus, for one slice of each scan, void and matrix regions were segmented by a manual tracing procedure based on gray-scale values within and along boundaries of the three phases and their variations with time [69]. Finally, for consistency, the segmented images were resized to yield the same resolution as that of the *ex-situ* images (0.65 μm per voxel edge), giving a total segmented image volume of $3156 \times 3156 \times 1$ voxels.

4.2.5 Image analysis

Several local and global microstructural characteristics were obtained from the segmented images. First, the volumes of matrix, fibers, and voids, denoted Y_m, Y_f and Y_v, respectively, were measured. The global fiber bed porosity, $\bar{\varepsilon}$, (that is, the volume fraction of dry fiber bed available for matrix impregnation) and the degree of matrix saturation, S, were calculated in accordance with $\bar{\varepsilon} = (Y_m + Y_v)/(Y_m + Y_v + Y_f)$ and $S = Y_m/(Y_m + Y_v)$. Sizes of individual voids were characterized by the square-root of their cross-sectional area in transverse sections, $\sqrt{A}$, computed via a 2D connected components analysis (connectivity = 8). (Most voids extend out of the longitudinal field-of-view, precluding meaningful measurement of their volumes.) Reported distributions and statistics for void size include all measurements of $\sqrt{A}$ from all voids in all transverse slices. The global metric of void size is taken as the area-weighted median of $\sqrt{A}$, henceforth referred to as the median void size, $\widetilde{\sqrt{A}}$. The range of $\sqrt{A}$, indicated by error bars in subsequent plots, is characterized by the area-weighted quartiles (Q1 and Q3). Distributions of void size are presented in terms of area-weighted relative frequencies. In this form, each frequency represents the fraction of fillable area in the fiber bed occupied by voids of the specified size, while the sum of all frequencies equals $1 - S$.

Spatial distributions of fibers and their changes during processing were inferred from distributions of local fiber bed porosity, ε, measured at each pixel location using a circular cell of radius 34 μm (52 pixels) centered at the pixel of interest. This radius was selected to ensure that, for all specimens, every cell contained at least one fiber pixel and at least one matrix or void pixel and hence the local porosity at each point fell in the range $0 < \varepsilon < 1$. The results are presented as normalized frequency distributions of local porosities, spatial distributions of local porosity, and changes in spatial distributions following impregnation, pressure removal and curing. Additionally, distributions of *fillable* local porosity – counting only local porosity values within fillable regions, in the spaces between fibers – and distributions of *voided* local porosity – counting only local porosity values within void regions – are also presented. Distributions of fillable local porosity are normalized to yield a total area of 1. The voided local porosity distribution is normalized by the fillable local porosity distribution such that the ratio of the area under the voided distribution to the area under the fillable distribution is equal to $1 - S$. Reported distributions include all transverse slices.

Non-uniformity of local fiber bed porosity was measured by local porosity entropy [85], $E(r_c)$, defined in this work by

$$E(r_c) = -\sum_{i=1}^{256} P_i(r_c) log_2 P_i(r_c) \tag{4.3}$$

where r_c is the radius of the circular cell used to compute local porosity, and $P_i(r_c)$ are the discrete relative frequencies of local porosity values. Since local porosity values are computed using an 8-bit image, ε can take on $2^8 = 256$ possible values: $\frac{0}{255}, \frac{1}{255}, \frac{2}{255}, ..., \frac{255}{255}$. This sets the limit on the number of discrete values of local porosity and hence the number of terms in the summation. Selection of r_c for the present calculations was done in the following way.

The dependence of local porosity entropy on r_c for one slice of a representative specimen imaged in dry, wet, and cured states is shown in Fig. 4.4(A). For all three states, the maximum value of porosity entropy occurs at r_c = 9 pixels (5.8 μm), which corresponds approximately to the fiber radius. This correlation is unsurprising, since the entropy length – the length scale at which the local entropy becomes extremal – is typically an accurate measure of linear size of features in an image [85]. Plots of the changes in local porosity entropy between states show that, for this particular specimen, the local porosity entropy at r_c = 9 pixels decreases over the course of processing (Fig. 4.4(B)). However, as we show later, fiber rearrangement during impregnation and curing is typically manifested by local expansion or contraction of large channels between the fibers over a length scale of several (2-10) fiber radii: significantly greater than the entropy length scale. In order to detect such changes, the local porosity entropy must be calculated over a comparable length scale. Here we find it convenient to use a cell radius of 52 pixels (34 μm). As noted earlier, this cell radius ensures that $0 < \varepsilon < 1$ for all specimens and thus ensures that changes in fiber packing near large channels are captured (Fig. 4.4 inset). The results in Fig. 4.4(B) show that the porosity entropy at r_c = 52 pixels increases over the course of processing. The observation that changes in porosity entropy at low and high r_c values are opposite in sign suggests that increases in non-uniformity over long length scales can lead to reductions in non-uniformity at shorter length scales. In the case of large channels expanding to make the fiber bed, as a whole, less uniform, an increase in porosity entropy at r_c = 52 pixels is expected, as this measure of local porosity is sensitive to changes in large channels. At the same time, closely packed fibers must become more closely packed and, in doing so, may move closer to (ideal) hexagonal close packing, resulting in an increase in uniformity in those regions. Since local porosity entropy at r_c = 9 pixels is not sensitive to changes in the larger channels (which have local porosity saturated at 1 for r_c = 9 pixels), changes in porosity entropy will largely reflect fiber rearrangement only in closely-packed regions. Results for changes in local porosity entropy vs. r_c for all specimens imaged dry, wet after pressure removal, and cured are given in Fig. 4.5. Between dry and cured states, local porosity entropy invariably decreases at smaller length scales ($r_c \approx 9$ pixels) and increases by a larger amount at larger length scales ($r_c \approx 52$ pixels). This behavior is also observed in most cases between dry and wet states and wet and cured states, with the exception of a couple specimens that show increases at small length scales and decreases at large length scales from the wet state to the cured state (one of these specimens, designated s2, is discussed in detail later). In this work, changes in non-uniformity for the entire fiber bed are of interest and thus local porosity entropies reported and discussed below are all computed for r_c = 52 pixels (unless otherwise stated). Henceforth, the symbol E represents the porosity entropy at r_c = 52 pixels.

4.3 Results

4.3.1 Scope and organization

In this study, 26 specimens were imaged with XCT in each of one or more states. Results presented here correspond to four general states:

1. Dry, prior to impregnation (indicated by subscript d) [*in-situ* and *ex-situ* specimens]
2. Wet, immediately before pressure removal (BPR) (indicated by subscript w combined with superscript o) [only *in-situ* specimens]
3. Wet, after pressure removal (APR) (indicated by subscript w) [*in-situ* and *ex-situ* specimens]
4. Cured (indicated by subscript c) [only *ex-situ* specimens]

We present comprehensive sets of results for six exemplary specimens in figs. 4.6 to 4.11. The specific examples were selected to illustrate the full range of microstructural observations, including extreme and intermediate behaviors. These specimens, designated s1-s6, are labeled in subsequent figures. Each set of figures shows, for the same center transverse slice: (A) segmented data in the pertinent imaged states; (B) corresponding spatial distributions of local fiber bed porosity; and (C) changes in the latter porosity distribution associated with changes in state. For segmented images of the dry states, empty spaces between fibers are shown in purple. For segmented images of wet and cured states, void regions are color-coded in the following way: blue for voids present *only* in the first imaged impregnated state (state 2 for specimens imaged *in-situ* and state 3 for specimens imaged *ex-situ*), red for voids present *only* in the final imaged state (state 3 for specimens imaged *in-situ* and state 4 for specimens imaged *ex-situ*), and light green for voids that are present in both states. Fibers are white and regions between fibers are gray. The figures also show: (D) distributions of local fiber bed porosity, (E) distributions of fillable and voided local fiber bed porosity, and (F) distributions of void sizes. Our discussion of results begins with a synopsis of broad trends in measurements and observations and later returns to the six exemplary test specimens.

4.3.2 Fiber arrangement

The fiber beds exhibit global porosities that vary from about 0.32 to 0.39. The corresponding local porosity entropy of specimens imaged *ex-situ* varies from about 5.4 to 6.2 and increases approximately linearly with global porosity in the dry, wet (APR), and cured states (Fig. 4.12). To provide context for the latter result, the sensitivity of entropy to porosity alone was calculated for the center transverse slice of three different *ex-situ* specimens. This was accomplished by computationally either expanding or shrinking the fiber diameters by a small amount, thereby decreasing or increasing fiber bed porosity without altering fiber locations. Changes in fiber diameter were selected to achieve porosity levels that span the full range of interest, from about 0.3 to 0.4. For each fiber arrangement, the entropy (indicated by filled blue circular plot markers and thin black lines in Fig. 4.12) *decreases* only very slightly with increasing porosity. The inference is that the measured increase in entropy with porosity across all specimens is largely attributable to the increased capacity for fibers to arrange into less uniform configurations at higher porosity levels, not to the porosity level per se.

The preceding results also indicate that porosity is sensitive to segmentation parameters that might slightly expand or shrink the fiber diameters. This explains the deviation of the trends for specimens imaged *in-situ* and *ex-situ*. The four specimens imaged *in-situ* had lower image quality and required use of slightly different parameters in fiber segmentation. However, similarly to the *ex-situ* specimens, the sensitivity of entropy to porosity for an individual *in-situ* specimen is negligible (indicated by filled purple square plot markers and thin black line in Fig. 4.12). Thus, in the remaining results, entropies of *in-situ* specimens are reported alongside those of *ex-situ* specimens, while global porosity results of *in-situ* specimens are excluded. Specimens imaged *in-situ* are designated as s1, s7, s8, and s9 in subsequent figures.

4.3.3 Microstructure evolution during impregnation and pressure removal

In cases where fiber beds are not completely saturated with fluid after impregnation and pressure removal, the remaining voids show common geometric characteristics (figs. 4.6 to 4.11 and Fig. 4.13). Most voids are very long parallel to the fiber axis (Fig. 4.13). Indeed, for all specimens containing observable voids, an average of 95% of the total imaged void volume was connected to either the top, the bottom, or both the top and the bottom of the segmented volume. As a result, the voids can be characterized principally by their appearance in transverse sections; in turn, void area in a transverse section can be interpreted effectively as void volume per unit length. In transverse views, voids are bounded by closely-packed fibers. Void dimensions are typically less than 5 fiber diameters wide and of a length that varies from a few to tens or hundreds of fiber diameters. They typically form in the largest pre-existing (dry state) channels between fibers, where the local fiber bed porosity in both dry and wet states is particularly high (figs. 4.6 to 4.10). Comparisons of distributions from the wet state of local porosity within all fillable regions and within voids alone show that voids form preferentially in regions of high local porosity (parts B and E of figs. 4.6 to 4.11. In some cases, channels where voids form during impregnation expand slightly, increasing the local porosity in those regions.

Impregnation also typically leads to a slight increase in porosity entropy, on average by about 0.06 (Fig. 4.14(A)). Because these changes are small compared to the observed range of entropies, E_d is fairly predictive of E_w. Thus, the following analysis uses entropy of the wet fiber beds (because only a subset of the specimens was imaged dry), and we can infer that trends with E_w would be similar to those with E_d.

The median void size and the amount of void space (characterized by S_w) appear to be governed by a combination of the instantaneous capillary number and the local porosity entropy. Specifically, the degree of saturation increases from about 0.8 at $Ca_{ff} \approx 3 \times 10^{-5}$ to 1 at $Ca_{ff} \approx 10^{-2}$ (Fig. 4.15(A)); local porosity entropy of the fiber bed (either dry or wet) does not appear to have an effect (Fig. 4.16(A)). Global porosity shows a very weak positive correlation with S_w (Fig. 4.16(B)). In contrast, the median void size, $\widetilde{\sqrt{A_w}}$, appears to depend most strongly on local porosity entropy and is not correlated with Ca_{ff} (Fig. 4.15(B,C)). But this dependence does not follow a one-to-one mapping, in the sense that the void size *may* increase with increasing entropy, but it does not necessarily do so (Fig. 4.15(B)). The nature of this trend is elucidated by splitting the void size data into three groups: one for $S_w < 0.95$, another for $0.95 < S_w < 0.999$, and another for $S_w > 0.999$. For the first group, void size appears to increase with E_w. But this increase is not observed for the latter groups (where the degree of saturation is high). These results suggest that high porosity entropy *allows* for the formation of large voids, but it does not necessarily *cause* formation of large voids. In light of the relationship between global fiber bed porosity and local porosity entropy, the void size shows a corresponding, albeit weaker, relationship with global porosity, (Fig. 4.15(D)).

While the preceding results reveal the effect of Ca_{ff} on degree of saturation after impregnation *and* pressure removal, they fail to capture effects of pressure removal alone. To this end, results for four test specimens imaged *in-situ* immediately before and immediately after pressure removal are presented here (Fig. 4.17). To provide a baseline, impregnation by capillary imbibition alone (without applied pressure) leads to incomplete saturation (on average, $S_w = 0.85$) (green points in Fig. 4.17(A)). When impregnation is driven by applied pressure, the degree of saturation immediately before pressure removal, S_w^o, increases with pressure, reaching complete saturation at $P_I \approx 180$ kPa (blue points in Fig. 4.17(A)). Despite the attainment of complete saturation during impregnation, pressure removal can lead to a loss in saturation. The effects appear to be greatest at intermediate pressures ($P_I \approx 80 - 200$ kPa) (Fig. 4.17(B)). In the most extreme case obtained in the present experiments (at $P_I = 151$ kPa), the degree of saturation drops by 0.16, from 0.99 to 0.83, during pressure removal (s1, Fig. 4.6). Images of this specimen (in Fig. 4.6) show that many new voids are formed during pressure removal while only a small number are eliminated. Meanwhile, at sufficiently high pressures (exceeding 300 kPa), complete saturation is maintained after pressure removal. The inferences and implications of these results are addressed in the discussion.

4.3.4 Microstructure changes during curing

Curing leads to changes in the quantity, locations, sizes and shapes of voids. Some voids present after curing show similar characteristics to those observed after impregnation (figs. 4.7 to 4.11 and Fig. 4.13); they are long parallel to the fiber axis and are bounded by closely packed fibers in transverse sections. In other cases, voids consist of long clusters of smaller voids aligned with the fiber axis (Fig. 4.13). The bridges between these bubbles can be thick (tens of microns), very thin (less than a voxel width) or, in some cases, appear to be broken (Fig. 4.13). These voids are typically bounded by a film of matrix material surrounding the individual bubbles and beyond the film by other columns of bubbles, long non-bridged voids, or closely-packed fibers.

Similarly to voids found after impregnation, voids found after curing are mainly in the largest channels between fibers (evident in local porosity distributions within voided regions and in transverse sections in figs. 4.7 to 4.11. They are also typically less than 5 fiber diameters wide and up to hundreds of fiber diameters in length.

Curing also typically leads to an increase in fiber disorder, as manifested in an elevation in local porosity entropy, on average by about 0.07 relative to the wet impregnated state (Fig. 4.14(B)). Furthermore, the combination of impregnation and curing invariably leads to an increase in local porosity entropy, on average by about 0.11 relative to the dry state (Fig. 4.14(C)). Again, these changes in entropy are small relative to the full range of entropies observed, and thus E_d and E_w are fairly predictive of E_c.

Changes in saturation during curing, $S_c - S_w$, depend most strongly on the saturation *before* curing, S_w (Fig. 4.18(A)). Specimens with high saturation before curing tend to show the largest reductions in saturation, with changes of about -0.13 on average at $S_w = 1$, whereas specimens with low initial saturation ($S_w \approx 0.80 - 0.85$) undergo much smaller changes. In some cases, especially when the starting saturation is low, the saturation increases slightly during curing. Despite the larger reductions in saturation at high initial values of saturation, the degree of saturation after curing is still greatest in cases in which the instantaneous capillary number was high and hence the initial saturation was high (Fig. 4.18(B)). Neither the local porosity entropy nor the global porosity affect saturation after curing (Fig. 4.19).

As with the wet specimens, the median size of curing voids depends most strongly on the local porosity entropy (Fig. 4.20(A)) and shows a similar, yet weaker, relationship with global porosity (Fig. 4.20(D)). The largest median void sizes invariably occur in specimens with high entropy, although high entropy does not necessarily lead to large median void sizes. In most cases, the median void size after curing is greater than that after impregnation (Fig. 4.20(B)). The instantaneous capillary number has no effect on the median void size (Fig. 4.20(C)).

4.3.5 Detailed observations of exemplary test specimens

Further insights are gleaned from detailed examinations of the exemplary cases shown in figs. 4.6 to 4.11. The first (s1, Fig. 4.6) shows effects of impregnation and pressure removal for the case with the *largest reduction in saturation following pressure removal*. During impregnation (before pressure removal), saturation is nearly complete ($S_w^o = 0.99$) and the few existing voids are relatively small. The corresponding change in entropy, $E_w^o - E_d$, is also small, with a slight increase by 0.006. Upon pressure removal, the degree of saturation drops by 0.16, to $S_w = 0.83$. Many new voids (red) form in regions of high and intermediate local porosity in the wet state, which also correspond to regions of high and intermediate local porosity in previous wet and dry states. Thus, voids form primarily in large pre-existing channels (as opposed to creating said channels during void formation). Pressure removal is also associated with a decrease in entropy, $E_w - E_w^o = -0.04$, perhaps due to slight relaxation of the fibers.

The second (s2, Fig. 4.7) shows effects of impregnation and curing for a case in which the degree of saturation after impregnation was relatively low ($S_w = 0.85$) and increased slightly (to $S_c = 0.88$) during curing. During impregnation, voids form primarily in pre-existing large channels and those channels appear to expand slightly, leading to an increase in local porosity entropy of $E_w - E_d = 0.08$. During curing, as the saturation increases, both the median void size and the local porosity entropy exhibit reductions, contrary to the broader trends found with most test specimens. The increase in saturation is presumably due to migration of matrix material into the imaged region from adjacent regions, possibly driven by bubble formation in regions with higher saturation. Several regions containing large impregnation voids in the wet state are partially filled with matrix during curing (blue regions), creating several smaller voids (green regions) present after curing. Only a few new voids (red regions) formed during curing. These changes are evident in void size distributions before and after curing. Furthermore, in regions where large voids had been partially filled, large channels appear to have contracted slightly, causing the fiber bed to become more uniform with a change in local porosity entropy of $E_c - E_w = -0.07$.

The third example (s3, Fig. 4.8) shows a specimen that had been fully saturated after impregnation and exhibited a large reduction in saturation, from 1.00 to 0.85, upon curing. This specimen also has the *largest median void size after curing*. The largest void is highly elongated in the transverse section and appears near the tube wall and in the bed interior (presumably along prior tow boundaries). Void formation also appears to have caused significant fiber movement, resulting in expansion of several of the largest channels (visible in red in the images of $\Delta\varepsilon$ in (C) and evident in the changes in the histogram of local porosity in (D)). Meanwhile, previously-existing large channels that did not contain voids after curing (for example along the top of the specimen near the tube wall) appear to have contracted slightly. Overall, fiber movement results in a net increase in entropy, implying an increase in fiber bed non-uniformity.

The fourth example (s4, Fig. 4.9) shows the specimen with the *highest entropy* in the dry, wet, and cured states. During impregnation, voids form in pre-existing large channels near the tube wall and internally along possible prior tow boundaries. Some of the large channels in which voids form appear to expand slightly, leading to an increase in local porosity entropy of $E_w - E_d = 0.05$. Upon curing, this specimen shows the largest reduction in saturation, from 0.94 to 0.77. Several large voids present in the wet state remain after curing (shown in light green). Curing also leads to formation of several large (red) voids that appear in regions of pre-existing high local porosity near the tube wall and internally along possible prior tow boundaries. Expansion of old voids and formation of new voids cause significant displacement of nearby fibers and an increase in non-uniformity of fiber packing, with $E_c - E_w = 0.10$. Formation of large voids and regions of higher local porosity during curing are evident in changes in void size and local porosity distributions.

The fifth example (s5, Fig. 4.10) shows the specimen with the *lowest saturation* after impregnation ($S_w = 0.79$). This specimen shows almost no change in saturation upon curing ($S_c - S_w < 0.01$), and thus the integrated frequencies of the histograms of voided local porosity and void size are nearly the same. However, there is a significant redistribution of void locations and sizes. Several small impregnation voids in the specimen interior disappear (blue regions) while several larger voids (in regions of high local porosity) near the tube wall expand during curing. Overall, curing results in a slight increase in median void size and a moderate increase in entropy.

The final example (s6, Fig. 4.11) shows curing effects in an *intermediate case* (this specimen had not been imaged dry). Here, during curing, saturation decreases by a moderate amount, from 0.91 to 0.83, while both the median void size and the local porosity entropy increase by moderate amounts. Many of the large voids in both the wet and the cured states appear near the tube wall and internally along possible tow boundaries. Many of the new (red) voids appear to have expanded from pre-existing voids in the regions of high local fiber bed porosity, causing expansion of several large channels within the fiber bed.

4.4 Discussion

Here we examine the connections between processing conditions, fiber bed properties, and ensuing microstructures of unidirectional minicomposites. The discussion begins with the processes involved in impregnation, including fiber movement, void entrapment, void mobilization, gas dissolution and gas exsolution. This is followed by a discussion of effects of curing.

The results presented here along with those of our previous related study [69] of fluid impregnation into unidirectional fiber beds reveal the following operative mechanisms of fluid flow and defect formation. The schematic in Fig. 4.21 depicts the important trends. At low capillary number, the impregnation rate and the nature of the flow front are capillary-driven. Flow occurs preferentially within the narrowest channels between fibers where capillary forces are greatest [69]. Capillary forces further draw the affected fibers inward, thereby expanding adjacent channels. The process may lead to permanent entrapment of voids in the larger channels; further flow does not aid in void mobilization nor does it enable dissolution of any trapped gas.

With increasing impregnation pressure and hence increasing capillary number, the differential between flow rates in large and small channels is expected to be reduced and hence the flow front is expected to be more uniform. Under these conditions, the tendency for void entrapment in the wake of the flow front is reduced [32, 50]. Additionally, higher capillary numbers promote mobilization of entrapped voids during further fluid impregnation. The higher pressures also promote dissolution of trapped gas into the fluid, followed later (upon pressure removal) by exsolution of gas and formation of bubbles. This dissolution/exsolution process is clearly undesirable since it yields only a temporary enhancement in saturation. At yet higher pressure, the combination of increasing uniformity of fluid flow with increased void mobility lead to complete saturation, without gas entrapment and accompanying dissolution/exsolution.

The uniformity of fiber packing in the initial fiber bed, as measured by the local porosity entropy, does not appear to play a role in the degree of saturation. With respect to remnant voids after impregnation, however, fiber packing plays a role in void size. Notably, fiber beds with high porosity entropy contain larger channels; because the capillary pressure is lower within larger channels, these channels are the preferred void locations. Slight fiber movement accompanying impregnation causes a further increase in porosity entropy (by about 0.06).

Curing of the fluid of present interest (the SMP-10 ceramic precursor) leads to liberation of low molecular weight gases. In cases where the degree of saturation after impregnation is low, the reduced amount of precursor material leads to a reduced amount of gas that can form and that needs to be liberated. The gas that forms can readily escape via available pathways resulting from incomplete saturation. Consequently, changes in saturation following curing are small. In contrast, when complete saturation is obtained during impregnation, the amount of fluid and the amount of gas evolved are greater, but the pathways for gas escape are not initially present. In these cases, reductions in saturation following curing can be large. Capillarity favors formation of bubbles in the largest channels and thus such channels become preferred pathways for gas release. The latter channels are typically located near the tube walls, where fiber packing may be compromised somewhat by the encasement process, as well as in the interior of the fiber bed in regions of anomalously low fiber packing, such as those obtained along prior tow boundaries. The result is that pathways produced for gas liberation are highly heterogeneous, occurring preferentially in a small number of large channels. These effects are exacerbated by non-uniformity in the initial fiber packing; higher porosity entropy enables larger voids to form. Formation of these voids leads to a further increase in fiber bed non-uniformity.

Extrapolating the present trends to further steps in the PIP process, we expect that pyrolysis of impregnated and cured composites will further exacerbate the non-uniformity of the fiber bed. This is because the large volume change associated with pyrolysis will tend to further shrink small channels – where the precursor is abundant – at the expense of expansion of the large (voided) regions. Microstructural changes following additional impregnation and pyrolysis cycles are expected to continue along a similar path. One implication is that the degree of uniformity in the pore network following the first cycle may be crucial to the filling efficiency, especially in the larger channels, during subsequent process cycles.

4.5 Conclusions

The present study has revealed qualitative features and quantitative measures associated with microstructural evolution during axial impregnation and subsequent curing of a preceramic polymer in unidirectional ceramic fiber beds. The methods developed and demonstrated here are used to identify correlations between local fiber packing and regions where voids are formed as well as connections between impregnation conditions and the nature and extent of voids that result from impregnation and curing. Arguably, the present collection of experimental results could not be obtained through any route apart from XCT. Additionally, use of spatial local porosity distributions and local porosity entropy to characterize fiber bed uniformity before and after various processing stages represents a novel step forward in quantifying important microstructural changes during processing, especially those related to void location and void size.

Key conclusions and implications follow.

- Saturation after impregnation increases with instantaneous capillary number: a consequence of reduced void entrapment likely resulting from more uniform flow fronts and/or increased void mobilization during subsequent flow. Over the range of experimental conditions employed here, saturation does not appear to be affected by local porosity entropy.
- Because of the need to create pathways for gas escape, specimens with higher saturation after impregnation typically show the largest reductions in saturation during curing. Despite this, specimens with higher instantaneous capillary number during impregnation tend to have the highest saturation after curing.
- Because of capillarity, voids tend to form in the largest channels between fibers during both impregnation and curing. Increased fiber non-uniformity, as measured by local porosity entropy, allows for higher median void sizes. Median

void size is not influenced by instantaneous capillary number.

- As the fiber beds are taken from the dry state to the cured state, local porosity entropy drops slightly over length scales (characterized by the circular cell radius used to compute local porosity) comparable to the fiber radius (because of the tendency of closely packed fibers to become even more closely and uniformly packed) and increases by a greater amount at longer length scales ($\approx 34 \mu m$), the latter corresponding to the scales sensitive to changes in fiber packing near large channels. The trend is expected to continue with further processing steps, including pyrolysis and additional precursor impregnation and pyrolysis cycles, as needed to further densify the matrix.

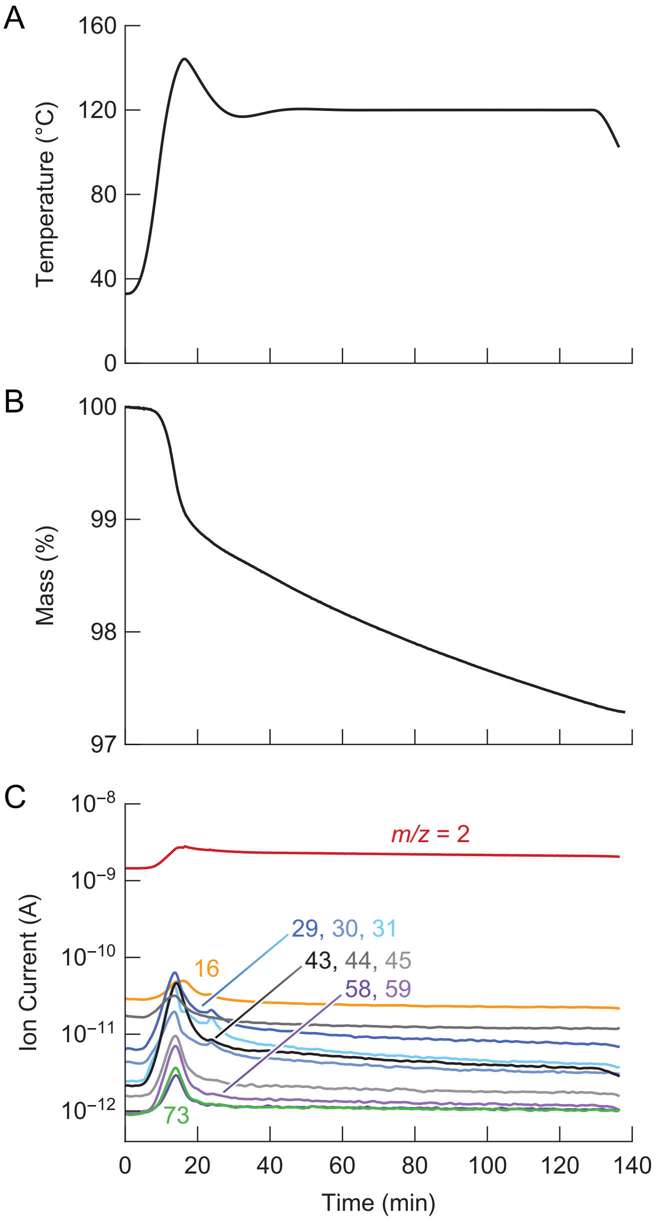

Figure 4.1: Thermogravimetric analysis and mass spectrometry (TGMS) during curing of a neat specimen of AHPCS + 0.2wt% DP. Measurements were made at NETZSCH Instruments North America, LLC (Burlington, MA) using an STA 449 *F1 Jupiter*® thermogravimetric analyzer with an Oxygen Trap System (OTS®) coupled to a QMS 403 *Aëolos*® quadrupole mass spectrometer. The tests were run under flowing argon. Liberation of hydrogen (ratio of mass number to charge number, $m/z = 2$), methane ($m/z = 16$), and silanes (silane, methylsilane, dimethylsilane, trimethylsilane, and tetramethylsilane, with $m/z = 29, 30, 31, 43, 44, 45, 58, 59, 73$) leads to a mass loss of 2.7% during curing.

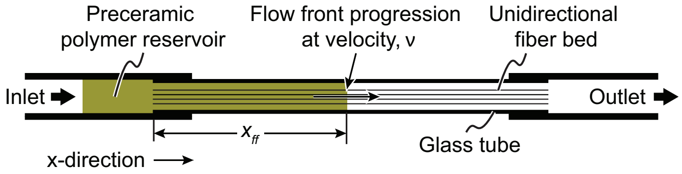

Figure 4.2: Test geometry consists of a capillary tube filled with fibers and impregnated axially with a preceramic polymer.

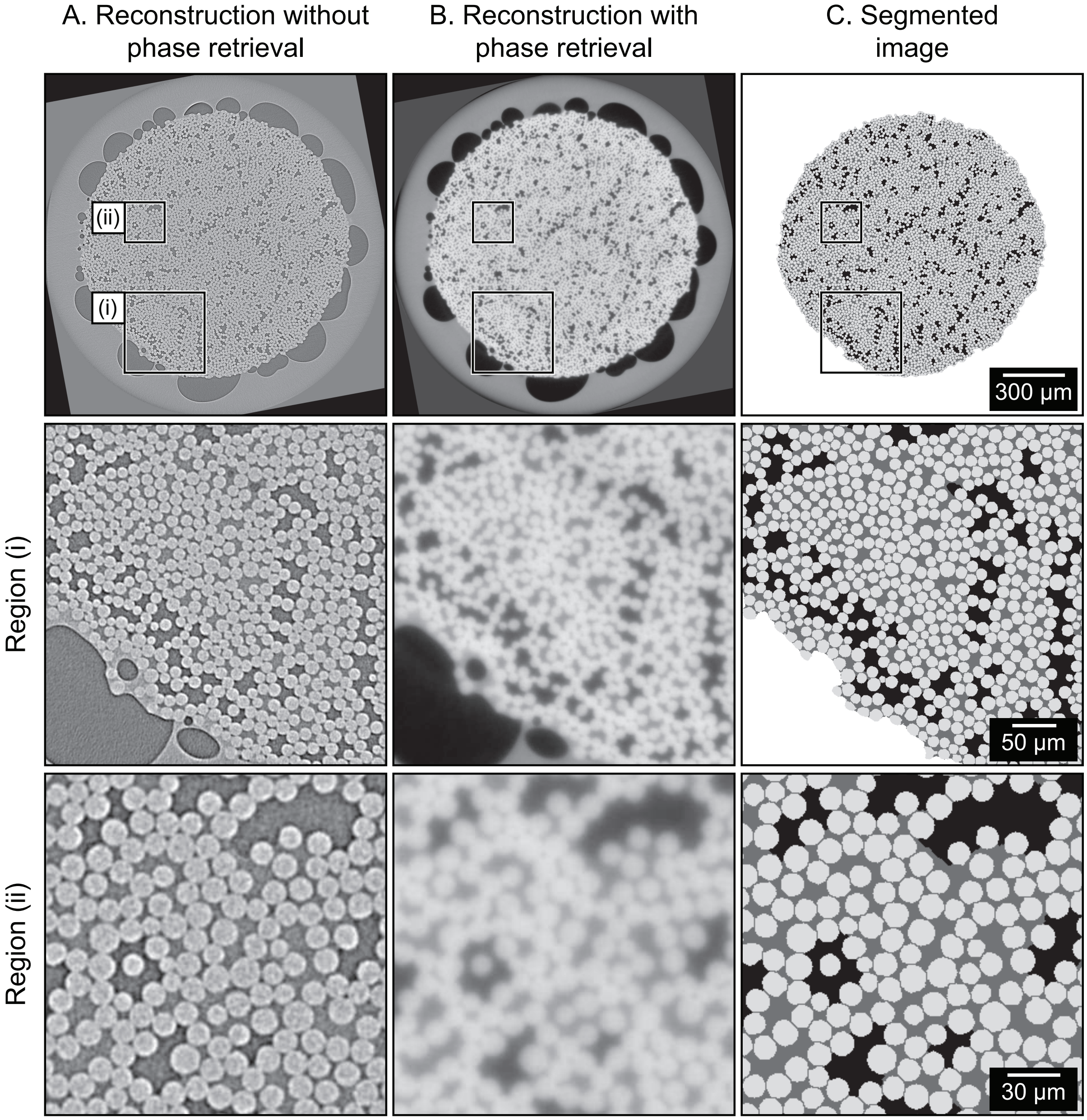

Figure 4.3: Representative transverse section from XCT reconstructed (A) without and (B) with phase retrieval. (C) The corresponding segmentation shows fibers in light gray, matrix in medium gray, voids in black, and regions outside the specimen in white.

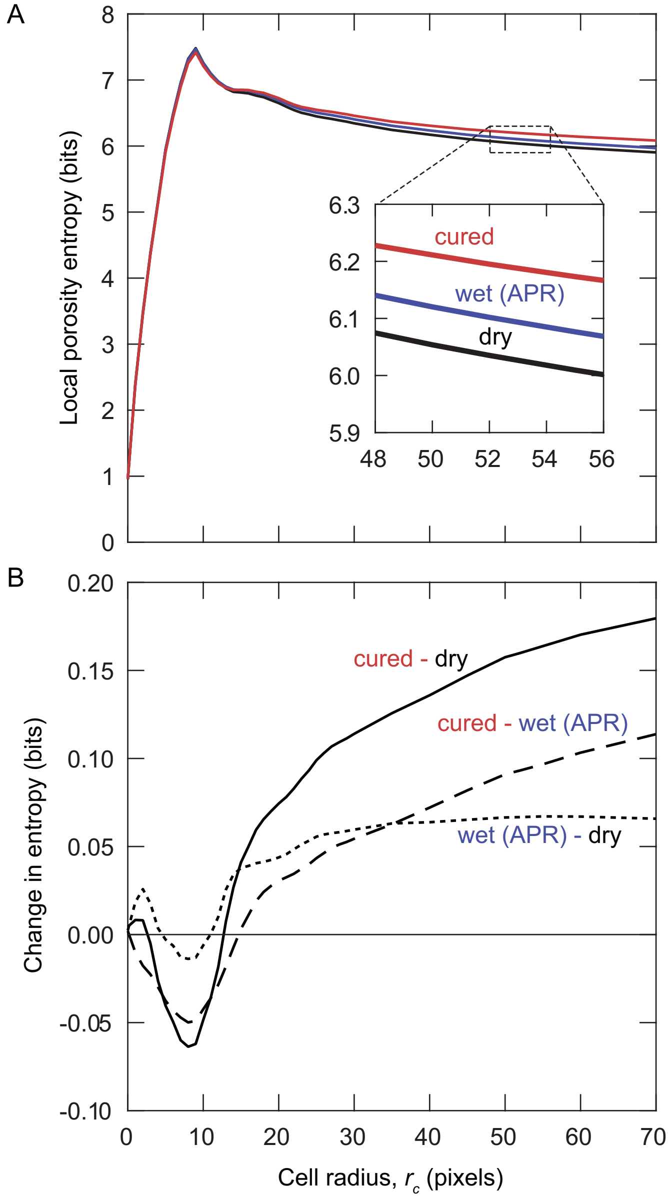

Figure 4.4: Cell radius used to compute local porosity influences (A) local fiber bed porosity entropy and (B) changes in entropy between processing states. Shown here are results for the center transverse slice of the specimen designated s4 (Fig. 4.9), which was imaged in dry, wet and cured states.

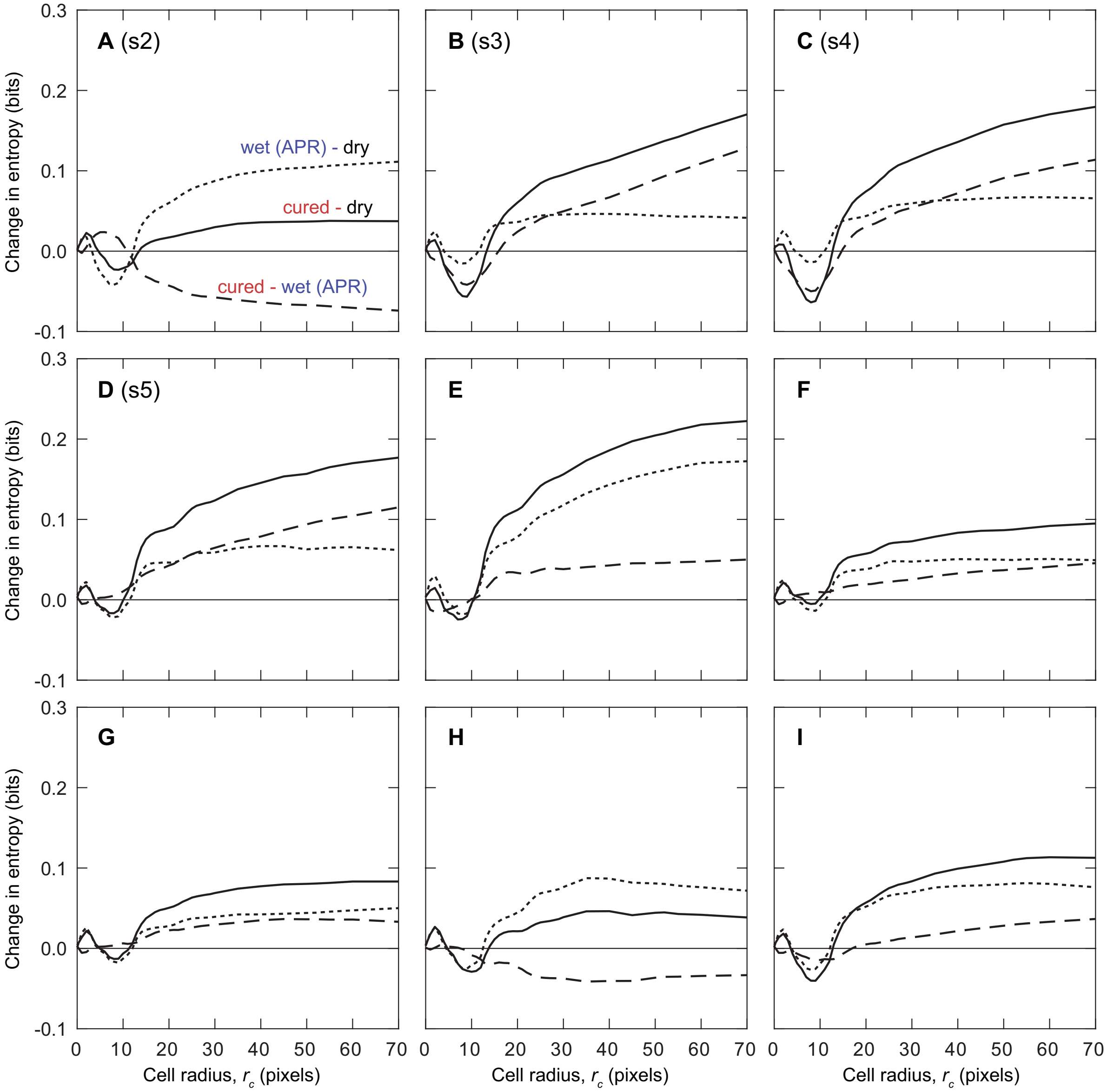

Figure 4.5: Changes in local fiber bed porosity entropy between processing states. Results are shown for all specimens imaged dry, wet after pressure removal (APR), and cured. Exemplary specimens s2-s5 are labeled for reference.

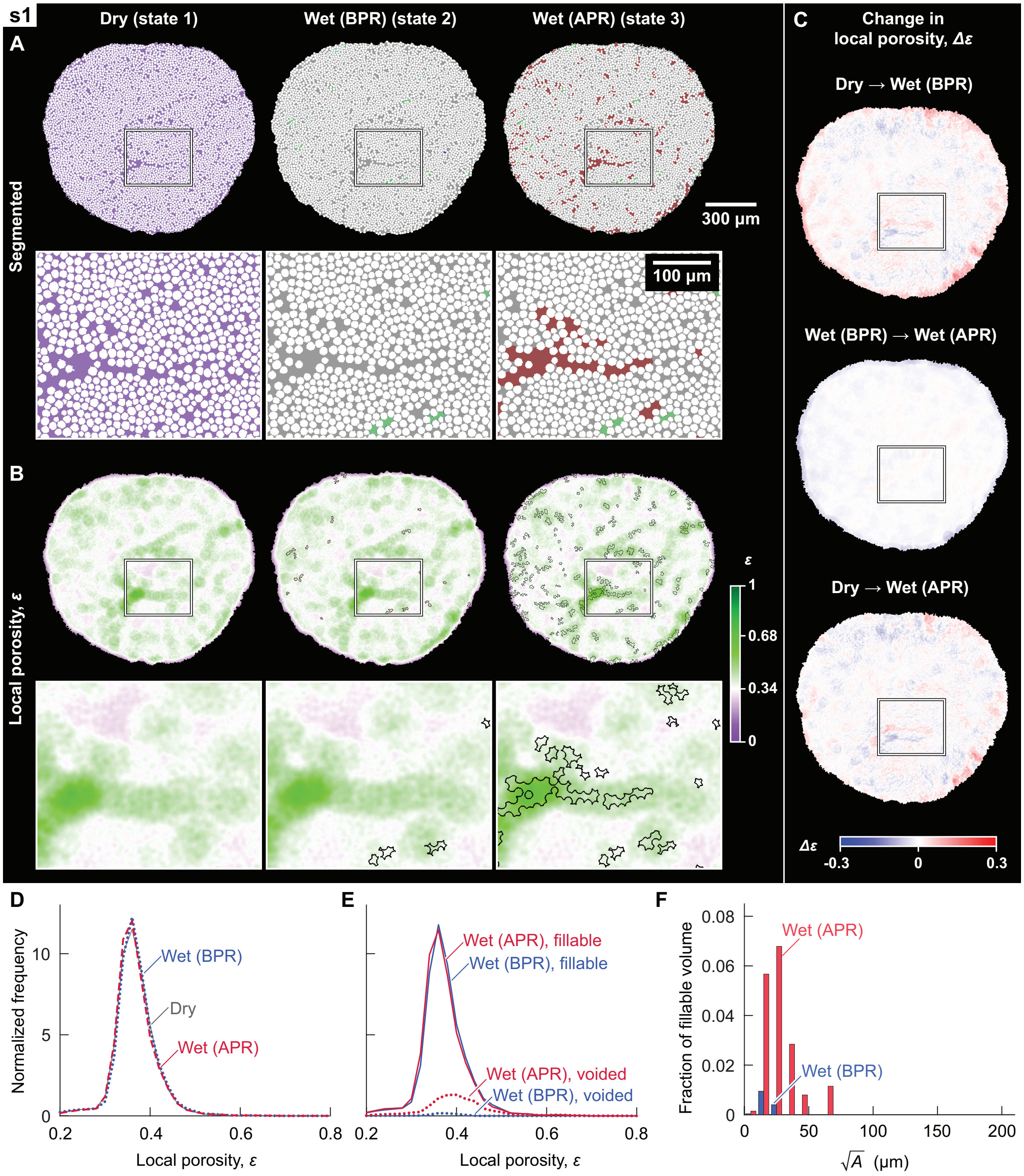

Figure 4.6: Results for exemplary specimen 1 (s1) imaged *in-situ* in the dry state and in the wet state immediately before pressure removal (BPR) and after pressure removal (APR). For this specimen, $Ca_{ff} = 7.1 \times 10^{-4}$ and $P_I = 151$ kPa. Detailed descriptions of images and plots here and in subsequent related figures are provided in sections 4.2.5, 4.3.1, and 4.3.5.

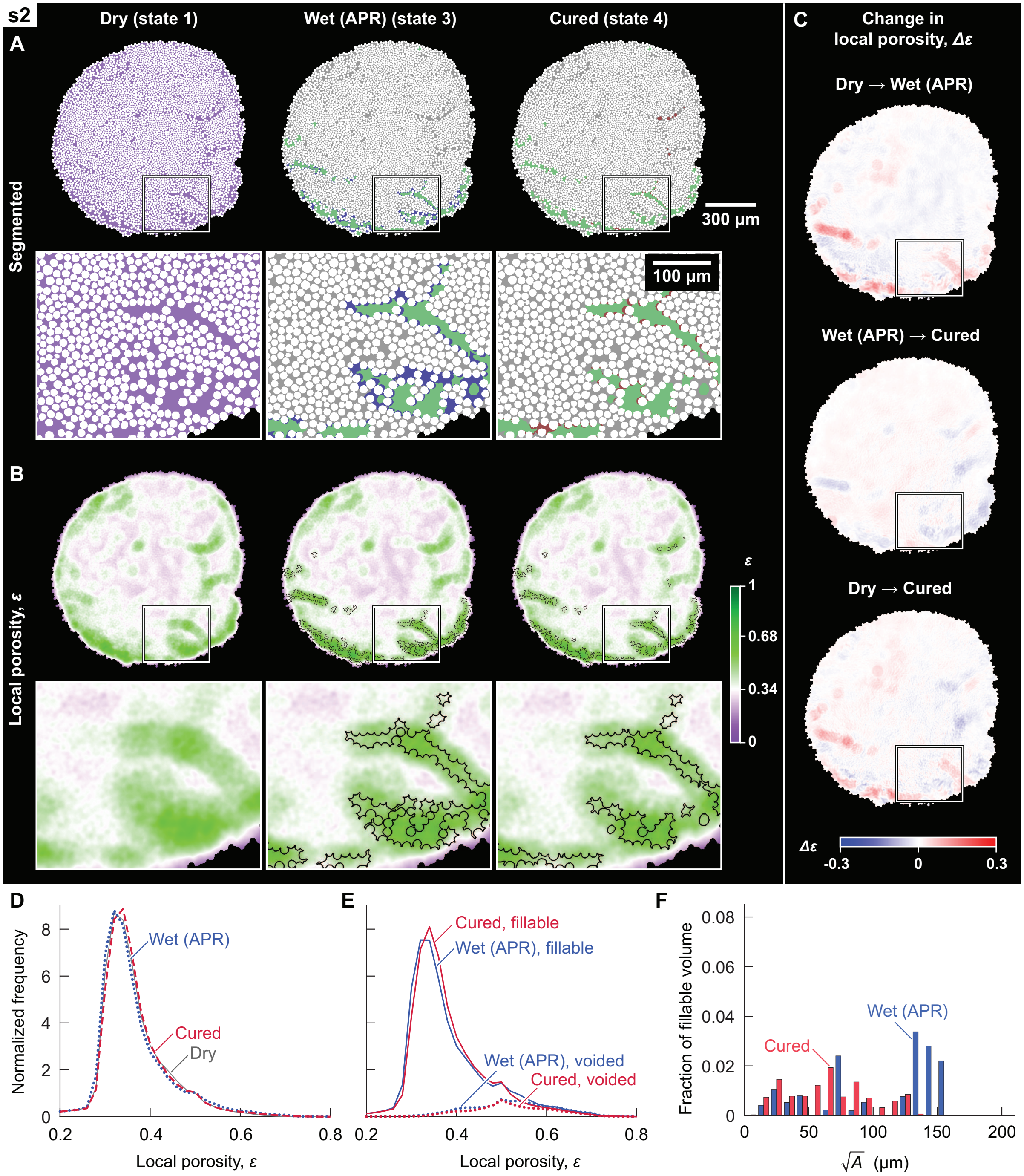

Figure 4.7: Results for specimen 2 (s2) imaged *ex-situ* in the dry state, the wet state after pressure removal (APR), and the cured state. For this specimen, $Ca_{ff} = 5.3 \times 10^{-4}$.

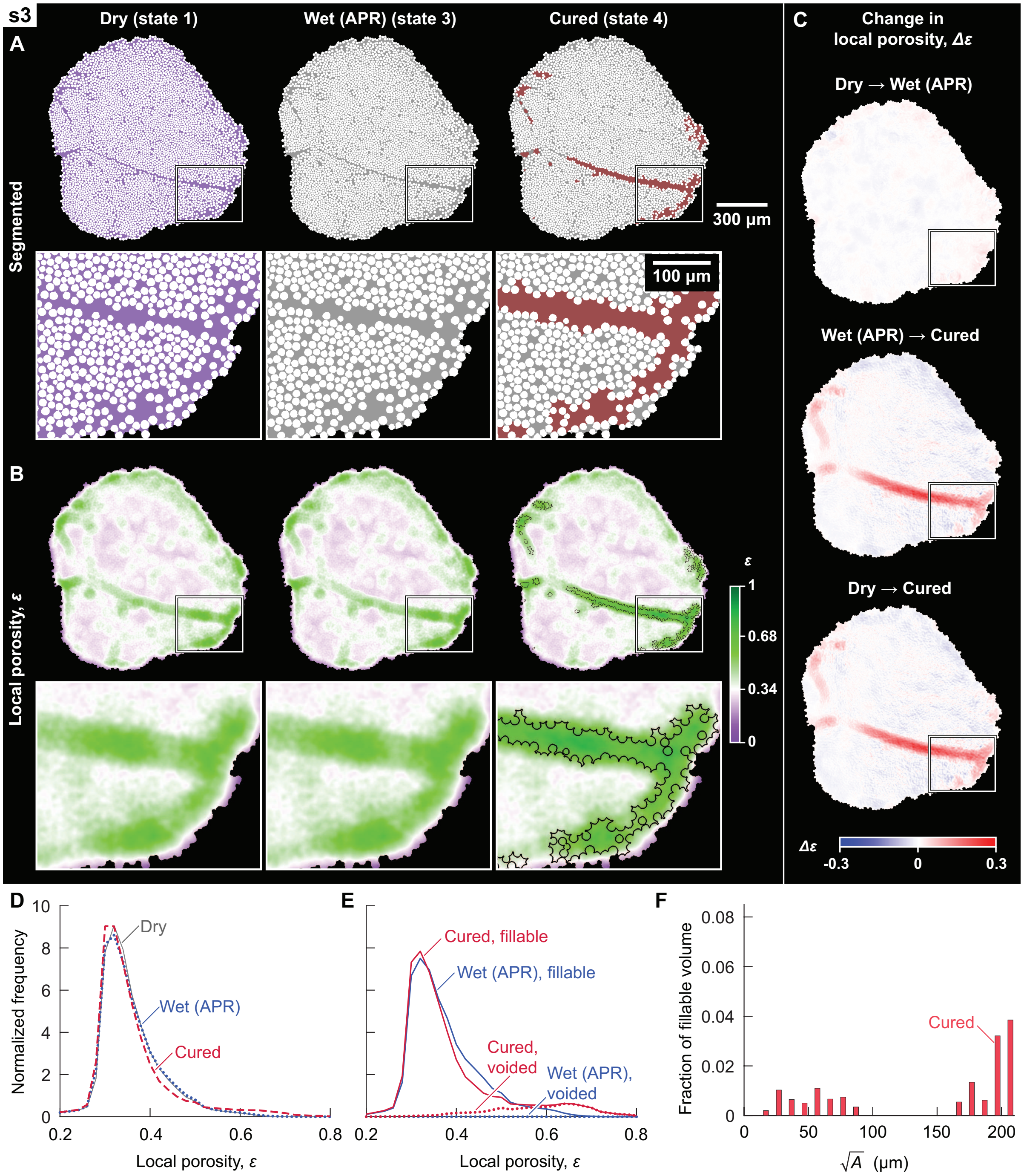

Figure 4.8: Results for specimen 3 (s3) imaged *ex-situ* in the dry state, the wet state after pressure removal (APR), and the cured state. For this specimen, $Ca_{ff} = 6.4 \times 10^{-4}$.

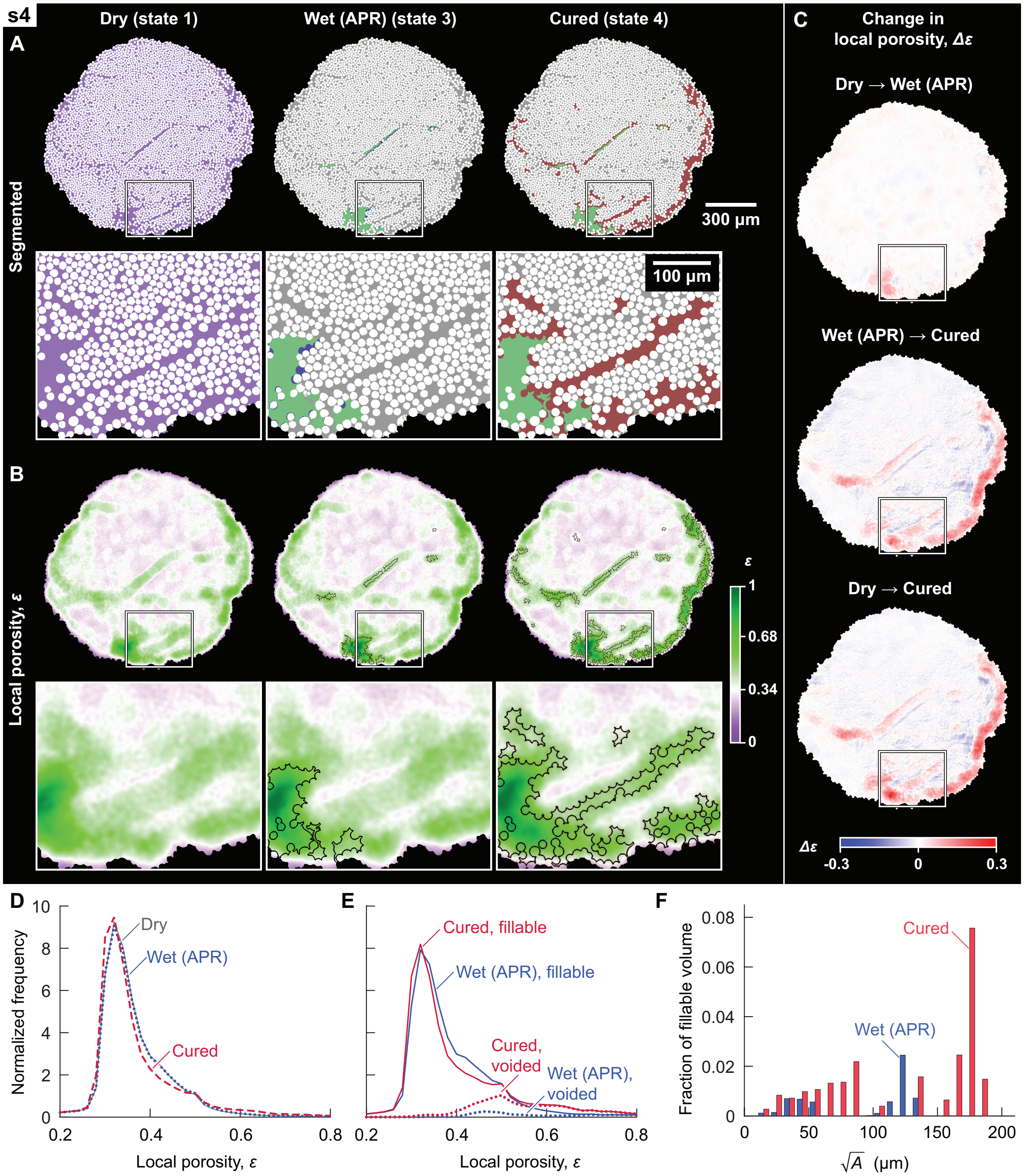

Figure 4.9: Results for specimen 4 (s4) imaged *ex-situ* in the dry state, the wet state after pressure removal (APR), and the cured state. For this specimen, $Ca_{ff} = 1.1 \times 10^{-3}$.

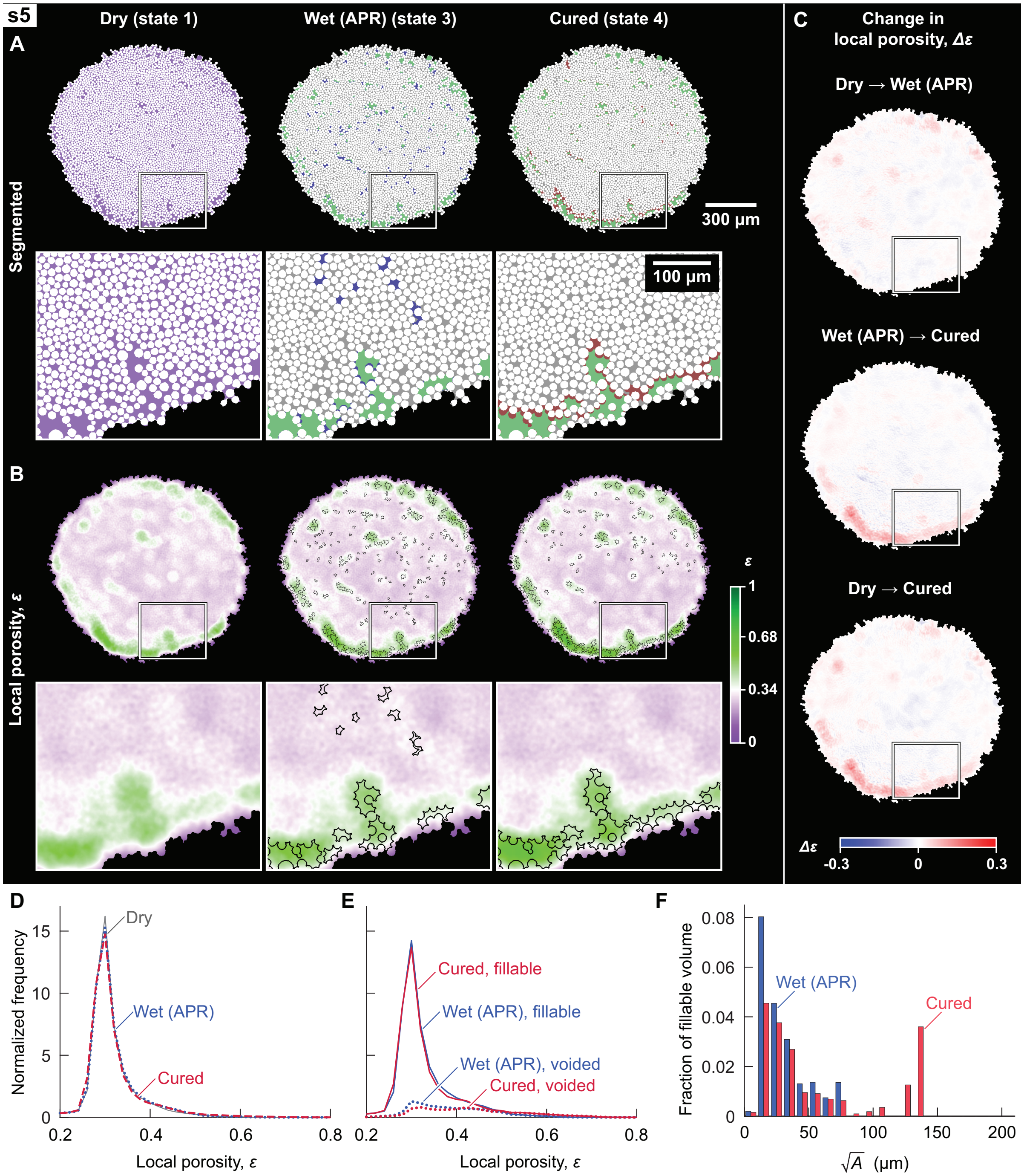

Figure 4.10: Results for specimen 5 (s5) imaged *ex-situ* in the dry state, the wet state after pressure removal (APR), and the cured state. This specimen was impregnated by capillary imbibition alone (without applied pressure) ($Ca_{ff} = 2.9 \times 10^{-5}$).

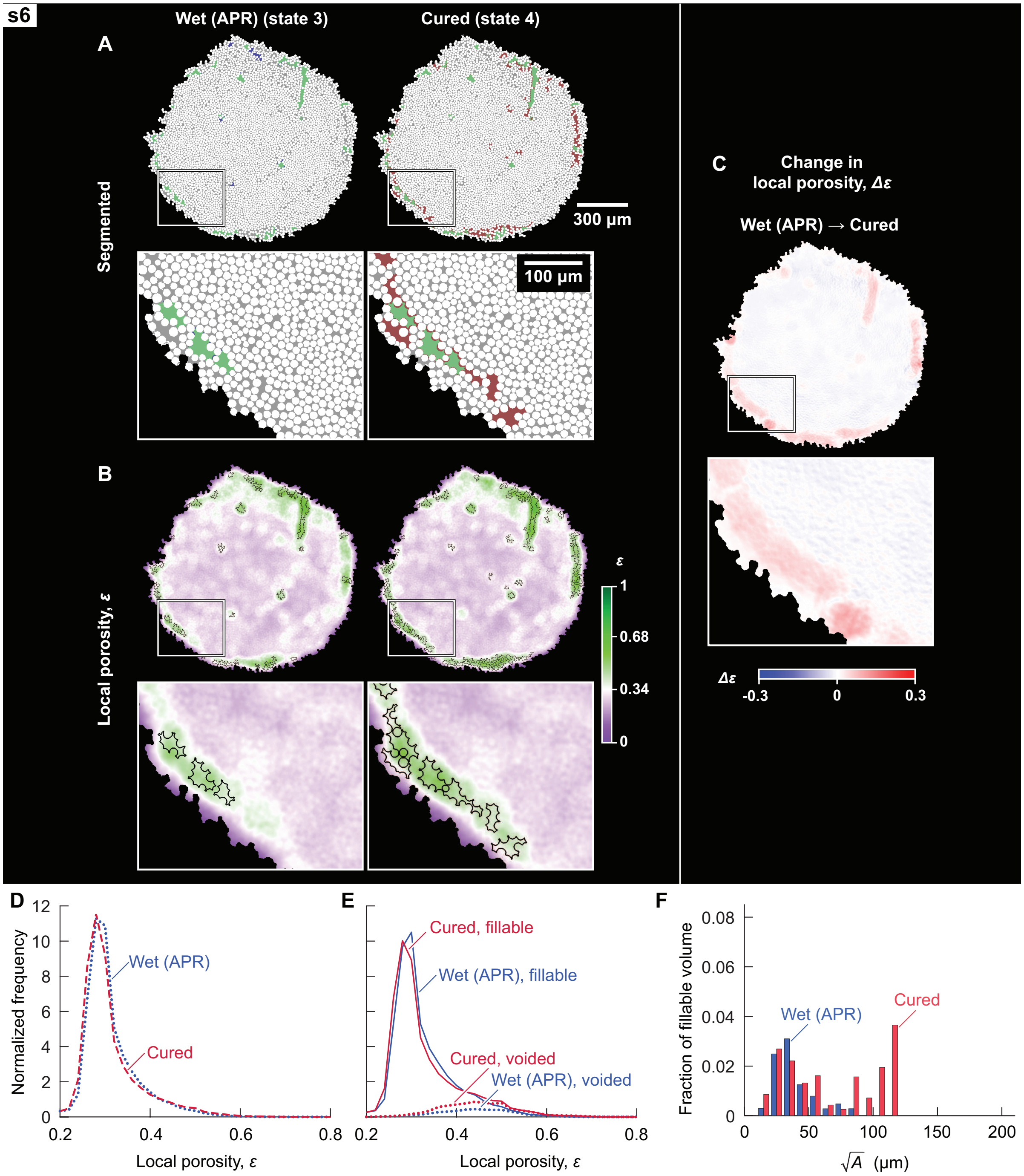

Figure 4.11: Results for specimen 6 (s6) imaged *ex-situ* in the wet state after pressure removal (APR) and the cured state. This specimen was impregnated by capillary imbibition alone (without applied pressure) ($Ca_{ff} = 9.1 \times 10^{-5}$).

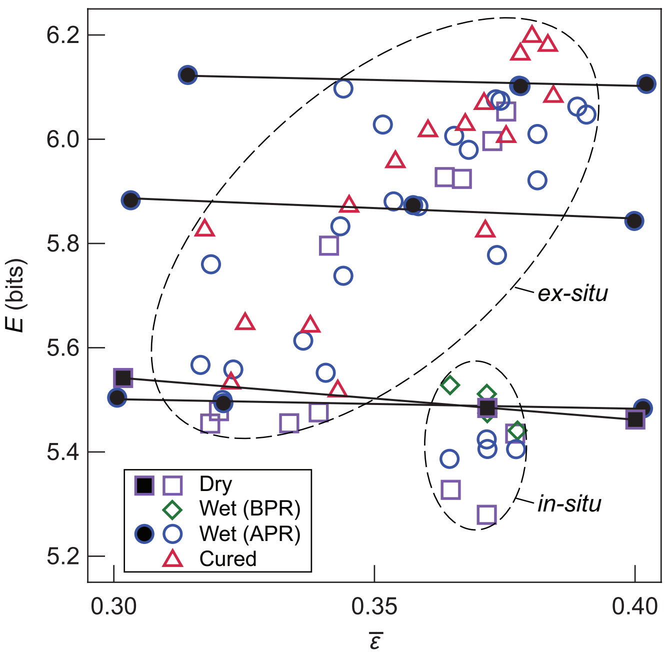

Figure 4.12: Unfilled plot markers show dependence of local porosity entropy on global porosity for all specimens in all imaged states using results from the standard segmentation procedure. For specimens imaged *ex-situ*, entropy increases approximately linearly with global porosity. Filled plot markers and corresponding black lines show the dependence of local porosity entropy on global porosity alone for four different specimens whose fibers were expanded or shrunk in the segmentation to alter the global porosity without altering fiber locations.

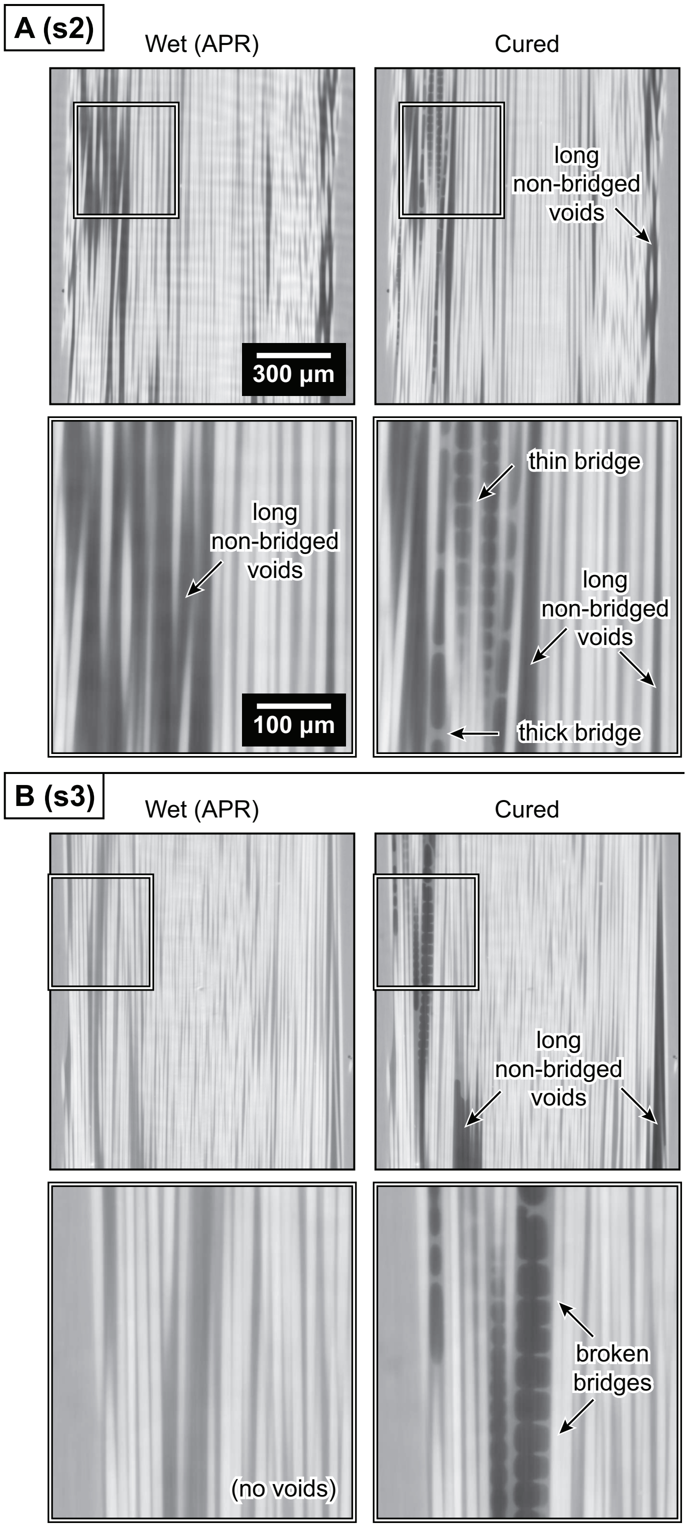

Figure 4.13: Longitudinal sections from corresponding locations within wet (APR) and cured specimens illustrate void formation and changes in void shape and size. All low-magnification images (with thin black borders) share the same scale bar and all high-magnification images (with compound black borders) share the same scale bar.

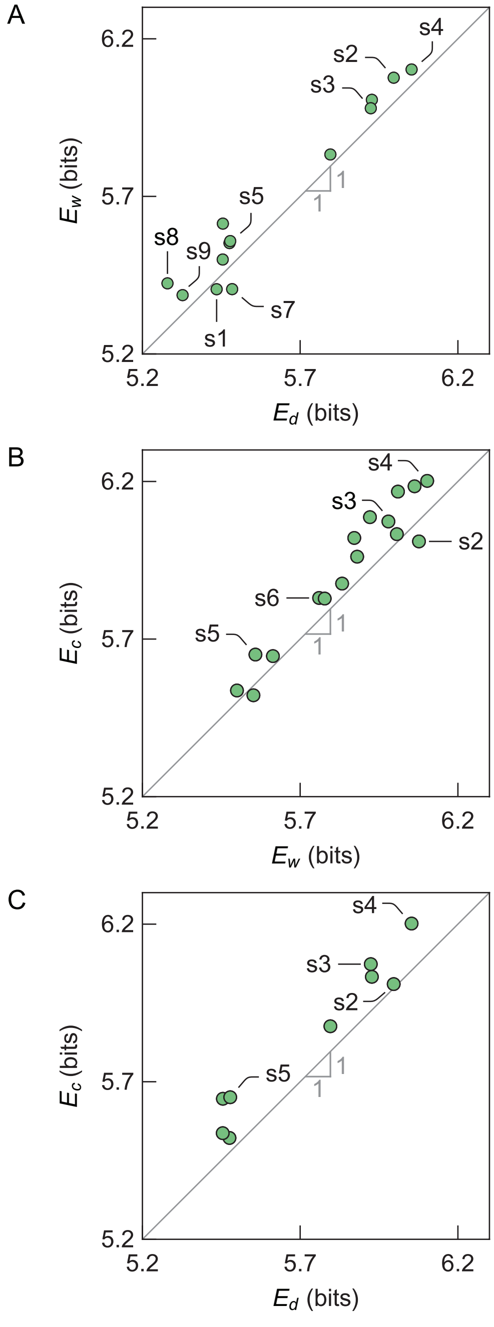

Figure 4.14: Local fiber bed porosity entropy (A) typically increases slightly from the dry state to the wet (APR) state and (B) from the wet (APR) state to the cured state, and (C) invariably increases slightly from the dry state to the cured state. Exemplary specimens s1-s6 and *in-situ* specimens (s1, s7-s9) are labeled for reference.

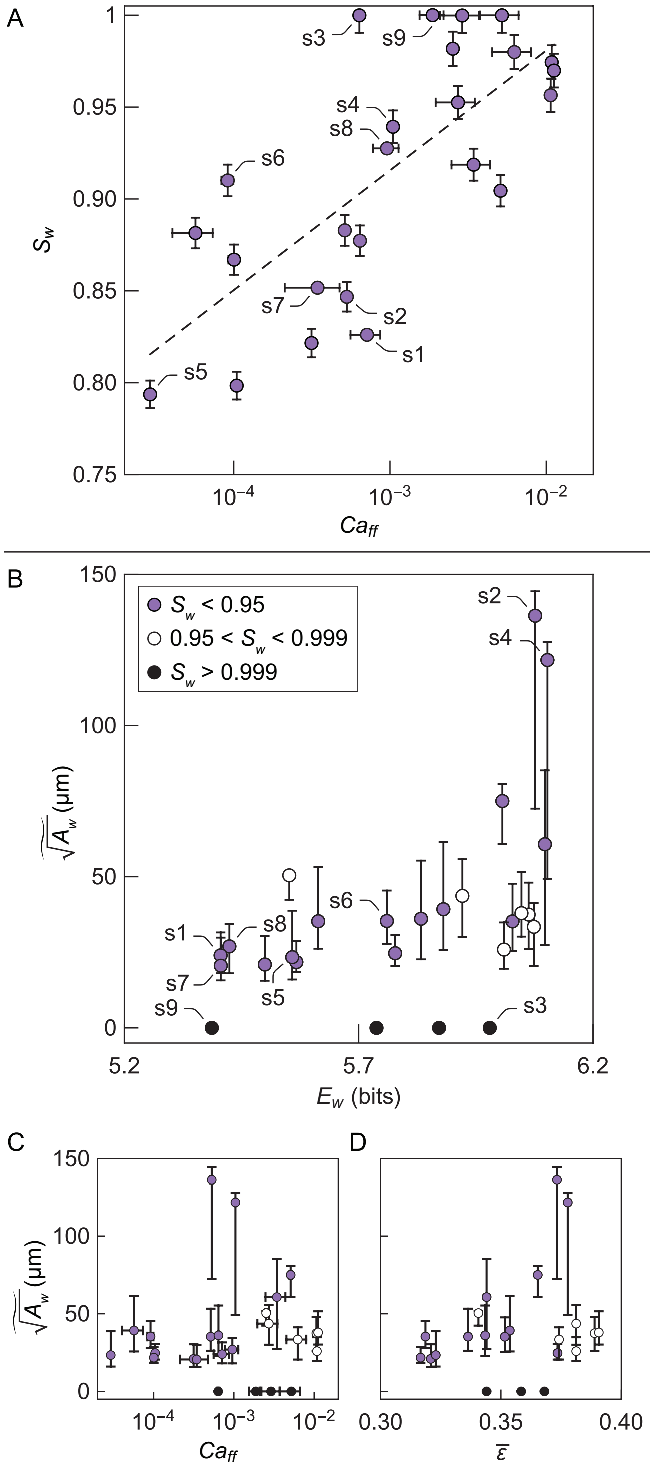

Figure 4.15: (A) Degree of saturation in wet state after pressure removal increases with instantaneous capillary number. The statistical significance of this trend was confirmed from a linear fit (dashed line) of S_w vs. $Log(Ca_{ff})$, which yields a p-value of 4×10^{-5} for the slope. (B-D) Median void size in the wet state after pressure removal, $\widetilde{\sqrt{A_w}}$, plotted against (B) local porosity entropy, (C) instantaneous capillary number, and (D) global porosity.

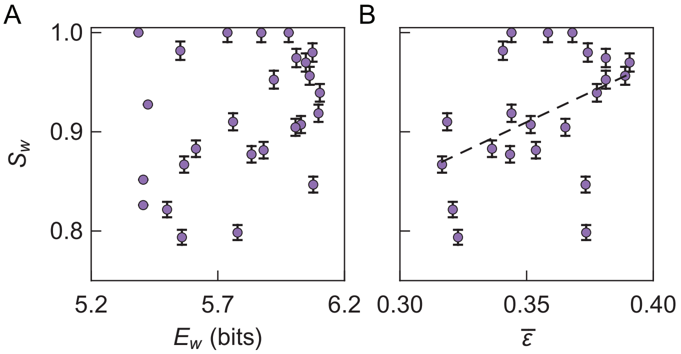

Figure 4.16: (A) Degree of saturation in the wet state after pressure removal does not show a significant dependence on local porosity entropy. (B) Global porosity shows a very weak positive correlation with S_w, with a p-value of 0.04 for the slope of the linear fit.

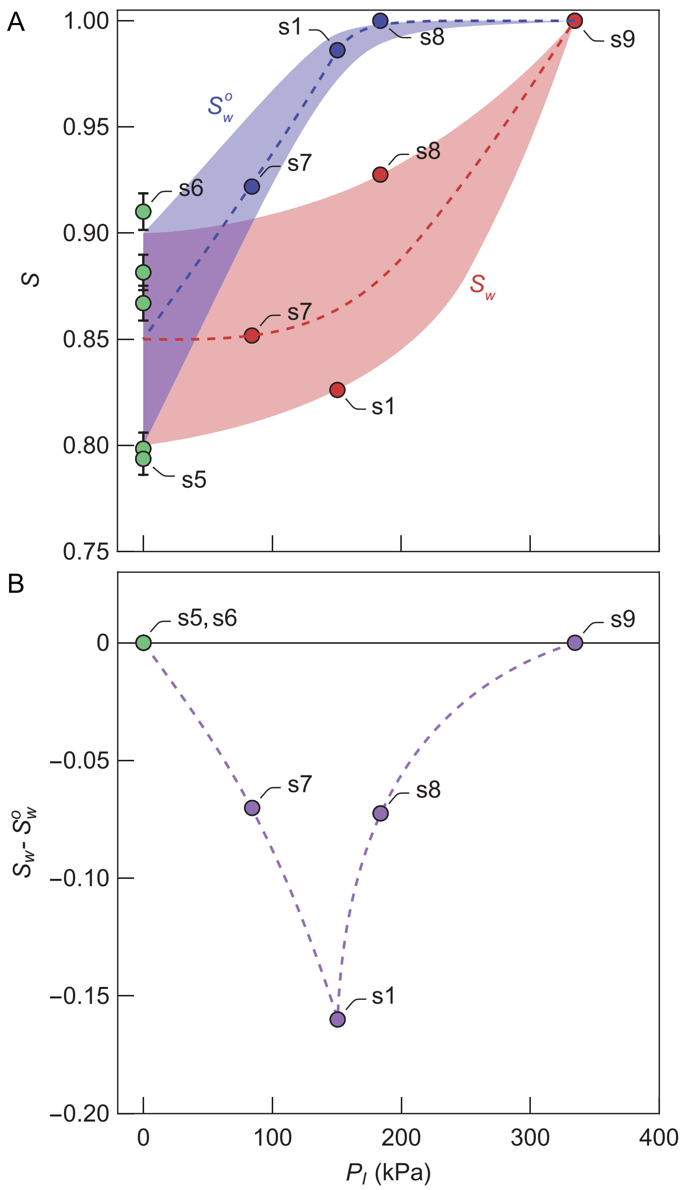

Figure 4.17: (A) Although the degree of saturation before pressure removal increases with pressure (blue), saturation is reduced following pressure removal at intermediate pressures (red). At sufficiently high pressures (over 300 kPa), complete saturation is obtained while the fluid is under pressure and is maintained following pressure removal. (B) As a result, the loss in saturation following pressure removal is greatest at an intermediate pressure, in this case 151 kPa. To provide a baseline, results for specimens impregnated by capillary imbibition alone (without applied pressure) are shown in green.

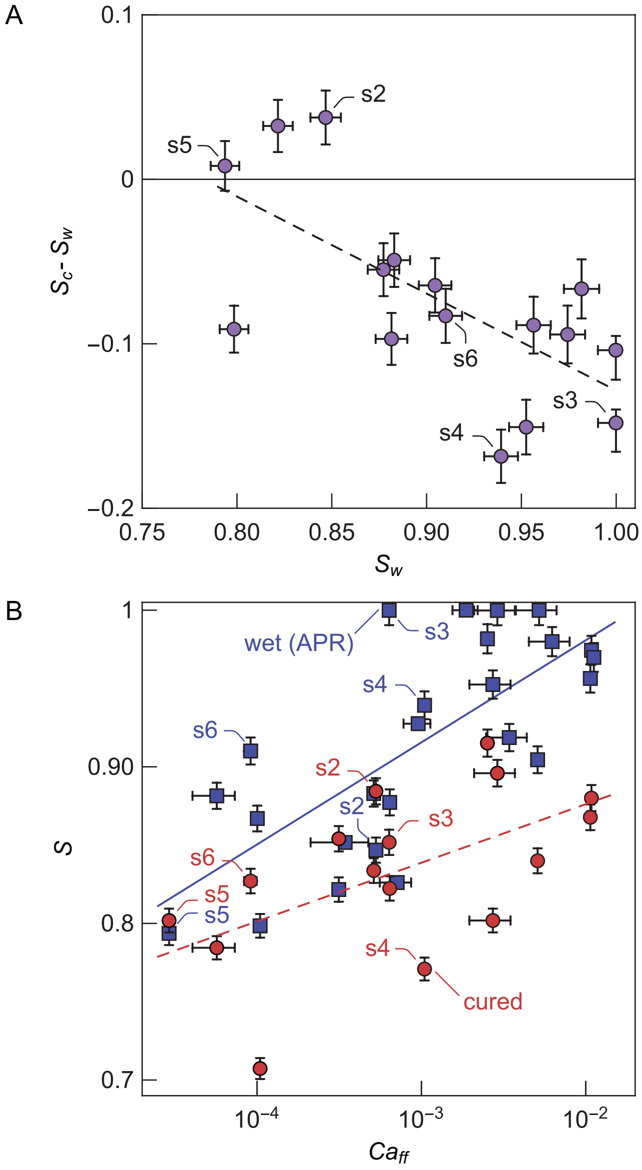

Figure 4.18: (A) Changes in saturation during curing, $S_c - S_w$, depend on the saturation before curing, S_w. The statistical significance of this trend was confirmed from a linear fit of $S_c - S_w$ vs. S_w, which yields a p-value of 4×10^{-3} for the slope. (B) The degree of saturation after curing is still greatest in cases in which the instantaneous capillary number during impregnation was high, albeit with a weaker correlation than that between S_w and Ca_{ff}. The p-value for the slope of the linear fit to S_c vs $Log(Ca_{ff})$ is 0.02.

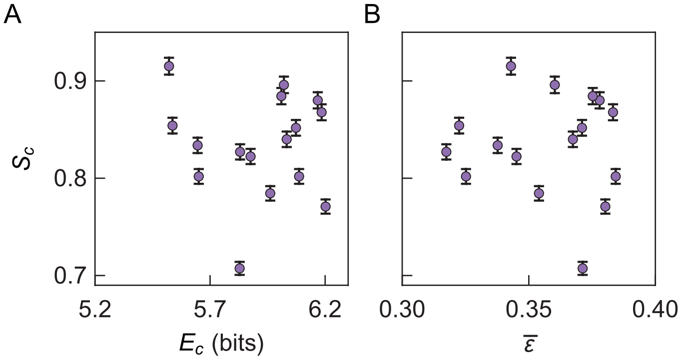

Figure 4.19: The degree of saturation after curing shows no dependence on (A) local porosity entropy or (B) global porosity. Linear fits to S_c vs. E_c and S_c vs. $\bar{\varepsilon}$ both yield p-values of 0.8 for the slopes.

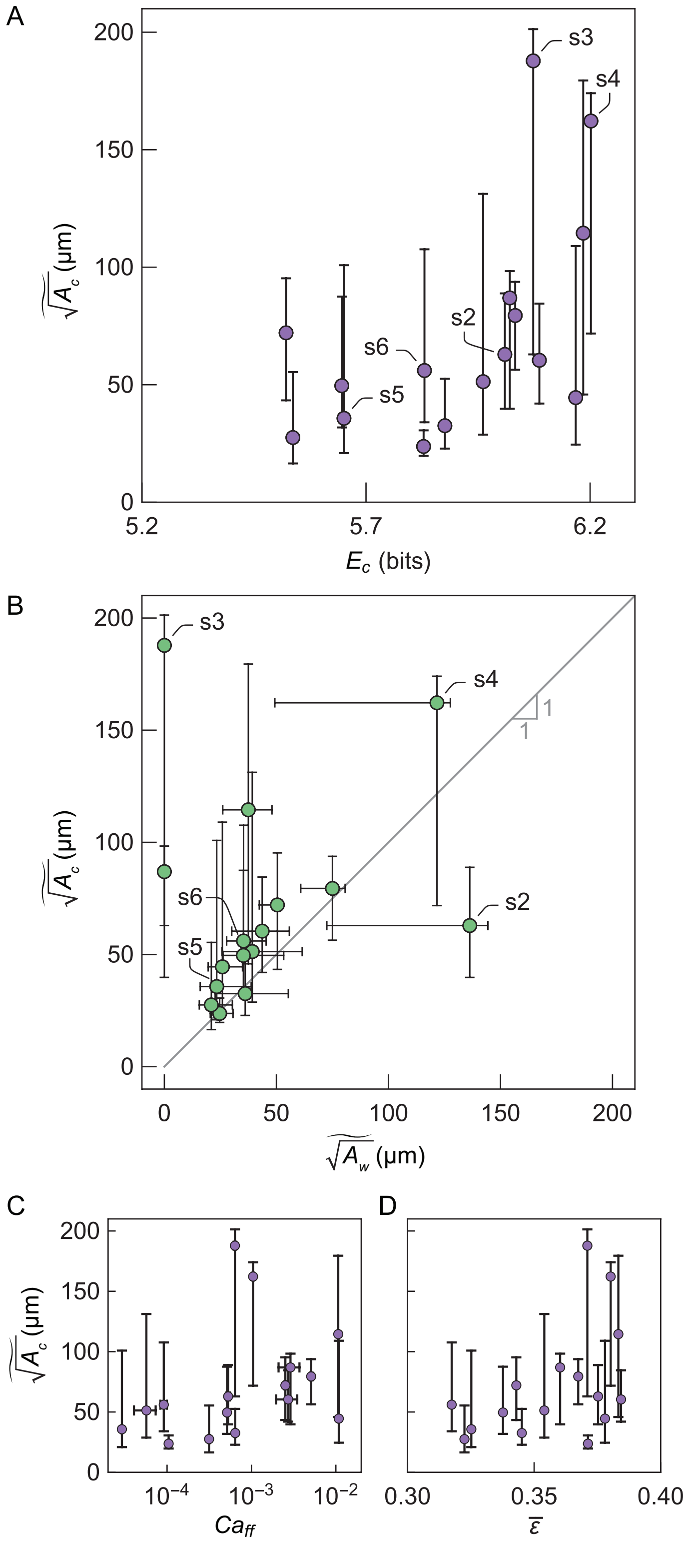

Figure 4.20: Median void size in the cured state, $\widetilde{\sqrt{A_c}}$, plotted against (A) local porosity entropy, (B) median void size in the wet state, (C) instantaneous capillary number, and (D) global porosity. Error bars on $\widetilde{\sqrt{A}}$ represent the area-weighted quartiles of the distributions of $\sqrt{A}$, as described in section 4.2.4.

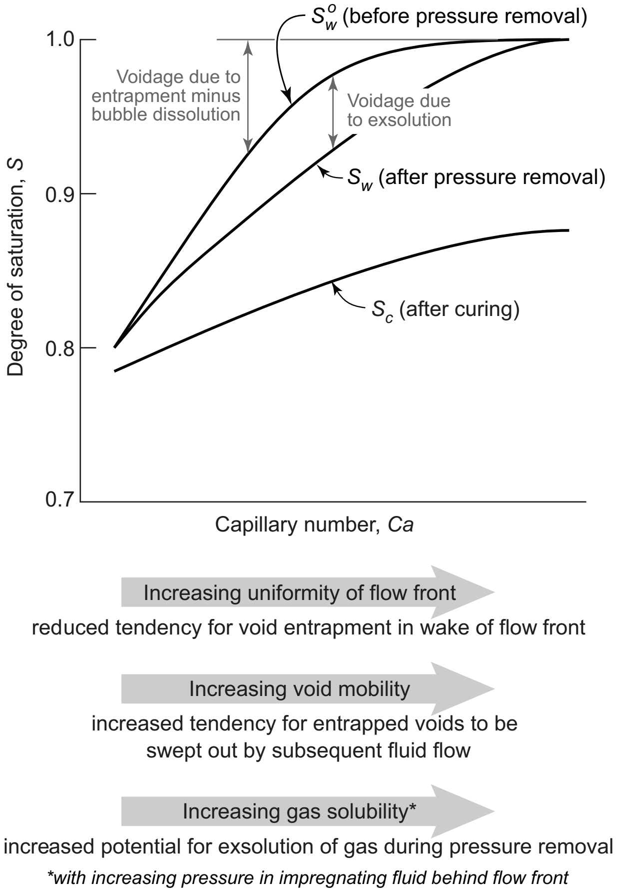

Figure 4.21: Schematic illustrating trends in saturation during processing and inferred mechanisms by which voids are introduced and removed.

Chapter 5

Microstructure Evolution During Polymer-to-Ceramic Conversion in Unidirectional Fiber Beds

Abstract

The PIP process relies crucially on the development of networks of *contiguous* cracks during pyrolysis, thereby allowing further impregnation to attain nearly-full densification. The present study employs *in-situ* x-ray computed tomography (XCT) to reveal in three dimensions the evolution of matrix structure during pyrolysis of a SiC-based preceramic polymer to 1200°C. Observations are used to guide the development of a taxonomy of crack geometries and crack structures and to identify the temporal sequence of their formation. A quantitative analysis is employed to characterize effects of local microstructural dimensions on the conditions required to form cracks of various types. Complementary measurements of gas evolution and mass loss of the preceramic polymer during pyrolysis as well as changes in mass density and Young's modulus provide context for the physical changes revealed by XCT. The findings pro-

vide a foundation for future development of physics-based models to guide composite fabrication processes[1].

5.1 Introduction

Preceramic polymers are used to produce CMCs through repeated polymer impregnation and pyrolysis (PIP) in fiber preforms [2, 3, 5, 11, 13, 14, 24]. Due to mass loss from gas evolution and a significant increase in mass density during pyrolysis, large shrinkage strains ensue. When shrinkage is constrained – as it is within the confines of a continuous fiber array – it is accommodated at least in part by formation of pyrolysis cracks. Importantly, to ensure complete impregnation of the void spaces in subsequent process cycles, the conversion process must ideally yield a matrix structure comprising a *contiguous* network of pyrolysis cracks. In some variants of the process, the final pyrolysis treatment may be followed by either melt or chemical vapor infiltration to produce SiC or other refractory Si-based compounds within the remaining void spaces. Here again a contiguous network of ingress pathways must be present after the final pyrolysis treatment in order to attain nearly-full densification during subsequent processing steps.

X-ray computed tomography (XCT) has been used previously to non-destructively characterize the 3D microstructure of SiC-based CMCs [86, 87]. Recent advancements in XCT instrumentation have enabled *in-situ* four-dimensional (3D+time) imaging of materials under load in controlled environments at very high temperatures [5, 88]. The current study demonstrates the use of XCT to observe microstructure evolution *in-situ* during material *processing* at high temperatures.

The study focuses specifically on the evolution of composite microstructure during

---

[1] The content of this chapter has previously appeared in Acta Materialia (**Natalie M. Larson**, Frank W. Zok. "In-situ 3D visualization of composite microstructure during polymer-to-ceramic conversion". *Acta Materialia* **144**, 579-589 (2018)) [23]. It is reproduced here with the permission of Elsevier.

pyrolysis of a SiC-based preceramic polymer contained within a bed of unidirectionally aligned SiC fibers. Intricate details of the three-dimensional nature of crack structures (each consisting of multiple individual cracks) and their evolution are obtained by *in-situ* x-ray computed tomography (XCT) during heating up to 1200°C. Examinations of over 140 crack structures are used to guide the development of a unified taxonomy of crack geometries and crack structures and to identify the temporal sequence of their formation. Crucially, the 3D nature of the observations enables insights into crack structures that would otherwise not be possible through, for example, *ex-situ* observations of specimens from interrupted tests or by 2D imaging alone. Effects of temperature and local geometry on the formation of various crack types are characterized. This work represents the first step in understanding crack evolution during the conversion process and sets the foundation for development of physics-based models to guide future composite fabrication processes.

5.2 Materials and Methods

5.2.1 Composite design and fabrication

In-situ XCT was conducted during pyrolysis of a composite specimen made with state-of-the-art fibers and a preceramic polymer. The composite specimen was fabricated by first inserting nine tows ($\approx$ 4500 fibers) of BN-coated Hi-Nicalon™ Type-S SiC fibers into a quartz tube with a 1.5mm inner diameter (VitroTubes™). The interstices between the fibers were filled with allylhydridopolycarbosilane (AHPCS) (SMP-10, Starfire® Systems), which yields SiC following pyrolysis above 850°C. Prior to impregnation, the AHPCS was mixed with 0.2 wt% dicumyl peroxide (DP) initiator to promote subsequent curing. The preceramic polymer was introduced into the composite via pressure-assisted impregnation. First, the fiber-filled quartz tube and a cup of liquid AHPCS were placed into a vacuum chamber and the chamber was evacuated. The AHPCS was then poured over the tube, fully submerging the specimen in the liquid. Next, the chamber was brought back up to atmospheric pressure. The submerged specimen was then transferred to a pressure chamber and the chamber was pressurized to 275 kPa using compressed air. The entire chamber (with the specimen) was placed in an oven at 120°C for two hours, during which the AHPCS was lightly pre-cured.

5.2.2 *In-situ* x-ray computed tomography

XCT was performed at the hard X-ray beamline 8.3.2 at the Advanced Light Source at Lawrence Berkeley National Laboratory. The specimen was imaged inside a high-temperature testing rig [5, 88]. Heating was accomplished with a hexapole arrangement of halogen lamps. The test specimen was mounted vertically in the testing rig in water-cooled grips. An inert environment was maintained by flowing argon through the chamber at a rate of $20g/h$. The testing rig was mounted on a rotation stage, and supply lines for argon gas, cooling water, and lamp power were carefully arranged to ensure negligible rig vibration during rotation. Specimen temperatures during pyrolysis were obtained from offline calibration experiments with an identical specimen containing an embedded R-type platinum-rhodium thermocouple, positioned in the center of the hot zone inside of the testing rig. With a calibrated temperature vs. lamp power relationship, a lamp power vs. time program was generated and used to produce the desired heating cycle for the pyrolysis experiments performed in the beamline. Over the course of about 20 hours, the specimen was heated to 1200°C according to the temperature profile shown in Figure 5.1(A) (25°C to 250°C at 2°C/min, 250°C to 700°C at 1°C/min, 700°C to 930°C at 3°C/min, 930°C hold 70min, 930°C to 1090°C at 3°C/min, 1090°C hold 70min, 1090°C to 1200°C at 2°C/min, 1200°C hold 70min, cool at -5°C/min. This profile is similar to that recommended by Starfire® Systems [31]; slight differences are due to limitations in calibration precision and temperature control).

XCT images were collected continuously during the entire pyrolysis cycle, with each complete scan taking about 12 minutes. The reported scan temperatures are the averages of those at the beginning and at the end of each scan. Each scan consisted of 4096 radiographs of $40ms$ exposure time, over a 180° rotation. Filtered white light was used for illumination. The light was passed through a $6mm$-thick aluminum filter to reduce the heat load on the scintillator. The specimen-to-detector distance was approximately $110mm$. Radiographs were collected with a pco.dimax camera. The field of view was approximately $2mm$ by $2mm$ by $2mm$. The resulting 3D tomograms have a spatial resolution of $0.98\mu m$ per voxel edge, which is sufficient to resolve the SiC fibers (each approximately $13\mu m$ in diameter) and the pyrolysis cracks within the matrix.

Tomographic slices were reconstructed using a commercial reconstruction algorithm (Octopus v8; IIC UGent, Zwijnaarde). The data were analyzed manually using ImageJ (Rasband, W.S., ImageJ, U. S. National Institutes of Health, Bethesda, Maryland, USA, http:// imagej.nih.gov/ij/, 1997-2016), and 3D visualizations were segmented manually and rendered in Avizo® version 9.2.0 (FEI Visualization Sciences Group). Crack initiation is characterized by the temperature at which the first signs of the crack are evident.

5.2.3 Characterization of polymer-to-ceramic conversion

During pyrolysis, AHPCS undergoes significant changes in physical, chemical, and mechanical properties [18, 20, 21, 89–92]. The conversion process includes crosslinking between about 100 and 650°C, ceramization between about 850 and 1100°C, and crystallization between about 1150 and 1650°C (Starfire® Systems documentation [31] and [18, 20, 21]). The polymer-to-ceramic conversion is accompanied by gas evolution and associated mass loss, an increase in mass density and corresponding volume reduction, and an increase in stiffness. The changes were characterized in the following ways.

Thermogravimetric analysis and mass spectrometry

Thermogravimetric analysis and mass spectrometry (TGMS) were performed on a neat specimen of AHPCS + 0.2wt% DP that had been pre-cured at 120°C for 2h in argon. The tests were performed at NETZSCH Instruments North America, LLC (Burlington, MA) with a STA 449 *F1 Jupiter*® thermogravimetric analyzer with an Oxygen Trap System (OTS®) coupled to a QMS 403 *Aëolos*® quadrupole mass spectrometer. The tests were run under flowing argon with a heating rate of 1.4$°C/min$ from room temperature to 1550°C. A constant heating rate was used to eliminate artifacts in the mass spectrometry data that would result from isothermal holds and changes in heating rate.

Mass density

Density measurements were performed at room temperature (21°C) on powders prepared from pellets of AHPCS + 0.2wt% DP. The pellets had been pre-cured in air at 120°C for 2h followed by interrupted pyrolysis treatments in argon to various temperatures (temperature profile: 25°C to 250°C at 2°C/min, 250°C to 650°C at 1°C/min, 650°C to 850°C at 3°C/min, 850°C hold 60min, 850°C to 1000°C at 3°C/min, 1000°C hold 60min, 1000°C to 1200°C at 3°C/min, 1200°C hold 60min, cool at -5°C/min, as recommended by Starfire® Systems [31]). The measurements reported for room temperature (21°C) are those of powders after pre-curing. The measurements reported for 375-1200°C are those of powders following pyrolysis to the designated temperature.

The density, ρ, was determined via mass measurements using an analytical scale and volume measurements using a Quantachrome Ultrapyc™ 1200e (Boynton Beach, Florida) pycnometer. The coefficients of variation of the measured densities at each temperature were $\leq$ 0.7%. The volumetric yield was estimated as $(m/m_0)/(\rho/\rho_0)$, where m is mass, m_0 is initial mass at room temperature, and ρ_0 is density at room temperature.

Young's modulus

The Young's modulus of pellets of AHPCS + 0.2wt% DP were measured at room temperature (21°C) by nanoindentation. The pellets had been pre-cured in air at 120°C for 2h followed by interrupted pyrolysis treatments in argon to various temperatures (temperature profile: 25°C to 250°C at 2°C/min, 250°C to 650°C at 1°C/min, 650°C to 850°C at 3°C/min, 850°C hold 60min, 850°C to 1200°C at 2°C/min, 1200°C hold 60min, cool at -5°C/min, as recommended by Starfire® Systems [31]). The measurements reported for room temperature (21°C) are those of pellets after pre-curing. The measurements reported for 375-1200°C are those of pellets following pyrolysis to the designated temperature.

Nanoindentation was performed with a Hysitron TriboIndenter® using a Berkovich tip for indentation and fused quartz for tip-shape calibration. The Young's modulus was calculated from the unloading curves following standard protocols [93]. The coefficients of variation of the measured moduli at each temperature were $< 6\%$.

5.3 Results and discussion

5.3.1 Polymer-to-ceramic conversion

The evolution of physical, chemical, and mechanical properties for the polymer-to-ceramic conversion is summarized in Figures 5.1(B-F). The TGMS results show a 21.5% mass loss caused by liberation of hydrogen ($m/z = 2$), methane ($m/z = 16$), and silanes (silane, methylsilane, dimethylsilane, trimethylsilane, and tetramethylsilane, with $m/z =$ 29, 30, 31, 43, 44, 45, 58, 59, 73). Furthermore, the combination of mass loss and density increase (from about 1.0 to 2.5 g/cm^3) results in a volumetric yield of 32% upon completion of pyrolysis. As a result of these changes, the Young's modulus increases by over three orders of magnitude, from 0.0234 ± 0.0005 GPa after pre-curing to 153 ± 7 GPa after heating to 1200°C. Most of the changes occur over the temperature range of 200 to 800°C. These results provide context for the physical changes revealed by XCT images of the composite specimen.

5.3.2 *In-situ* x-ray computed tomography

XCT images in Figures 5.2-5.5 show the progression of crack formation with increasing temperature. Figure 5.2 shows three 3D images of the same location at various stages of pyrolysis. The image after complete pyrolysis was taken at room temperature, after cooling from 1200°C. The cracks are the least absorbing features and are rendered transparent while the fibers, being most absorbing, are rendered light yellow. Meanwhile, as the matrix material converts from AHPCS to SiC, it becomes more highly absorbing (red to orange to yellow color scheme in Figure 5.2), nearly matching that of the fibers after complete pyrolysis. In the rendering of the CMC after complete pyrolysis (Figure 5.2(C)), the fibers bounding the crack planes can be seen behind the remaining cracked pieces of matrix material. The first cracks to form are evident at about 200°C. New cracks continue to form at temperatures as high as 700°C. Unsurprisingly, this temperature range corresponds to that of the most significant gas evolution, mass loss, and volume reduction. Throughout this process and at higher temperatures, the opening displacements of existing cracks progressively increase, a result of continued matrix evolution and constraints imposed by the fibers.

In the following discussion, crack geometries and crack evolution are discussed in the context of *local matrix regions* bounded by surrounding fibers. Because the fibers are nearly parallel with only gradual variations in their lateral spacing along the length of the composite, the size of the matrix region containing cracks is characterized by $\sqrt{A_n}$ where A_n is the cross-sectional area of that region measured normal to the fiber direction.

The focus here is on regions in which impregnation of the preceramic polymer between fibers was complete. (Although occasional mesoscale defects such as bubbles and long ($> 500\mu m$) longitudinal cracks were observed, the cracks around them are not considered here.) The results are based on exhaustive examinations and measurements of more than 140 crack structures.

5.3.3 Geometry, taxonomy and temporal sequence of pyrolysis cracks

Several prototypical crack types and evolution sequences are obtained. The first crack to form in a particular local matrix region is referred to as the *primary* crack. Other cracks can form in the same region as the matrix continues to evolve; these are referred to as *secondary*, *tertiary*, and *quaternary* cracks, dictated by the *temporal sequence*. The concatenation of connected cracks within a local matrix region at the completion of pyrolysis is referred to as a *crack structure*. Primary cracks are one of two broad types. The first comprises *alternating* (**A**) and *wavy* (**W**) cracks, collectively designated **A/W** (Figures 5.3(A), 5.4(A), and 5.6(A)). The cracks form rapidly (within a single XCT scan), and thus their temporal evolution is not directly observed. However, based on geometric analyses and reports of similar crack geometries in adhesive joints [62, 65, 68], we infer that both crack types *initiate* from putative interfacial cracks and grow nominally parallel to the fibers.

Alternating cracks of similar geometry have been observed previously in adhesive joints and other layered structures and have been analyzed using established fracture mechanics principles [65, 68]. We thus infer that these cracks extend through a repeating process in which an interfacial crack propagates to a critical length, kinks into the matrix at a shallow angle, follows a curved trajectory across the local matrix region, and deflects at the fiber-matrix interface on the opposite side of this region to form another interfacial crack (Figure 5.3(A), Figure 5.6(A)). Because of the characteristic angles at which alternating cracks emanate from one interface and deflect into another, the direction of propagation can be readily inferred from crack shape (*e.g.* vertical red arrow in Figures 5.3(A)(i) and 5.6(A)). The 3D crack surfaces form an occasionally kinked ribbon with the edges of the ribbon cupped inward toward the matrix region (the cupped feature is not observed in 2D adhesive joint geometries [65, 68]).

Wavy cracks have also been observed previously in adhesive joints [62]. Because the wavy cracks observed here do not begin or end in the middle of local matrix regions, we infer that they initiate similarly from putative interfacial cracks. In contrast to alternating cracks, wavy cracks exhibit a smooth (nearly sinusoidal) shape (Figures 5.4(A), 5.6(A)). Occasionally they contact the bounding fibers tangentially at their peaks and troughs. The 3D crack surfaces form smooth wavy ribbons with inwardly-cupped edges (Figure 5.4(A)).

The nature of alternating and wavy cracks cannot be ascertained from 2D sections alone. For example, when viewed within some longitudinal sections, alternating cracks can appear to be wavy in nature (seemingly without the kinked features); in other sections, they can appear to be periodically spaced cracks perpendicular to the fibers (Figure 5.3(A)(vii)). Only 3D imaging provides conclusive evidence of their true geometry.

Although both alternating and wavy cracks are observed, alternating cracks appear to be more common; about 75% of 91 cracks analyzed in the alternating/wavy family show a purely alternating geometry. However, alternating and wavy cracks are not always entirely distinct from one another; one type can morph into the other as the crack grows. For example, a crack can grow in an alternating fashion for some distance and then grow further in a wavy fashion, and vice versa. Because of the similarities in their geometric characteristics, the two crack types are grouped as one, alternating/wavy (**A/W**), in subsequent discussion.

In the second category, primary cracks are, for the most part, nearly perpendicular to the surrounding fibers. The edges of these cracks are bounded by a wall of nearly-touching fibers (Figures 5.5(A,E) and 5.6(B)). These are named *perimural* (**P**) cracks. (The term stems from the Greek root *peri*, meaning around, and the Latin root *mur*, meaning wall.)

Most perimural cracks appear to be preceded by and emanate from one end of a small interfacial crack. The cracks kink into the matrix and grow predominantly perpendicular to the fibers. Similarly to the **A/W** cracks, primary crack formation occurs rapidly (within a single XCT scan). Figure 5.5(A) shows an example in which two parallel perimural cracks were spawned by two ends of a single thin interfacial crack; a 2D section revealing the interfacial crack is shown in Figure 5.7. Among 51 sets of perimural cracks examined, about 80% show clear evidence of originating at a fiber-matrix interface. Indeed, among the perimural cracks with evident interfacial cracks, each was connected to only *one* interfacial crack in the early stages after formation. From this observation we infer that the interfacial cracks precede and nucleate the perimural cracks, not vice versa. (Otherwise, if perimural cracks were to nucleate within the matrix and then kink into the interface, at least some of these cracks would be expected to kink at two or more locations.) This nucleation process is similar to that associated with alternating cracks. In some sense perimural cracks formed this way can be viewed as incipient alternating cracks that failed to grow past the first half-wavelength. It is important to note that, because of the localized nature of the putative interfacial cracks that spawn the (typically much larger) perimural cracks, 2D cross-sections (*e.g.* Figure 5.5(F-I)) rarely reveal the presence of the initiating crack, leading to the false conclusion that most perimural cracks nucleate homogeneously within the central regions of the matrix pockets.

Additional cracks often form within matrix regions containing primary cracks. Their geometry and temporal sequence depend on the primary crack type.

For alternating/wavy primary cracks, secondary and tertiary cracks may be of two types: (i) interfacial (**I**) cracks, which form and propagate along fibers still attached to the matrix; and (ii) cracks perpendicular to the fibers, bounded partially by fibers and partially by another crack surface (in this case, the alternating/wavy crack surface, and possibly an interfacial crack surface). The latter are referred to as semi-perimural (**SP**) cracks. Similarly to perimural cracks, semi-perimural cracks may also be spawned from putative interfacial cracks. The potential temporal sequences of these secondary and tertiary cracks are summarized in Figure 5.6(C); examples are shown in Figure 5.3, as well as Figures 5.4 and 5.6(A). Each crack type labeled in Figures 5.3-5.6 (*e.g.*, **P**, **A/W**, and **I**) forms independently as a unique event, with purely interfacial (**I**) cracks distinct from the interfacial cracks included within the **P** and **A/W** crack geometries.

In addition to the preceding crack taxonomy based on temporal sequence (*e.g.*, primary - quaternary), we define the *final hierarchical order* (FHO) as the *number of unique crack types* within a crack structure in a local matrix region after completion of pyrolysis. For example, the crack sequence in Figure 5.3 begins with a primary alternating crack followed by secondary semi-perimural cracks and tertiary interfacial cracks. The crack structure is characterized by its FHO (3) and the primary crack type, together denoted **3A/W**. Figure 5.4, on the other hand, shows a primary wavy crack with secondary semi-perimural cracks in some segments and secondary interfacial cracks in others; these are **W-SP** and **W-I** cracks. Both are crack structures with FHO of 2 in the alternating/wavy family, abbreviated as **2A/W**.

Following formation of perimural primary cracks, two types of secondary cracks may form: (i) straight longitudinal (**L**) cracks, oriented approximately parallel to the fibers, within the matrix between two perimural cracks (Figures 5.5(B,G) and 5.6(B));

and (ii) interfacial (**I**) cracks between the fibers and the remaining matrix. These may be followed by tertiary/quaternary interfacial (**I**) and semi-perimural (**SP**) cracks (Figure 5.5(B-D)). The semi-perimural cracks are bounded partially by the fibers and partially by a longitudinal crack and/or an interfacial crack. The potential temporal sequences are summarized in Figure 5.6(C); examples are shown in Figures 5.5 and Figure 5.6(B). Final crack structures in the perimural family may be composed of perimural, longitudinal, semi-perimural, and interfacial cracks. For example, the crack structure in Figure 5.5 is a **P-L-SP-I** crack. This is a crack structure with a FHO of 4 in the perimural family, abbreviated as **4P**.

5.3.4 Initiation temperatures and characteristic length scales

With a view toward future development of a mechanistic framework to describe the spatial and temporal evolution of pyrolysis cracks, we present measurements and preliminary analyses on the effects of the size of matrix regions, characterized by $\sqrt{A_n}$, on: (i) the temperatures at which *primary* cracks initiate, T_i^p; (ii) the FHO; and (iii) the characteristic spacings, L_c, associated with the two types of primary cracks – the half-wavelength, $\lambda/2$, for alternating/wavy cracks and the longitudinal spacing, l_P, between perimural cracks.

A process flow diagram depicting the steps followed to make these measurements is illustrated in Figure 5.7[2]. In the first step, primary cracks were identified and categorized by crack type (**P**, **A**, or **W**) by scrolling through longitudinal image stacks taken at a variety of temperatures (Figure 5.7(A)). For example, the primary cracks in Figure 5.7(A) (same as those in Figures 5.5(A,F)) are identified as perimural because they are predominantly perpendicular to fibers. Each emanates from one end of an interfacial crack. The interfacial crack is identified by two key features: (1) the curved trajectory

---

[2] Although all data in the current study were collected manually, the resulting database may be used in the future to inform machine learning algorithms to automate measurements of a similar nature. Data are available upon request.

of the perimural cracks near the interface, and (2) the large opening displacement of the interfacial crack after complete pyrolysis (Figure 5.7(C)). Next, the crack initiation temperature is determined by examining image stacks taken at progressively lower temperatures until the primary crack is no longer visible (Figure 5.7(B)). In the third step, the FHO is determined by examining the same region in the image stack after complete pyrolysis (Figure 5.7(C)). For example, in Figure 5.7(C), longitudinal, semi-perimural, and interfacial cracks are identified (in addition to the primary perimural crack). Thus, the FHO for this crack structure is 4. Purely interfacial cracks are identified as those that do not kink into the matrix to form perimural, semi-perimural or alternating cracks. Such cracks can only be identified when their opening displacements are large enough to differentiate them from the fiber-matrix interface. Thus, crack initiation temperatures reported for purely interfacial cracks are only approximate. Additionally, not every interfacial crack in the local matrix regions is shown in Figures 5.3, 5.4, 5.5, and 5.7; only the minimum number of such cracks needed to determine the FHO are presented. Finally, crack areas, A_n, and characteristic spacings, L_c, were measured, as described below and illustrated in Figures 5.3-5.5.

For alternating cracks, $\lambda/2$ was measured from the start of the fiber-matrix interface crack through the end of the trans-matrix crack that kinked from the interface (Figure 5.3(A)(i,vi)). The cross-sectional area normal to the fibers, A_n, corresponds to the area traversed by the trans-matrix crack (Figure 5.3(A)(ii-v)). For wavy cracks, $\lambda/2$ was measured from the peak to the adjacent trough of the crack path (Figure 5.4(A)). Here, A_n corresponds to the area traversed by the sinusoidal crack between the peak and adjacent trough. For alternating/wavy cracks, the average cross-sectional area was measured for each half-wavelength; 530 segments from 91 distinct cracks were analyzed.

Areas of perimural cracks were measured in the way illustrated in Figure 5.5(E). Often, multiple perimural cracks formed nearly simultaneously, *i.e.* within the same

XCT scan, in the same local matrix region. Their longitudinal spacings, l_P, were measured only at this point in the pyrolysis cycle. (Additional perimural cracks can form between the initial cracks at higher temperatures and thus the reported crack spacings do *not* necessarily represent the spacings after the completion of pyrolysis.) 51 regions containing perimural cracks were analyzed.

The results are summarized in Figures 5.8 and 5.9. The results in Figure 5.8(A) show that the initiation temperatures for both types of primary cracks decrease as $\sqrt{A_n}$ increases. This trend is consistent with other cracking phenomena in thin films and sandwich layers, wherein the driving forces for cracking generally increase with the local dimensions of the cracking phase [62, 63]. Figure 5.8(A) also shows that for primary cracks that initiate at temperatures below approximately 350°C, alternating/wavy cracks tend to form in smaller matrix regions than perimural cracks. As noted earlier, most perimural cracks initiate at the fiber-matrix interface and then kink into the matrix, akin to the first half-wavelength of alternating cracks. These results suggest that continued growth of such cracks into alternating cracks (rather than termination as perimural cracks) is more favorable in smaller channels.

The crack initiation temperatures in Figure 5.8(A) are further sorted according to the FHO of the terminal crack structures and re-plotted in Figure 5.8(B) for **A/W** cracks and in Figure 5.8(C) for **P** cracks. (Information about initiation temperatures of secondary, tertiary and quaternary cracks is not contained in these figures.) The largest matrix regions typically crack first (at the lowest temperatures) and contain crack structures with higher FHO following complete pyrolysis, *e.g.* **4P** cracks, represented by orange diamonds in Figure 5.8(C). Conversely, the smallest regions are last to crack and contain crack structures with lower FHO following complete pyrolysis, *e.g.* **1P** cracks, represented by purple circles in Figure 5.8(C). We find that, for both families of primary crack, the crack initiation temperatures progressively decrease while the FHO increases with increasing $\sqrt{A_n}$. This trend is also consistent with cracking phenomena in thin films, wherein the driving forces for additional cracking between existing cracks increase with further increase of the loading and with the local dimensions of the cracking phase [62].

The characteristic spacings associated with the two types of primary cracks – $\lambda/2$ for alternating/wavy cracks and l_P for perimural cracks – follow similar scalings with $\sqrt{A_n}$ (Figure 5.9). Notably, $(\lambda/2)/\sqrt{A_n} = 2.2 \pm 0.7$ for alternating/wavy cracks and $l_P/\sqrt{A_n} = 2.1 \pm 1.0$ for perimural cracks (± are standard deviations). In sandwich structures, the ratios of the characteristic length scales to film thickness for both alternating cracks and tunneling cracks have been shown to depend on film thickness, the elastic moduli of the film and substrate, and the misfit strain, among other factors [63, 65]. Here we find that, despite significant changes in the Young's modulus of the matrix and the misfit strain, $L_c/\sqrt{A_n}$ appears to be essentially constant, independent of T_i^p and $\sqrt{A_n}$ for both alternating/wavy and perimural cracks.

5.4 Conclusions and outlook

In-situ x-ray computed tomography has been used to ascertain the nature of crack structures and their evolution during pyrolysis of a SiC-based preceramic polymer contained within a unidirectional fiber bed. Importantly, the true character of these cracks can only be definitively identified with 3D imaging; 2D images can readily lead to false impressions of crack nucleation locations and of crack geometry and topology. Examinations of a large number of such cracks have guided the development of a unified taxonomy of crack geometries and crack structures and revealed the temporal sequences of their formation. Primary cracks appear to nucleate almost exclusively from putative interfacial flaws and evolve in one of two ways: either through the formation of alternating/wavy cracks or perimural cracks. The observations further suggest that the primary crack types and their formation are not entirely distinct; perimural cracks appear to form analogously to the first half-wavelength of alternating cracks. As pyrolysis continues, secondary, tertiary and quaternary cracks also form.

The primary crack initiation temperature decreases and the final hierarchical order increases with increasing size of the local matrix region. For primary cracks that initiate below approximately 350°C, alternating cracks form in preference to perimural cracks within the smaller channels. Furthermore, the characteristic crack spacings – longitudinal spacing between perimural cracks and half-wavelengths of alternating/wavy cracks – are approximately proportional to the size of the regions in which these cracks are contained.

The findings reported here provide a framework for describing crack networks that result from a single impregnation and pyrolysis cycle and that, in practice, will ultimately need to be re-impregnated. Simple imbibition models using the crack geometries identified here may streamline the optimization of subsequent impregnation cycles or be used to identify optimal target shrinkage crack geometries. Furthermore, the present observations provide a foundation for development of a mechanics framework to describe pyrolysis cracking within fiber beds. These findings may simplify efforts to optimize and tailor crack formation, perhaps via altering the pyrolysis thermal cycle or more precisely tailoring the fiber packing characteristics.

Development of a mechanics framework will require measurements of additional inputs, including the driving forces for cracking (*e.g.* local shrinkage strains) as well as changes in matrix toughness and interfacial properties over the course of pyrolysis. Furthermore, descriptors of crack topology (*e.g.* connectivity) and channel dimensions may provide insights into the limits of densification that can be attained with this processing route.

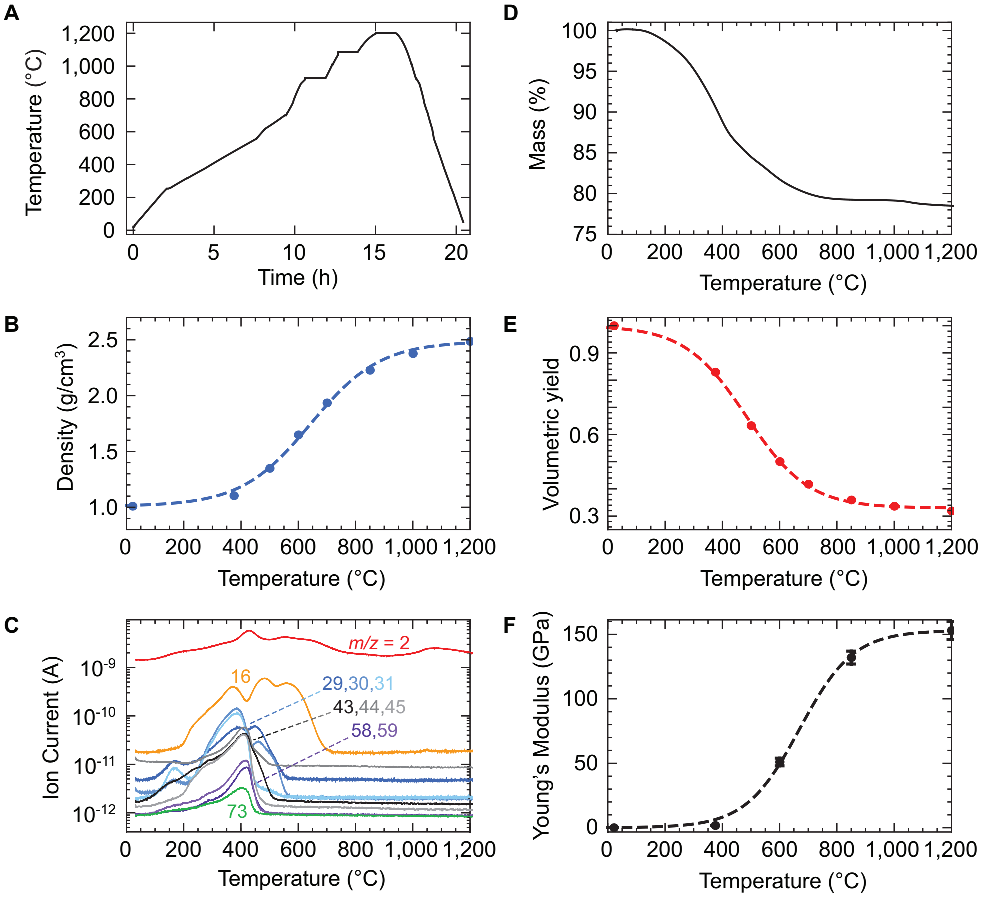

Figure 5.1: Characterization of polymer-to-ceramic conversion. (A) Temperature profile for pyrolysis experiment performed *in-situ* in the beamline. (B) Changes in mass density of the preceramic polymer alone. (C) Mass spectrometry results labeled with m/z values. Also shown are changes in (D) mass, (E) volumetric yield, and (F) Young's modulus. (Error bars in (F) are standard deviations.) Curves in (B,E,F) are hyperbolic tangent fits to the experimental data.

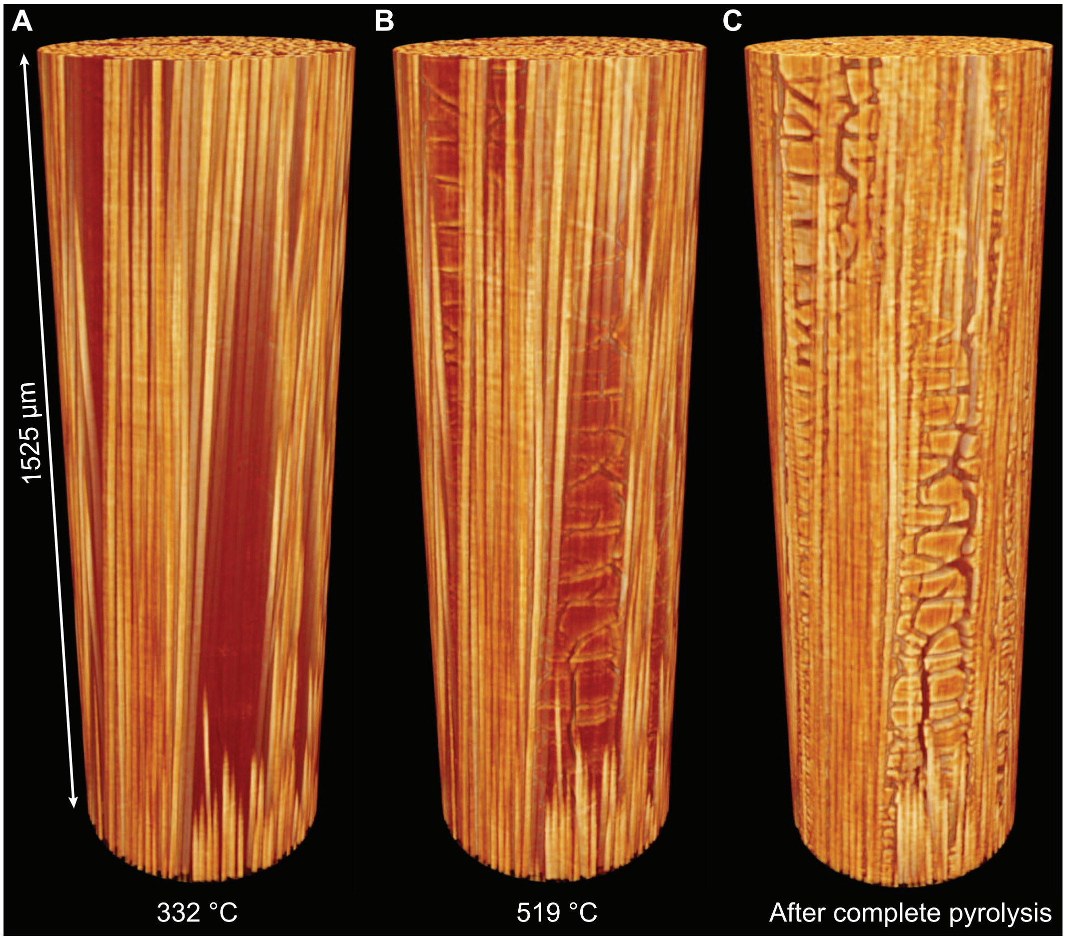

Figure 5.2: Three-dimensional volume renderings of a select region of the composite during pyrolysis. Images obtained (A) at 332°C, (B) at 519°C, and (C) after complete pyrolysis.

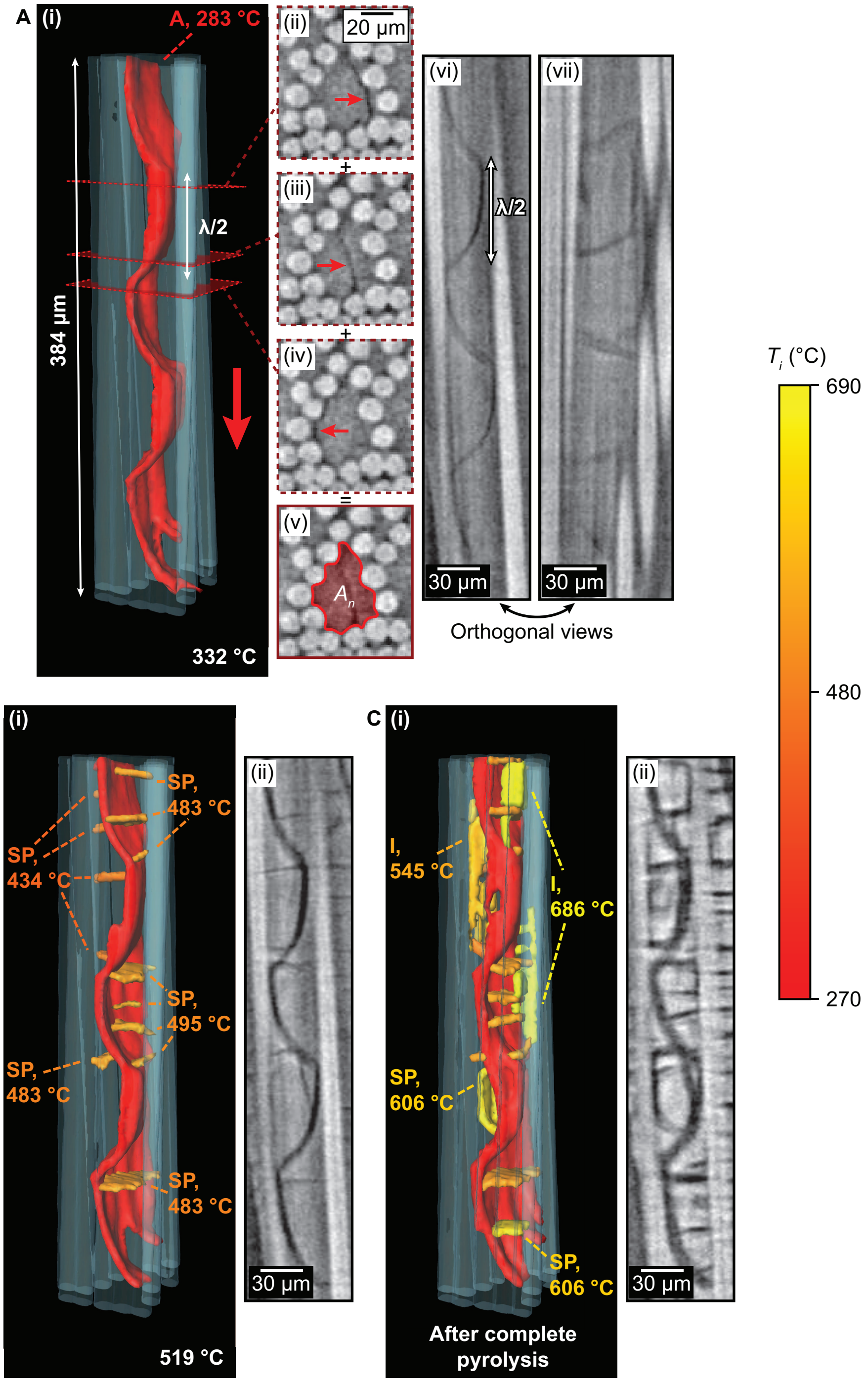

Figure 5.3: Evolution of a crack structure in the alternating family. (A)(i),(B)(i),(C)(i) Three-dimensional renderings of a crack structure with FHO of 3. In these renderings, fibers are semi-transparent blue, pyrolysis cracks are shown on a red-yellow scale that indicates initiation temperature, and matrix material is transparent. Each crack is labeled with its geometric type and its initiation temperature. Vertical red arrow in (A)(i) indicates the crack growth direction. (A)(ii-iv) Transverse (2D) views of the

alternating crack at three points along the crack trajectory shortly after formation. Red arrows indicate the crack front. (A)(v) Transverse view showing the area spanned by the alternating crack in (A)(ii-iv). (A)(vi), (B)(ii), (C)(ii) Longitudinal 2D sections of raw XCT images taken from the same location in the 3D image stacks showing crack evolution during pyrolysis. (A)(vii) A longitudinal 2D section of the alternating crack, viewed in a plane orthogonal to that in (A)(vi).

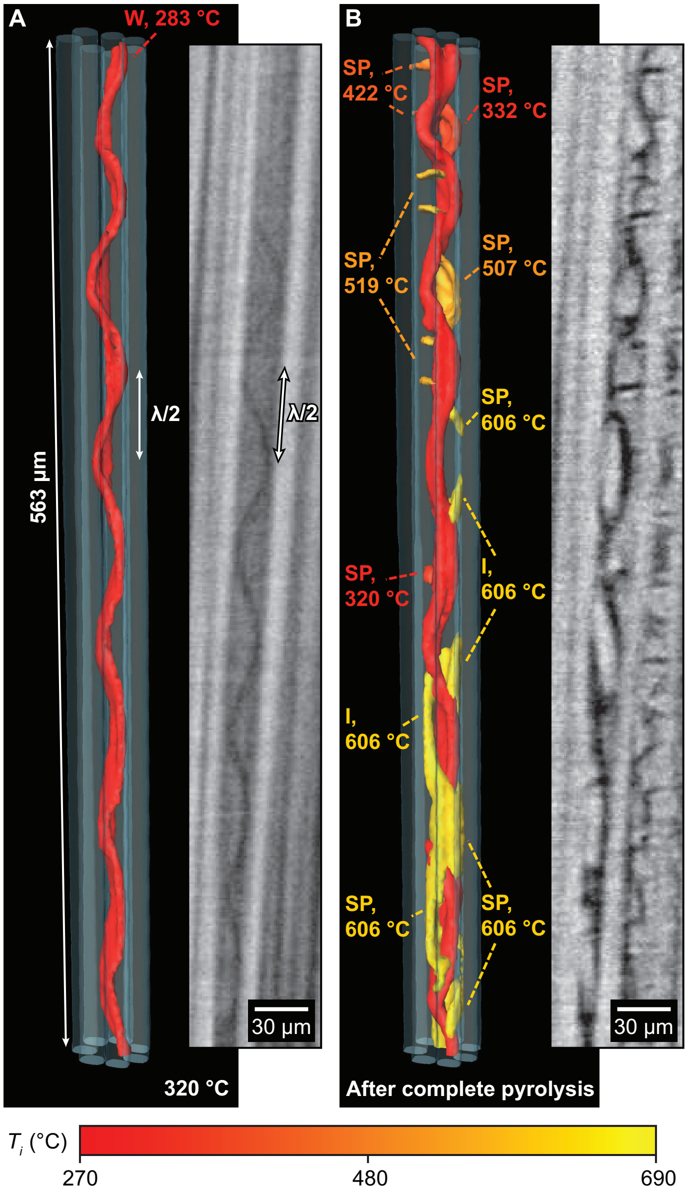

Figure 5.4: Evolution of a crack structure in the wavy family. (A-B) Three-dimensional XCT renderings with complementary longitudinal sections of raw XCT images. The crack structure has a FHO of 2. Labels and color schemes are the same as those in Figure 5.3.

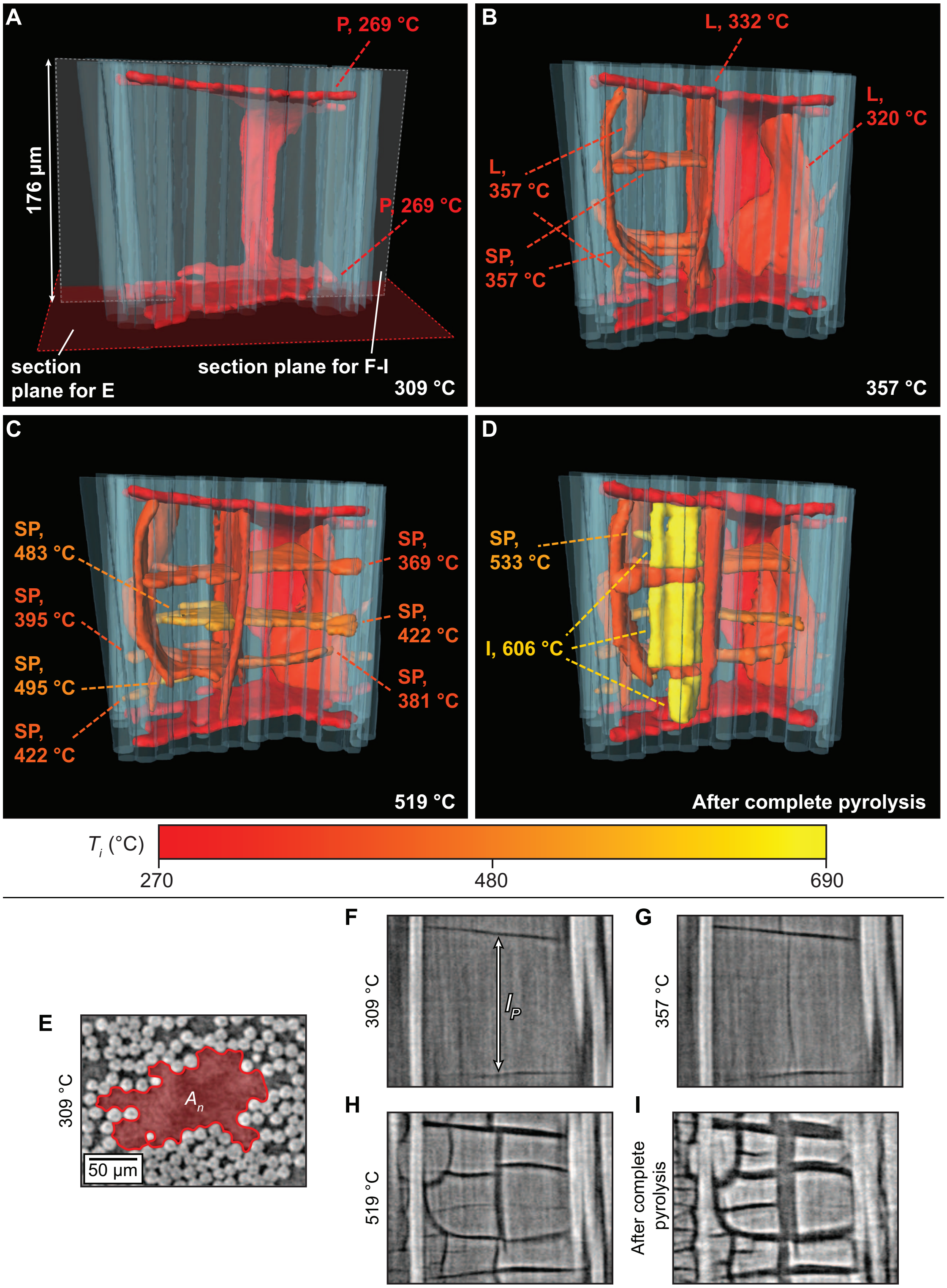

Figure 5.5: Evolution of a crack structure in the perimural family. (A-D) Three-dimensional renderings of a crack structure with FHO of 4. Labels and color schemes are the same as those in Figure 5.3. (E) Transverse 2D section of raw XCT image

(indicated by red plane in (A)) showing the area spanned by the perimural crack. (F-I) Longitudinal sections (indicated by the gray plane in (A)) showing cracks at the temperatures corresponding to images in (A) through (D).

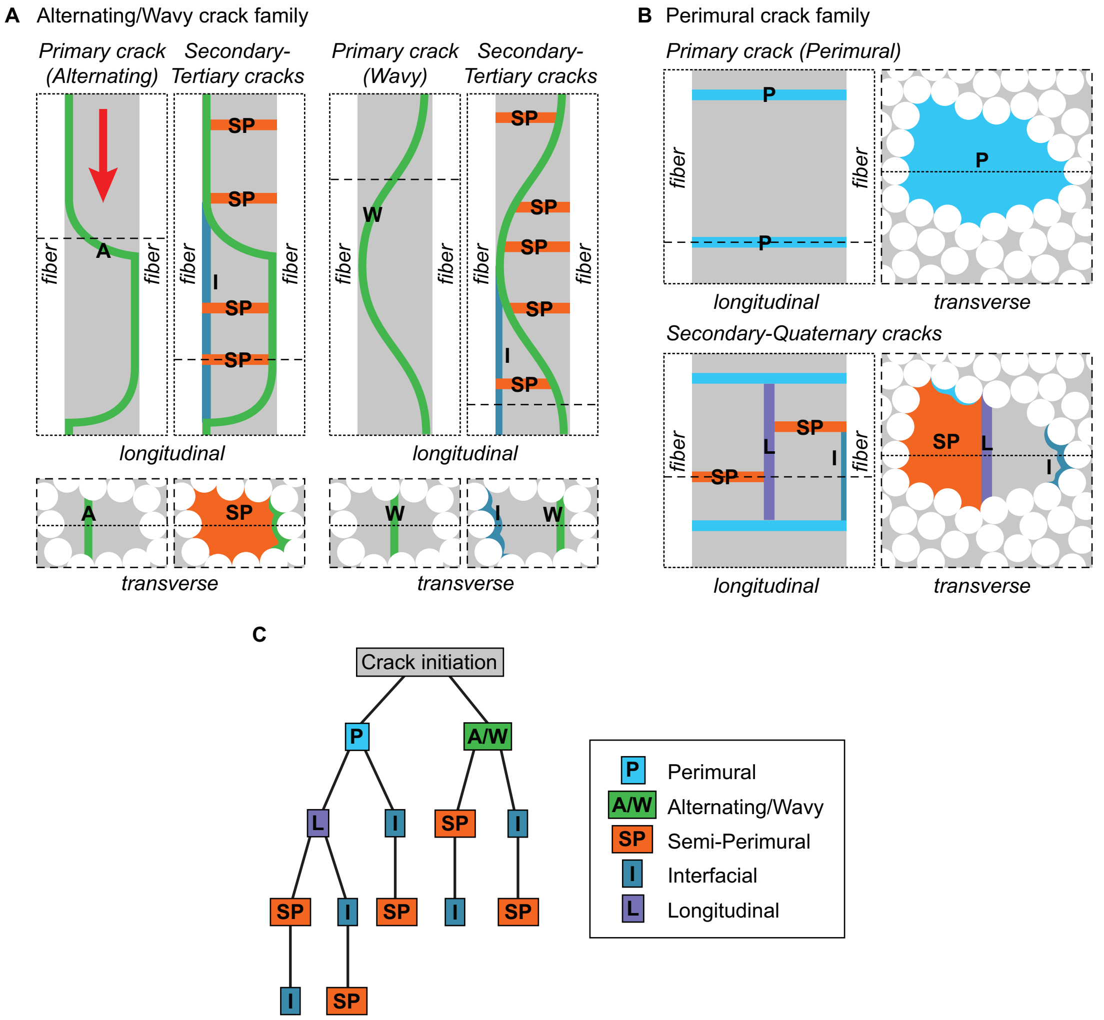

Figure 5.6: Temporal evolution of pyrolysis crack structures. (A) Evolution of crack structures in the alternating/wavy family. Shown here are the evolution of crack structures with FHO of 3: alternating and wavy primary cracks followed by secondary semi-perimural and tertiary interfacial cracks. (B) Evolution of a crack structure in the perimural family. Shown here is the evolution of a crack structure with FHO of 4: primary perimural cracks followed by a secondary longitudinal crack, tertiary semi-perimural cracks, and a quaternary interfacial crack. (C) Crack evolution tree illustrating potential temporal sequences.

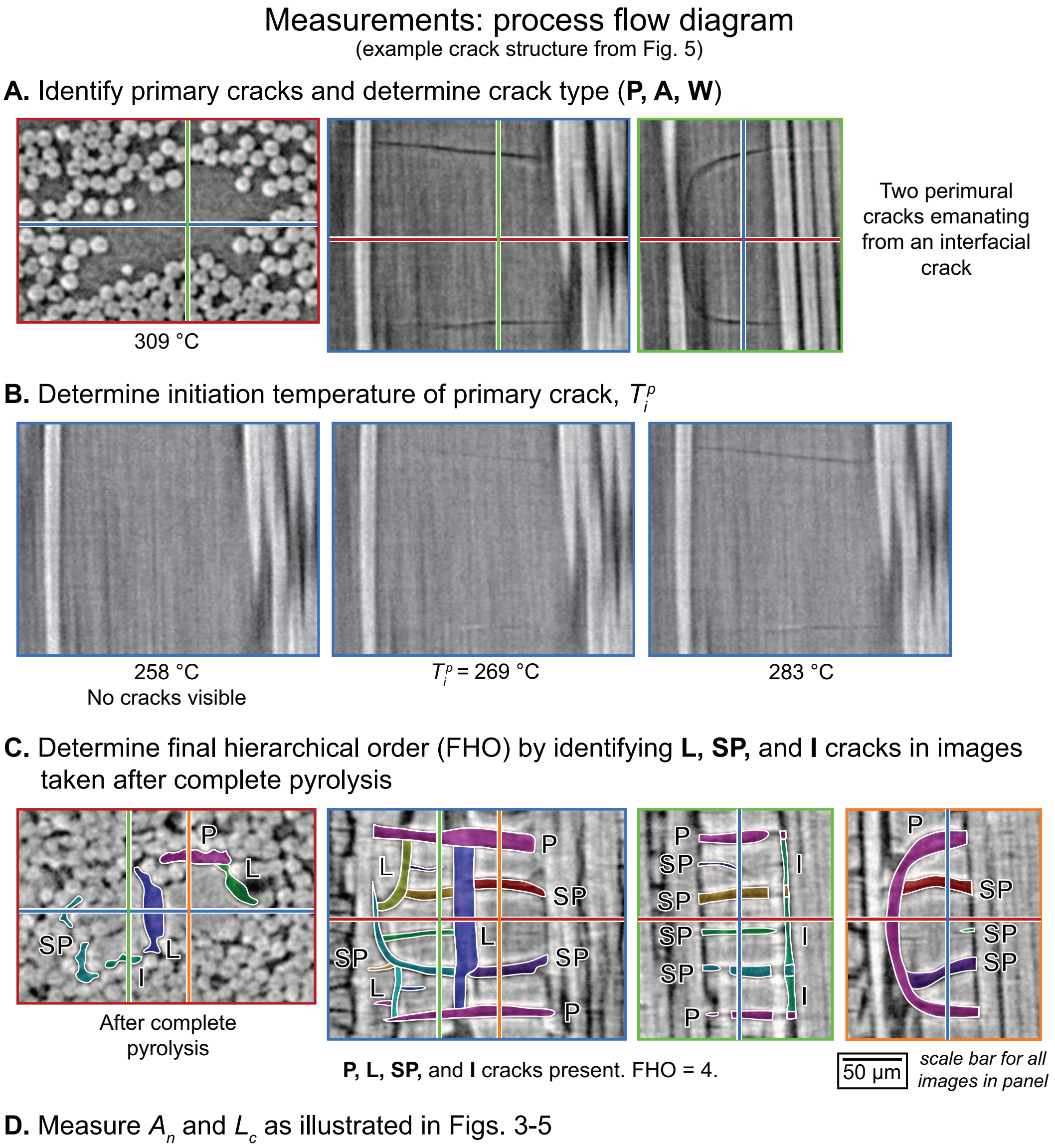

Figure 5.7: Process flow diagram for crack identification and measurements. Sample images are from cracks rendered in Figure 5.5. Colored lines on XCT images indicate intersectionality of perpendicular planes in the 3D image data.

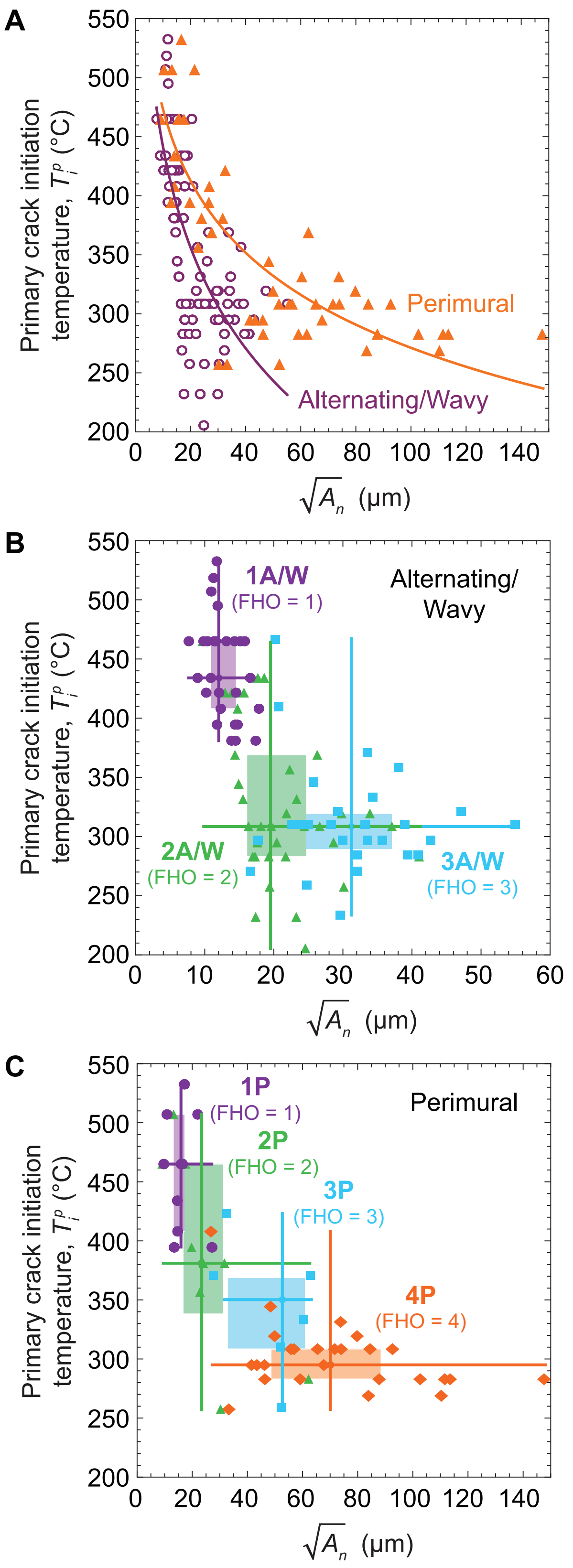

Figure 5.8: Relationships between crack areas and primary crack initiation tempera-

tures. (A) All data, for alternating/wavy cracks (open purple circles, purple line) and for perimural cracks (closed orange triangles, orange line). Lines are logarithmic fits. (B-C) Data in (A) separated by primary crack type and FHO (purple circles represent FHO=1, green triangles represent FHO=2, blue squares represent FHO=3, orange diamonds represent FHO=4). Semi-transparent boxes indicate boundaries of first and third quartiles in T_i^p and $\sqrt{A_n}$ for each data cluster. Solid lines indicate the full range of T_i^p and $\sqrt{A_n}$, and intersect at the median of each data cluster.

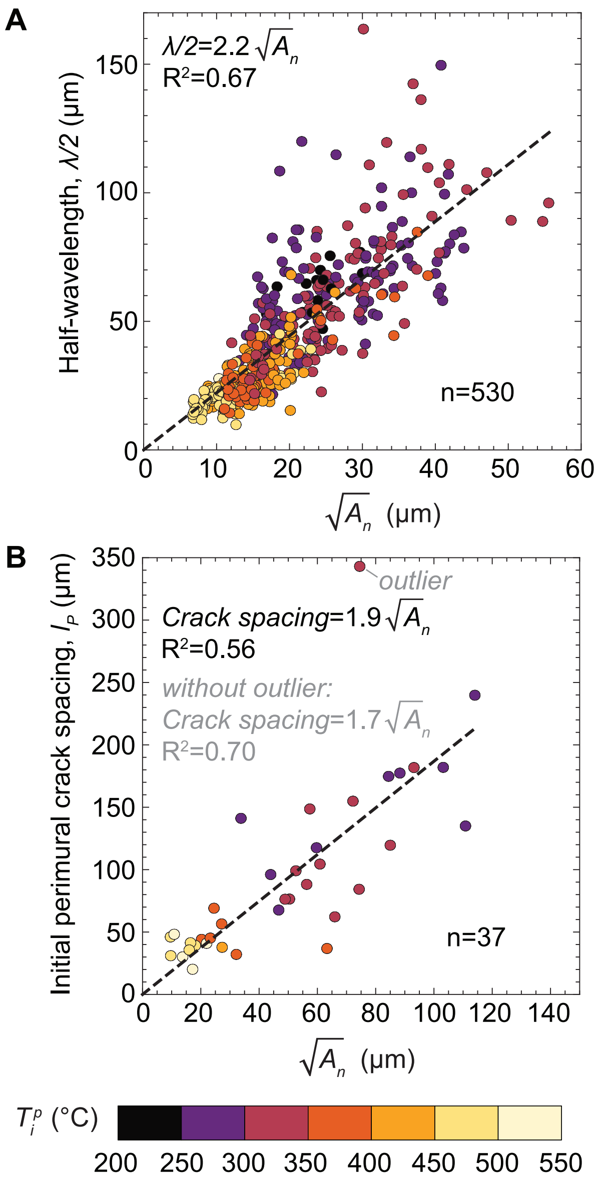

Figure 5.9: Characteristic length scales of pyrolysis cracks. (A) Half-wavelength of alternating/wavy cracks and (B) longitudinal spacing of initial perimural cracks. Color scale indicates primary crack initiation temperature.

Chapter 6

Conclusions and Recommendations

New experimental methods and analysis techniques have been developed for probing and characterizing microstructure evolution during impregnation, curing and pyrolysis of preceramic polymers in unidirectional fiber beds. Insights gleaned regarding fiber bed permeability, void formation, fiber movement, and crack evolution during pyrolysis provide a foundation for development of a physics-based modeling framework for continued advancement of the PIP process. This chapter presents a summary of the key conclusions and cross-cutting themes from this work, recommendations for future research, and several illustrative examples of approaches that might be employed in carrying out that research.

6.1 Conclusions

Axial Permeability of Unidirectional Fiber Beds: Large (nearly ten-fold) increases in axial permeability of unidirectional fiber beds with increasing capillary number (ranging nearly two orders of magnitude) have been partially rationalized through a combination of *in-situ* XCT observations and use of a new computational tool (GPE) for predicting axial permeability of large fiber arrays. The GPE tool yields useful quantitative predictions of permeability, with fidelity superior to that of methods based on assemblages of unit cells.

Changes in permeability arise from coupled effects of capillary number, fiber movement, and preferred flow channeling. Specifically, when the capillary number is high, complete saturation is attained behind the flow front. During this process, fibers rearrange into less uniform configurations with higher overall permeability. In contrast, when the capillary number is low, preferred flow channeling is observed in the smallest channels. This has two important consequences: (i) it leads to incomplete saturation behind the flow front with voids typically remaining in the largest channels, and (ii) it causes fibers bounding the small channels to be pulled closer together, leading to expansion of the largest (often unfilled) channels. The net result is a reduced unsaturated permeability.

Microstructure Evolution During Impregnation and Curing: Correlations between local fiber packing and locations of void formation as well as relationships between processing conditions and void formation have been elucidated through a combination of XCT observations and the use of new metrics to describe locations and arrangements of fibers and voids. The new metrics utilize spatial local porosity distributions and local porosity entropy to characterize fiber bed uniformity, fiber rearrangement, and heterogeneity in void locations.

During both impregnation and curing, voids tend to form in the largest channels between the fibers (i.e., regions of high local porosity). Increased non-uniformity in fiber arrangement, as measured by local porosity entropy, allows for higher median void sizes. Fiber rearrangement also occurs during impregnation and curing, evidenced by changes in local porosity entropy and qualitative observations of XCT images. As fiber beds are taken from the dry (unimpregnated) state to the cured state, fiber arrangements tend to become less uniform. Furthermore, the degree of saturation after impregnation and pressure removal increases with capillary number and appears to be independent of non-uniformity in fiber packing. However, specimens with high saturation after impregnation show the largest reductions in saturation during curing because of the need to create pathways for gas escape. Despite this, saturation after curing also increases with capillary number.

Microstructure Evolution During Polymer-to-Ceramic Conversion: Pyrolysis of a preceramic polymer within a unidirectional fiber bed leads to the formation of a myriad of rich and varied crack patterns with geometries, initiation locations and evolution sequences that would almost certainly be impossible to discern using only 2D imaging. Through exhaustive examinations and analyses of a large number of cracks imaged in 3D *in-situ* during pyrolysis, the study has enabled development of a taxonomy of crack geometries and crack structures and has revealed the temporal sequences of their formation.

Primary cracks – the first cracks to form in a local matrix region – typically initiate at fiber-matrix interfaces. They subsequently grow into the matrix and evolve into either alternating, wavy, or perimural cracks. Although the final geometries of the three cracks differ, the cracks appear to follow similar evolutionary processes. For instance, wavy and alternating cracks both follow paths that are, on average, parallel to the fiber axis; alternating cracks periodically impinge on the interfaces with fibers and re-enter the matrix a short distance later, whereas wavy cracks reach their crests very near the interfaces before veering away. Perimural cracks appear to form analogously to the first half-wavelength of alternating cracks. Whether the transition from perimural to alternating is achieved depends on the size of the matrix region in which the cracks form. When, for example, the local matrix regions are large, perimural cracks form in preference to alternating cracks. As the size of the local matrix region increases, the primary crack initiation temperature decreases and the characteristic primary crack spacing increases. Secondary, tertiary and quaternary cracks may also form as pyrolysis continues, depending on the size of the local matrix regions and the nature of cracks that precede them. With increasing size of the local matrix region, the final hierarchical order of the crack structure increases.

6.2 Cross-cutting Themes

A cross-cutting theme of this study is microstructural heterogeneity as both an input parameter – for example the heterogeneity of the fiber array – and an output parameter – for example the rearrangement of the fiber array, the distribution in void size and location, and the variation in crack geometry and final hierarchical order. Specifically, changes in permeability with capillary number during impregnation are due to both fiber rearrangement and preferred flow channeling in non-uniformly packed fiber beds. Fiber beds tend to become less uniform over the course of impregnation and curing, which in turn influences void size and location. These findings have implications for existing models for permeability and void formation which often assume static arrays of uniformly packed fibers (single-scale media) or uniformly packed tows within a uniform weave (dual-scale media). Such models would be enhanced by incorporating fluid-fiber interactions and accounting for non-uniformity. The sizes of the local matrix regions between fibers also influence the characteristics of cracks formed during pyrolysis, including crack type, initiation temperature, and characteristic spacing as well as the final hierarchical order of crack structures. These findings provide a foundation for development of a mechanics framework to be used in predicting the geometry of the crack networks remaining after PIP. The deleterious effects of heterogeneity in fiber packing and the compounding nature of heterogeneous defect formation throughout the PIP process suggest that strategies for creating and maintaining uniformity in fiber arrays may yield dividends in improvements in the terminal microstructures.

A second theme emerging from this work (though not explicitly addressed in the preceding chapters) involves challenges in identifying representative volume elements (RVEs) for the observed phenomena – fiber movement, bubble formation, and crack evolution – even within the seemingly simple geometry of a unidirectional fiber bed. The fiber beds display non-uniformities in fiber packing over length scales comparable to the dimensions of the transverse cross-section of the specimen. Long regions of high local fiber bed porosity are typically located near the tube walls, where fiber packing may have been compromised by the encasement process, as well as in the interior of the fiber bed along paths that may have been prior tow boundaries. Unsurprisingly, transverse fiber movement and void formation during both impregnation and curing occur highly heterogeneously. Furthermore, the geometric features of the hierarchical pyrolysis crack structures described earlier depend on local fiber arrangement. Thus, the combination of non-uniform fiber movement, relatively large features in the spatial distribution of local fiber bed porosity, and non-uniformity in void formation precludes immediate identification of a representative transverse subset of the composite for further study.

There are also challenges in identifying a representative longitudinal length scale. Voids that form during impregnation and curing are either very long parallel to the fiber axis, or, in the case of some post-curing voids, consist of long clusters of smaller voids aligned with the fiber axis. These voids and void-clusters are often longer than the longitudinal field of view (LFOV) for a single XCT scan. Furthermore, the pore network after pyrolysis consists of voids that may have formed during impregnation and curing, as well as meso-scale longitudinal and interfacial cracks, and hierarchical pyrolysis crack structures. Meso-scale longitudinal and interfacial cracks as well as primary wavy and alternating cracks can persist over length scales comparable to that of the LFOV for a single XCT scan. Subsequent impregnation into this pore network depends on geometric features (e.g., connectivity and pore dimensions) that vary locally with pore type (e.g. bubbles vs. hierarchical cracks) and globally based on arrangements of various pore types. Without knowledge of the lengths scales over which features of the voids and pore networks change along the specimen length, it is not possible to identify the appropriate length of an RVE.

6.3 Recommendations

6.3.1 Geometry of pore networks

The present study has focused on the processes governing the *first* PIP cycle. The remaining pore network will ultimately need to be re-impregnated through either PIP, CVI, or RMI. The network includes the hierarchical crack structures identified in Chapter 5, meso-scale longitudinal and interfacial cracks, and bubbles formed during impregnation and curing of the matrix prior to pyrolysis (Chapter 4). Success of any of the three prospective densification methods will depend on the geometry of the pore network, which may be assessed using segmented XCT data of pore networks in the following ways.

First, an estimate of the upper densification limit of subsequent processing may be provided by computing the fraction of pores connected to the external composite surface(s). To be useful, measurements of connectivity must reflect the possible pathways for material ingress. One consideration in this analysis is the resolution of the volumetric data ($\approx$ 0.7-1.0μm per voxel edge in this work), which represents the minimum channel size that can be considered in the analysis. Another consideration involves definition of the ″open″ surfaces from which connectivity is measured. At the simplest level, in unidirectional fiber composites, impregnation may occur either parallel or perpendicular to the fiber direction. Thus, connectivity measurements from surfaces parallel and perpendicular to the two principal directions would be desirable.

A preliminary connectivity analysis of a 3D volume, about 2mm long, extracted from a unidirectional CMC after one PIP cycle is presented in Fig. 6.1. The resolution is 0.98μm per voxel edge. In this example, connectivity to the top surface of the volume was computed using a voxel connectivity of 6 (i.e. voxels are considered connected if their *faces* touch). Here, the total porosity is 20.0% whereas the porosity not connected to the top surface is 1.4%. The porosity includes both bubbles and shrinkage cracks which vary significantly in transverse cross sectional area. Non-connected regions typically have lower transverse cross sectional areas. To develop a deeper understanding of the contribution of different pore types (e.g., bubbles, cracks of varying FHO) on connectivity, classification of the results on the basis of pore type and paths of various pore types would be desirable.

Another important geometric feature of the pore network is the size of the pores and the spatial distribution of small pores. Pore dimensions are highly relevant to the RMI process, where the smallest channels may become blocked by reaction choking [2, 16], and the CVI process, where the smallest channels may become closed off during deposition [2, 3, 8]. Measurements of pore sizes must consider the smallest dimensions along the possible pathways for material transport. One approach is to compute the local thickness of the pore network in 3D. These results could then be used to investigate channel size variation in the bulk and over various potential flow paths through the pore network. To assess the viability of an RMI or CVI process with a known minimum critical channel size, a connectivity analysis on the pore network excluding regions that fall below the minimum critical channel size could be performed. Depending on the spatial distribution of small channels in the connected network, blockage of small channels may significantly increase the amount of closed porosity within the network, or it may simply close off access to a small volume of other smaller dead-end channels.

Finally, computational fluid dynamics (CFD) tools offer a more sophisticated approach for indirectly assessing the geometry of the pore network and more directly assessing effects of the pore network on densification. CFD could be used to model impregnation of matrix precursors into pore networks. This approach could reveal the effects of dead-end pathways and spatial distributions in pore size and pore type (e.g., bubbles vs. cracks of varying FHO). For example, consider a crack structure consisting of a wide primary wavy crack with thinner semi-perimural cracks branching off the primary crack. Impregnation at a high capillary number might cause the fluid to advance along the wavy crack before the branches are filled, trapping voids within the branches. Subsequent fluid rearrangement due to the higher capillary pressure within the branches may cause the branches to fill at the expense of void formation within the primary wavy crack. Continued impregnation at higher capillary numbers may enable mobilization and removal of voids trapped within the wavy crack. Models accounting for capillary effects and bubble formation would enable prediction of void formation and mobilization as a function of capillary number. The results would inform identification of optimal processing conditions (e.g., capillary number and flow direction) and may reveal pore geometries that are more favorable for subsequent impregnation. Similar approaches could be taken to study RMI and CVI by accounting for reaction and deposition products, respectively.

One important consideration in implementation of the methods described above is the quality of the XCT image segmentation and the sensitivity of the metrics (e.g., connectivity, fluid flow characteristics) to the parameters used in image segmentation (e.g., threshold values for various filters and detection algorithms). Features such as small pathways (on the order of a single voxel width) could have minimal effects on total porosity while having significant effects on connectivity.

The preceding proposed analyses also face potential challenges with identification of a suitable RVE. One approach to simplify these efforts could involve classifying geometric properties of the pores on the basis of pore type or transverse area between fibers. This information could be used to develop coarse-grained models based on assemblages of pore types. This approach could also be used to identify optimal pore geometries that give the highest degree of connectivity, encourage full saturation during impregnation, and/or give channel sizes amenable to subsequent RMI or CVI processing.

6.3.2 Shrinkage cracking in simple geometries

The work presented in Chapter 5 revealed the geometries and evolution sequences of pyrolysis cracks within a large number of very complex and locally unique fiber bed geometries. To build on this foundation, complementary studies on simpler, uniform microtube geometries is recommended. The work would seek to: (i) determine whether the crack geometries observed in fiber beds can be reproduced in microtubes; (ii) establish connections between crack geometry, crack initiation temperature, and tube shape and size; and (iii) combine the preceding results with measurements of the physical and mechanical properties (e.g., volumetric shrinkage, elastic modulus) of the precursor material during pyrolysis. Collectively these results could form the experimental basis for development of a 3D fracture mechanics framework for pyrolysis cracking. Development of this framework would also be informed by existing solutions for cracking in 2D bimaterial systems [62–68].

Preliminary experimental work has demonstrated that alternating and wavy cracks form in microtube geometries. The specimens consist of microtubes (VitroTubes™) filled with allylhydridopolycarbosilane (AHPCS) (SMP-10, Starfire® Systems) mixed with 0.2 wt% dicumyl peroxide (DP). Microtubes were filled by spontaneous capillary wicking from a beaker of the precursor. The microtubes were oriented vertically in the beaker during filling. Several microtube geometries and sizes were investigated. Borosilicate microtubes with rectangular cross sections of the following dimensions were used: $100\mu\text{m}\times1000\mu\text{m}$, $50\mu\text{m}\times1000\mu\text{m}$, $40\mu\text{m}\times400\mu\text{m}$, $30\mu\text{m}\times300\mu\text{m}$, $20\mu\text{m}\times200\mu\text{m}$, and $10\mu\text{m}\times100\mu\text{m}$. Additionally, quartz microtubes with 50μm and 100μm diameter circular cross sections were used. The specimens were imaged with XCT at the hard X-ray beamline 8.3.2 at the Advanced Light Source (ALS) at Lawrence Berkeley National Laboratory. Figs. 6.2 and 6.3 show orthogonal views and 3D renderings of pyrolysis cracks observed in filled microtubes after pyrolysis to 500°C in flowing argon. A highly periodic alternating crack is observed in the $10\mu\mathrm{m}\times100\mu\mathrm{m}$ rectangular microtube (Fig. 6.2). Short longitudinal cracks bridge several individual half-wavelengths within the alternating crack, suggesting that the longitudinal cracks formed after the alternating crack. In the circular microtubes, alternating (Fig. 6.3(A)) and wavy (Fig. 6.3(B)) cracks are observed. In both specimens, additional cracks appear to branch off of the alternating and wavy cracks. Due to the smoothness and continuity of the alternating and wavy cracks, it is inferred that these additional cracks form after alternating and wavy crack formation.

In order to resolve sequences of crack formation and crack initiation temperatures, XCT imaging was performed *in-situ* during pyrolysis for collections of filled microtubes. The specimens were imaged inside the same high-temperature testing rig used in Chapter 5 [5, 88]. A sequence of XCT images (Fig. 6.4) from these experiments shows expansion of an alternating crack that forms along one edge of a $100\mu\mathrm{m}\times1000\mu\mathrm{m}$ rectangular microtube. The initiation temperature of the alternating crack is 371°C (Fig. 6.4(A)(iv)); scans taken below this temperature show no pyrolysis cracks. An interesting feature of this alternating crack is that it propagates longitudinally and exists only in a small region near one of the short sides of the rectangular cross section. Following the alternating crack profile towards the center of the tube reveals that the alternating crack flattens out to form a relatively straight crack in the center of the preceramic polymer layer (Fig. 6.4(A)(iii)). Alternating cracks in other rectangular microtubes also often appear only near the short sides of the rectangular cross section and may morph into straight cracks or other yet-unnamed crack geometries toward the center of the tube. In addition to the alternating crack, several other crack features of varying geometries are observed. Continuing work involves identifying crack geometries and crack evolution sequences as well as measuring crack initiation temperatures within microtubes of varying shape and size.

6.3.3 Microstructure evolution in complex fiber architectures

The research presented in this dissertation has focused on simple unidirectional minicomposite systems. However, in practice, fiber architectures typically consist of 2D or 3D weaves, customized integral ceramic textile structures, or 2D laminates of unidirectional plies [1–5, 9]. Thus, it is recommended that the experimental methods and analysis techniques presented in this work be extended to study microstructure evolution in representative fiber architectures.

In-situ XCT during impregnation of a woven preform would elucidate the coupled effects of flow parallel and perpendicular to the fibers as well as through large intertow channels on fiber rearrangement, preferred flow channeling, permeability and void formation. The setup envisaged for these experiments consists of a woven fiber preform encapsulated in a glass tube or within a vacuum bag, with ports for fluid inlet and outlet above and below the specimen as in the setup described in Chapters 3 and 4. Here the challenge would be to find the balance between specimen size and image resolution that would reveal the features of interest. Using current imaging capabilities, specimens about $4\times4\times4$ mm^3 could be imaged at a resolution of 2μm per voxel (equivalent to $\approx$ 6 voxels across a fiber diameter). More recent developments at the ALS have led to significant increases in X-ray flux, enabling faster scan times without loss of image quality. These capabilities could prove highly desirable in the proposed experiments.

A corresponding extension of the methods in Chapter 5 could be used to study pyrolysis crack evolution within the constraints of a woven fiber bed. One of the primary constraints of the high-temperature testing rig used in those experiments is the size of the hot zone, which is limited to a spherical region less than 5mm in diameter [5, 88].

To expand those capabilities, a new high-temperature furnace system (Fig. 6.5) was recently developed at the ALS. The system allows *in-situ* XCT imaging of specimens up to several centimeters in length and about 6mm in diameter, up to temperatures of 1800°C [94]. It consists of a stationary vertically-oriented tube furnace with a $6 \times 6\text{mm}^2$ beam port [94]. Specimens are mounted inside a quartz tube which is closed on one end and connected to an environmental flow cell on the other end [94]. This capability would facilitate meaningful *in-situ* experiments on multidirectional CMCs.

6.3.4 Microstructure evolution during repeated PIP cycles

The research presented in this dissertation has focused on microstructural evolution during the first round of PIP. Recognizing that, in practice, 6-14 PIP cycles are typically used to densify the matrix, a more complete understanding of microstructure evolution would emerge from analogous studies on unidirectional minicomposites subjected to multiple PIP cycles. Results presented in Chapter 2 suggest that repeatable patterns in microstructure evolution are likely to emerge after only a few process cycles. The observations could inform process models for PIP-based CMCs.

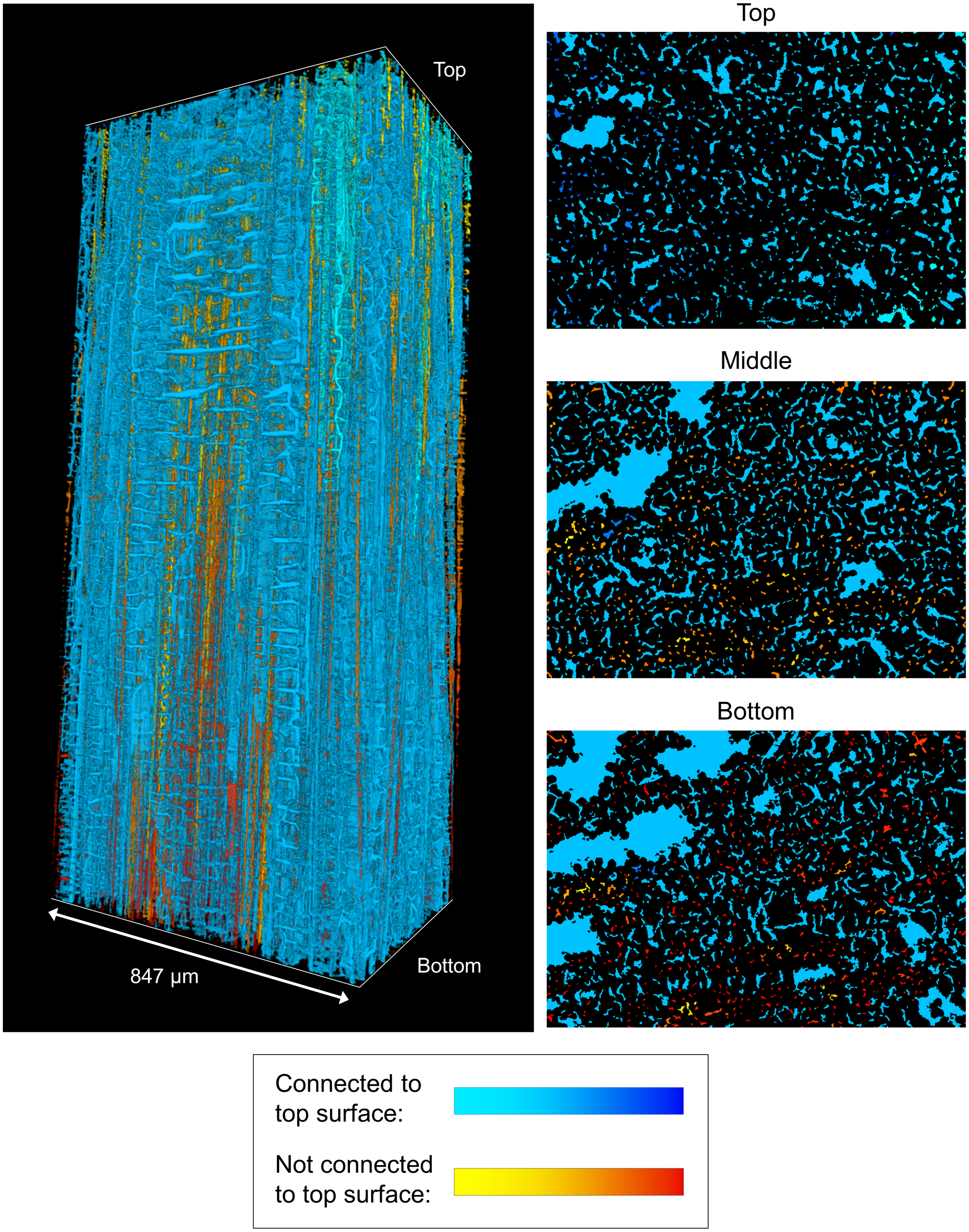

Figure 6.1: Connectivity analysis for porosity in a 3D volume extracted from a unidirectional CMC after one PIP cycle. Each 3D connected pore is assigned a single color based on its connectivity to the top surface. Pores that are connected to the top surface

are assigned a color in the blue color range, while pores that are not connected to the top surface are assigned a color in the yellow-red color range. A 3D rendering is shown on the left, and transverse sections from the top, middle, and bottom of the volume are shown on the right.

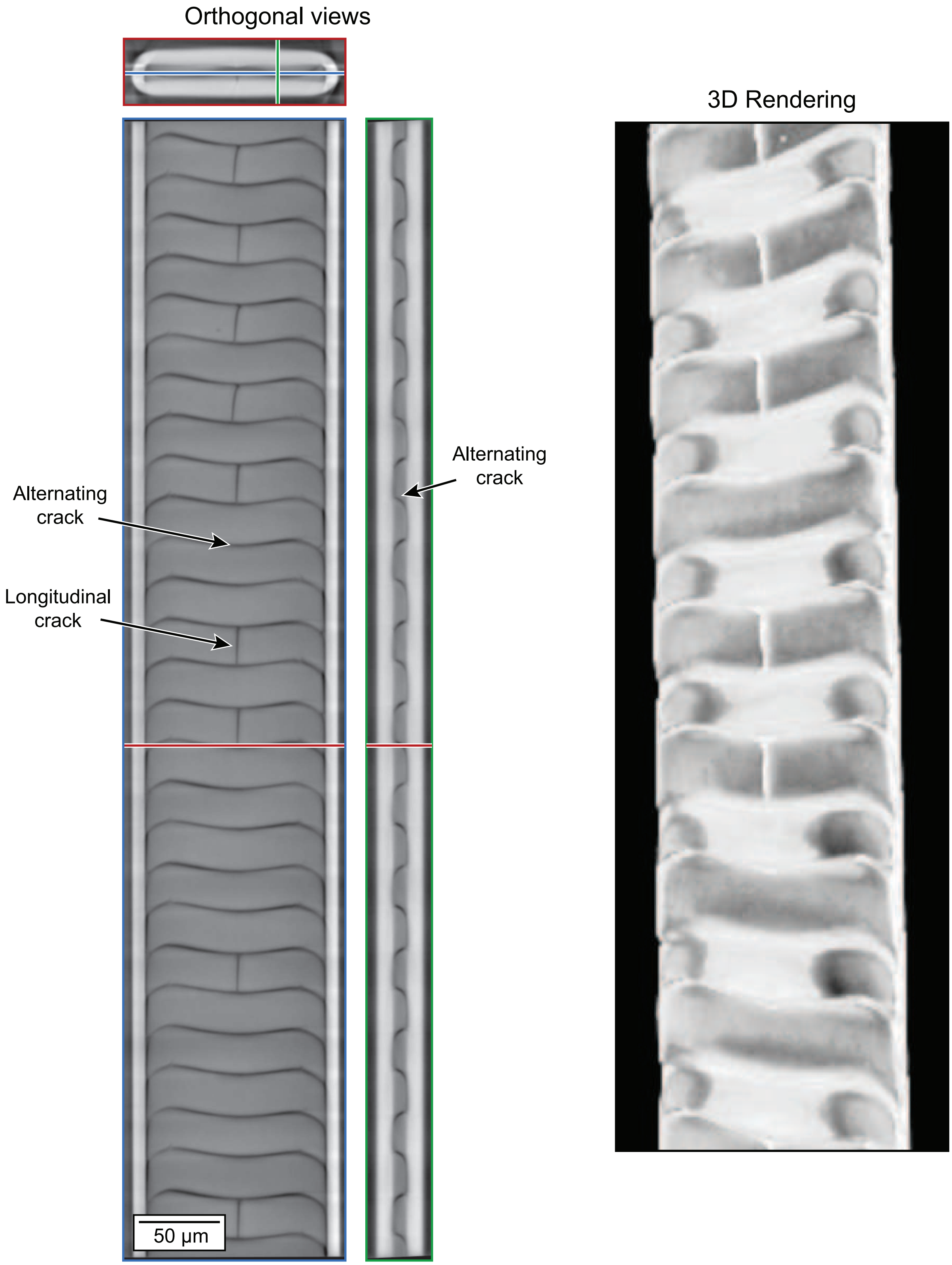

Figure 6.2: Orthogonal views and 3D rendering of pyrolysis cracks in a $10\mu m \times 100\mu m$ rectangular microtube. Colored lines on orthogonal views indicate intersectionality of perpendicular planes in the 3D image data.

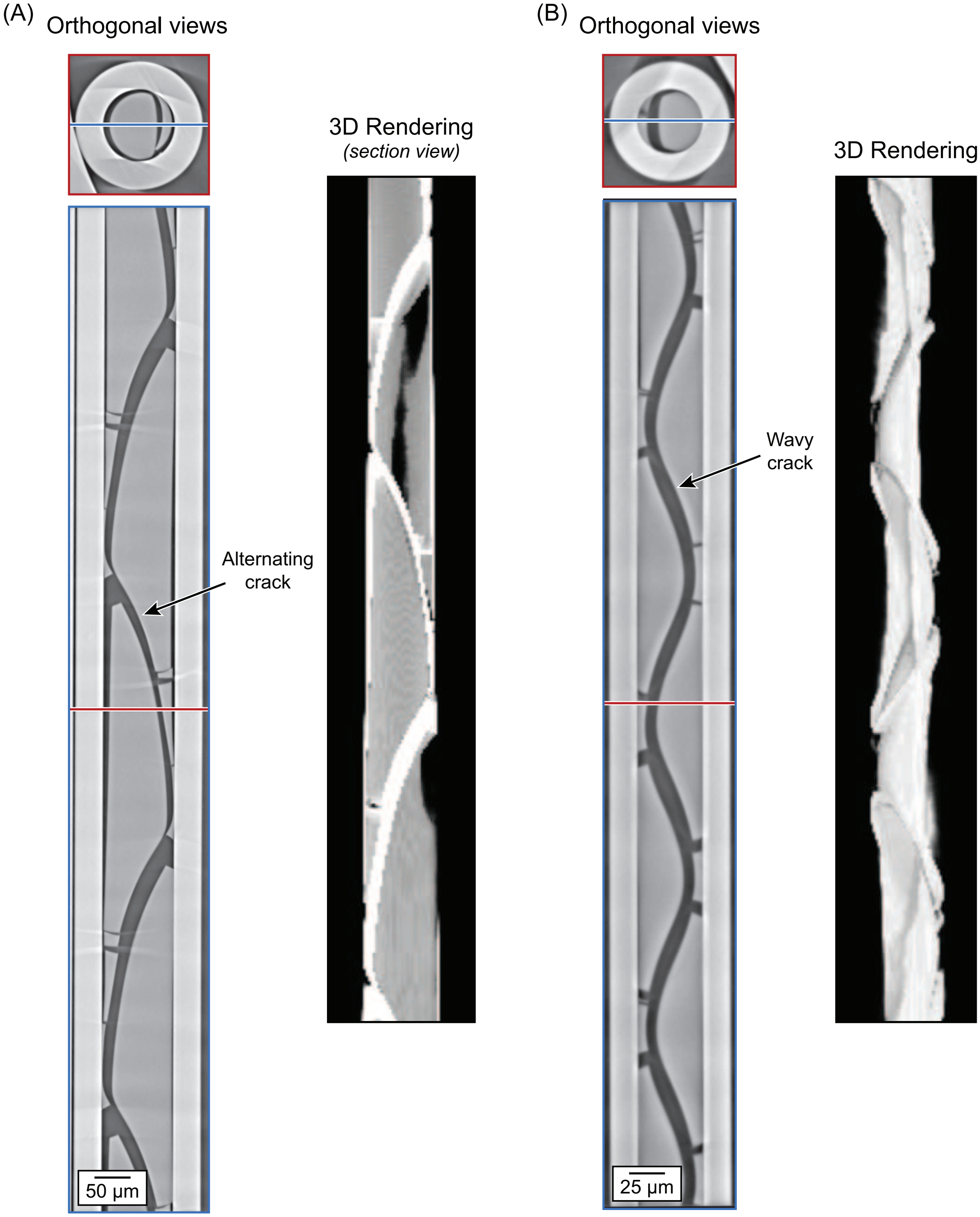

Figure 6.3: Orthogonal views and 3D rendering of pyrolysis cracks in (A) a circular microtube with 100μm diameter and (B) a circular microtube with 50μm diameter. The 3D rendering in (A) shows a section view of the crack network within the microtube. Colored lines on orthogonal views indicate intersectionality of perpendicular planes in the 3D image data.

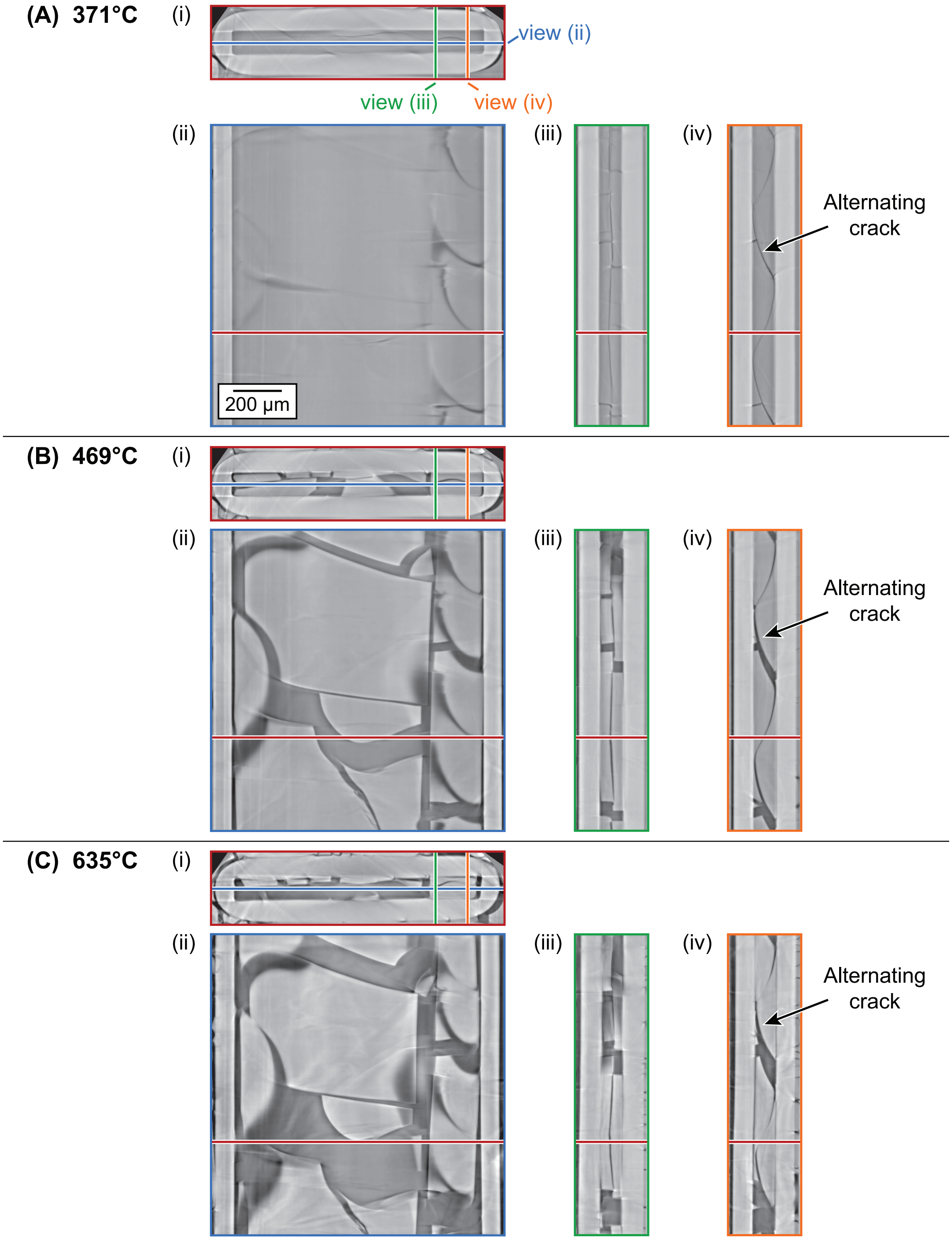

Figure 6.4: Sequence of orthogonal views showing pyrolysis crack evolution with increasing temperature in a 100μm$\times$1000μm rectangular microtube. Orthogonal views are shown for (A) 371°C, (B) 469°C, and (C) 635°C. Colored lines on orthogonal views indicate intersectionality of perpendicular planes in the 3D image data.

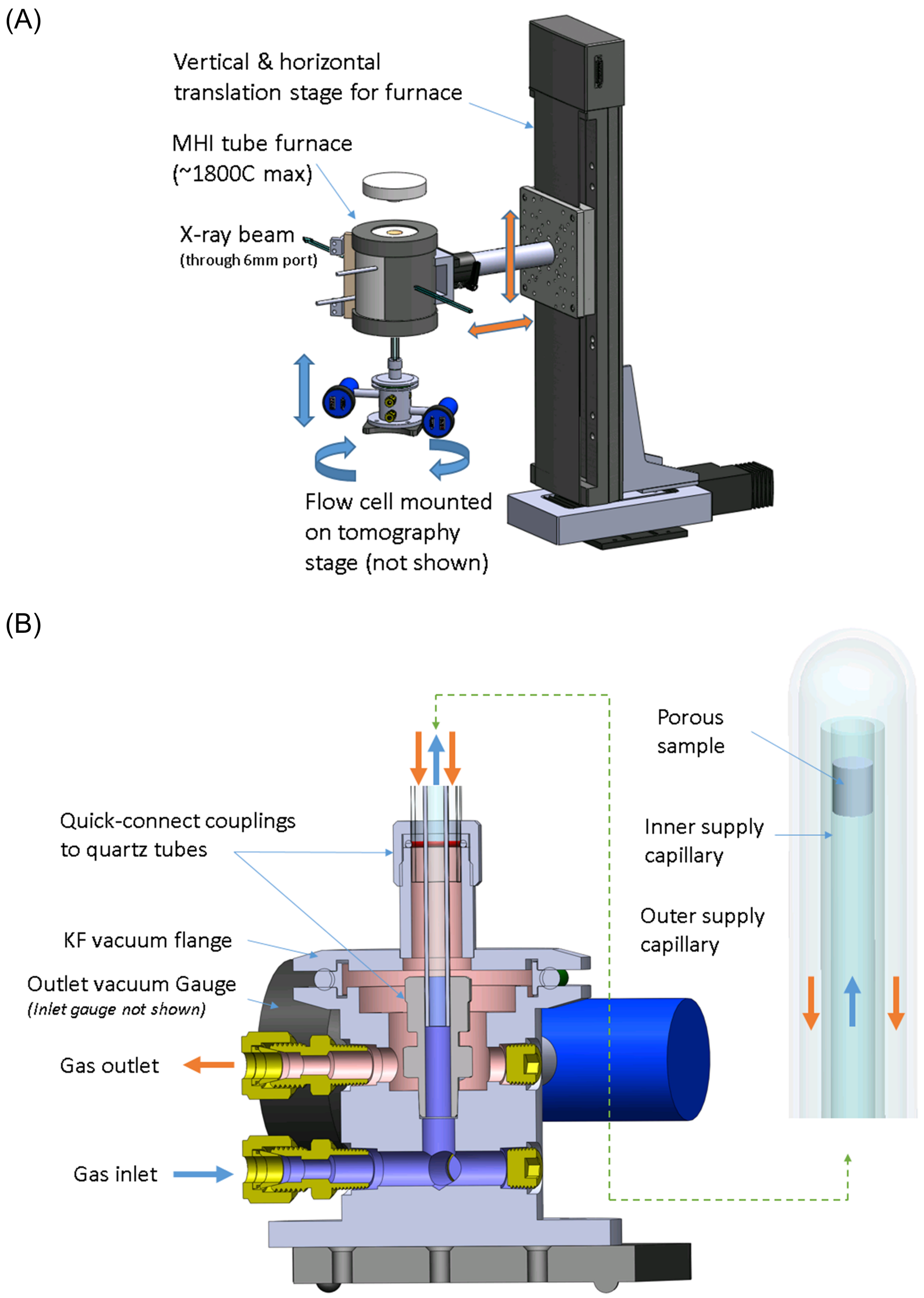

Figure 6.5: High-temperature furnace system for *in-situ* XCT of heated specimens in controlled environments [94]. (A) The furnace is mounted on a translation stage used to align the beam port with the X-ray beam. The environmental flow cell is inserted into the furnace from below using the tomography stage. (B) Sectional view of the environmental flow cell shows gas flow paths. Images courtesy of Harold Barnard, Lawrence Berkeley National Laboratory.

References

[1] N. P. Padture. “Advanced structural ceramics in aerospace propulsion”. *Nat. Mater.* 15.8 (2016), pp. 804–809.

[2] R. Naslain. “Design, preparation and properties of non-oxide CMCs for application in engines and nuclear reactors: an overview”. *Compos. Sci. Technol.* 64.2 (2004), pp. 155–170.

[3] F. W. Zok. “Ceramic-matrix composites enable revolutionary gains in turbine engine efficiency”. *Am. Ceram. Soc. Bull.* 95.5 (2016), pp. 22–28.

[4] D. B. Marshall and B. N. Cox. “Integral Textile Ceramic Structures”. *Annual Review of Materials Research* 38.1 (2008), pp. 425–443.

[5] H. A. Bale et al. “Real-time quantitative imaging of failure events in materials under load at temperatures above 1,600°C”. *Nat. Mater.* 12.1 (2012), pp. 40–46.

[6] D. L. Poerschke et al. “Crystallization behavior of polymer-derived Si-O-C for ceramic matrix composite processing”. *Acta Mater.* 147 (2018), pp. 329–341.

[7] D. L. Poerschke, M. N. Rossol, and F. W. Zok. “Intermediate Temperature Internal Oxidation of a SiC/SiCN Composite with a Polymer-Derived Matrix”. *J. Am. Ceram. Soc.* 99 (2016), pp. 3120–3128.

[8] J. A. DiCarlo. “Advances in SiC/SiC Composites for Aero-Propulsion”. In: *Ceramic Matrix Composites: Materials, Modeling and Technology*. Ed. by N. P. Bansal and J. Lamon. 1st ed. John Wiley & Sons, Inc., 2015. Chap. 7, pp. 217–235.

[9] J. Y. Yang et al. “Processing of Oxide Composites with Three-Dimensional Fiber Architectures”. *Journal of the American Ceramic Society* 92.5 (2009), pp. 1087–1092.

[10] “Fabrication of SiCf/SiC composites by hybrid techniques of electrophoretic deposition and polymer impregnation and pyrolysis”. *Ceramics International* 42.14 (2016), pp. 16431–16435.

[11] C. A. Nannetti et al. “Manufacturing SiC-fiber-reinforced SiC matrix composites by improved CVI/slurry infiltration/polymer impregnation and pyrolysis”. *Journal of the American Ceramic Society* 87.7 (2004), pp. 1205–1209.

[12] D. King et al. “Novel processing approach to polymer-derived ceramic matrix composites”. *International Journal of Applied Ceramic Technology* 15.2 (2017), pp. 399–408.

[13] M. Kotani et al. "Effect of SiC particle dispersion on microstructure and mechanical properties of polymer-derived SiC/SiC composite". *Materials Science and Engineering: A* 357.1 (2003), pp. 376–385.

[14] M. Kotani et al. "Consolidation of polymer-derived SiC matrix composites: processing and microstructure". *Composites science and technology* 62.16 (2002), pp. 2179–2188.

[15] S. M. Dong et al. "Microstructural evolution and mechanical performances of SiC/SiC composites by polymer impregnation/microwave pyrolysis (PIMP) process". *Ceramics international* 28.8 (2002), pp. 899–905.

[16] R. B. Reitz, F. W. Zok, and C. G. Levi. "Reactive alloy melt infiltration for SiC composite matrices: Mechanistic insights". *J. Am. Ceram. Soc.* 100.12 (2017), pp. 5471–5481.

[17] P. Colombo et al. "Polymer-Derived Ceramics: 40 Years of Research and Innovation in Advanced Ceramics: Polymer-Derived Ceramics". *J. Am. Ceram. Soc.* 93.7 (2010), pp. 1805–1837.

[18] R. Lee. *Carbosilanes: Reactions & Mechanisms of SMP-10 Pre-Ceramic Polymers*. 2009.

[19] R. M. Laine and F. Babonneau. "Preceramic polymer routes to silicon carbide". *Chemistry of Materials* 5.3 (1993), pp. 260–279.

[20] S. Kaur, R. Riedel, and E. Ionescu. "Pressureless fabrication of dense monolithic SiC ceramics from a polycarbosilane". *Journal of the European Ceramic Society* 34.15 (2014), pp. 3571–3578.

[21] S. C. Zunjarrao, A. Rahman, and R. P. Singh. "Characterization of the Evolution and Properties of Silicon Carbide Derived From a Preceramic Polymer Precursor". *Journal of the American Ceramic Society* 96.6 (2013). Ed. by R. Reidel, pp. 1869–1876.

[22] J. Yin et al. "The effects of SiC precursors on the microstructures and mechanical properties of SiCf/SiC composites prepared via polymer impregnation and pyrolysis process". *Ceramics International* 41.3, Part A (2015), pp. 4145–4153.

[23] N. Larson and F. Zok. "In-situ 3D visualization of composite microstructure during polymer-to-ceramic conversion". *Acta Mater.* 144 (2018), pp. 579–589.

[24] M. Kotani, A. Kohyama, and Y. Katoh. "Development of SiC/SiC composites by PIP in combination with RS". *Journal of nuclear materials* 289.1 (2001), pp. 37–41.

[25] "Properties and microstructure evolution of Cf/SiC composites fabricated by polymer impregnation and pyrolysis (PIP) with liquid polycarbosilane". *Ceramics International* 43.10 (2017), pp. 7387–7392.

[26] L. Zoli et al. "Additive Manufacturing of Ceramics Enabled by Flash Pyrolysis of Polymer Precursors with Nanoscale Layers". *J. Am. Ceram. Soc.* 99.1 (), pp. 57–63.

[27] S. Azarnoush et al. “Additive Manufacturing of SiCN Ceramic Matrix for SiC Fiber Composites by Flash Pyrolysis of Nanoscale Polymer Films”. *J. Am. Ceram. Soc.* 99.6 (2016), pp. 1855–1858.

[28] R. Riedel et al. “Silicon-Based Polymer-Derived Ceramics: Synthesis Properties and Applications - A Review”. *Journal of the Ceramic Society of Japan* 114.6 (2006), pp. 425–444.

[29] Z. C. Eckel et al. “Additive manufacturing of polymer-derived ceramics”. *Science* 351.6268 (2016), pp. 58–62.

[30] Y. Katoh et al. “Properties and radiation effects in high-temperature pyrolyzed PIP-SiC/SiC”. *Journal of Nuclear Materials* 289 (2001), pp. 42–47.

[31] *Storage and Handling Instructions - SMP-10, RD-201, RD-388: The Curing and Pyrolysis of Starfire® SMP Series Polymers, Rev 19*. Starfire® Systems. Glenville, New York, 2009.

[32] C. H. Park and L. Woo. “Modeling void formation and unsaturated flow in liquid composite molding processes: a survey and review”. *J. Reinf. Plast. Compos.* 30.11 (2011), pp. 957–977.

[33] Y.-T. Chen, C. W. Macosko, and H. T. Davis. “Wetting of fiber mats for composites manufacturing: II. Air entrapment model”. *AlChE J.l* 41.10 (1995), pp. 2274–2281.

[34] J. S. Leclerc and E. Ruiz. “Porosity reduction using optimized flow velocity in Resin Transfer Molding”. *Composites Part A* 39.12 (2008), pp. 1859–1868.

[35] L. Skartsis, J. L. Kardos, and B. Khomami. “Resin flow through fiber beds during composite manufacturing processes. Part I: Review of Newtonian flow through fiber beds”. *Polym. Eng. Sci.* 32.4 (1992), pp. 221–230.

[36] M. K. Um and W. I. Lee. “A Study on Permeability of Unidirectional Fiber Beds”. *J. Reinf. Plast. Compos.* 16.17 (1997), pp. 1575–1590.

[37] D. Shou, L. Ye, and J. Fan. “On the longitudinal permeability of aligned fiber arrays”. *J. Compos. Mater.* 49.14 (2015), pp. 1753–1763.

[38] B. Yang and T. Jin. “Micro-geometry Modeling Based on Monte Carlo and Permeability Prediction of Yarn”. *Polym. Polym. Compos.* 22.3 (2014), pp. 253–260.

[39] X. Chen and T. Papathanasiou. “Micro-scale modeling of axial flow through unidirectional disordered fiber arrays”. *Compos. Sci. Technol.* 67.7 (2007), pp. 1286–1293.

[40] S. Amico and C. Lekakou. “An experimental study of the permeability and capillary pressure in resin-transfer moulding”. *Compos. Sci. Technol.* 61.13 (2001), pp. 1945–1959.

[41] K. M. Pillai. “Modeling the Unsaturated Flow in Liquid Composite Molding Processes: A Review and Some Thoughts”. *J. Compos. Mater.* 38.23 (2004), pp. 2097–2118.

[42] B. R. Gebart. “Permeability of unidirectional reinforcements for RTM”. *J. Compos. Mater.* 26.8 (1992), pp. 1100–1133.

[43] N. Naik, M. Sirisha, and A. Inani. “Permeability characterization of polymer matrix composites by RTM/VARTM”. *Prog. Aerosp. Sci.* 65 (2014), pp. 22–40.

[44] V. H. Hammond and A. C. Loos. “The effects of fluid type and viscosity on the steady-state and advancing front permeability behavior of textile preforms”. *J. Reinf. Plast. Compos.* 16.1 (1997), pp. 0050–0072.

[45] J. G. I. Hellström, V. Frishfelds, and T. S. Lundström. “Mechanisms of flow-induced deformation of porous media”. *J. Fluid Mech.* 664 (2010), pp. 220–237.

[46] A. W. Chan, D. E. Larive, and R. J. Morgan. “Anisotropic permeability of fiber preforms: constant flow rate measurement”. *J. Compos. Mater.* 27.10 (1993), pp. 996–1008.

[47] C. Lekakou et al. “Measurement techniques and effects on in-plane permeability of woven cloths in resin transfer molding”. *Composites Part A* 27A (1996), pp. 401–408.

[48] W. a. Young et al. “Analysis of resin injection molding in molds with preplaced fiber mats. II: Numerical simulation and experiments of mold filling”. *Polymer Composites* 12.1 (1991), pp. 30–38.

[49] Sun Kyoung Kim and I. M. Daniel. “Observation of Permeability Dependence on Flow Rate and Implications for Liquid Composite Molding”. *Journal of Composite Materials* 41.7 (2007), pp. 837–849.

[50] Y. Wielhorski, A. B. Abdelwahed, and J. Bréard. “Theoretical Approach of Bubble Entrapment Through Interconnected Pores: Supplying Principle”. *Transport Porous Med.* 96.1 (2013), pp. 105–116.

[51] J. Schell et al. “Numerical prediction and experimental characterisation of meso-scale-voids in liquid composite moulding”. *Composites Part A: Applied Science and Manufacturing* 38.12 (2007), pp. 2460–2470.

[52] Y.-T. Chen, H. T. Davis, and C. W. Macosko. “Wetting of fiber mats for composites manufacturing: I. Visualization experiments”. *AIChE Journal* 41.10 (1995), pp. 2261–2273.

[53] S. Hernández et al. “Effect of curing cycle on void distribution and interlaminar shear strength in polymer-matrix composites”. *Compos. Sci. Technol.* 71.10 (2011), pp. 1331–1341.

[54] T. Mesogitis, A. Skordos, and A. Long. “Uncertainty in the manufacturing of fibrous thermosetting composites: A review”. *Composites Part A* 57 (2014), pp. 67–75.

[55] Y. K. Hamidi, L. Aktas, and M. C. Altan. “Formation of Microscopic Voids in Resin Transfer Molded Composites”. *J. Eng. Mater. Technol.* 126.4 (2004), p. 420.

[56] S. C. Amico. “Permeability and Capillary Pressure in the Infiltration of Fibrous Porous Media in Resin Transfer Moulding”. PhD thesis. University of Surrey, 2000.

[57] Y. Ledru et al. “Coupled visco-mechanical and diffusion void growth modelling during composite curing”. *Compos. Sci. Technol.* 70.15 (2010), pp. 2139–2145.

[58] J. L. Kardos, M. P. Duduković, and R. Dave. “Void growth and resin transport during processing of thermosetting—Matrix composites”. In: *Epoxy resins and composites IV*. Springer, 1986, pp. 101–123.

[59] A. C. Loos and G. S. Springer. “Curing of Epoxy Matrix Composites”. *Journal of Composite Materials* 17 (1983), pp. 135–169.

[60] Y. Eom et al. “Stress-Initiated Void Formation During Cure of a Three-Dimensionally Constrained Thermoset Resin”. *Polymer engineering and science* 41.3 (2001), pp. 492–503.

[61] T. S. Lundström and B. R. Gebart. “Influence From Process Parameters on Void Formation in Resin Transfer Molding”. *Polymer Composites* 15.1 (1994), pp. 25–33.

[62] J. W. Hutchinson and Z. Suo. “Mixed mode cracking in layered materials”. In: *Advances in Applied Mechanics*. Vol. 29. 1992, pp. 63–191.

[63] S. Ho and Z. Suo. “Tunneling cracks in constrained layers”. *Transactions of the ASME* 60 (1993), pp. 890–894.

[64] V. B. Shenoy, A. F. Schwartzman, and L. B. Freund. “Crack patterns in brittle thin films”. *International journal of fracture* 103.1 (2000), pp. 1–17.

[65] A. R. Akisanya and N. A. Fleck. “Analysis of a wavy crack in sandwich specimens”. *International journal of fracture* 55.1 (1992), pp. 29–45.

[66] M.-Y. He and J. W. Hutchinson. “Kinking of a crack out of an interface”. *Transactions of the ASME* 56 (1989), pp. 270–278.

[67] J. Rice. “Elastic fracture mechanics concepts for interfacial cracks”. *Transactions of the ASME* 55 (1988), pp. 98–103.

[68] A. R. Akisanya and N. A. Fleck. “Brittle fracture of adhesive joints”. *International Journal of Fracture* 58.2 (1992), pp. 93–114.

[69] N. Larson and F. Zok. “Insights from in-situ X-ray computed tomography during axial impregnation of unidirectional fiber beds”. *Composites Part A* 107 (2018), pp. 124–134.

[70] S. C. Amico and C. Lekakou. “Axial impregnation of a fiber bundle. Part 2: theoretical analysis”. *Polym. Compos.* 23.2 (2002), pp. 264–273.

[71] A. Shojaei. “An Experimental Study of Saturated and Unsaturated Permeabilities in Resin Transfer Molding Based on Unidirectional Flow Measurements”. *J. Reinf. Plast. Compos.* 23.14 (2004), pp. 1515–1536.

[72] J. Vilà et al. “An in situ investigation of microscopic infusion and void transport during vacuum-assisted infiltration by means of X-ray computed tomography”. *Compos. Sci. Technol.* 119 (2015), pp. 12–19.

[73] L. V. Interrante, C. Whitmarsh, and W. Sherwood. “Fabrication of SiC matrix composites by liquid phase infiltration with a polymeric precursor”. *Mater. Res. Soc. Symp. Proc.* 365 (1995), pp. 139–146.

[74] K. J. Ahn, J. C. Seferis, and J. C. Berg. “Simultaneous measurements of permeability and capillary pressure of thermosetting matrices in woven fabric reinforcements”. *Polym. Compos.* 12.3 (1991), pp. 146–152.

[75] D. Chandra and S. Yang. “Capillary-Force-Induced Clustering of Micropillar Arrays: Is It Caused by Isolated Capillary Bridges or by the Lateral Capillary Meniscus Interaction Force?” *Langmuir* 25.18 (2009), pp. 10430–10434.

[76] D. Chandra and S. Yang. “Stability of High-Aspect-Ratio Micropillar Arrays against Adhesive and Capillary Forces”. *Acc. Chem. Res.* 43.8 (2010), pp. 1080–1091.

[77] C. Duprat et al. “Wetting of flexible fibre arrays”. *Nature* 482.7386 (2012), pp. 510–513.

[78] J. Bico et al. “Elastocapillary coalescence in wet hair”. *Nature* 432 (2004), p. 690.

[79] C. Py et al. “3D aggregation of wet fibers”. *EPL* 77.4 (2007), p. 44005.

[80] N. M. Larson, C. Cuellar, and F. W. Zok. “X-ray computed tomography of microstructure evolution during matrix impregnation and curing in unidirectional fiber beds”. *Composites Part A* (2018).

[81] V. Michaud. “A Review of Non-saturated Resin Flow in Liquid Composite Moulding processes”. *Transport in Porous Media* 115 (3 2016), pp. 581–601.

[82] D. Salvatori et al. “Permeability and capillary effects in a channel-wise non-crimp fabric”. *Composites Part A: Applied Science and Manufacturing* 108 (2018), pp. 41–52.

[83] J. Hemmer et al. “Unloading during the infusion process: Direct measurement of the dual-scale fibrous microstructure evolution with X-ray computed tomography”. *Composites Part A* 115 (2018), pp. 147–156.

[84] D. Gürsoy et al. “TomoPy: a framework for the analysis of synchrotron tomographic data”. *J. Synchrotron Rad.* 21 (2014), pp. 1188–1193.

[85] C. Andraud et al. “Local entropy characterization of correlated random microstructures”. *Physica A* 235 (1997), pp. 307–318.

[86] H. Bale et al. “Characterizing Three-Dimensional Textile Ceramic Composites Using Synchrotron X-Ray Micro-Computed-Tomography”. *J. Am. Ceram. Soc.* 95.1 (2012). Ed. by R. Kerans, pp. 392–402.

[87] J. H. Kinney et al. “X-ray tomographic study of chemical vapor infiltration processing of ceramic composites”. *Science* 260.5109 (1993), pp. 789–792.

[88] A. Haboub et al. “Tensile testing of materials at high temperatures above 1700° C with in situ synchrotron X-ray micro-tomography”. *Review of Scientific Instruments* 85.8 (2014), p. 083702.

[89] J. Yin et al. “The effects of SiC precursors on the microstructures and mechanical properties of SiC_f/SiC composites prepared via polymer impregnation and pyrolysis process”. *Ceram. Int.* 41.3 (2015), pp. 4145–4153.

[90] S. Kaur et al. “Single-source-precursor synthesis of novel V_8C_7/SiC(O)-based ceramic nanocomposites”. *J. Eur. Ceram. Soc.* 36.15 (2016), pp. 3553–3563.

[91] V. Proust et al. “Polymer-derived Si-C-Ti systems: From titanium nanoparticle-filled polycarbosilanes to dense monolithic multi-phase components with high hardness”. *J. Eur. Ceram. Soc.* 36.15 (2016), pp. 3671–3679.

[92] A. Rahman, S. C. Zunjarrao, and R. P. Singh. “Effect of degree of crystallinity on elastic properties of silicon carbide fabricated using polymer pyrolysis”. *J. Eur. Ceram. Soc.* 36.14 (2016), pp. 3285–3292.

[93] *TriboIndenter® Users Manual*. Minneapolis: Hysitron Incorporated, 2003.

[94] H. S. Barnard et al. “Synchrotron X-ray Micro Tomography at the Advanced Light Source: In-Situ Sample Environments for Advanced Aerospace Materials”. *Microscopy and Microanalysis* 24.S2 (2018), pp. 444–445.